

# Politecnico di Torino

Corso di Laurea Magistrale in Ingegneria Civile



Tesi di Laurea Magistrale

## **EXPERIMENTAL MODAL ANALYSIS OF STRUCTURAL SYSTEMS BY USING THE VECTOR FITTING METHOD**

**Relatore:** Prof. Ing. Rosario Ceravolo

**Candidato:** Giulia Calamai

**Correlatori:** Ing. Luca Zanotti Fragonara

Ing. Marco Civera

**ANNO ACCADEMICO 2018/2019**



# Index

1	Introduction .....	1
1.1	Thesis structure .....	2
1.2	Aim and objectives.....	3
2	Theoretical background: signal processing .....	4
2.1	Fourier analysis .....	4
2.2	Impulse Response Function (IRF).....	5
2.3	The Laplace Domain. Transfer Function .....	6
2.4	The Frequency Response Function (FRF).....	8
2.5	Frequency response functions in terms of displacement,.....	8
	velocity and acceleration.....	8
2.6	Properties of FRF .....	10
3	System identification.....	12
3.1	General classification .....	12
3.2	Frequency Domain Methods .....	14
3.3	Time Domain Methods.....	16
4	Vector Fitting algorithm.....	18
4.1	State of art .....	18
4.2	Comparison between electronic and mechanical systems.....	18
4.3	Basics of Vector Fitting.....	22
4.4	Poles identification.....	23
4.4.1	Selection of initial poles.....	24
4.4.2	Pole-zero.....	25
4.4.3	Poles location .....	27
4.4.4	Poles stability .....	30
4.5	Residue identification.....	31
4.6	Fast and Relaxed Implementation of Vector Fitting Method.....	32

4.7	Weighting.....	34
4.8	Vector Fitting state space model .....	35
4.9	Root Mean Squared Error .....	36
5	Modal Analysis with Vector Fitting.....	37
5.1	Modal Analysis: numerical and experimental approach .....	37
5.2	Modal parameters.....	39
5.2.1	Estimation of modal parameters.....	39
5.3	Modal Assurance Criterion (MAC).....	40
5.4	Model Order .....	40
5.5	Stabilization diagram.....	40
5.6	Clustering .....	41
6	Numerical tests.....	43
6.1	3Dof frame .....	43
6.2	Noise problems.....	52
6.3	9Dof Frame .....	53
6.3.1	Systematic study.....	53
6.3.1	Simulations without noise .....	53
6.3.2	Simulations with noise .....	57
6.4	Analysis of results .....	62
6.4.1	Noise in input and output signals .....	63
6.4.2	Noise in input signal.....	64
6.4.3	Noise in output signals .....	65
7	Experimental tests .....	67
7.1	Preliminary tests.....	67
7.1.1	Prototype HAR Wing.....	67
7.1.2	Cantilever box beam.....	76
7.2	Three storey structure.....	88
7.2.1	Structure description.....	88

7.2.2	Data acquisition system.....	90
7.2.3	Pre-processing phase.....	92
7.2.4	System identification.....	95
7.3	Masonry arch bridge.....	111
7.3.1	Description of case study .....	111
7.3.2	Preliminary studies.....	115
7.3.3	Experimental test.....	118
7.3.4	Pre-processing phase.....	125
7.3.5	System identification.....	128
8	Conclusion.....	138
	Figure Index.....	139
	References.....	145





# 1 Introduction

The increasingly requested maintenance and redevelopment of the architectural and infrastructural heritage has led to the use of structural health monitoring, as a useful tool for assessing the state of conservation of the structures and their behaviour, both in operating conditions and in specific conditions, such as in presence of an earthquake. This method is fundamental to increase the knowledge of the overall response of the structure and to identify any structural problems.

Therefore, the use of monitoring in the study of civil structures is increasing and it involves both existing and new construction structures. Thanks to this approach, it is possible to assess the structural reliability allowing higher durability and resistance. Unnecessary periodical inspections can be avoided leading to a reduction of maintenance costs.

For this reason, in the last years the research of new methods, also used in other engineering research ambits, has become very important.

This thesis focuses on the implementation of an algorithm in the frequency domain, known as the Vector Fitting (VF), commonly used in electronic engineering, such as high-voltage power systems, high-speed electronics and microwave systems.

Since its introduction, Vector Fitting has gained much popularity due to its simplicity, robustness and higher performance. The Vector Fitting scheme calculates poles and residues of a rational function in order to fitting the raw data points. The optimization process is relaxed to a weighted linear least squares problem, which is reformulated and solved iteratively until convergence.

This work shows the implementation of this algorithm under the influence of typical parameters of civil structures. In particular, modal analysis and estimation of modal parameters by using Vector Fitting are described.

Firstly, the Vector Fitting method is applied on numerical case studies in order to validate the new implementation. The effectiveness of the proposed method is verified on numerically-simulated noisy data. The influence of high level of noise on the Vector Fitting's results is discussed.

Subsequently, it is applied on experimental data sets related to different cases study of structures developed in laboratory. The confidence of the results has been estimated by using modal criteria, such as Modal Assurance Criterion (MAC), stabilisation diagram and statistical relations.

## 1.1 Thesis structure

This work focuses on the application of Vector Fitting algorithm on structural dynamic identification.

After introducing the basics and the importance of signals theory, the thesis outlines the motivation of implementation of Vector Fitting and the use of it in a new engineering field. To this purpose, the analogies between mechanical and electrical system are highlighted. Then, the state of art of method are described and the last implementation of it, called Fast Relaxed Vector Fitting (FRVF), which will be used for the tests in this dissertation. Subsequently, this section focuses on the physical definitions of poles and residue and on the physical meaning of linear system's stability.

Then, we present the theory underlying dynamic characterization. Modal analysis and estimation of modal parameters from poles and residue of Vector Fitting are described, dwelling on the state space of algorithm.

The validation of Vector Fitting is realized, firstly on a case of 3Dof frame and then on 9Dof frame under an artificial simulation force. In particular, in this chapter the influence of noise in input and output's signals is analysed. It is very interesting to note how the algorithm's results can differ from the real ones. This difference is attributed to the frequency response affected by noise data and it will be demonstrated by specific statistical parameters and relations.

Then the modal parameters for model validation are illustrated such as Modal Assurance Criterion (MAC), that compares numerical and experimental modal shapes, and stabilization and cluster diagram.

Finally, the dissertation ends with the application of this algorithm at different cases studies on experimental data sets in order to point out the strengths and limitations of Vector Fitting method. The first two cases are an aluminium prototype airwing (HAR) and a cantilever box beam with two u-shaped slots, both developed in the Cranfield University Laboratory. The choice was made in order to start with two simpler models and then to continue more complex ones.

The second case consists of an aluminium three-storey frame; data come from Literature as a well-known experiment performed at the Engineering Institute (EI) at Los Alamos National Laboratory (LANL). 17 scenarios of damage are simulated either with a reduction of stiffness of columns or addition mass (linear damage) or with an introduction of nonlinearities into the structure using a bumper and a suspended column.

The last experimental test is a masonry arch bridge formerly placed in the laboratory of the Department of Structural, Geotechnical and Building Engineering of the Polytechnic of Turin. In

this case, the high number of degrees of freedom, the non-linearity of material, the noise in measured data will lead to a complex analysis.

## **1.2 Aim and objectives**

The general aims of this thesis are to:

- Explain the basics of signals analysis;
- Evaluate Frequency Response Function as ratio of Fast Fourier Transforms between output and input of the system;
- State of art of the proposed algorithm, the so-called Vector Fitting, already used in electronic engineering to identify circuits;
- Highlight some useful mechanical-electrical systems analogies;
- Validate of Vector Fitting for structural dynamic identification;
- Analyse Vector Fitting behaviour under specific conditions in different numerical cases studies;
- Investigate variations of Vector Fitting results with increasing of noise level in input/output signals;
- Explain the main concepts regarding Modal Analysis and the estimation of modal parameters;
- Application of Vector Fitting on experimental cases studies;
- Investigate correlations between different types of data;
- Understand Vector Fitting behaviour under damage specific conditions;
- Apply of stabilisation and clustering diagrams on Vector Fitting method;
- Use of statistical procedures to analyse the results;
- Compare between numerical and experimental data

# 2 Theoretical background: signal processing

In this section some notions of signals analysis are recalled. They are necessary for the definition of the Frequency Response Function, which is in turn fundamental for the rest of this discussion. Starting from this formulation, the methods in the frequency domain are capable to obtain the dynamic characteristics of the structures.

## 2.1 Fourier analysis

Periodic signals with period  $T_0$  can be written as a sum of harmonic functions for every instant of time  $t$ , through the Fourier series:

$$x(t) = \sum_{k=-\infty}^{\infty} X_k(\omega) e^{jk\omega t} \quad (1)$$

where the  $X_k$  coefficients are defined as:

$$X_k(\omega) = \frac{1}{T_0} \int_{-\frac{T_0}{2}}^{\frac{T_0}{2}} x(t) \cdot e^{-jk\frac{2\pi}{T_0}t} dt \quad (2)$$

When they are non-periodic, it is not possible to use Fourier series. Considering the limit which is approached by a Fourier series as the period becomes infinite, it is found that an arbitrary function  $x(t)$  can be defined by an integral  $X_k(\omega)$ :

$$X_k(\omega) = \int_{-\infty}^{\infty} x(t) \cdot e^{-j\omega t} dt \quad (3)$$

Equation (3) constitutes what is defined as a Fourier transform. The Fourier transform of the response is the product of the complex frequency response function  $H(\omega)$  and the Fourier transform of the excitation force (Maia & Silva, 1997).

$$X(\omega) = H(\omega) F(\omega) \quad (4)$$

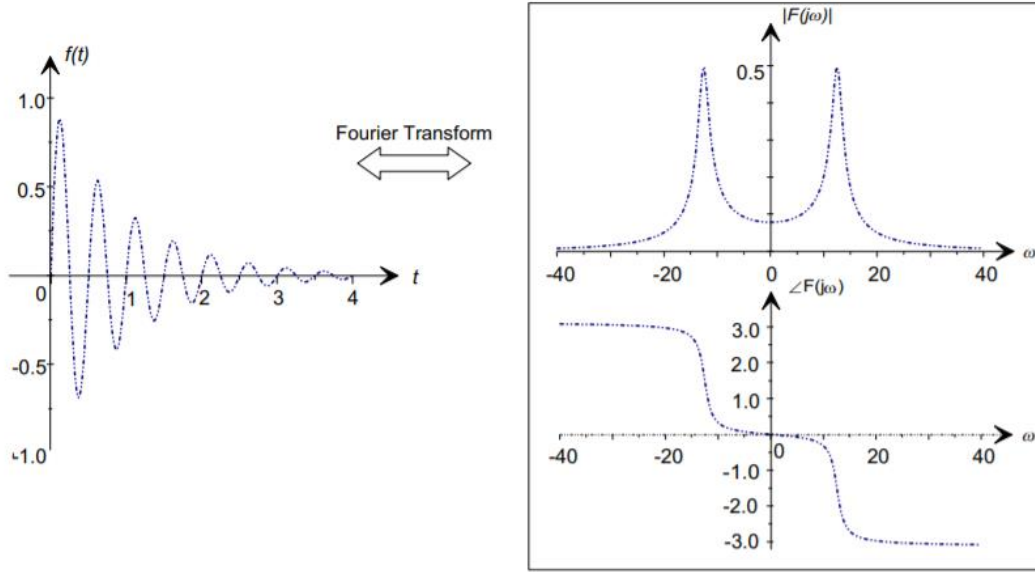


Figure 1. A damped sinusoidal function and its spectrum (mirrored function at negative frequencies shown for completeness)

For the estimation of the Fourier coefficient corresponding to the  $k^{th}$  harmonic (with time interval  $\Delta t$ ) the Equation (2) should be fitted as follow:

$$X_k = \frac{1}{N\Delta t} \sum_{n=0}^{N-1} x(n\Delta t) \cdot e^{-jk\frac{2\pi}{N\Delta t}n\Delta t} = \frac{1}{N} C_k \quad (5)$$

where:

$$C_k = \sum_{n=0}^{N-1} x(n\Delta t) \cdot e^{-jk\frac{2\pi}{N}n} \quad (6)$$

is the Fast Fourier Transform (FFT), also called Discrete Transform.

## 2.2 Impulse Response Function (IRF)

The answer to a impulsive input is defined by the *unit impulse response function* (IRF). It can be evaluated from the definition of Dirac  $\delta$ -function:

$$f(t) = \delta(t - \tau) \quad (7)$$

where is equal to zero for all values of  $t$  except for  $t = \tau$ , where:

$$\lim_{\Delta t \rightarrow 0} \int_{\tau}^{\tau+\Delta t} f(t) dt = 1 \quad (8)$$

If indicates with  $f(t)$  the input submitted to the system and with  $y(t)$  the response, the unit impulse response function is defined by the following expression:

$$h(t) = y(t) \text{ when } f(t) = \delta(t) \quad (9)$$

where  $t$  is the time measured from the instant in which the function  $\delta$  is applied.

For an arbitrary input  $f(t)$ , the response of the system  $x(t)$  is given from the convolution integral:

$$x(t) = \int_{-\infty}^{\infty} h(t) f(t - \tau) d\tau \quad (10)$$

This is the convolution of the forcing function  $f(t)$  with the impulse response function  $h(t)$ . Thus, may be written as:

$$x(t) = h(t) * f(t) \quad (11)$$

where the symbol  $*$  shows the convolution operation. Taking the Fourier transform of the equation (11):

$$\mathcal{F}[h(t) * f(t)] = \mathcal{F}[h(t)] \mathcal{F}[f(t)] \quad (12)$$

And we obtain the same equation found before (4):

$$X(\omega) = H(\omega) F(\omega) \quad (13)$$

## 2.3 The Laplace Domain. Transfer Function

One way of deriving the dynamic response of a system under different types of excitation, including obviously the periodic and harmonic ones, is by means of the Laplace transform method. The Laplace transform method converts differential equations into analytical ones which are easier to manipulate (Maia & Silva, 1997).

The Laplace transform of a function  $x(t)$ , denoted as  $X(s)$  is defined as:

$$X(s) = \mathcal{L}[x(t)] = \int_0^{+\infty} e^{-st} x(t) dt \quad (14)$$

where  $s$  is a complex parameter called the *Laplace variable*. Taking the Laplace transform to equation of motion:

$$\mathcal{L}[m\ddot{x}(t) + c\dot{x}(t) + kx(t)] = m[s^2X(s) - sx(0) - \dot{x}(0)] + c[sX(s) - x(0)] + kX(s) = (ms^2 + cs + k)X(s) - msx(0) - m\dot{x}(0) - cx(0) \quad (15)$$

and considering also:

$$\mathcal{L}[f(t)] = F(s) \quad (16)$$

or

$$(ms^2 + cs + k)X(s) = F(s) + m\dot{x}(0) + (ms + c)x(0) \quad (17)$$

Where  $x(0)$  and  $\dot{x}(0)$  are initial displacement and velocity respectively and the right side of the equation (17) can be regarded as a generalised transformed excitation. If the initial conditions are

zero, which equivalent to ignoring the solution of the homogeneous equation, the ratio of the transformed response to the transformed force can be defined as (Maia & Silva, 1997):

$$H(s) = \frac{X(s)}{F(s)} \quad (18)$$

where:

$$H(s) = \frac{1}{ms^2 + cs + k} \quad (19)$$

is called system transfer function of a SDOF system.  $H(s)$  is a complex function of  $s$  and represented as a surface in the Laplace Domain (Maia & Silva, 1997). The values  $s_1$  and  $s_2$  of the characteristic equation can be written:

$$s_{1,2} = \sigma \pm i\omega_d \quad (20)$$

with

$$\sigma = -\xi\omega_n \quad (21)$$

and

$$\omega_d = \omega_n\sqrt{1 - \xi^2} \quad (22)$$

The transfer function can now be rewritten as:

$$H(s) = \frac{1}{m(s - s_1)(s - s_2)} \quad (23)$$

where  $s_1 = \sigma + i\omega_d$  and  $s_2 = s_1^* = \sigma - i\omega_d$  are the so-called poles of the transfer function:

$$H(s) = \frac{1}{m(s - s_1)(s - s_2)} = \frac{A}{(s - s_1)} + \frac{A^*}{(s - s_1^*)} \quad (24)$$

where the complex conjugates  $A$  and  $A^*$  are defined as the residues of the transfer function.

The residue can be easily found and are given by:

$$A = -\frac{1}{i 2 m \omega_d} \quad (25)$$

The residue represents an imaginary value which expresses the robustness of the mode.

## 2.4 The Frequency Response Function (FRF)

The Laplace domain describes the system under analysis in terms of poles and residues. Evaluating the transfer function only in the frequency domain, it is possible to obtain (Maia & Silva, 1997):

$$H(\omega) = H(s)|_{s=i\omega} = \left[ \frac{A}{(s-s_1)} + \frac{A^*}{(s-s_1^*)} \right] |_{s=i\omega} = \frac{A}{(i\omega-s_1)} + \frac{A^*}{(i\omega-s_1^*)} = \frac{A}{i(\omega-\omega_d)+\xi\omega_n} + \frac{A^*}{i(\omega+\omega_d)+\xi\omega_n} \quad (26)$$

Equation represents the partial fraction expansion form of the Frequency Response Function (FRF) of a SDOF system. The same transfer function can be obtained under the form more commonly presented in the literature:

$$H(\omega) = \frac{1}{(k-\omega^2m)+i\omega c} \quad (27)$$

Free vibration behaviour may be obtained assuming that the system was excited by an impulse type forcing function at time  $t=0$ . The impulse response function of a single-degree-of-freedom system can be estimated from (18) and (24) assuming zero initial conditions and that  $F(s) = 1$  for an impulse force.

$$X(s) = H(s)|_{F(s)=1} = \frac{A}{(s-s_1)} + \frac{A^*}{(s-s_1^*)} \quad (28)$$

## 2.5 Frequency response functions in terms of displacement, velocity and acceleration

In the previous section we have defined Frequency Response Function (FRF) as the ratio of the Fourier transform of the generic response (displacement, velocity, acceleration ...) e the Fourier transform of the applied force module.

The input and output can both be described in terms of displacement, velocity or acceleration and the relationship is explained as a ratio of motion/force or its inverse, force/motion (Silva, 1978). For this reason, the Frequency Response can be expressed in different forms. More precisely, the *receptance function*  $\alpha$  is defined as the relation between the transform of displacement  $y(t)$  of a point of the system and the Fourier transform forcing  $f(t)$  applied:

$$\alpha(\omega) = \frac{Y(\omega)}{F(\omega)} \quad (29)$$

In the same way we can call the *mobility function* that is the ratio between the derivative of the displacement  $y(t)$  and the force  $f(t)$ . Finally, the *inertance*  $A$  depends from the second derivative of displacement:

$$A(\omega) = \frac{\ddot{Y}(\omega)}{F(\omega)} \quad (30)$$

These three are by far the most commonly found definitions of FRF; they are shown in Figure 2:

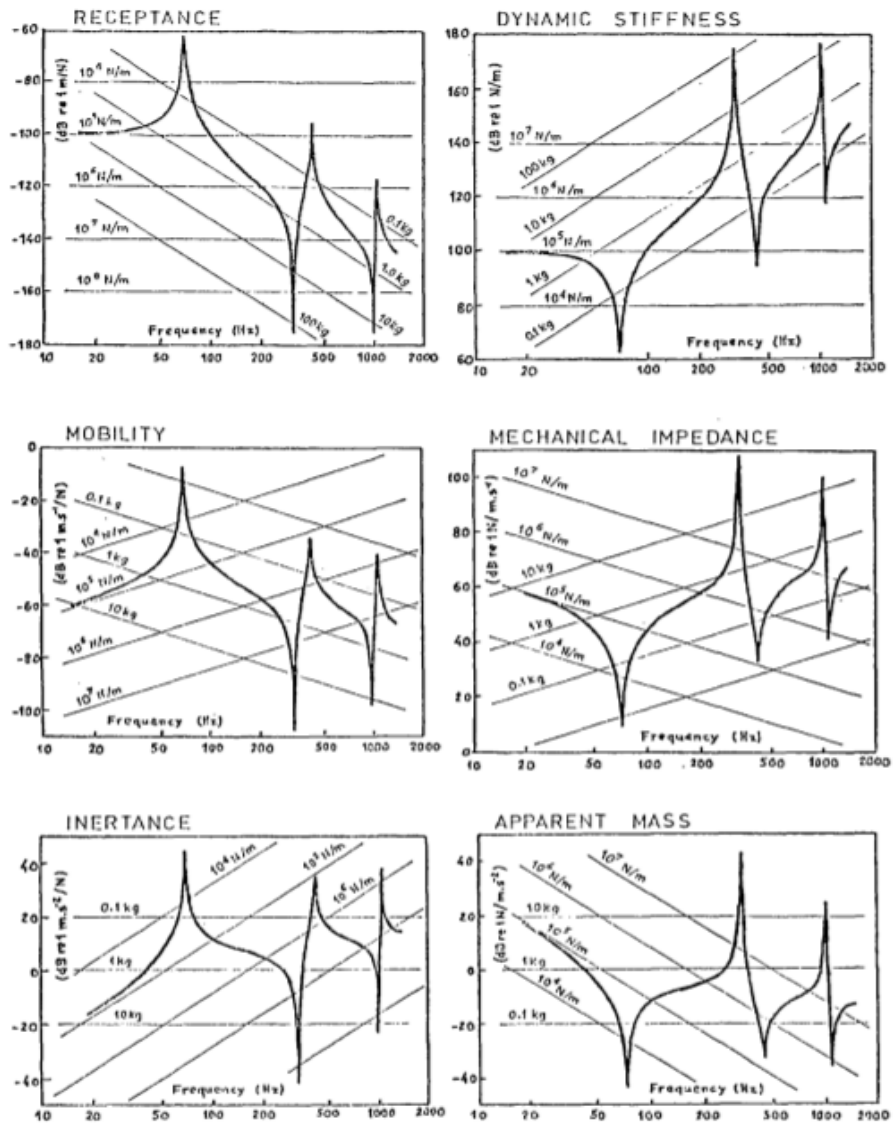


Figure 2. Receptance, mobility, inertance (Silva, 1978)

The inertance is related to receptance thanks to the relation:

$$A(\omega) = -\omega^2 \cdot \alpha(\omega) \quad (31)$$

## 2.6 Properties of FRF

The Frequency Response Function is a complex function of the frequency. It is described from three different quantities: real part, imaginary part and frequency. Complex number may, as usually done, also be expressed in terms of absolute value and phase angle; in this latter case we talk about *rectangular* coordinates, while the real and the imaginary part, when plotted versus the frequency, are generally referred to as the *polar* coordinates. In this way, it is usually convenient graphically representing the FRF in two separate plots, real and imaginary (Figure 3).

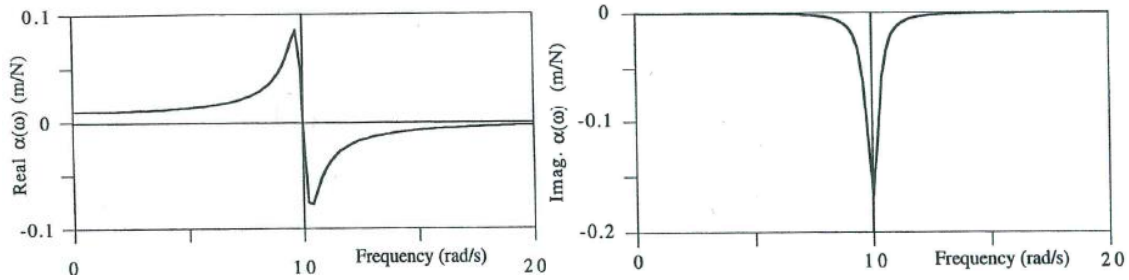


Figure 3. On the left the real part of receptance and on the right the imaginary part (example with  $m=1$  kg,  $k=100$  N/m and  $c=0.6$  Ns/m) (Maia & Silva, 1997)

It is important to note that the real part of the FRF cuts the frequency axis close to the peak, in the same frequency region, while the imaginary part presents a minimum. A second representation is defined as a Nyquist plot. As is defined in the book intituled “*Theoretical and Experimental Modal Analysis*” written by Maia and Silva:” A Nyquist plot shows on the complex plane the real part of an FRF against its imaginary part with frequency as an implicit variable. The advantage of Nyquist method is the circularity of an FRF on the complex plane, because has the particularity of improving the resonant region as the circular loop occurs only close to resonance.” Nyquist plot is shown in Figure 4.

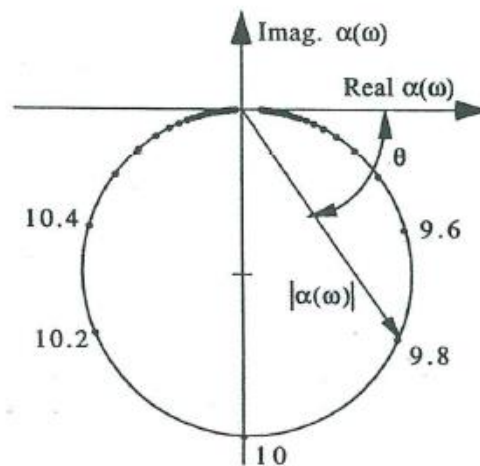


Figure 4. Nyquist plot of FRF (example with  $m=1$  kg,  $k=100$  N/m and  $c=0.6$  Ns/m) (Maia & Silva, 1997)

Now, the most usual representation of a frequency response function is the Bode plot, that shows magnitude and phase as a function of frequency (Figure 5). It is a common way to visualize the characteristic of the receptance  $\alpha(\omega)$  (Maia & Silva, 1997).

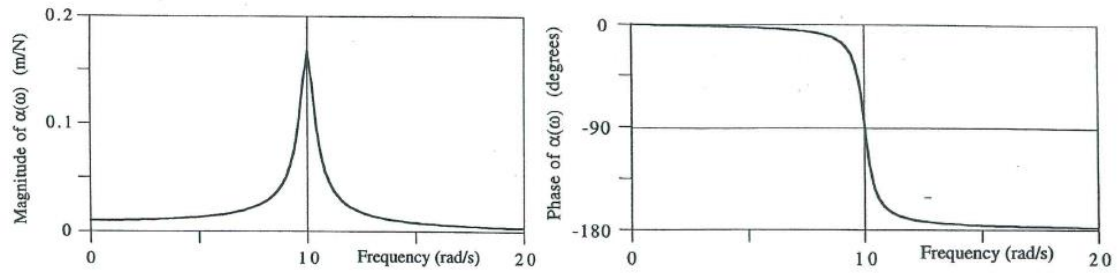


Figure 5. On the left the magnitude of receptance and on the right the phase (example with  $m=1$  kg,  $k=100$  N/m and  $c=0.6$  Ns/m) (Maia & Silva, 1997)

# 3 System identification

## 3.1 General classification

During the last years, researches have dedicate their time to the development of methods that aim to produce news techniques for systems identification. This research is based on the definition of Fast Fourier Transform (FFT) and to the enhancement in recent years of very powerful multi-channel spectrum analysers. In this way, it was possible to progress from very simple techniques to highly refined ones where data from multi-input excitation and multi-output responses (SIMO and MIMO respectively) are considered simultaneously. (Maia & Silva, 1997)

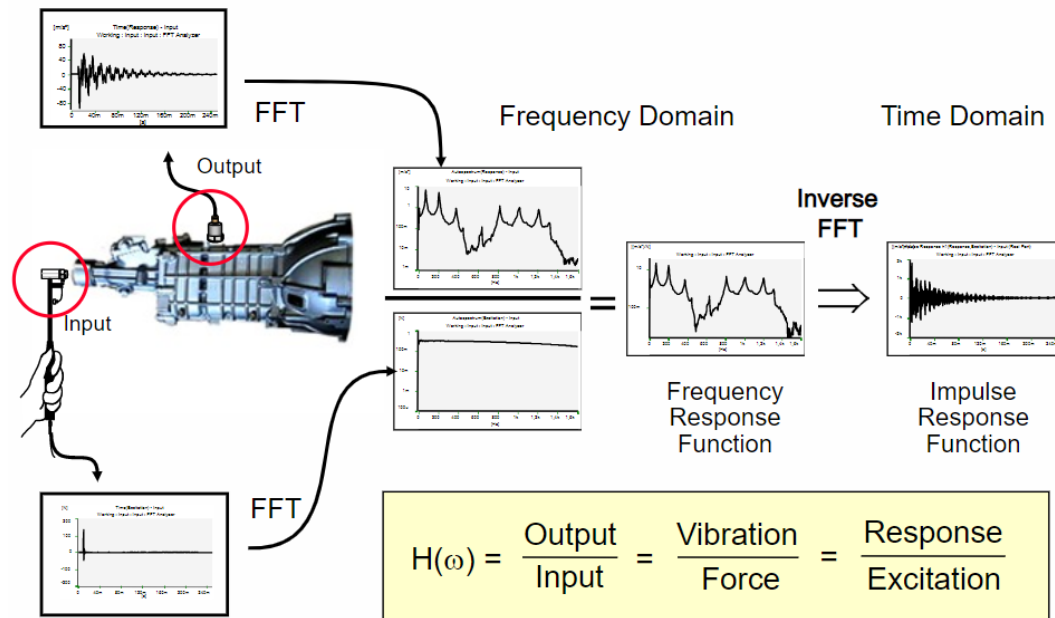


Figure 6. Definition of Transfer Function

The available modal identification methods can be classified according to different criteria. The most important group concerns the domain in which the data are considered. There are time-domain and frequency-domain methods. Time-domain models tend to have the best results when a structure possesses a large number of modes. Frequency-domain models tend to provide the successful when the frequency range of interest is limited and the number of modes is relatively small.

However, time domain methods have the disadvantage that they can only estimate modes inside the frequency range of analysis, and take no account of the residual effects of modes that lies outside the range. For this reason people returned to frequency-domain techniques, which can improve the confidence of the results considering residual terms or increasing the model order.

Time-domain and frequency domain methods can be divided into direct and indirect method. The indirect methods mean that the identification is based on the modal parameters such as natural frequencies, damping ratios, modal constants and their phases.

The direct methods mean that the identification is directly based on the general matrix equation of dynamic, the primitive equation from which all the methods are derived.

Other division consider the number of modes that can be analysed. In this way, we can have single-degree-of-freedom (SDOF) and multiple-degree-of-freedom (MDOF) analyses.

*“When a structure is tested in order to collect the measured data, we usually have a set of FRF’s. These FRFs are the result of exciting the structure at each selected point and measuring the response at several locations along the structure. Some modal analysis methods can be applied only to a single FRF at a time. These are called single-input-single-output (SISO) methods. Other methods allow for several FRFs to be analysed simultaneously, with responses taken at various points on the structure, but using one excitation point (SIMO). The philosophy behind this category of methods is that the natural frequencies and damping ratios do not vary (theoretically) from FRF to FRF and, thus, it should be possible to obtain a consistent and unique set of those properties by processing several FRFs at the same time” (Maia & Silva, 1997).*

Finally, there are methods usually called multi-input-multi-output (MIMO) methods that can process all FRFs simultaneously. Multi-input-single-output (MISO) analysis are also possible, but are not much used.

Another general classification is related to the type of excitation source which is applied in the experimental analysis. Vibration tests can be carried out by exciting the structure with shakers, hammer impacts, earthquakes or environmental vibrations such as the traffic in the case of bridges or wind. When both input and output response are known the system is defined as input-output. In the case of environmental vibration, the input force is unknown and we have output-only system.

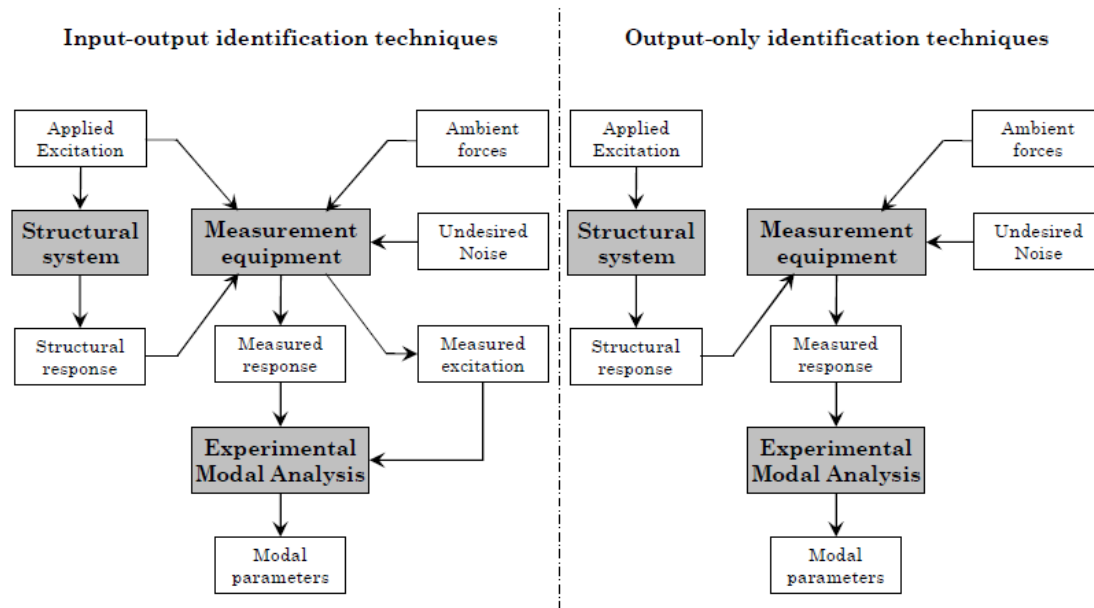


Figure 7. Schematic representation of the input-output and output-only identification methods ( Ruocci G. , 2009)

“Therefore, in the logic of the diagnostic monitoring design, the choice of the excitation source also entails the adopted modal identification technique. In the case of input-output identification techniques the target is the determination of the Frequency Function (FRF) of the system. The techniques operating in the frequency domain generally try to approximate the FRF by means of procedures like the curve fitting, whereas in the time domain identification methods are based on autoregressive models or Markov processes, as in the case of the realization algorithms. The output-only methods require the fulfilment of some hypotheses referred to the nature of the excitation and the dynamic response”. (Ruocci, 2009).

### 3.2 Frequency Domain Methods

After having introduced the main aspects of the techniques of structural identification and having defined the criteria for their classification it is useful to mention some of them in the frequency domain. As mentioned in the preceding section of this chapter, the algorithms in the frequency domain involve the acquisition of accelerations from the experimental tests usually providing the structure with one forced excitation. The methods defined in the frequency domain operate by obtaining the Function of Frequency Response (FRF) from which it is possible to identify modal parameters of the structure. FRFs are typically obtained by means of analysis using the Fast Fourier Transform (FFT).

Now some of the frequency domain methods are listed. Due to the enormous quantity of available methods, it is not possible to explain all of them in great details. Some of the most important method are:

- *Peak - Picking method (PP)*: this is the simplest known method for identifying the modal parameters of a structure. The natural frequencies are simply taken from the values of the peaks on the plots of the magnitude of the response. Damping is estimated from half power points only, considering the width of peaks. The mode shape are calculated from the ratio of the peak amplitudes. This method assumes that the modes are real and are well separated and if the damping is not very high. If that does not happen, the application of his method can be difficult.
- *The Circle-Fitting method* (Ewins, 2000): it is among the most widespread methods operating in the domain of frequency. It is based on the observation that, around a frequency of the system, the points of the complex function, if represented in the complex Nyquist plane, describe a circumference. The procedure consists therefore in trying to interpolate the circle with a circle produced by the  $r^{\text{th}}$  way of vibrating, with greater accuracy in the proximity of the resonance frequency.

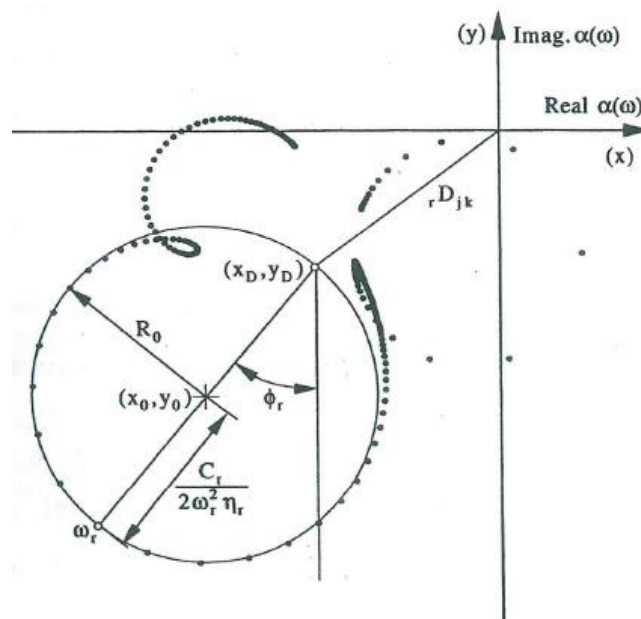


Figure 8. Nyquist plot of the receptance, showing the SDOF circle-fit approach (Maia & Silva, 1997)

- *The Rational Fraction Polynomial method (RFP)*: this is a method and it is now one of the most famous fitting technique in the frequency domain used in civil field. The formulation of the frequency response is defined in rational fraction form instead of the partial form. The rational fraction form is the ratio of two polynomials, where in general the orders of the numerator and denominator polynomials are independent of one another. "Because the resulting linear system of equations involves matrices that ill-conditioned, the rational fraction form of the FRF is expressed in terms of Orthogonal Polynomials.

For this reason, this method is also known as the Rational Fraction Orthogonal (RFOP).” (Maia & Silva, 1997)

The FRF, with N degrees of freedom and damping  $\xi$ , can be written by partial fraction form:

$$\alpha(\omega) = \sum_{r=1}^N \frac{A_r + i\omega B_r}{\omega_r^2 - \omega^2 + i2\xi_r \omega_r \omega} \quad (32)$$

where  $A_r$  and  $B_r$  are constants. The expression (32) can be explained also as a ratio of two polynomials in  $i\omega$ :

$$\alpha(\omega) = \frac{\sum_{k=0}^{2N-1} a_k (i\omega)^k}{\sum_{k=0}^{2N} b_k (i\omega)^k} \quad (33)$$

The RFP and PP are proven frequency methods in civil and mechanical fields and will be used in the Chapter 7 in order to compare the results of Vector Fitting algorithm.

### 3.3 Time Domain Methods

For completeness, two most important algorithms in the time domain are also illustrated.

*Eigensystem Realization Algorithm (ERA)*: it is time-domain method that is applied to free decay signals (damped free oscillations). The ERA method adopts the state-space formulation associated to the equation of motion which leads as follow (Juang and Pappa 1984):

$$\{u_{k+1}\} = [A]\{u_k\} + [B]\{\delta_k\} \quad k = 0,1,2, \dots \quad (34)$$

where

$\{u_k\}$  = state vector

$\{\delta_k\}$  = impulsive excitation

Assuming that the initial time  $\{u_0\} = \{0\}$  and  $\{\delta_0\} = \{1,0, \dots, 0\}$  and  $\{\delta_0\} = \{0\}$  and by considering all loading points, for all subsequent time intervals:

$$[X_k] = [A]^{k-1}[B] \quad k > 0 \quad (35)$$

The  $k$  Markov parameters  $[X_k]$  are the measured signals and can be organized in a Hankel matrix. This process is based on the determination of the  $[A]$  and  $[B]$  matrices from redundant data. There is an infinite number of solutions for the Eq. (34). “The aim is to obtain the realization that, whereas giving origin to the state space formulation with the lowest degree, still represents the dynamic behaviour of the structure. The system’s modal parameters are obtained by resolving the eigenvalue problem from the realized matrix  $[A]$ ” (Ceravolo & Abbiati, 2013). The ERA

method will be resumed later in the phase of analysis of masonry arch bridge in the Section 7.3 where the modal analysis with Vector Fitting is compared with that of ERA carried out in the laboratory of Politecnico di Torino.

*Stochastic Subspace Identification (SSI)*: it is an output-only method that requires the assumption that the input is a white Gaussian noise. It is a technique used for the identification of mechanical systems in which a linear model is adapted to the measurements from the study. The state space formulation associated to the equation of motion becomes:

$$\{u_{k+1}\} = [A]\{u_k\} + \{e_k\} \quad k = 0,1,2, \dots \quad (36)$$

SSI method starts by building large-block Hankel matrices from the output sequence, divided into past and future data matrices (Van Overschee and DeMoor 1996). “*The Kalman filter state sequence can be obtained by projecting the row space of the future block Hankel matrix into the row space of the past block Hankel matrix. This can be done using the concept of angles between subspaces. Once that state sequence is obtained, the estimation of the system’s modal parameters follows from solving a least-squares problem*” (Ceravolo & Abbiati, 2013). In Section 7.2 we will discuss the input- output implementation of SSI, called N4SID.

# 4 Vector Fitting algorithm

## 4.1 State of art

Vector Fitting (VF) is a method useful for approximating the state equations of a system by accurately locating its dominant poles and residues over an observed domain. The name “Vector Fitting” stems from how the method may be easily generalized to simultaneously fit a vector of system transfer functions. The method is commonly applied to the frequency domain where a scalar or vector transfer function is the assumed observation to be fitted. It is commonly used in microwave systems and high-speed electronics.

Vector Fitting (VF) has, since its first introduction in 1999 by B. Gustavsen and Semlyen, become an important applied technique for fitting a rational model to frequency domain data, thanks to its robust and efficient formulation, and enforcement of guaranteed stable poles. Their research was influenced by an earlier work published in 1963 by C. Sanathanan and J. Koerner in “*Transfer function synthesis as a ratio of two complex polynomials*,” where a procedure known as Sanathanan-Koerner (S-K) iterations demonstrated how to synthesize a transfer function as a ratio of two complex polynomials based on polynomial curve fitting.

From 1999 several implementations of Vector Fitting are realized and published.

In this dissertation the last implementation of VF is used which is published in 2008 by B. Gustavsen in the article intituled “*Macromodeling of Multiport Systems Using a Fast Implementation of the Vector Fitting Method*”. Last VF version is presented in Section 4.7 of this dissertation.

## 4.2 Comparison between electronic and mechanical systems

The term analogous can be used in different engineering fields where the systems can be express by the same mathematical, but with different physical meaning. The mechanical-electronic analogy has been detected very important to solve specific problems. This section demonstrates the dependence of the transfer functions in the two systems. To do it , two analogies exist: the mobility analogy, also called admittance analogy or Firestone analogy, can be both derived from the same equivalent electrical circuit, depending if voltage or current is considered, and the impedance analogy, also known as the Maxwell analogy. The impedance analogy is based on the concept that force and voltage are analogous, while the mobility analogy makes force and current analogous. Thus, the two analogies are the dual of each other; two different electrical networks are analogous to the mechanical system of interest and indeed they happen to be dual circuit of each other. Conversely, a unique electrical equation has two mechanical analogous, that is to say, a Force-Current and a Force-Voltage system; yet a more detailed discussion would be off-topic here.

In an electrical network system there are three passive elements: resistance, inductance and capacitance; and two active elements: the current generator and the voltage generator.

If we indicate with  $v(t)$  and  $i(t)$  the current and the tension, the following equations can be explained:

$$\text{Resistance } v(t) = R \cdot i(t) \quad (37)$$

$$\text{Inductance } v(t) = L \cdot \frac{di(t)}{dt} \quad (38)$$

$$\text{Capacitance } v(t) = \frac{1}{C} \cdot \int_0^t i(t)dt \quad (39)$$

As in electrical systems, even in mechanical systems (in a single degree of freedom) it is possible to identify the ideal elements that characterize them:

- Damping: dissipative friction element with symbol  $\beta$  since its characteristic parameter is the viscous friction coefficient [Force / Velocity];
- Mass: conservative element with symbol  $m$  with dimensions [Force / acceleration];
- Stiffness (spring): a conservative element with symbol  $k$ , elasticity coefficient with dimensions [Force / Displacement].

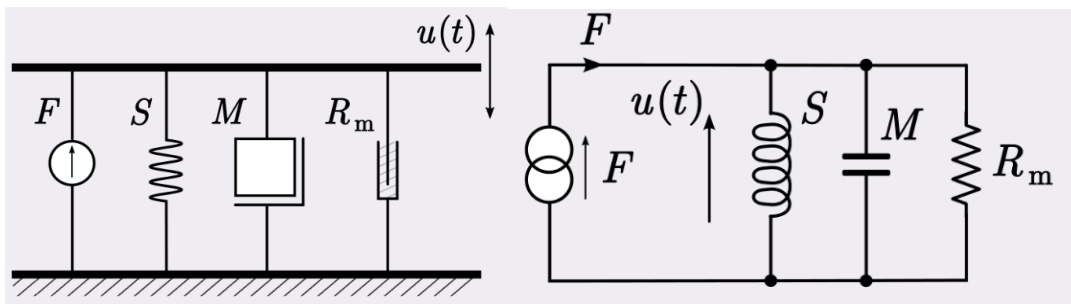


Figure 9. Mechanical and electrical analogy

For these quantities, indicating with  $F(t)$  the force and the  $w(t)$  the velocity, the following relations are reported:

$$\text{Damping } F(t) = \beta \cdot w(t) \quad (40)$$

$$\text{Mass } F(t) = m \cdot \frac{dw(t)}{dt} \quad (41)$$

$$\text{Stiffness } F(t) = k \cdot \int_0^t w(t)dt \quad (42)$$

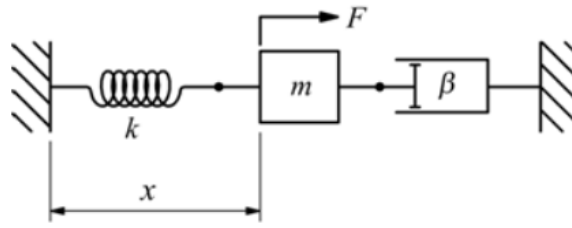


Figure 10. Mechanical system

Remembering that for Newton equation  $F(t) = m \cdot a$  with  $a = \frac{d\omega}{dt}$ , while for the stiffness the Hooke relation  $F(t) = k \cdot x$  with  $\omega(t) = \frac{dx}{dt} \rightarrow x = \int_0^t \omega(t) dt$ . Applying the Alembert principle we obtain the motion equation:

$$mx'' = -kx - \beta\omega + F(t) \quad (43)$$

$$F(t) = +mx'' + kx + \beta\omega \quad (44)$$

$$m \frac{d\omega}{dt} + \beta\omega + k \int \omega dt \quad (45)$$

For electrical systems the following equations are evaluated (Figure 11):

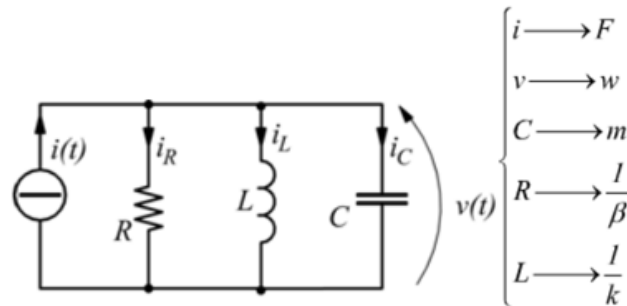


Figure 11. Electrical system: mobility analogy

$$i(t) = i_C + i_R + i_L \quad (46)$$

$$i(t) = C \frac{dv}{dt} + \frac{v}{R} + \frac{1}{L} \int v dt \quad (47)$$

This represents mobility analogy that makes force and current analogous. Instead, the relations that point out the impedance analogy which highlight the voltage and force analogous are reported below (Figure 12):

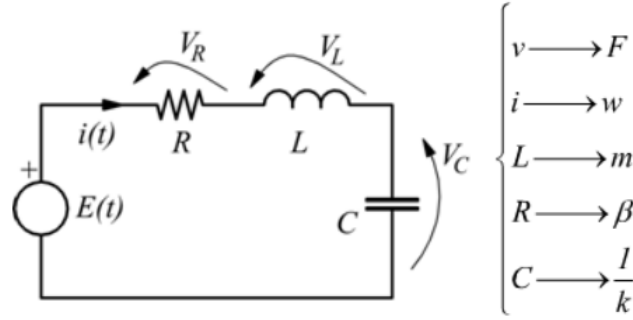


Figure 12. Electrical system: impedance analogy

$$V(t) = V_C + V_R + V_L \quad (48)$$

$$V(t) = L \frac{di}{dt} + Ri + \frac{1}{C} \int idt \quad (49)$$

Subsequently, the analogy between transfer function equation in mechanical system and the electrical ones is shown by using the voltage analogy. The Laplace transform of Equation (49) with assuming the initial condition equal to zero, become:

$$V_t(s) = RI(s) + sLI(s) + \frac{1}{sC}I(s) \quad (50)$$

$$V_t(s) = I(s)[R + sL + \frac{1}{sC}] \quad (51)$$

$$V_t = I(s) \frac{[sCR + s^2LC + 1]}{sC} \quad (52)$$

$$V_t = RI(s) + sLI(s) + \frac{1}{sC}I(s) \quad (53)$$

Since the output voltage is taken across the capacitor element in the circuit and ( $V_c=V_o$ ), then

$$V_c = I(s) \frac{1}{Cs} \quad (54)$$

The Equation (54) can be written as:

$$V_{in}(s) = V_o[sCR + s^2LC + 1] \quad (55)$$

The transfer function of the circuit will be obtained as in Equation (56):

$$\frac{V_o(s)}{V_{in}(s)} = \frac{1}{LCs^2 + CRs + 1} \quad (56)$$

### 4.3 Basics of Vector Fitting

The basic idea of this kind of algorithm is to construct a rational function that represents the system. Vector Fitting is an iterative method based on pole-zero relocation technique. It arrives at the optimal solution by solving two linear equations through few iterations. In fact, the two important advantages are numerical stability and convergence. The frequency response  $f(s)$  can be represented using rational function. For an  $N^{\text{th}}$  order system response, the rational function  $f(s)$  can be shown as (Gustavsen & Semlyen, 1999):

$$f(s) \approx \frac{\sum_{m=0}^M a_m s^m}{\sum_{n=0}^N b_n s^n} \approx \frac{a_0 + a_1 s + a_2 s^2 + \dots + a_M s^M}{b_0 + b_1 s + b_2 s^2 + \dots + b_N s^N} \quad (57)$$

where  $s = j\omega$ ,  $\omega$  is the frequency in rad/s.  $M$  and  $N$  are the orders of the numerator and denominator, respectively. Differently to the Rational Fraction Polynomials method, now the numerator order  $M$  and the denominator order  $N$  of the rational function are very similar. The transfer function can be scattering, admittance, or impedance parameters obtained from an electrical measurements or other ones generated from other engineering fields, such as mechanical one. As already been mentioned different definitions of transfer functions exist; three of the most important ones are illustrated in Figure 13.

$H(s) = \frac{a_0 + a_1 s + a_2 s^2 + \dots + a_M s^M}{b_0 + b_1 s + b_2 s^2 + \dots + b_N s^N}$	Rational Polynomial
$H(s) = \sum_{i=1}^n \frac{R_i}{s - p_i} + H_\infty$	Partial fractions
$H(s) = H_\infty \frac{(s - z_1)(s - z_2) \dots (s - z_n)}{(s - p_1)(s - p_2) \dots (s - p_n)}$	Pole-zero

Figure 13. Different definitions of Transfer Function

All coefficients in Eq. (57) are unknown, but this nonlinear equation can be written as a linear matrix system equation:

$$Ax = b \quad (58)$$

The confidence of Eq. (57) can be solved by using Singular Value Decomposition (SVD). This allows  $A$  to be factorized:

$$A = USV^T \quad (59)$$

$S$  is a diagonal matrix with the singular values of  $A$ , and  $U$  is a matrix with orthogonal columns. The columns of  $U$  may be considered as basic functions of the matrix  $A$ . (Gustavsen & Semlyen, 1999).

Equation (57) can be also expressed as a modal expression of partial fractions form:

$$\sigma(s) = \sum_{n=1}^N \frac{c_n}{s - a_n} + d + se \quad (60)$$

where  $c$  represents residues,  $a$  coincides with the poles,  $d$  and  $e$  are real quantities. Residues and poles can be real quantities or in complex-conjugate pairs. Compared to Rational Fraction Polynomial (RFP) method, in Vector Fitting the FRF is expressed as partial fractions form.

In order to calculate the above nonlinear equation, the problem can be decomposed into two linear problems. The first stage is a pole identification problem in which the poles are estimated from the given frequency sample data and initial starting poles. The second linear step is to calculate the residues starting from the new system poles calculated from the first linear problem (Gustavsen & Semlyen, 1999).

#### 4.4 Poles identification

Firstly, we analyse how calculate the poles of the system. In the transfer function, poles represent the eigenvalues of matrix A. From poles and residues, we can evaluate the modal parameters of the system that are important for dynamic identification. Poles can be real or complex values in order to ensure stability of the model. The number of the poles grows with the increasing of the order N of the system. From a series of starting poles  $\tilde{a}_n$ , we multiply  $f(s)$  with an unknown function  $\sigma(s)$ . The latter is defined as:

$$\sigma(s) = \sum_{n=1}^N \frac{\tilde{c}_n}{s - \tilde{a}_n} + 1 \quad (61)$$

We obtain the following problem:

$$\begin{bmatrix} \sigma(s)f(s) \\ \sigma(s) \end{bmatrix} = \begin{bmatrix} \sum_{n=1}^N \frac{c_n}{s - \tilde{a}_n} + d + se \\ \sum_{n=1}^N \frac{\tilde{c}_n}{s - \tilde{a}_n} + 1 \end{bmatrix} \quad (62)$$

The rational approximation of  $\sigma(s)$  has the same poles of the approximation  $\sigma(s)f(s)$ . The ambiguity in the solution for  $\sigma(s)$  has been removed by forcing  $\sigma(s)$  to approach unity at very high frequencies (Gustavsen & Semlyen, 1999). Then substituting the second equation in the first:

$$\sigma(s)f(s) = \left( \sum_{n=1}^N \frac{\tilde{c}_n}{s - \tilde{a}_n} + 1 \right) f(s) = \sum_{n=1}^N \frac{c_n}{s - \tilde{a}_n} + d + se \quad (63)$$

$$(\sigma f)_{fit}(s) \approx (\sigma)_{fit}(s)f(s) \quad (64)$$

Equation demonstrates its linearity with the unknown  $c_n, d, e, \tilde{c}_n$ . The equation above can be rewritten as follows (MEKONNEN, 2004):

$$\left( \sum_{n=1}^N \frac{c_n}{s - \tilde{a}_n} + d + se \right) - \left( \sum_{n=1}^N \frac{\tilde{c}_n}{s - \tilde{a}_n} \right) f(s) \approx f(s) \quad (65)$$

From equation above a rational function approximation is calculated and it is clear if each sum of partial fractions is written as a fraction:

$$(\sigma f)_{fit}(s) = \frac{\prod_{n=1}^{N+1}(s - z_n)}{\prod_{n=1}^N(s - \tilde{a}_n)}, \quad \sigma_{fit}(s) = \frac{\prod_{n=1}^N(s - \tilde{z}_n)}{\prod_{n=1}^N(s - \tilde{a}_n)} \quad (66)$$

$$f(s) = \frac{(\sigma f)_{fit}(s)}{\sigma_{fit}(s)} = \frac{\prod_{n=1}^{N+1}(s - z_n)}{\prod_{n=1}^N(s - \tilde{a}_n)} \cdot \frac{\prod_{n=1}^N(s - \tilde{a}_n)}{\prod_{n=1}^N(s - \tilde{z}_n)} = \frac{\prod_{n=1}^{N+1}(s - z_n)}{\prod_{n=1}^N(s - \tilde{z}_n)} \quad (67)$$

The Equations (66) and (67) show that the poles of  $f(s)$  become equal to the zeros of  $\sigma_{fit}(s)$ .

#### 4.4.1 Selection of initial poles

As is explained by B. Gustavsen in his paper: “For functions with resonance peaks, the initial poles should be complex conjugate with weak attenuation, with imaginary parts  $\beta$  covering the frequency range of interest. The weak attenuation assures that the least square problem (LSP) to be solved has a well-conditioned system matrix, and the distribution of the pairs over the frequency range reduces the probability that poles need to be relocated a long distance (avoiding need for many iterations).” Started poles should commonly be chosen as follows:

$$a_n = -\alpha + j\beta; \quad a_{n+1} = -\alpha - j\beta \quad (68)$$

where:

$$\alpha = \beta / 100$$

#### 4.4.2 Pole-zero

As before anticipated in the previous Section 4.1 the frequency response may be written as:

$$H = \frac{N(s)}{D(s)} = \frac{a_0 + a_1s + a_2s^2 + \dots + a_Ms^M}{b_0 + b_1s + b_2s^2 + \dots + b_Ns^N} \quad (69)$$

The solution for  $a_M$  cannot be found without prior knowledge of  $b_N$ . However, a simplification to this problem exists by considering the concept of zeros and poles as fundamentally the same; they are both roots of their respective polynomials in Eq. (69). Exploiting this similarity, the denominator poles can be viewed as zeros,  $z_n'$ , after dividing both the numerator and denominator by the set of initially guessed poles (Richards, 2014):

$$H(s) = \frac{N(s)}{D(s)} = \frac{\prod_n(s - z_n)}{\prod_n(s - a_n)} = \frac{\prod_n(s - z_n)}{\prod_n(s - z_n')} = \frac{d + \sum_n \frac{c_n}{s + a_n}}{(1 + d') + \sum_n \frac{c'_n}{s + a_n}} \quad (70)$$

The relation between the true transfer function,  $H$ , and the fitted residues,  $[c_n, c'_n]$ , poles  $[a_n, a'_n]$ , and constant terms  $[d, d']$  is then linearized to:

$$d + \sum_n \frac{c_n}{s + a_n} = H(s) \left( (1 + d') + \sum_n \frac{c'_n}{s + a_n} \right) \quad (71)$$

As the solution converges, the right-hand side of Eq. (71) approaches  $H$ . From this perspective, the primed variables may be conceptualized as error terms that approach zero upon convergence. Another perspective, from the original authors of the method, is that  $H$  is called by “smoothing” function. This is why Vector Fitting was originally titled “Vector Fitting with Optimal Scaling”.

$$\sigma(s) = \left( (1 + d') + \sum_n \frac{c'_n}{s + a_n} \right) \quad (72)$$

Without  $\sigma$ , the Least Squares solution for the residues would be biased by the trivial assumption of initially guessed poles. If  $\sigma$  were converted back to pole-zero form, according to Eq. (71) the relocated poles are then the roots of the denominator polynomial,  $D$ . Rather than implement a numeric root solver (such as Newton's method, bi-section, etc.) to find the roots of  $D$ , the state space allows the new poles to be realized directly from the solved residues,  $c'_n$ , and current pole estimates,  $a'_n$ , by stating it as an eigenvalue problem. Updating the current estimate of with the state space realisation approach can be conceptually thought of as inverting  $\sigma$  such that now appear in the denominator. This is equivalent to changing the input,  $Y$ , with the output,  $U$ , such that  $\sigma = Y/U$  becomes  $1/\sigma = U/Y$  (Richards, 2014). Therefore, using the state space realisation

this can be achieved directly without explicitly realizing the pole-zero form of Eq. (72). Consider the explicit state equations:

$$\dot{x}(t) = Ax(t) + By(t) \quad (73)$$

$$y(t) = Cx(t) + Dy(t) \quad (74)$$

The second expression is substituted in the following equation in time-domain:

$$\dot{x}(t) = Ax(t) + Bu(t) \quad (75)$$

$$y(t) = Cx(t) + Du(t) \quad (76)$$

It is then solved for in terms of  $y$ :

$$u(t) = C \cdot x(t) + B \cdot y(t) \quad (77)$$

$$u(t) - C \cdot x(t) = D \cdot y(t) \quad (78)$$

$$D^{-1}(u(t) - C \cdot x(t)) = y(t) \quad (79)$$

This is the expression for the output of the inverted transfer function. Substituting this new expression for  $y$  into the differential equation and then collecting the  $C$  matrix (containing  $c'_n$ ) with the  $A$  matrix (containing  $a_n$ ),

$$\dot{x}(t) = A \cdot x(t) + B \cdot D^{-1}(u(t) - C \cdot x(t)) \quad (80)$$

$$\dot{x}(t) = (A - B \cdot D^{-1}C) \cdot x(t) + B \cdot D^{-1} \cdot u(t) \quad (81)$$

Although  $A = \text{diag}(a_n)$ , the  $N \times N$  matrix  $B \cdot D^{-1}C$  is not diagonal and therefore the new poles must be solved as the roots of  $\det[sI - (A - B \cdot D^{-1}C)]$  from the highlighted expression in Eq. (81). As discussed earlier,  $D$  contains only a constant term,  $[d]$ ,  $C$  is a column vector of residues,  $B$  is a column vector of ones, and in addition if the eigenvalue solution process is lumped into a single function, eig, we get that the relocated poles are (Richards, 2014):

$$a_n = \text{eig}[A - BC^T/d] \quad (82)$$

Solving the roots of a polynomial as an eigenvalue problem is a robust approach and is not an uncommon practice. After a single iteration of relocating has been completed, the current estimate of the poles is updated with these new locations. This concludes the pole relocation process. In summary, the pole-relocation process is a linear solution that is made possible by assuming a basis consisting of partial fractions. This is evaluated by dividing the numerator and denominator of the rational polynomial approximation by a common set of poles. That does not change the problem but allows it to be reformulated such that all unknowns are linear. (Richards, 2014)

### 4.4.3 Poles location

This section focuses on the importance of poles location, since from that it is possible to understand the characteristics of the system response. Considering a second-order system, sinusoidal frequency response some considerations are reported below:

*“If a system has an excess of poles over the number of zeros, the magnitude of the frequency response tends to zero as the frequency becomes large. Similarly, if a system has an excess of zeros the gain increases without bound as the frequency of the input increases. This cannot happen in physical energetic systems because it implies an infinite power gain through the system.*

*If a system has a pair of complex conjugate poles close to the imaginary axis, the magnitude of the frequency response has a “peak”, or resonance at frequencies in the proximity of the pole. If the pole pair lies directly upon the imaginary axis, the system exhibits an infinite gain at that frequency.*

*If a system has a pair of complex conjugate zeros close to the imaginary axis, the frequency response has a “dip” or “notch” in its magnitude function at frequencies in the vicinity of the zero. Should the pair of zeros lie directly upon the imaginary axis, the response is identically zero at the frequency of the zero, and the system does not respond at all to sinusoidal excitation at that frequency.*

*A pole at the origin of the s-plane (corresponding to a pure integration term in the transfer function) implies an infinite gain at zero frequency.*

*Similarly, a zero at the origin of the s-plane (corresponding to a pure differentiation) implies a zero gain for the system at zero frequency”. (MIT, 2004)*

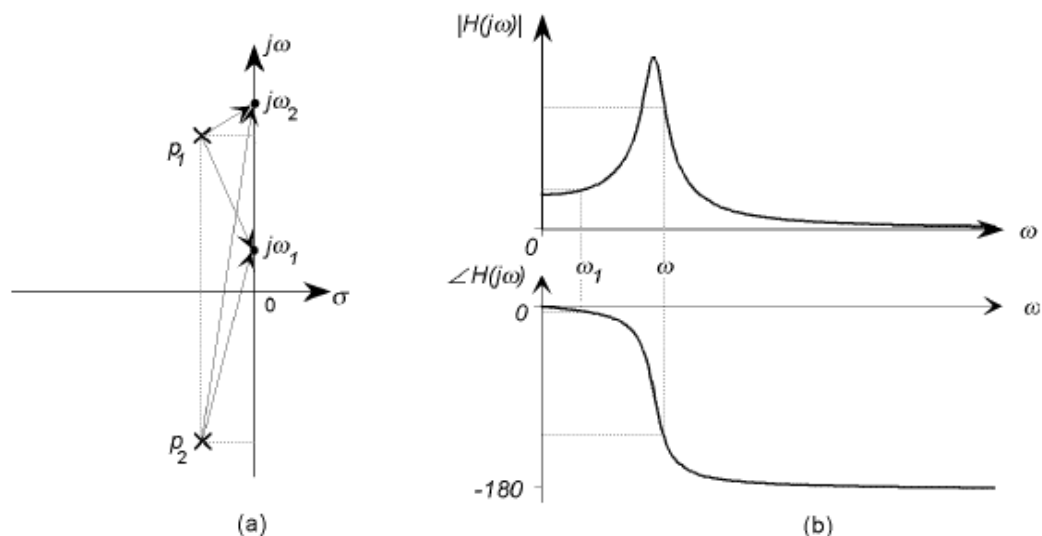


Figure 14. The pole-zero plot for a second-order system and its frequency response functions (MIT, 2004).

In general, the poles and zeros of a transfer function (in mechanical systems frequency response function) are complex values, and the system dynamics are represented by plotting their positions on the complex  $s$ -plane, where axes represent the real and imaginary parts of the complex parameter  $s$ . The first step in the VF algorithm is to refine the best guess of the location of the system's poles. This implies that at start, the user initially guesses the quantity and location of poles,  $p_n$ , which are usually assumed linearly spaced or logarithmically spaced throughout the frequency band of the observation (complex starting poles may also be assumed as spaced along the imaginary axis with small real components). VF then iteratively refines this initial guess or *relocates* the poles until the modelled transfer function approximates the observed system to within an acceptable error tolerance (Richards, 2014). The poles'  $s$  position in the  $s$ -plane describes the characteristic of solution. For example, it is possible to evaluate information about frequency and damping (Figure 15).

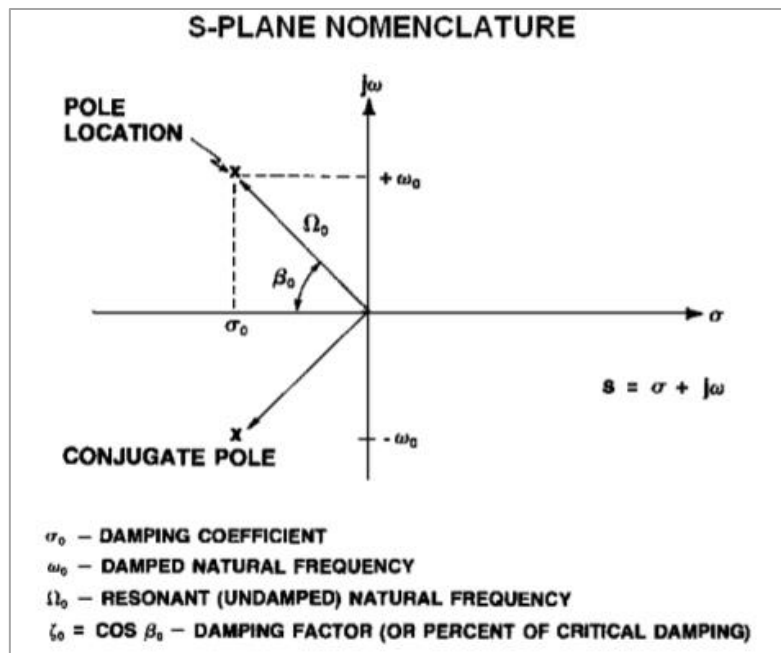


Figure 15.  $S$ -plane nomenclature

Six different cases are followed below:

- A pole at the origin  $p_i = 0$  defines a component that it is constant in amplitude and defined by the initial condition.
- A real pole  $p_i = -\sigma$  in the left-half of the  $s$ -plane describe an exponentially decaying component. The rapidity of the decay is determined by the pole position. Slowly decaying components correspond to poles near the origin, while rapidly decay correspond to poles far from it.

- A real pole in the right- half-plane corresponds to an unstable system whit an exponentially increasing component.
- A complex conjugate pole pair  $\sigma \pm j\omega$  in the left-half of the plane generates a response component of a decaying sinusoid of the form  $A e^{-\sigma t} \sin(\omega t + \varphi)$ , where  $A$  and  $\varphi$  are determined by the initial conditions.  $\sigma$  and  $\omega$  represent, respectively, the rate of decay and the frequency of oscillation. That also allows ranking the modes of the structure accordingly to a slow-to-fast-decaying criterion.
- An imaginary pole pair  $\pm j\omega$  generates an oscillatory component with a constant amplitude determined by the initial conditions.
- A complex pole pair in the right half-plane corresponds an exponentially increasing component.

According to this theory, for a mechanical system under a damped excitation the poles obtained with Vector Fitting algorithm will be complex conjugate pole pair. Since the system is a real one, all modes have necessarily to be stable and thus confined in the left (negative) half-plane. Moreover, the trend of poles presents an exponentially decaying behaviour. Below are also reported the analytical demonstration (Marconi, 2010):

$$\frac{N(s)}{D(s)} = K \prod_{i=1}^q \frac{s + z_i}{(s + a_i)} = \sum_{i=1}^n \frac{c_i}{(s + a_i)} \quad (83)$$

Residues are expressed:  $c_{ij} = (s + a_i) \frac{N(s)}{D(s)} \Big|_{s=a_i}$

From linearity of anti-transformed operator:

$$\mathcal{L}^{-1} \left( \frac{N(s)}{D(s)} \right) = \sum_{i=1}^n c_i \mathcal{L}^{-1} \left( \frac{1}{(s + a_i)} \right) \quad (84)$$

From the rules of transformation of elementary signals  $\mathcal{L}^{-1} \left( \frac{1}{(s+a_i)} \right) = e^{-a_i t}$

$$g(t) = \mathcal{L}^{-1} \left( \frac{N(s)}{D(s)} \right) = \sum_{i=1}^n c_i e^{-a_i t} \quad (85)$$

The effect of a pair of complex poles conjugated to multiplicity single is given by a periodic frequency signal equal to imaginary part of the poles modulated in amplitude by a signal exponential governed by the real part of the poles. The value of the residuals associated influences the multiplicative constant  $M$  and the phase  $\varphi$ :

$$\begin{aligned} \mathcal{L}^{-1} \left( \frac{c_i}{s + p_i} + \frac{c_i^*}{s + p_i^*} \right) &= c_{i,1} e^{-a_{i,1} t} + c_{i,2} e^{-a_{i,2} t} = M (e^{-j\varphi} e^{-(\sigma+j\omega)t} + e^{j\varphi} e^{-(\sigma+j\omega)t}) \\ &= M e^{-\sigma t} (e^{-j(\varphi+\omega t)} + e^{j(\varphi+\omega t)}) = 2M e^{-\sigma t} \cos(\omega t + \varphi) \end{aligned} \quad (86)$$

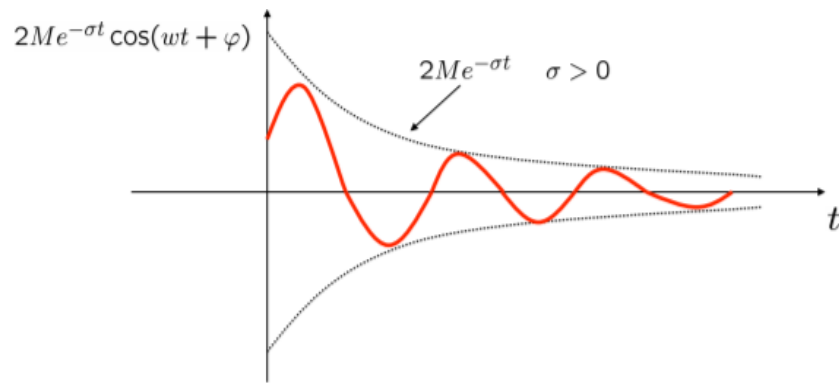


Figure 16. Response of system under a damped excitation: demonstration of trend of pole (Marconi, 2010)

#### 4.4.4 Poles stability

Poles stability is a key concept, because every system must meet this condition in order to not stray too much from the bias condition.

The stability of a linear system is estimated directly from its transfer function. A  $N^{\text{th}}$  order linear system is considered stable only if all of the components of the response decay to zero as time increases. If any pole has a positive real part, there is a component in the output that increases without bound. In this way the system become unstable. The condition of system stability is that all of its poles must have negative real parts. A component in the system response that raises without bound from any finite initial conditions generates an “unstable” pole, located in the right half of the  $s$ -plane. A system having one or more poles staying on the imaginary axis of the  $s$ -plane has non-decaying oscillatory components in its homogeneous response, and is marginally stable (MIT, 2004).

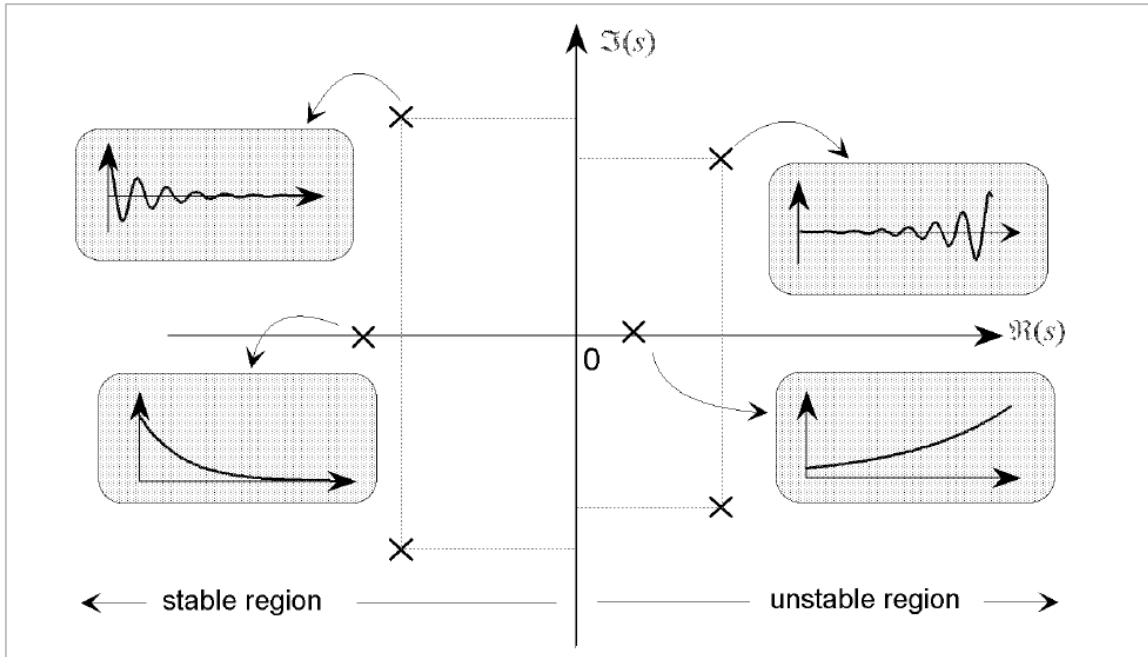


Figure 17. The specification of the form of components of the homogeneous response from the system ( MIT, 2004)

## 4.5 Residue identification

Residues are finally calculated by solving the Least Squares problem with known poles. The Least Squares Analysis (LSA) is a standard regression analysis technique. The principle of LSA is that “the most probable value of the unknown quantities will be that one for which the sum of the squares of the differences between the actually observed and computed values multiplied by numbers that measure the degree of precision is a minimum” (Strejc, 1980). The residue represents an imaginary value which expresses the robustness of the mode. It is a mathematical concept with a difficult physical interpretation. It carries the absolute scaling of the FRF, and thus the level of the magnitude curve. In the next chapter, the relation between the residue and mode shape will be explained. The residue is also called *the pole-strength*, but the magnitude of a mode is not given only by the residue (Brüel & Kjaer, 1988). It is defined as the ratio of the residue to the decay rate:

$$H(\omega_d) \approx \frac{R}{\sigma} \quad (87)$$

## 4.6 Fast and Relaxed Implementation of Vector Fitting Method

From 2006 to 2008 Björn Gustaven published a new implementation of Vector Fitting Method called Fast Relaxed Vector Fitting (FRVF). This version is used in cases studies of this dissertation. The advantages of this new version are:

- A relaxed non-triviality constraint is used in the pole identification stage of Vector Fitting for acquiring faster convergence and less biasing (Gustavsen, 2006);
- The linear problem related to the pole identification stage of Vector Fitting is solved in a fast way (Mrozowski et al.,2008).

The paper “*Improving the Pole Relocating Properties of Vector Fitting*” (Gustavsen, 2006) describes an implementation of VF (Relaxed Vector Fitting, RVF) that increases the ability of it to relocate poles to better positions. This implementation improves its convergence performance especially whit presence of noisy in the fitting response. Starting from the original equation of Vector Fitting expressed in the Section 4.3:

$$f(s) = \sum_{n=1}^N \frac{c_n}{s - a_n} + d + se \quad (88)$$

$$\sigma(s)f(s) = p(s) \quad (89)$$

$$\sigma(s) = \sum_{n=1}^N \frac{\tilde{c}_n}{s - q_n} + 1 \quad (90)$$

$$p(s) = \sum_{n=1}^N \frac{c_n}{s - q_n} + d + se \quad (91)$$

where  $\sigma(s)$  is a scalar while  $p(s)$  is generally a vector and  $q_n$  are the initial poles.

An efficient solution to this problem is presented, where the high frequency asymptotic constraint on  $\sigma(s)$  is removed. This is achieved by making a free variable, and adding an additional relaxation condition to the LS equations. This is achieved by replacing Eq. (90) with:

$$\sigma(s) = \sum_{n=1}^N \frac{\tilde{c}_n}{s - q_n} + \tilde{d} \quad (92)$$

where  $\tilde{d}$  is real. In order to avoid null solution, we add one equation to the LS problem:

$$Re \left\{ \sum_{k=1}^{N_s} \left( \sum_{n=1}^N \frac{\tilde{c}_n}{s_k - q_n} + \tilde{d} \right) \right\} = N_s \quad (93)$$

Equation (93) enforces that the sum of the real part of  $\sigma(s)$  over the given frequency samples equals some nonzero values, without fixing any of the free variables. As RVF converges,  $\sigma(s)$  will approach unity at all frequencies ( $\{\tilde{c}_n\} = 0, \tilde{d} = 1$ ) similarly as in the original VF formulation. It follows that the criterion (93) does not impose any constraint on the least squares problem other than preventing from becoming zero (Gustavsen, 2006).

Relaxed VF (RVF) reduces the magnitude of pole relocation bias by allowing the constant term of  $\sigma$  to take on any real value to compensate for large residue coefficients. The LS problem can be assumed the form in the following form:

$$A = \begin{pmatrix} \frac{1}{s_0-p_0} & \cdots & \frac{1}{s_0-p_N} & 1 & -\frac{H(s_0)}{s_0-p_0} & \cdots & -\frac{H(s_0)}{s_0-p_N} & -H(s_0) \\ \vdots & \ddots & \vdots & \vdots & \vdots & \ddots & \vdots & \vdots \\ \frac{1}{s_M-p_0} & \cdots & \frac{1}{s_M-p_N} & 1 & -\frac{H(s_M)}{s_M-p_0} & \cdots & -\frac{H(s_M)}{s_M-p_N} & -H(s_M) \\ 0 & \cdots & 0 & 0 & \text{Re}\left\{\sum_{m=0}^M \frac{1}{s_m-p_0}\right\} & \cdots & \text{Re}\left\{\sum_{m=0}^M \frac{1}{s_m-p_N}\right\} & \sum_{m=0}^M 1 \end{pmatrix} \quad (94)$$

The matrix A should be weighted as:

$$weight = \frac{\|\omega(s) \cdot f(s)\|_2}{N_s} \quad (95)$$

If  $\sigma(s)$  during iterations does not approach unity at high frequencies, Eq. (82) is replaced with:

$$\{a_m\} = eig(A - b \cdot \tilde{d}^{-1} \cdot c^T) \quad (96)$$

The zeros calculation by (96) is only applicable with a non-zero  $\tilde{d}$ . If the absolute value of  $\tilde{d}$  is found to be smaller than  $tol=1E-8$ , the solution is discarded and the LS problem is solved again with a fixed value for  $\tilde{d}$  in (74):  $\tilde{d} = tol \cdot (\tilde{d}/abs(\tilde{d}))$ .

In 2008 Fast Relaxed Vector Fitting implementation was published in the paper “*Macromodeling of Multiport Systems Using a Fast*” (Mrozowski et al. 2008). It consists of an application of the QR decomposition to the single-element LS equations to lead to a simplified set of equations. These equations are computed for each matrix element to identify a common pole set.

A *QR decomposition* is a decomposition of a matrix  $A$  into a product  $A = QR$  of an orthogonal matrix  $Q$  and a triangular matrix  $R$ . First, a QR decomposition is applied to the Least Squares equation, which coincide with the pole identification of each matrix:

$$[X - H_v X] = [Q_v] \begin{bmatrix} R_v^{11} & R_v^{12} \\ 0 & R_v^{22} \end{bmatrix} \quad (97)$$

Combining the factorization for all matrix a reduced set of equations is carried out:

$$\begin{bmatrix} R_2^{22} \\ \dots \\ R_V^{22} \end{bmatrix} [\tilde{C}] = \begin{bmatrix} Q_1^T H_1 \hat{1} \\ \dots \\ Q_V^T H_V \hat{1} \end{bmatrix} \quad (98)$$

In this work, the version 3 of the Vector Fitting is used. The systems identification is evaluated by using the software Matlab R2918b code *vectfit3.m*. It offers higher performance in speed and memory consumption thanks to the new implementation of poles relocation.

## 4.7 Weighting

Weighting is a powerful way of controlling the accuracy of the resulting approximation. This is achieved via array weight. Two dimensions are permitted:

1. weight (n, Ns)
2. weight (1, Ns)

where n is the number of elements to be fitted, that is the number of rows in array of transfer function  $f$ , while Ns is the of frequency samples that corresponds to columns in array  $f$ . The first dimension's option allows to specifying independent weighting for the elements of  $f(s)$ , while the second dimensions option a common weighting. When modelling systems/devices that can interact with the remainder of the system, error magnifications can easily result when the impedance of the connected network is very different from the impedance used in the "measurement" (for example in electronics it corresponds to short circuit in admittance representation). The likelihood of large magnifications can be avoided by sensible weighting (Gustavsen, 2008).

Scheme	Independent weighting	Common weighting
1) No weight	<code>weight=ones(Nc,Ns);</code>	<code>weight=ones(1,Ns);</code>
2) Strong inverse weight	<code>weight=1./abs(f);</code>	<code>weight=zeros(1,Ns);</code> <code>for k=1:Ns</code> <code>  weight(1,k)=1/norm(f(:,k));</code> <code>end</code>
3) Weaker inverse weight	<code>weight=1./sqrt(abs(f));</code>	<code>weight=zeros(1,Ns);</code> <code>for k=1:Ns</code> <code>  weight(1,k)=1/sqrt(norm(f(:,k)));</code> <code>end</code>

Figure 18. Weighting scheme (Gustavsen, 2008)

The inverse weighting schemes in Figure 18 gives a strong weight on elements in  $f(s)$  where they are small. For instance, if  $f(s)$  is a scalar, weight scheme 2) in Figure 18 results in a high weight where the magnitude of  $f(s)$  is small, thus tending to minimize the relative deviation instead of the absolute deviation. (Gustavsen, USER'S GUIDE FOR VECTFIT3.m, 2008). When fitting a vector, higher weight is also placed on small elements than on large elements. One difficulty with using the inverse weight is when  $f(s)$  contains noise since content relative to the signal strength

tends to be high where elements are small. This problem can be solved by using a weaker inverse weight, such as scheme 3) in Figure 18.” *It is remarked that for pure transfer function modelling, one should normally not use any weight, but when a certain frequency band is very important the weighting is necessary. Also, note that the sampling effectively represents a weighting: increasing the sampling density in some frequency band makes the LS solver place more weight on this band*” (Gustavsen, USER’S GUIDE FOR VECTFIT3.m, 2008).

## 4.8 Vector Fitting state space model

In this section the state-space model of Vector Fitting algorithm is illustrated. As was anticipated in the previous section Vector Fitting approximates  $H(s)$  as a sum of partial fraction (Equation (70)):

$$f(s) \approx \sum_{n=1}^N \frac{c_n}{s - a_n} + d + s \cdot e$$

For a system with  $n$  channels and  $N$  degrees of freedom:

$$f(s) \approx C(sI - A)^{-1}b + d + se \quad (99)$$

where the state space matrices are  $A \in \mathbb{R}^{N \times N}$  a diagonal matrix containing poles,  $B \in \mathbb{R}^{N \times 1}$  a unitary vector,  $C \in \mathbb{R}^{N \times n}$  a row vector holding the residues,  $D \in \mathbb{R}^{n \times n}$  and  $E \in \mathbb{R}^{n \times n}$ . It is possible to choose between a model with real-only parameters or a model with real and complex conjugate parameters, depending on the choose of the input options.

The matrix  $D$  represents a constant that is equivalent to the value of  $H(s)$  for  $s = 0$ , namely the ‘static’ response of the structure to the applied load. However, if the data has undergone pre- or post-processing, it could be scaled. Therefore, it is physically sensible that it isn’t a constant equal to zero.

The matrix  $E$  is a matrix that represents the dependence of the output on the input derivative. In the case of a physical system such as mechanical system, it has no physical sense. In this way it is equal to zero. It means that all unmodeled components influence on  $D$ . For this reason, we will consider it as discard of the model. After these considerations, we impose  $D \sim 0$  and  $E=0$  in the options of Vector Fitting:

$$f(s) \approx C(sI - A)^{-1}b + d \quad (100)$$

This procedure is based on an iterative procedure and is solved repeatedly with the new poles replacing the previous poles. This pole relocation procedure usually converges in 2-5 iterations. In this work the set number of iterations is 5.

## 4.9 Root Mean Squared Error

In statistic field, the RMSE of an specific estimator, with respect to the estimated value, is a real parameter that calculate how much the estimator differs from the estimated one. It is described by the equation below:

$$RMSE(\hat{\theta}) = \sqrt{E((\hat{\theta} - \theta)^2)} \quad (101)$$

The RMSE is a measure of the differences between values estimated and the values actually measured. For a time series from a random variable  $X$  with  $n$  measurements in the form of  $x_1, \dots, x_n$ , Eq. (101) becomes:

$$RMSE(\hat{x}) = \sqrt{\frac{1}{n} \sum_{i=1}^n (x_i - \hat{x}_i)^2} \quad (102)$$

# 5 Modal Analysis with Vector Fitting

In 1970 Experimental Modal Analysis (EMA) was characterized by a revolutionary change with the implementation of the Fast Fourier Transform (FFT).

*“FFT-based EMA on the other hand, required the development of new digital signal processing methods. Modal parameter estimation is a key step in FFT-based EMA. This step, also called curve fitting, has received more attention than any other during the past 30 years. Numerous methods have been developed and the technical literature contains hundreds of papers documenting many different approaches. Modal analysis is used to characterize resonant vibration in machinery and structures. A mode of vibration is defined by three parameters; modal frequency, modal damping and mode shape. Modal parameter estimation is the process of determining these parameters from experimental data. Furthermore, a set of modal parameters can completely characterize the dynamic properties of a structure. This set of parameters is also called a modal model for the structure” (Richardson & Schwarz, January 2003).*

This dissertation promotes a new implementation of Vector Fitting in experimental modal analysis of structural systems. Firstly, the VF validation is carried out from numerical tests. Subsequently, the method is applied on experimental case studies with different level of damage in order to give real structure conditions.

## 5.1 Modal Analysis: numerical and experimental approach

Firstly, it is necessary to explain the different approaches of modal analysis. The preliminary modal analysis allows, starting from the realization of a model, to hypothesize the dynamic behaviour of a structure in order to define a monitoring of a structure that is able to provide useful information on the building. The experimental modal analysis characterizes the structure, from a dynamic point of view in a reliable way. It consists in the application of the structural identification technique to the signal acquired, after the realization of the experimental tests. In general, it is worth mentioning that the possible approaches in the modal analysis are two:

- Numerical approach: it is possible to start from the geometry of the structure, the boundary conditions and the characteristics of the materials, solving the eigenvalue problem, to reach the regulation of the modal parameters of the system (preliminary modal analysis).
- Experimental approach: starting from the measurement of the dynamic input and the response of the structure, the dynamic parameters of the same are calculated (identification of the structure).

The objective of the modal analysis is the definition of the dynamic behaviour of a structure that depends on:

- Frequencies;
- Mode shapes;
- Damping.

Therefore, as previously mentioned, the experimental modal analysis, also known as the "inverse problem", notes which are the response of the construction and the dynamic input, selected to intrinsically characterize the structure in question. It is also interesting to point out that the dynamic behaviour of a structure means a sort of "digital imprint" (Giovanni Fabbrocino, 2007); in fact, it depends on the intrinsic characteristics of the product (masses, stiffness, damping, constraints, etc.) and not on the applied loads. On the contrary, the appearance of changes inside the building, such as for example the repaired damages, can determine the changes in the dynamic behaviour of the structure in terms of frequencies and proper ways of vibrating. The hypotheses underlying the theory of experimental modal analysis are:

- **Linearity:** applicability of the principle of superposition of effects in the combination of the various responses of the structure;
- **Stationarity:** dynamic characteristics of the structure that does not exist over time;
- **Observability:** measurability of the data necessary to define the dynamic characteristics of the structure.

Finally, this process, by means of experimental modal analysis, can be explained by the flow diagram in Figure 19 (Giovanni Fabbrocino, 2007):

## ANALISI DINAMICA SPERIMENTALE

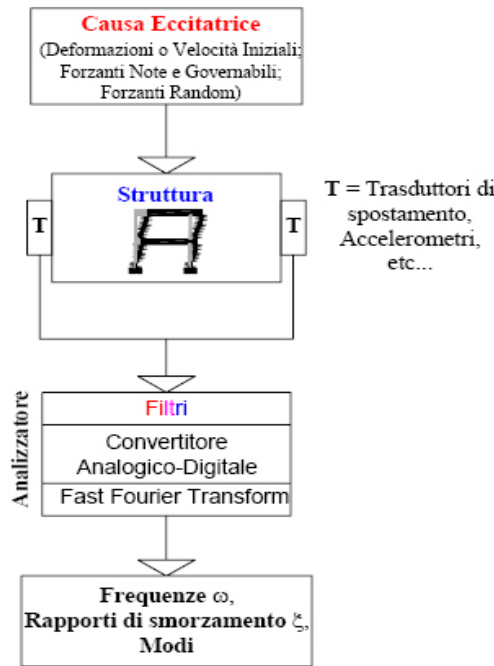


Figure 19. Flow chart: experimental modal analysis (Giovanni Fabbrocino, 2007)

## 5.2 Modal parameters

From the matrix of state-space model, it is possible to evaluate modal parameters that are fundamental for dynamic identification. This dissertation promotes the innovation and implementation of Vector Fitting to evaluate, from poles and residues, modal parameters such as frequency, damping and mode shape. Moreover, from poles matrix  $A$ , it is possible to estimate frequencies and damping ratios of the system, while the mode shapes can be evaluated from residues matrix  $C$ .

### 5.2.1 Estimation of modal parameters

Once the system matrices are estimated, one can compute the modal parameters of the structural system. Natural frequencies  $f_i$ , damping ratios  $\xi_i$  and mode shapes  $\phi_i$  can be determined from (Zanotti & Pretrunin, Cranfield University):

$$A = \Psi \Lambda \Psi^{-1}, \quad \Lambda = \text{diag}(\lambda_i) \in \mathbb{C}^{n \times n}, \quad i=1, \dots, n \quad (103)$$

$$\lambda_i^c = \frac{\ln \lambda_i}{\Delta t}, \quad i=1, \dots, n \quad (104)$$

$$f_i = \frac{|\lambda_i^c|}{2\pi}, \quad i=1, \dots, n \quad (105)$$

$$\xi_i = \frac{\text{real}(\lambda_i^c)}{|\lambda_i^c|}, \quad i=1,\dots,n \quad (106)$$

$$\Phi = C\Psi, \quad \Phi = [\phi_1, \dots, \phi_n] \quad (107)$$

These analytical relations have been used to implement Vector Fitting where matrix  $A$  coincides with poles matrix and  $C$  with the residue matrix. The values  $\lambda_i$  represents the eigenvalues and they coincide with the poles of the algorithm.

### 5.3 Modal Assurance Criterion (MAC)

An important point is the comparison between the experimental data and the numerical data. Especially in structure with high number of degrees of freedom this passage may be very complex. In this way it is necessary the research of parameters which compare the results obtaining from identification algorithm. One of these is the Modal Assurance Criterion (MAC) that it is defined as follows:

$$MAC_{JK} = \frac{(\{\phi_m\}_j^T \{\phi_a\}_k)^2}{(\{\phi_a\}_k^T \{\phi_a\}_k)(\{\phi_m\}_j^T \{\phi_m\}_j)} \quad (108)$$

where  $\{\phi_m\}_j^T$  are eigenvector corresponding to the  $j^{\text{th}}$  experimental mode of vibration and  $\{\phi_a\}_k$  eigenvector relative to the  $k^{\text{th}}$  theoretical mode. A value of the MAC index of 1 represents a perfect match between the two mode shapes while a value of 0 expresses the complete dissimilarity. Thus, the reduction of a MAC value may be an indication of damage. However, MAC values close to 0.8 is considered acceptable.

### 5.4 Model Order

The complexity of the model depends on the order  $n$ , which represents the number of auxiliary variables used in the space model. Given an order to the model, you will get  $n$  eigenvectors of the matrix  $A$ , but not all of which correspond to the structure's own modes.

Due to its own modes being functions of the characteristics of the structure and independent of the numerical process, one's own methods must not vary with variation model order. For this reason, it is possible to distinguish the modes from purely numerical ones, gradually increasing the order of model and checking the stability of the results obtained.

### 5.5 Stabilization diagram

In order to select vibration modes, Vector Fitting was implemented with Stabilisation Diagram. The algorithm is modified to fitting for a range order  $N$ . The Stabilisation Diagram, traceable in the frequency-order domain of the model, is very important in identifying the real modes of a

structure. In fact, if the order of the model on which identifications are made change and they are stabilised around recurring frequency values, this means that the frequencies are 'stable' and therefore are associated with real ways of vibrating of the structure. On the contrary, all frequencies that are not present recursively are considered 'unstable' and therefore must be separated from the first ones and excluded from that study. However, in order to verify the stability of the various identifications, it is necessary to set stabilization parameters:

- Maximum permissible damping capacity;
- minimum permissible damping;
- maximum difference in frequency;
- minimum difference in damping;
- the MAC lower limit value.

In addition, Power Spectral Density (PSD) curves for the various acquisition channels are also reported within these diagrams in order to check whether the stabilization of identifications takes place around high-energy frequencies. At the end of this process, it is possible to separate the stable frequencies from the unstable ones, and precisely these are associated with modes of vibration defined as '*spurious*'. Most of the time the poles may be "locked" in a wrong location due to the noise. This concept is illustrated in the chapter (6). The advantage of Vector Fitting is that it allows seeing how the structure behaves with low model order.

## 5.6 Clustering

Subsequently to the Stabilization Diagram, it is possible to trace the clustering one by applying the linkage technique. It is a representation through which it is possible to determine the damping values associated with the real vibration frequencies of the structure. In fact, around the specific frequencies of the structure it is possible to observe the formation of clusters. As for the stabilization, also for clustering it is necessary to define the appropriate criteria that guide the process:

- maximum frequency difference allowed within the cluster;
- maximum MAC in cluster;
- stabilization percentage, which specifies the number of frequencies that make up the cluster with respect to the order of the model;
- weight for frequency deviation;
- weight for MAC.

The fundamental relationship to which reference is made is based on the definition of a distance summing up three different contributions:

1. Distance in term of frequency:

$$d_f = |f_i - f_j| \quad (109)$$

2. Distance in term of damping:

$$d_\xi = |\xi_i - \xi_j| \quad (110)$$

3. Distance in term of MAC:

$$d_{MAC} = 1 - MAC \quad (111)$$

## 6 Numerical tests

This section focuses on the validation of Vector Fitting algorithm on numerical tests. Firstly, the technique is applied on a 3Dof frame without noise. Then, the degrees of freedom of the frame are increased to 9. In this specific case, a noise level in the output and input's signals is added. The aim is to assess the confidence of Vector Fitting increasing the number of degrees of freedom and the perturbations on the measurements.

### 6.1 3Dof frame

To validate the ability of Fast Relaxed Vector Fitting (FRVF) algorithm in the frequency domain in order to obtain the sought modal characteristics, a 3Dof frame is used. It has been possible thanks to the use of the software Matlab R2018b and the previous implementations of Vector Fitting available in the Sintef website <sup>1</sup> of Bjørn Gustaven and his team. The structure is a sheartype frame with three different floors. The masses are considered concentrate on each floor. The damping is considered as viscous with a default value of 3%. The mass and stiffness matrices are given by:

$$[M] = \begin{bmatrix} m_1 & \dots & 0 \\ \vdots & \ddots & \vdots \\ 0 & \dots & m_n \end{bmatrix} \quad [K] = \begin{bmatrix} k_1 + k_2 & -k_2 & \dots & 0 \\ -k_2 & k_2 + k_3 & -k_3 & 0 \\ \vdots & -k_3 & \ddots & -k_n \\ 0 & 0 & -k_n & k_n \end{bmatrix} \quad (112)$$

where for  $n = 1, \dots, 3$ ,  $m_n$  denotes the mass at the  $i^{\text{th}}$  floor and  $k_n$  denotes the stiffness of the  $i^{\text{th}}$  story. In our case study, stiffness and mass coefficients are respectively  $k_i = 5e3$  and  $m_i = 1$ .

In Figure 20 the three masses frame scheme and its structure matrices are shown below:

---

<sup>1</sup> <https://www.sintef.no/projectweb/vectfit/> retrieved in October 2019

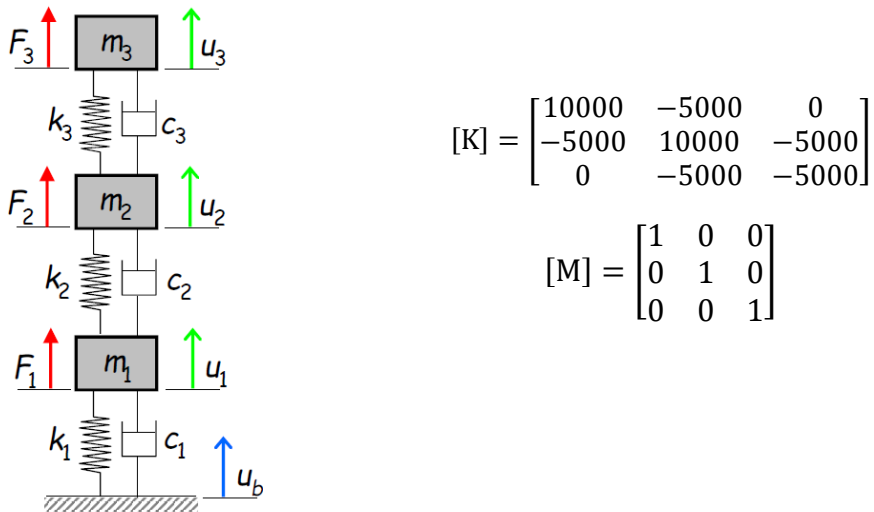
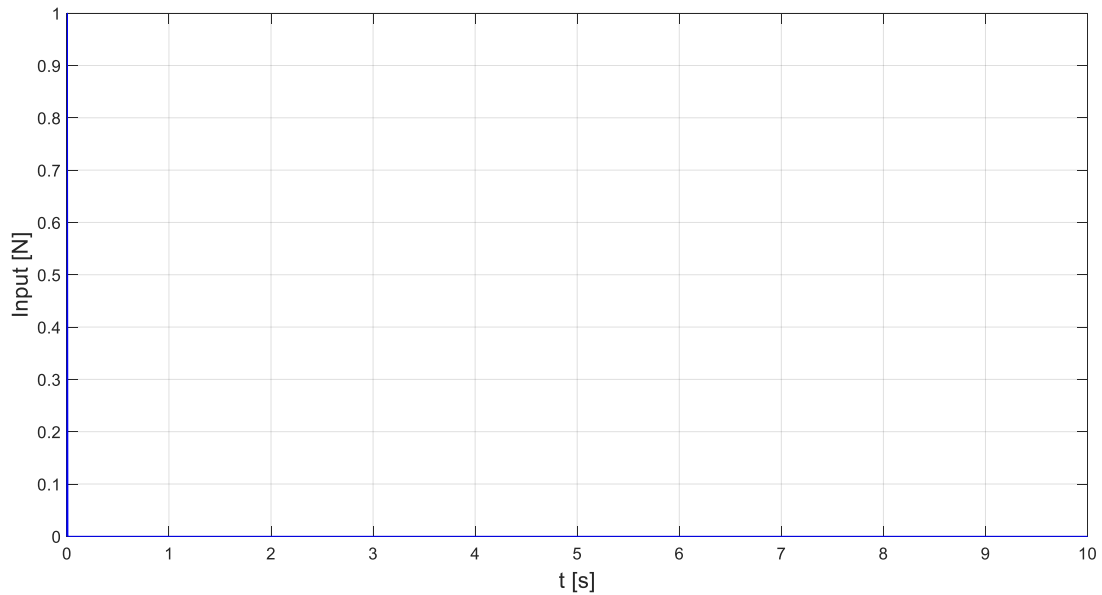


Figure 20. Three masses frame scheme (on the left) and structure matrices (on the right)

A sampling frequency of 200 Hz and a frequency resolution equal to 0.05 are imposed. To obtain the structure response to the various plans, a simulated unitary impulse type forcing was generated. The impulsive force is a unitary artificial force and it is represented with the respective displacement response in the next Figure 21:



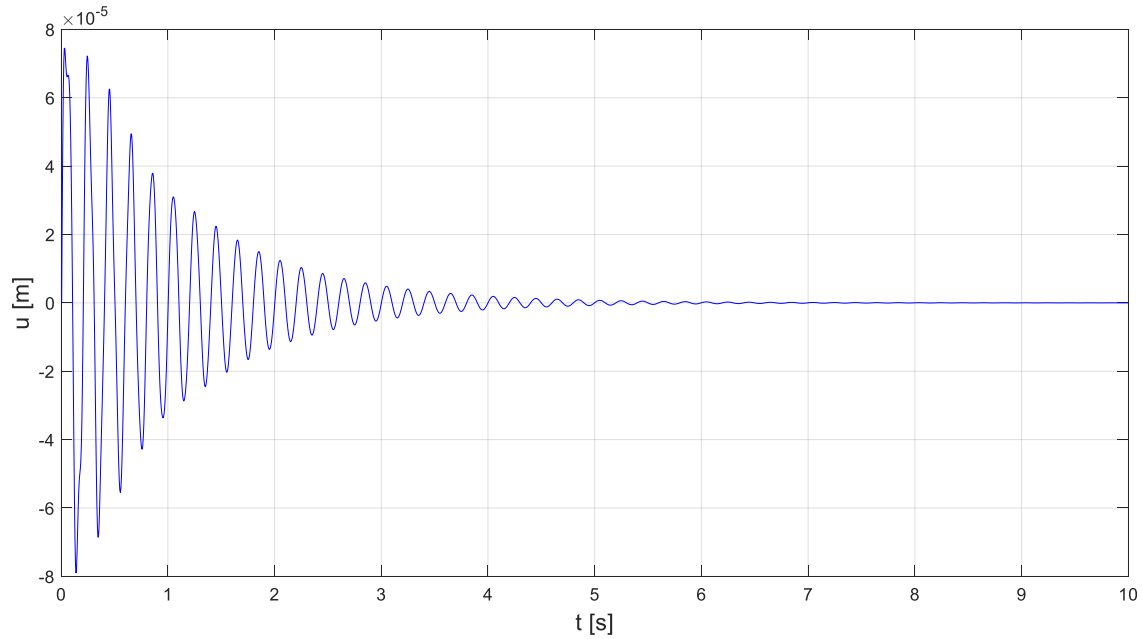


Figure 21. Excitation force (on the top) and displacement response (on the bottom)

As has been previously explained, Vector Fitting works commonly in the frequency domain. Therefore, the calculate of transfer function is necessary and in the frequency domain modal analysis, this is nothing more than the Frequency Response Function (FRF). The FRF is a typical characteristic of input-output systems. To measure the frequency response functions of a mechanical system, the spectra of both the input force and the system response have to be calculated. It is a complex measurement and includes both a real and imaginary component that can be expressed by magnitude and phase. In this way the transfer function  $H(f)$  is expressed as the ratio between the output and the input of the system as follow:

$$H(f) = \text{OUTPUT}(f) / \text{INPUT}(f) \quad (113)$$

where output and input are respectively represented by the response of the frame under the unitary excitation and the unitary impulsive excitation. Both input and output are converted in the frequency domain calculating the FFT of signals, that represents the inverse of Fourier Transform.

Vector Fitting can be applied both as a single input-single output method (SISO) and as single input-multi outputs method (SIMO). Discussing a case study with three different channels, a SIMO analysis is presented in this work. The order of the system is  $N=3$ . In reality Vector Fitting generates a couple of conjugate poles, so model order corresponds to double times the number of degrees of freedom of the system ( $N=6$ ). Therefore, three different Frequency Response Functions for each channel are obtained (three columns for FRF complex matrix) and are represented in Figure 22. The peaks of FRFs represent the resonance frequencies of the mechanical system.

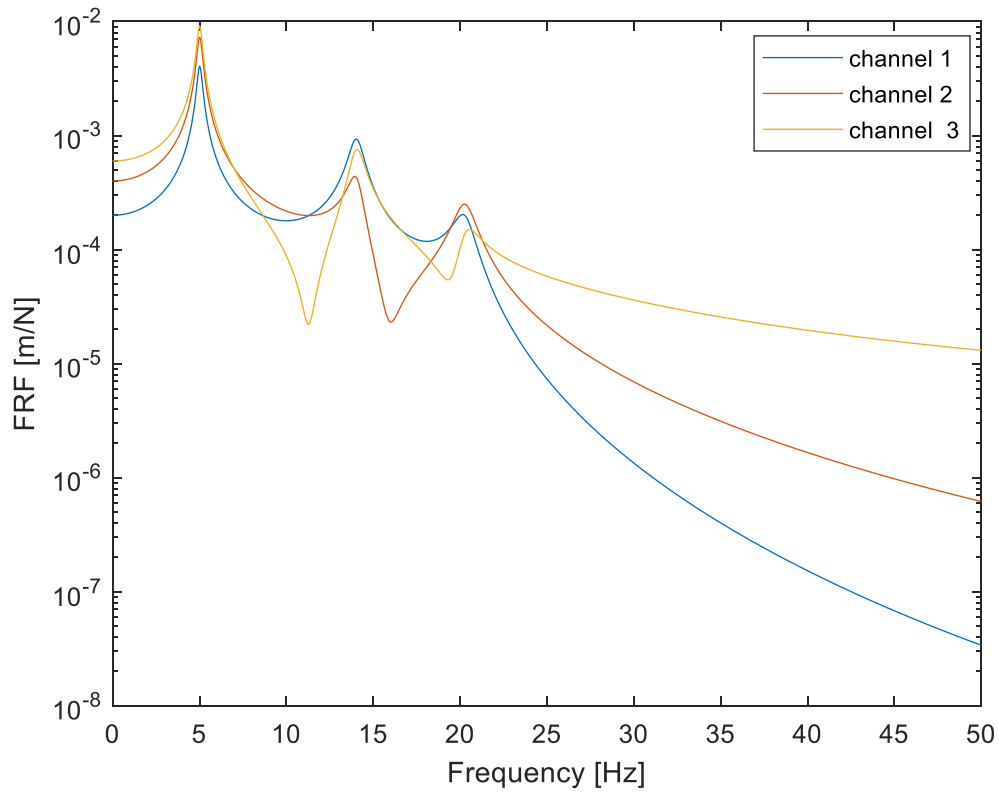


Figure 22. FRFs of the response Channels 1-3 (plotted with reduced range of frequency 0-50Hz)

Notice that the FRF is in semilogarithmic scale to compress the large signal amplitude and expand the small ones, allowing easier visualization of all frequencies in the signal.

Frequency domain models bring optimal results when the frequency range of interest is small and when the structure has a limited number of modes. So, the analysed frequency frame is reduced. Considering only the range of frequencies of interest, 0-25 Hz, the algorithm manages to better fit the transfer functions (Figure 24). Generalizing this concept, a frequency range, with an upper end similar to the value of the maximum peak of resonance frequency, is selected.

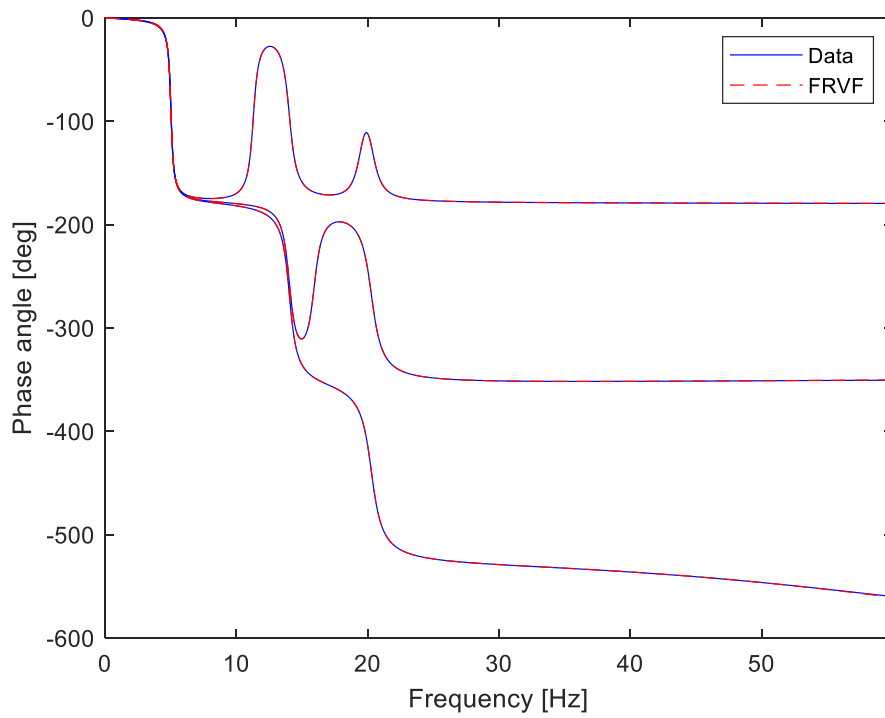
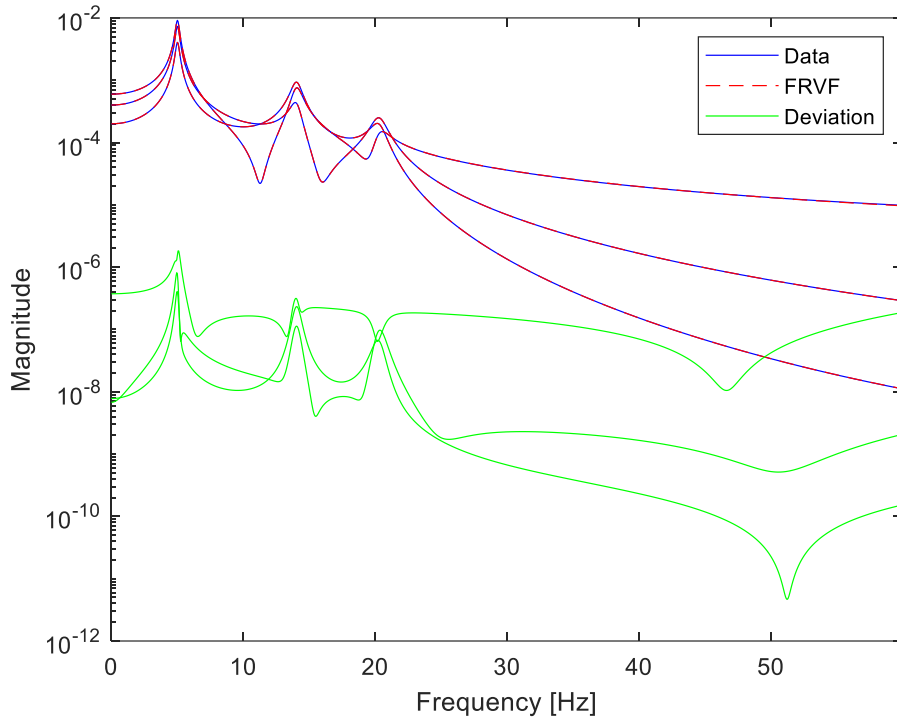


Figure 23. Vector Fitting process in the range of frequency 0-50 Hz (magnitude and phase)

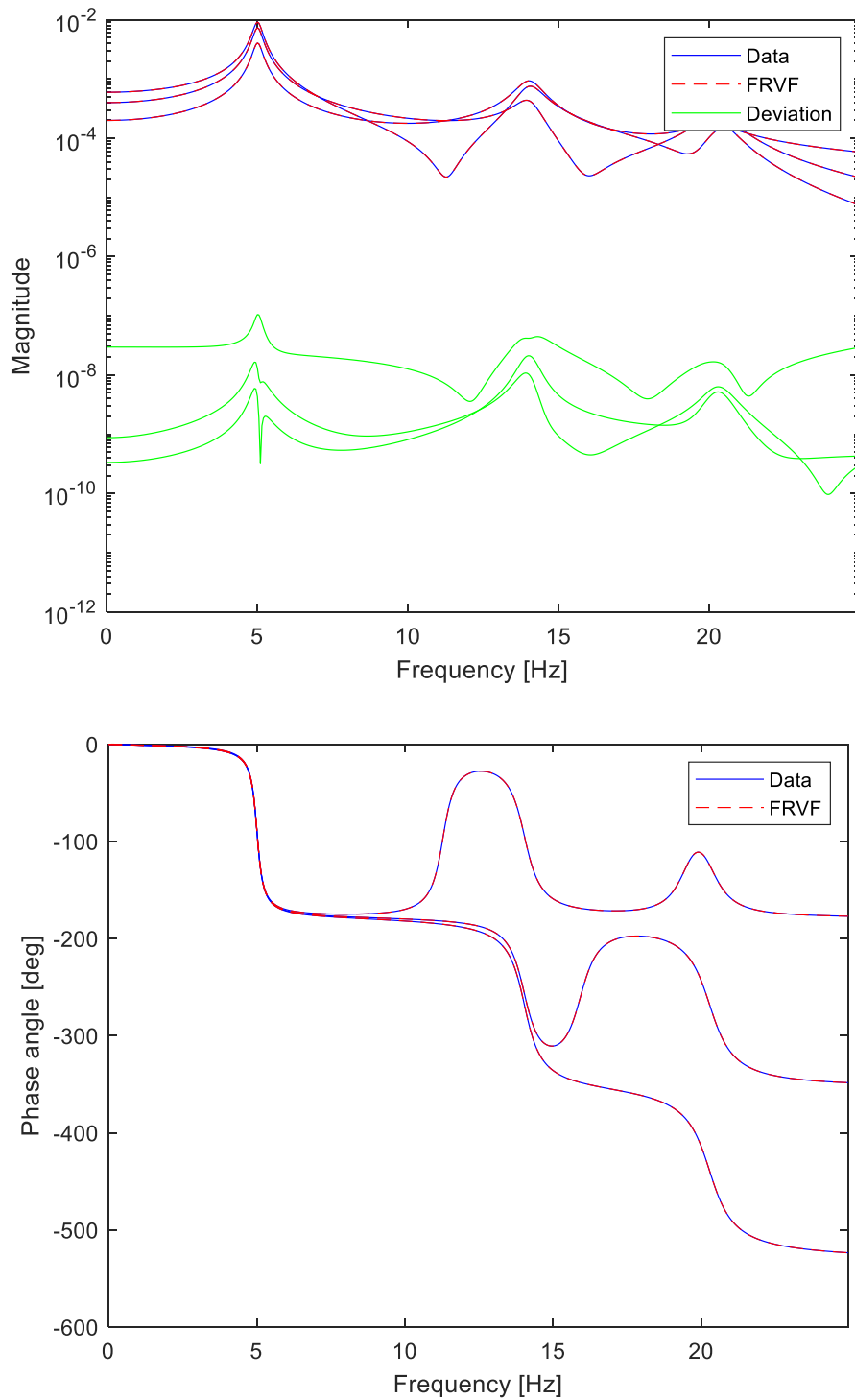


Figure 24. Vector Fitting process in the range of frequency 0-25 Hz (magnitude and phase)

The root-mean-square error (RMSE) is found to be  $9E-4$ . Figures 23-24 show the fitting curves generated by Vector Fitting algorithm, respectively FRF's magnitude and phase. During the calculations, the magnitude and phase plots are presented for the fitting of each columns of FRF function. It produces rational approximations  $\sigma_{fit}(s)$  and  $(\sigma f)_{fit}(s)$ . The deviation between  $(\sigma)_{fit}(s)f(s)$  and  $(\sigma f)_{fit}(s)$  is illustrated, which corresponds to the error in Eq. (65). The difference

is seen to be smaller than 1E-8. In SIMO generation, Vector Fitting uses a common set of poles. The trend of poles presents an exponential behaviour and they are complex conjugate pairs.

<b>n° Mode</b>	<b>Pole</b>
<b>1</b>	$-0.944311113599998 \pm 31.4629102940707i$
<b>2</b>	$-2.64599523567058 \pm 88.1571161384678i$
<b>3</b>	$-3.82357080457380 \pm 127.390841042171i$

*Table 1. Set of poles 3Dof frame (N=6)*

<b>n° Mode</b>	<b>Residue</b>
<b>1</b>	$7.0842228920488e-09 \pm 0.00384322542350051i$
	$8.3793904612277e-10 \pm 0.0024716254668379i$
	$-1.313063866346e-08 \pm 0.00076120939819478i$
<b>2</b>	$2.0699028380268e-08 \pm 0.0069252531980191i$
	$1.3035891953862e-08 \pm 0.0010999768925689i$
	$1.363367911949e-08 \pm 0.00094921222306324i$
<b>3</b>	$-6.2364749685578e-08 \pm 0.0086356265110537i$
	$-6.6019859905458e-10 \pm 0.001982240742972i$
	$-2.699674626710e-08 \pm 0.00042250707319706i$

*Table 2. Residues of 3Dof frame (N=6)*

In Table 1 the poles obtained from Vector Fitting curve-process are reported and belong to diagonal matrix  $A$  with dimension  $N \times N$ . In keeping with the previous theoretical chapter, the poles real part is negative. In Table 2 the residue matrix  $C$  of the state space model is illustrated

and has a dimension of  $N \times n$ , where  $N$  represents the order of model ( $N=6$ ) and  $n$  the number of channels ( $n=3$ ).

In Vector Fitting algorithm the user can choose between a model with real-only parameters or a model with real and complex conjugate parameters, depending on input parameter `opts.complex_ss`. As already mentioned in Section 4.8, poles are physically correct because the damping generates a system decay after perturbation.

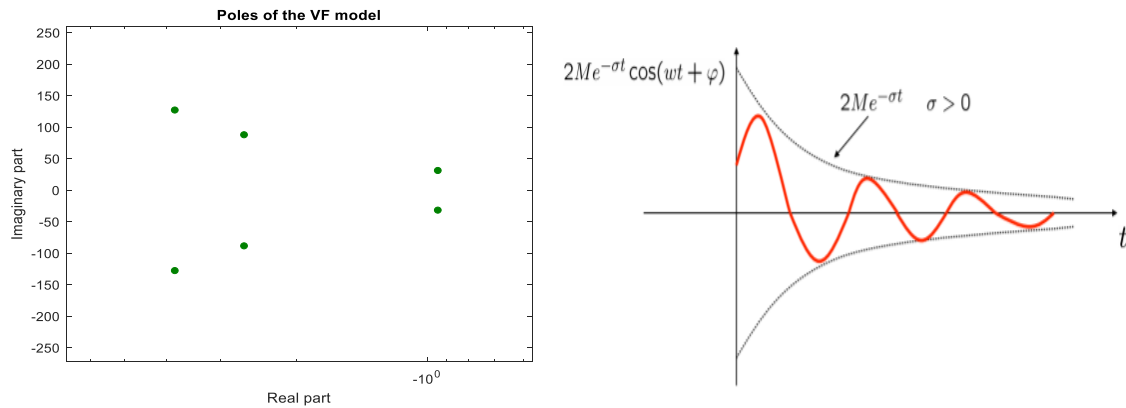


Figure 25. Trend of VF poles in comparison with demonstration in Section 4.4.3

The modal parameters of frequencies, damping and mode shapes are shown in Table 3. The parameters are almost identical to the real ones.

Mode n°	Frequency [Hz]	Damping	Mode shape		
			0.4450	0.8019	1
1	5.009	0.030	0.4450	0.8019	1
2	14.04	0.030	-1	-0.4450	0.8020
3	20.28	0.030	0.8090	-1	0.4450

Table 3. Modal parameters of 3Dof frame from VF process

The components of the modal deformations are normalized to the value maximum displacement and are evaluated at less than one constant. In Figure 26 the three mode shapes are shown:

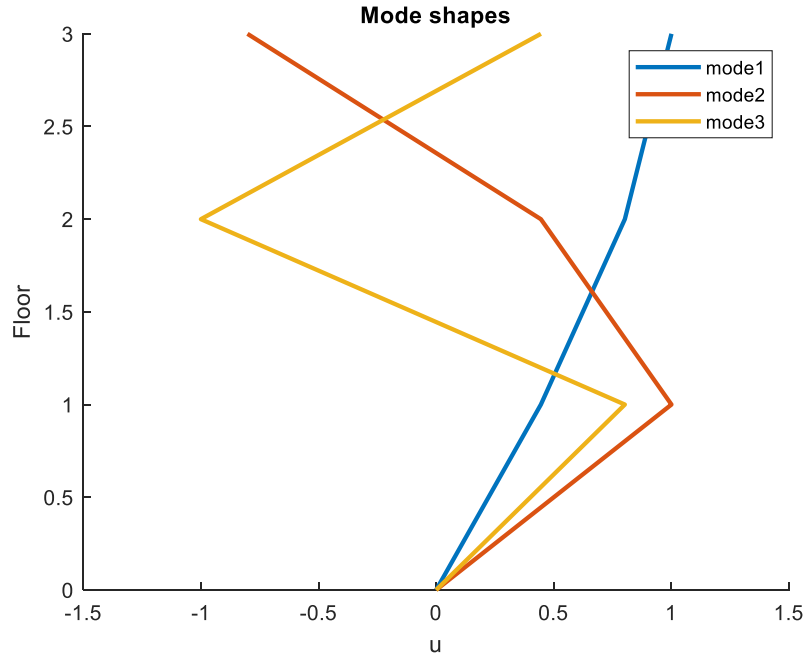


Figure 26. VF mode shapes of three storey frame test

Secondly, the comparison between the FRVF and numerical modal parameters is used to carry out the confidence of the algorithm. The theoretical modal parameters are calculated from the eigenvalue analysis from mass and stiffness matrices. The reliability of the frequencies is demonstrated calculating the error percentage from real and estimated values by using the following equation:

$$\%Error = \left| \frac{Theoretical - Estimated}{Theoretical} \right| \times 100 \quad (114)$$

Without noise, frequency error is in the range of 2E-4 and it is almost similar for each mode. Instead the Modal Assurance Criterium (MAC) is used to compare the mode shapes. Figure 27 shows that for mode shapes associating at the same mode, MAC value is 1, for others is zero. It means that Vector Fitting has an optimal behaviour to approximate a mechanical system with three degrees of freedom and without perturbations in input and output.

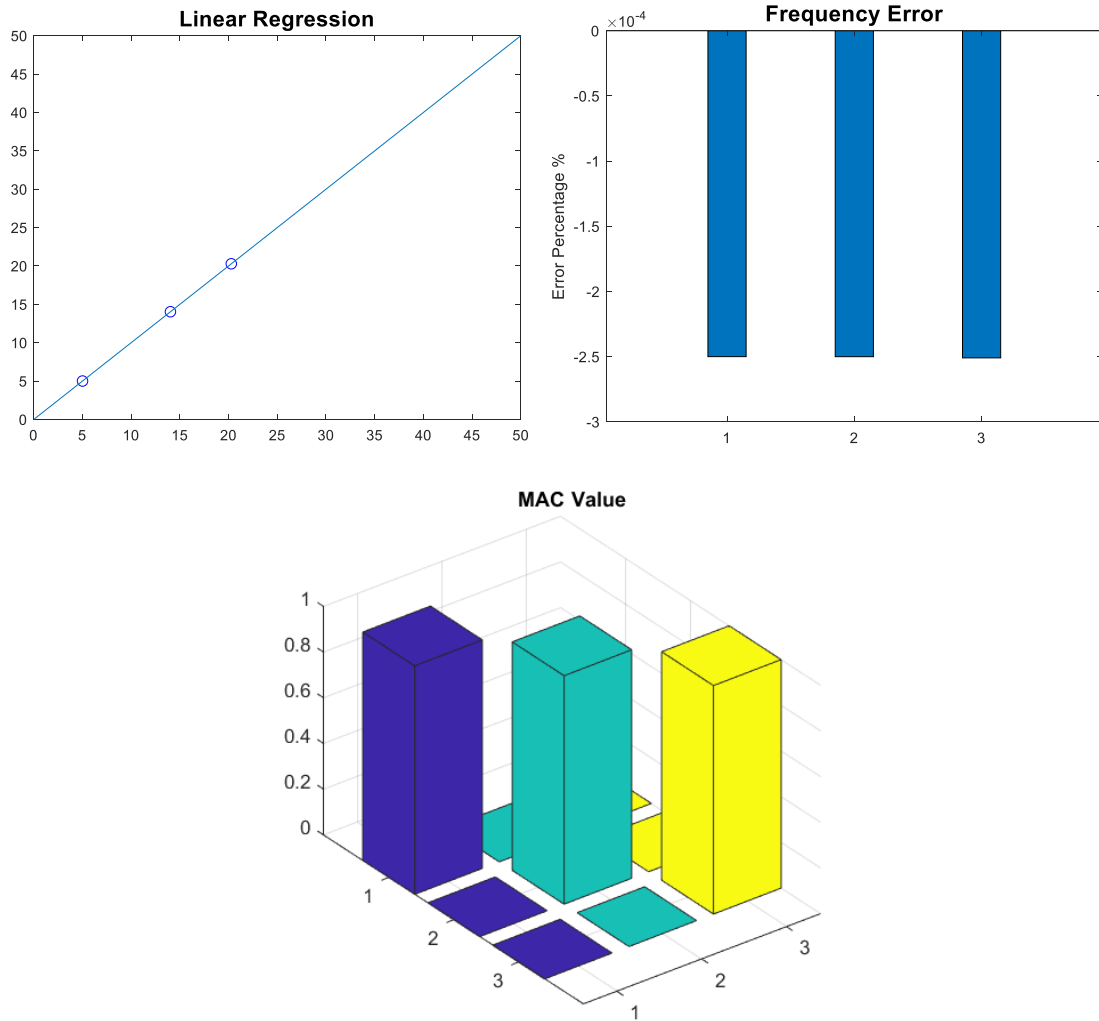


Figure 27. Correlation between numerical and VF parameters: on the top the linear regression (left) and percentage of error (right) between numerical and VF frequencies, on the bottom correlation between numerical and VF mode shapes with MAC.

In the next chapter, the thesis describes effects of different cases of noise level applied to the numerically-simulated mechanical system with different degree of freedom.

## 6.2 Noise problems

This chapter illustrates the convergence properties of FRVF when the frequency samples are affected by noise. It is known that even small amounts of noise are disruptive and seriously impair or destroy convergence. This is due to the presence of spurious poles that compare during the iterations. These spurious poles are responsible of the absence of the convergence. It can be easily seen that poles try to fit the noise instead of the real data (Grivet-Talocia, 2006). This section is intended to test the robustness to noise of the proposed methodology, which performed good overall. The simple numerical tests presented here illustrate that the good convergence properties of the basic Vector Fitting algorithm can be significantly deteriorated by noise in the raw data. To illustrate this effect, a frame with 9 degrees-of-freedom is generated with varying noise level.

## 6.3 9Dof Frame

The case study is characterized by a 9Dof frame with the same characteristics of the previous frame system. The coefficients of mass and stiffness matrices are  $k_i = 5e3$  and  $m_i = 1$ . As the previous section, the impulsive force is a unitary artificial force for a duration of 10. A sampling frequency of 200 Hz and a frequency resolution equal to 0.05 Hz are imposed.

### 6.3.1 Systematic study

First of all, the ability of the algorithm to derive correctly the modal parameters of the structure has been selected. After an uncertainty was added to the input and outputs signals, updated by adding to accelerometric recordings, obtained by integrating the equation of the way, a random variable equal respectively to a percentage of the standard deviation of impulsive force and structure's response, according to the expression:

$$y = y + (j/100) \cdot std(y) \cdot random(length(t),N) \quad (115)$$

The modified signal is called the "*pseudo-experimental*" signal, because it intends to describe the measurement errors of the registrations. The coefficient  $j/100$ , indicating the weight of the disturbance, has been set equal to values gradually increasing, and in particular equal to 0.01, 0.05, and, finally, 0.2 (1%,5%,20%). Estimates of the resonance frequencies  $f$  and the damping coefficients  $\xi$  are shown in the section below. The reference values are those of the original structure. The comparison is obtained by performing 20 tests for each noise level.

### 6.3.1 Simulations without noise

First, we illustrate the result of 9Dof without noise. Figure 28 shows the FRFs relating the 9 channels calculated with Eq. (113). The dimension of the frequency response functions is a displacement (m) on force (N).

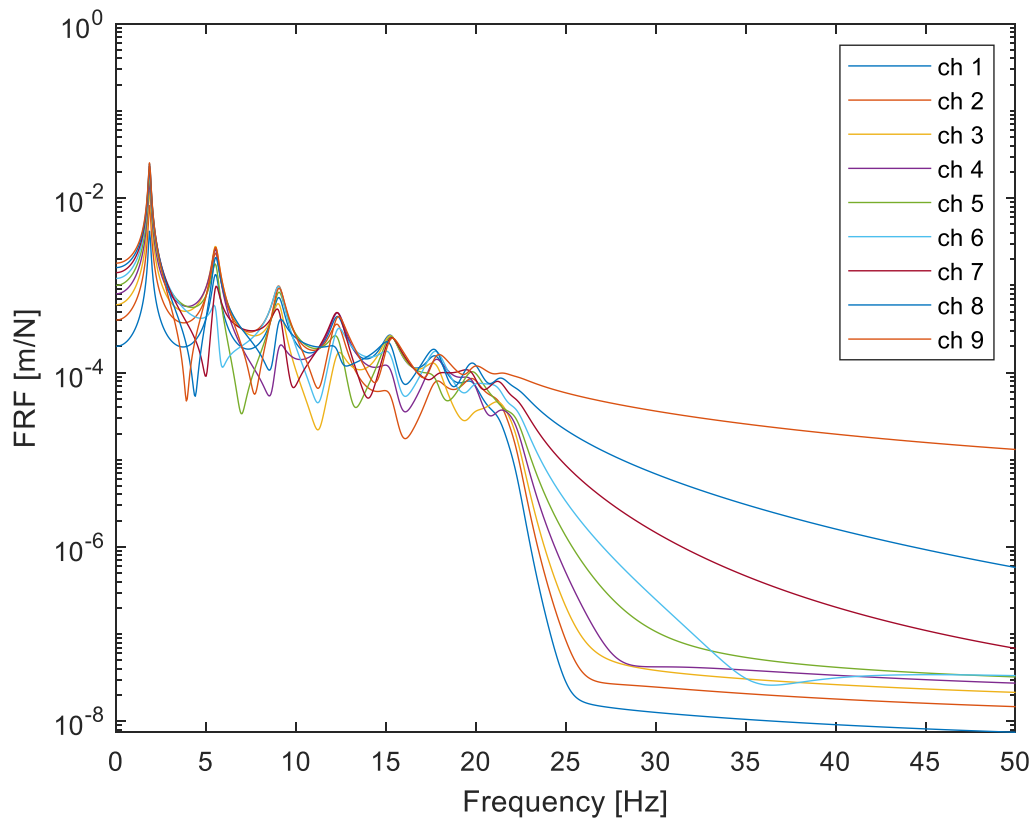
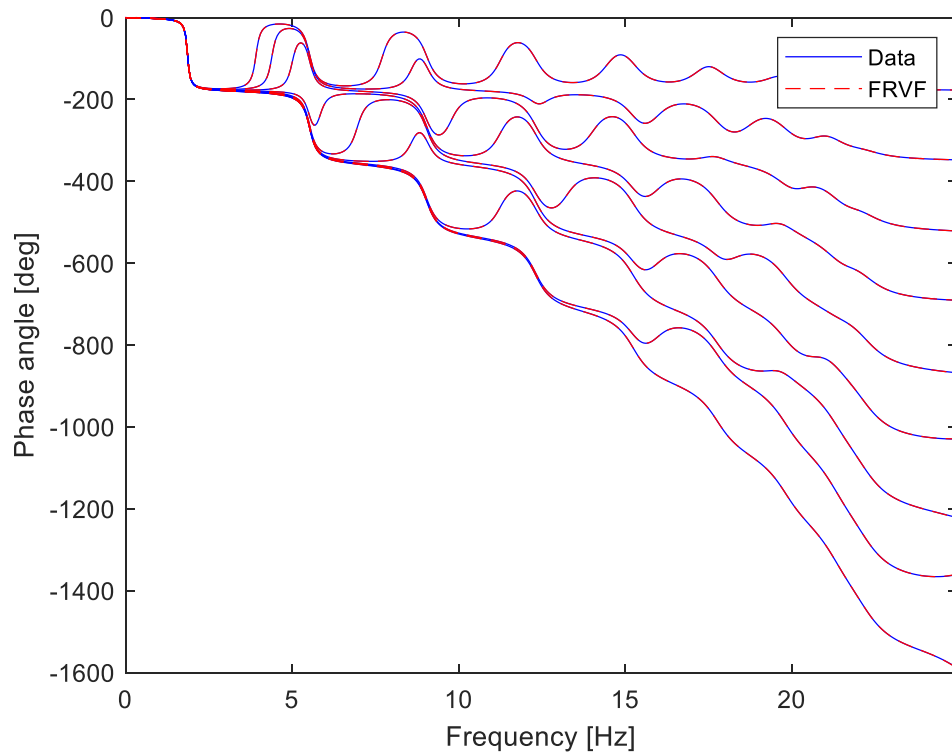
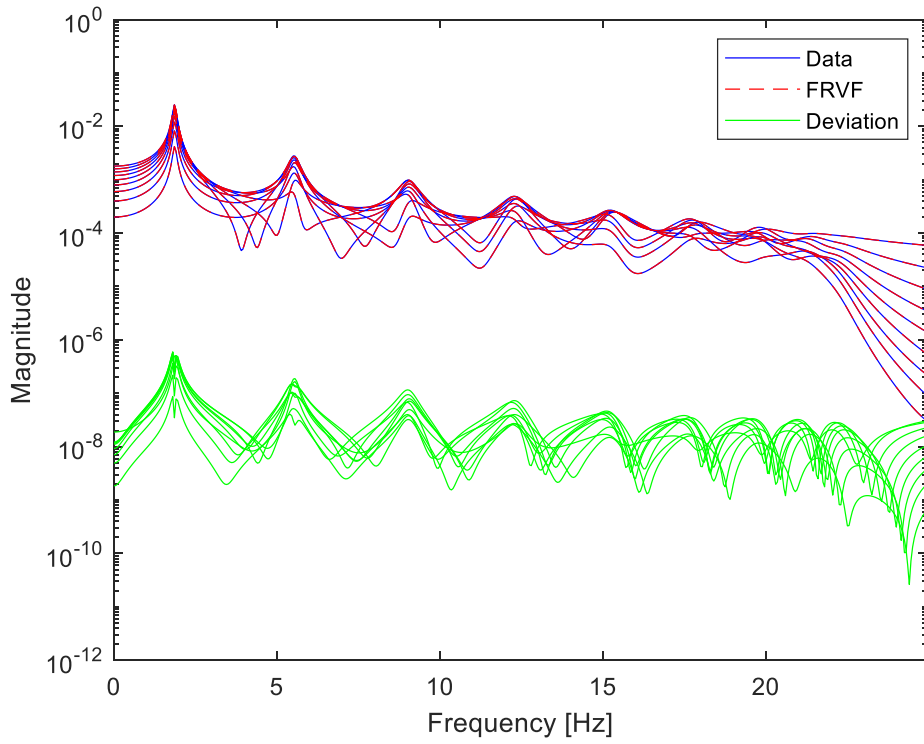


Figure 28. FRFs of the response Channels 1-9

Then, the results of FRVF curve -process are reported in Figures 29. All the responses are fitted with excellent accuracy, since there is no visible difference between model and data; Figure 29 reports how the deviation between the data and the macro model is never larger than  $10^{-6}$  in terms of absolute value.



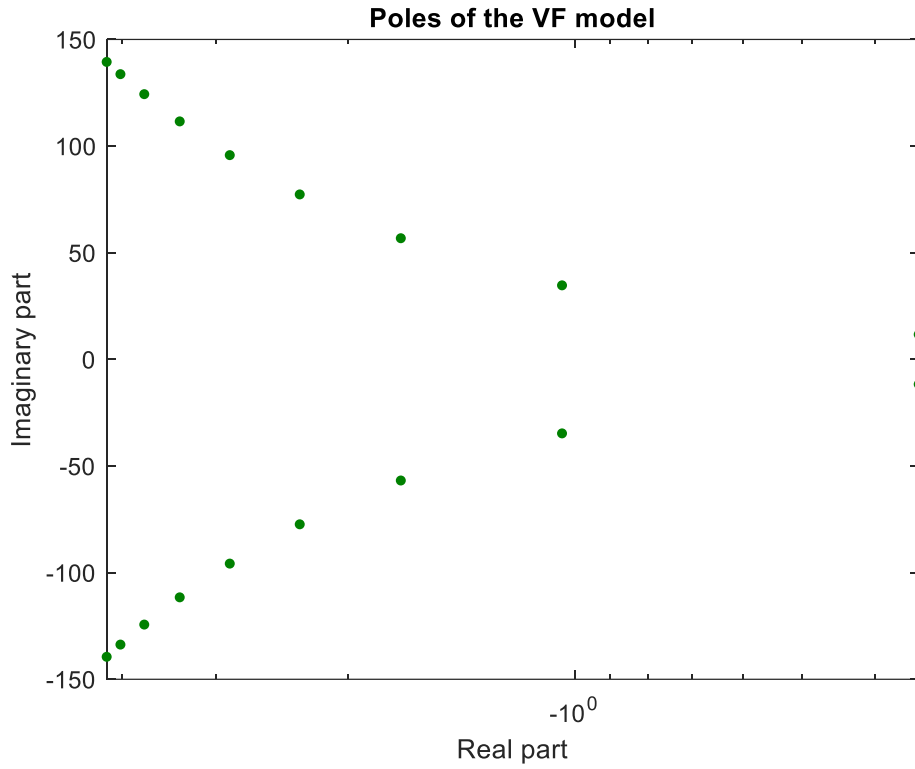
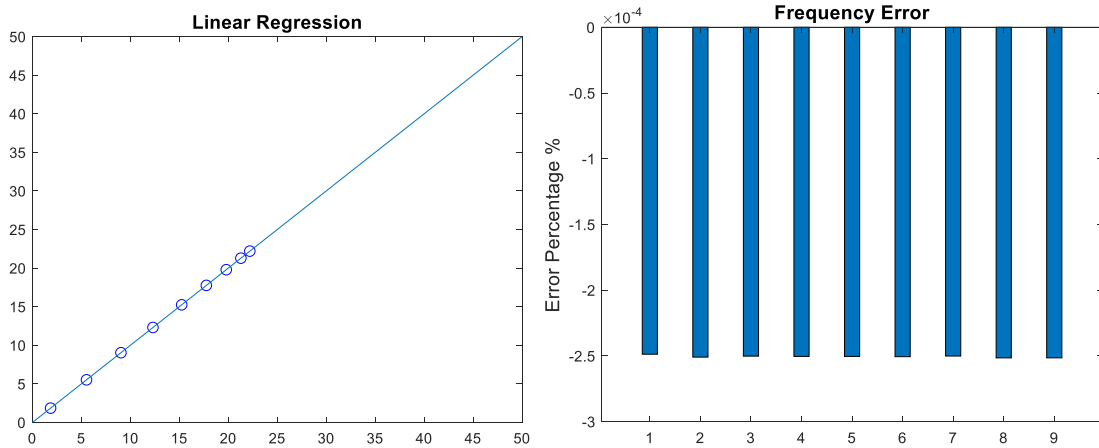


Figure 29. Comparison between model response and the corresponding raw data and trend of poles.

It is possible to see the optimal behaviour of the algorithm without noise. The linear regression (Figure 30) shows that the estimated frequencies follow the same pattern of the numerical ones.



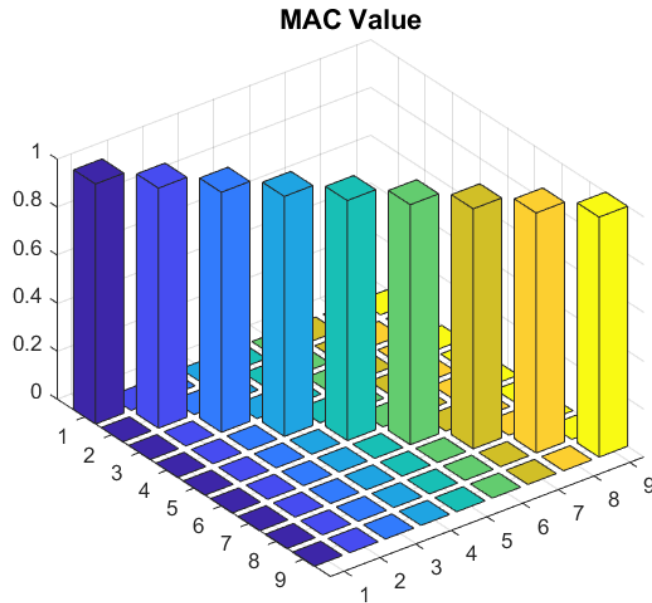
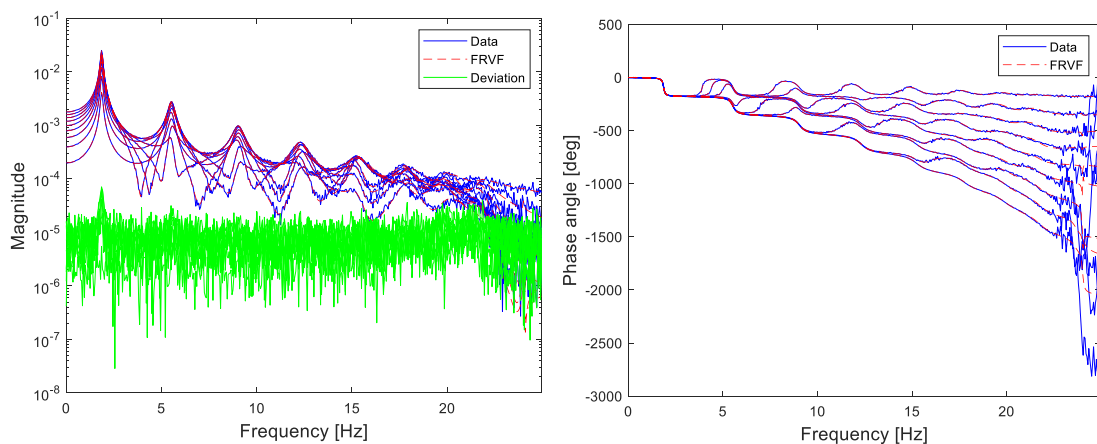


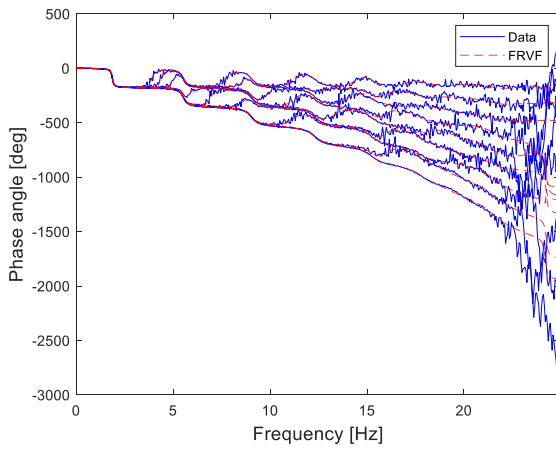
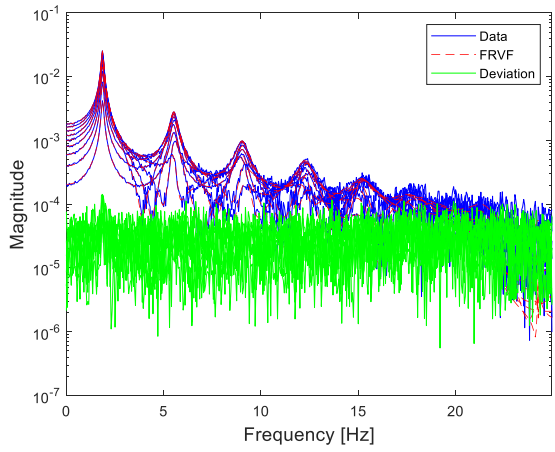
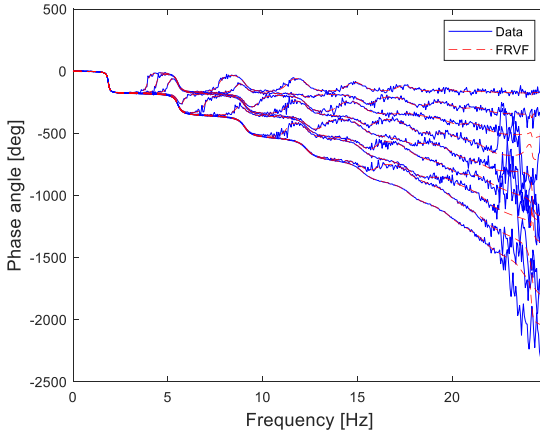
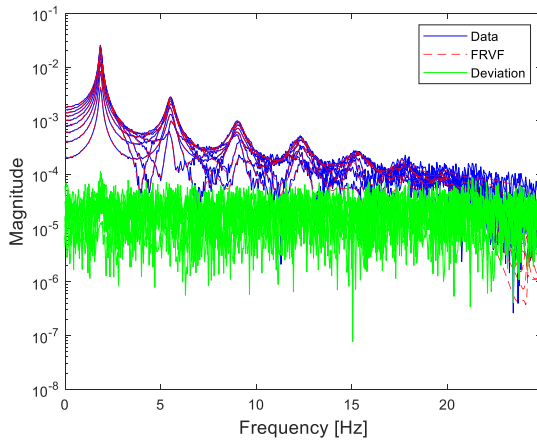
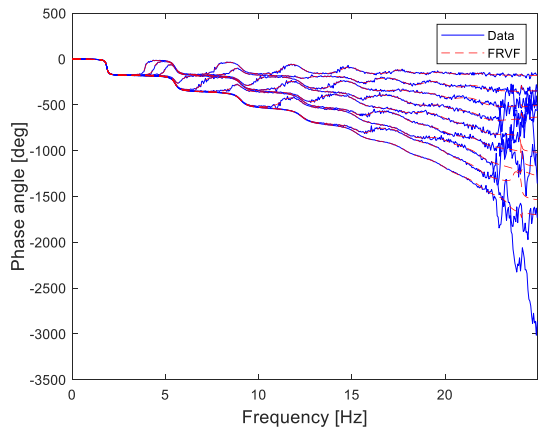
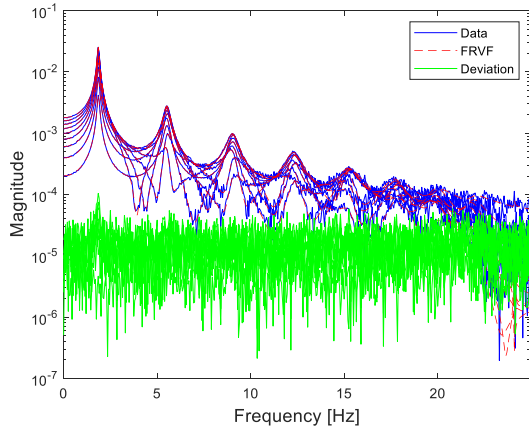
Figure 30. Correlation between numerical and VF parameters: on the top the linear regression (left) and percentage of error (right) between numerical and VF frequencies, on the bottom correlation between numerical and VF mode shapes with MAC

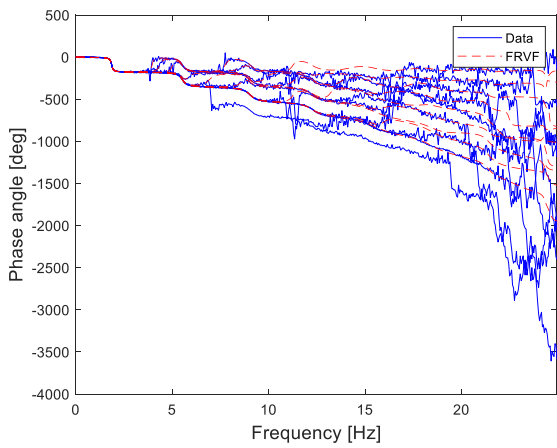
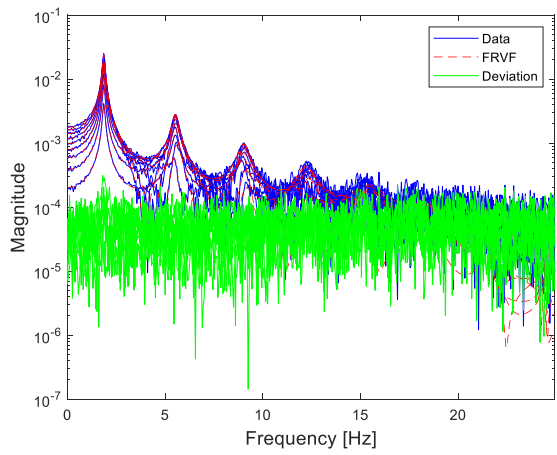
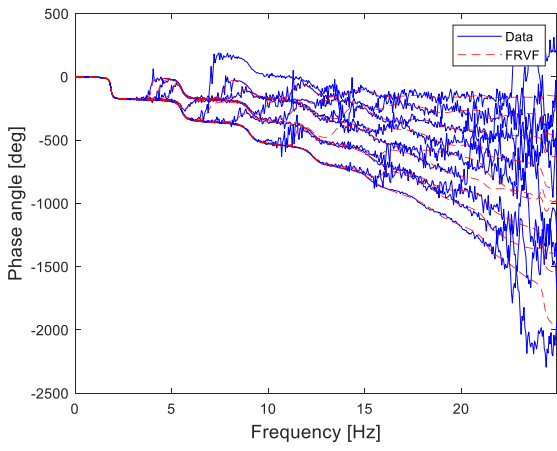
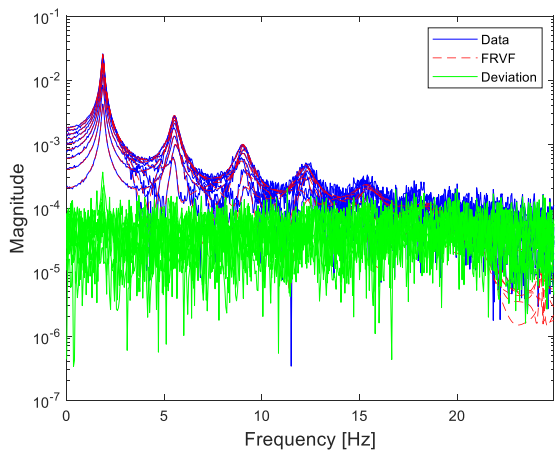
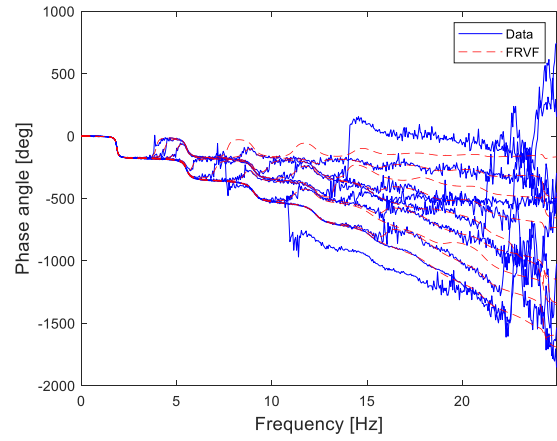
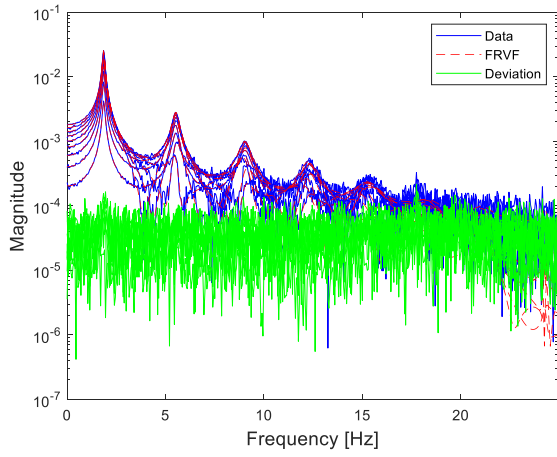
The results, reported in Figures 30, show very modest errors in no disturbance added to the accelerometric recordings used as input for the identification process: on the natural frequencies the error is equal to 1/10000. The MAC values are over 99%.

### 6.3.2 Simulations with noise

In the following Figure 31 magnitude and phase of Vector Fitting identification for 9Dof frame, with variable noise level, are shown. Only the results simulating adding a percentage of noise in the range of 1-10% are reported:







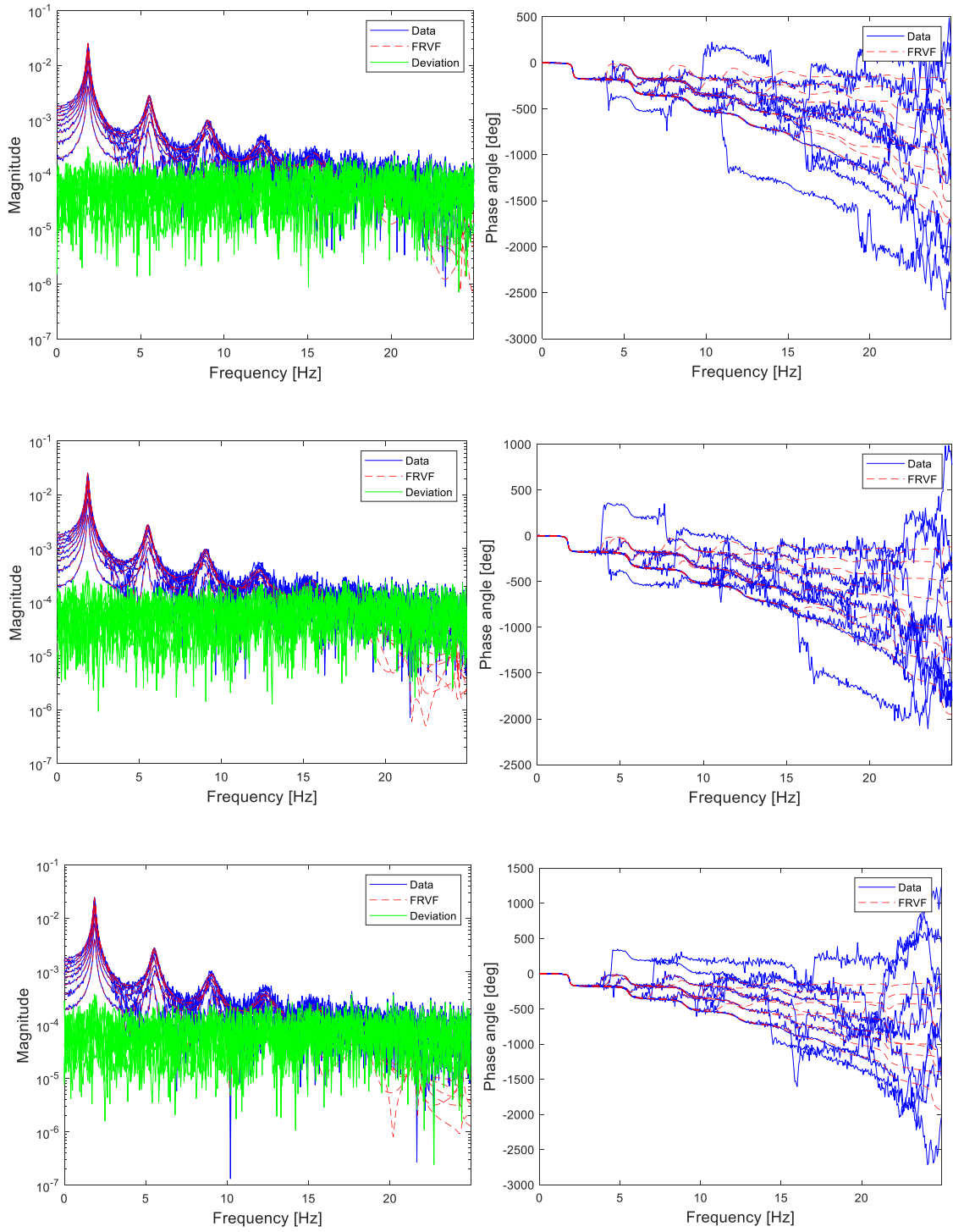
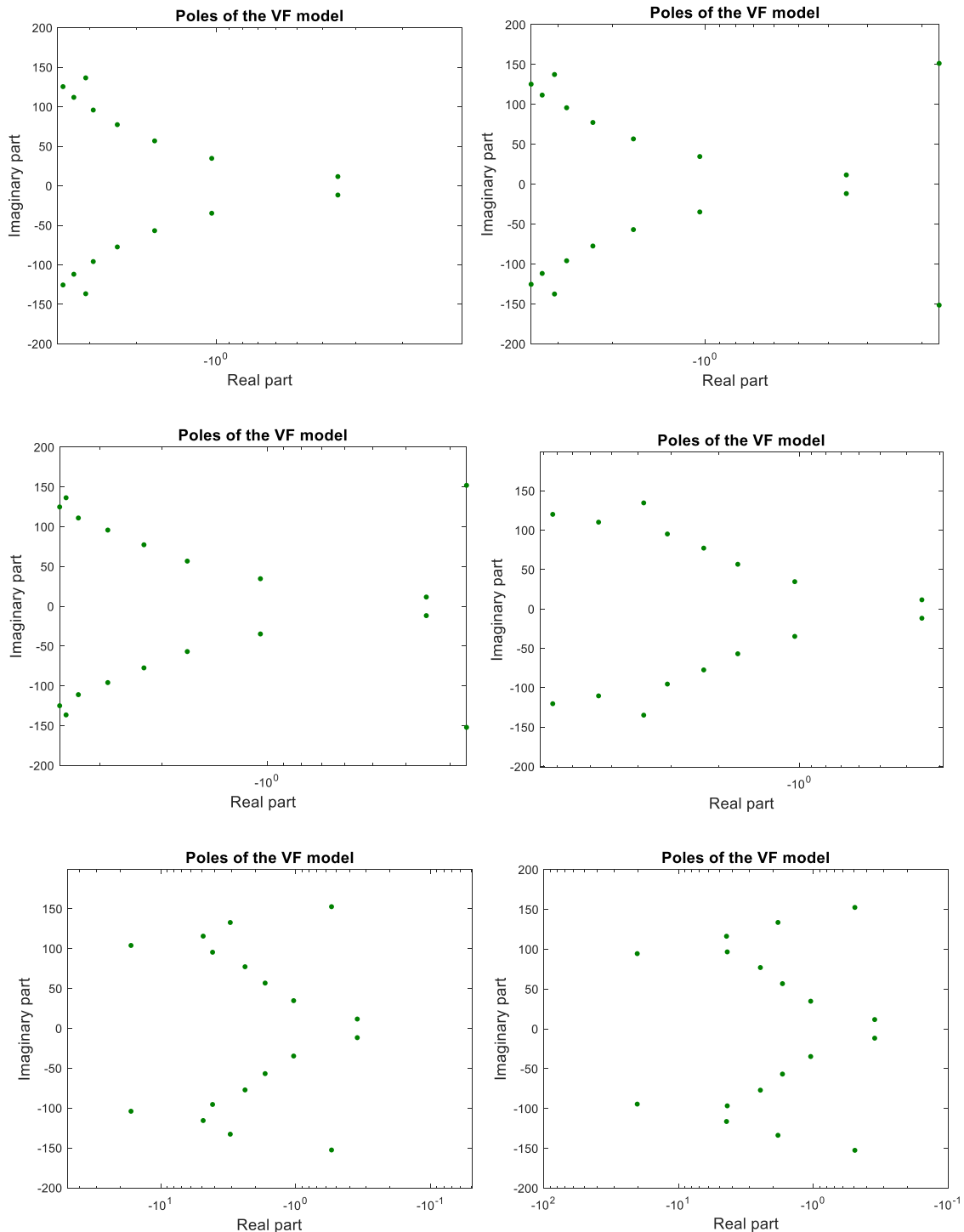


Figure 31. Comparison between model response and the corresponding raw data for noise percentage 1-10% of signals: on the left the magnitude and on the right the phase

It is interesting to compare the different stages of the fitting curves. For lower noise level the perturbation affects only on the last frequencies. For noise values of 5-10%, a different situation happens. Therefore, FRVF differs from data and the fitting is more difficult, especially for the last modes. The deviation between the fitting curve and the data set increases. The poles evolution is shown in the following figures. The variant of curves behaviour is highlighted. The poles related to the last modes change their position with increasing of noise.



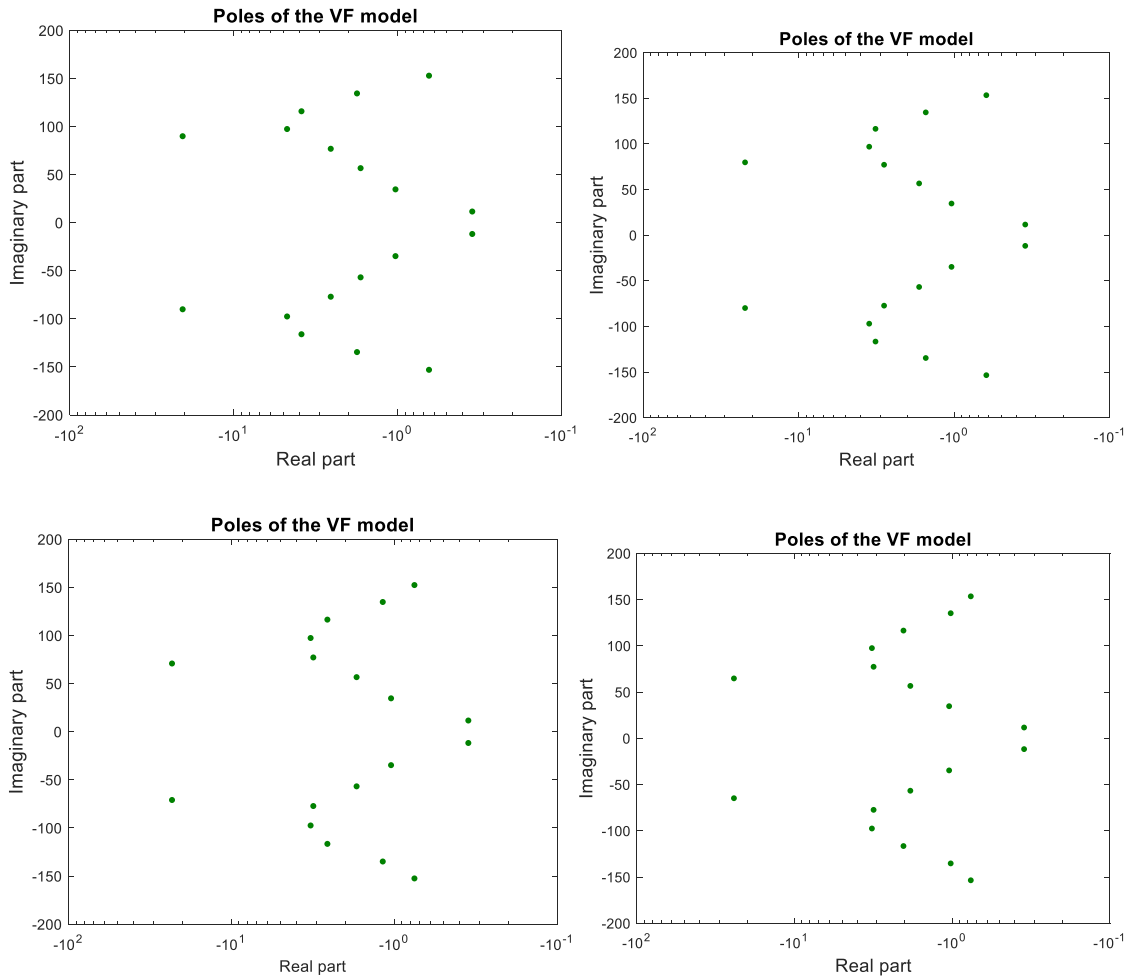


Figure 32. Evolution of the trend of poles of 9Dof (noise percentage 1-10%)

## 6.4 Analysis of results

To show properly the results of the fitting process, we decide to create matrices that will be plotted with the Matlab R2018b command *image*. It displays the data in array as an image that uses the full range of colors in the colormap. Each element of array specifies the color for one pixel of the image. The resulting image is an m-by-n grid of pixels where m is the number of rows and n is the number of columns in the matrix. The row and column indices of the elements determine the centers of the corresponding pixels. In this case, m and n represent respectively the n<sup>th</sup> mode of 9Dof and percentage of noise level. Three different cases are selected:

- Noise in input and output signals;
- Noise in input signal;
- Noise in output signals.

For each case reported above, three plots are made:

- [%] Error numerical vs VF frequency;
- [%] Error numerical vs VF damping ratio;
- MAC value between numerical vs VF mode shape.

The percentage of error is calculated with Eq. (114) both for damping ratio and frequency, while the MAC value with the relation (108).

#### 6.4.1 Noise in input and output signals

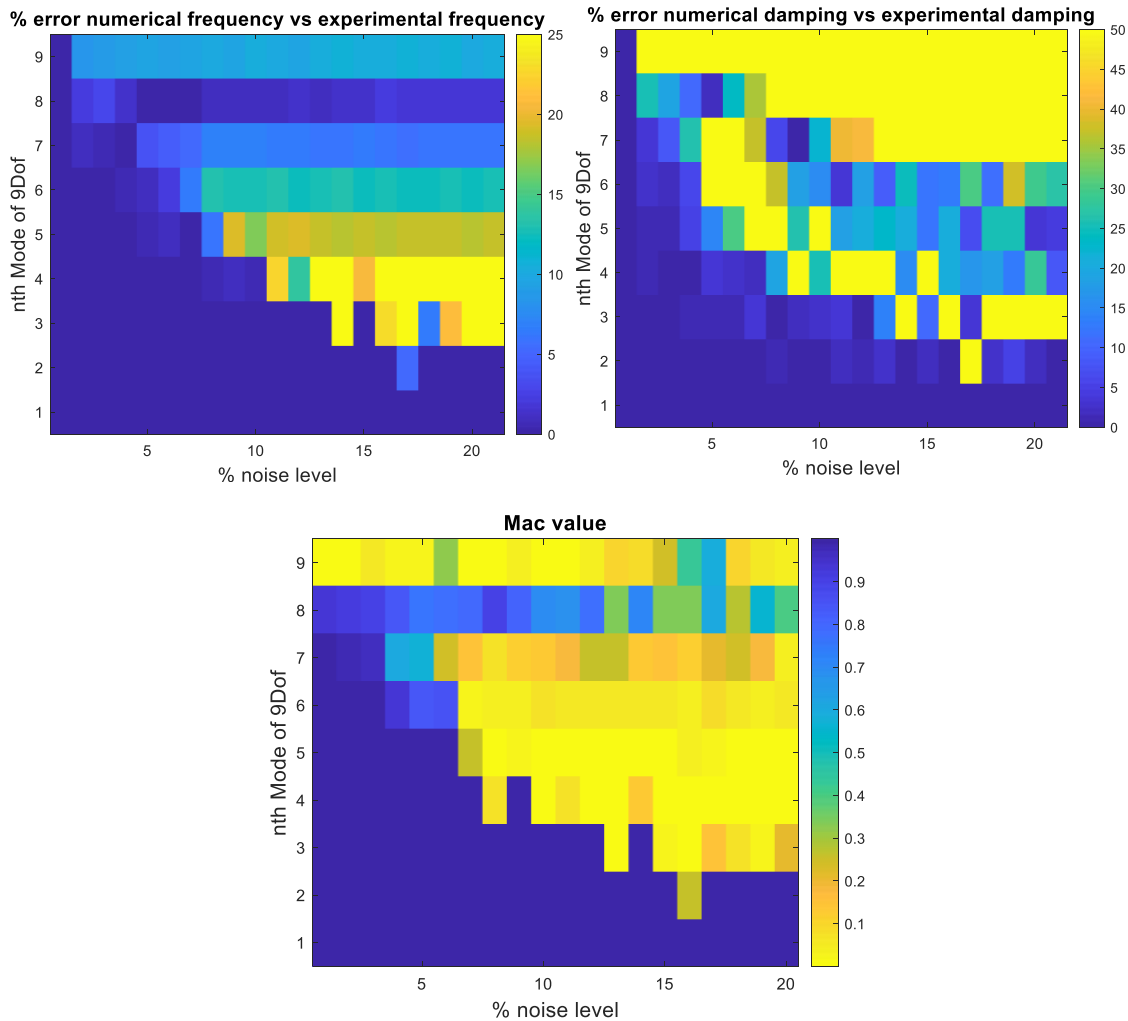


Figure 33. Noise in input and output signals. On the top: [%] error numerical vs VF frequency (on the left), [%] Error numerical vs VF damping (on the right); MAC value between numerical vs VF mode shape

In presence of disturbance both on the output and input signals (percentage of noise equal to 2%, 10% and 20%), the identification process provides results by means that are more distant from the exact solution. A percentage of noise equal to 2% corresponds to a Signal-To-Noise-Ratio (SNR) value higher than 50 dB, which is already very noisy. However, the error is modest on the evolution of frequency: it is approximately equal to 1-5% for noise range of 1-10% and 20% for very high noise level. The errors on the damping, instead, increase confirming the difficulty of

estimating the structural history. The dispersion, in the presence of noise equal to 20% of the signal, can be very high and the coefficient of error is equal to 0.5 (50%). In Figure 33 MAC coefficient is represented and shows a high similarity for the first mode shapes with a value close to 1. For noise level equal to 10% of signal, to catch exactly the modes becomes difficult. In conclusion, we always have positive results for the first fourth modes for whatever noise level. As for the last modes, the noise can seriously impair or destroy convergence.

### 6.4.2 Noise in input signal

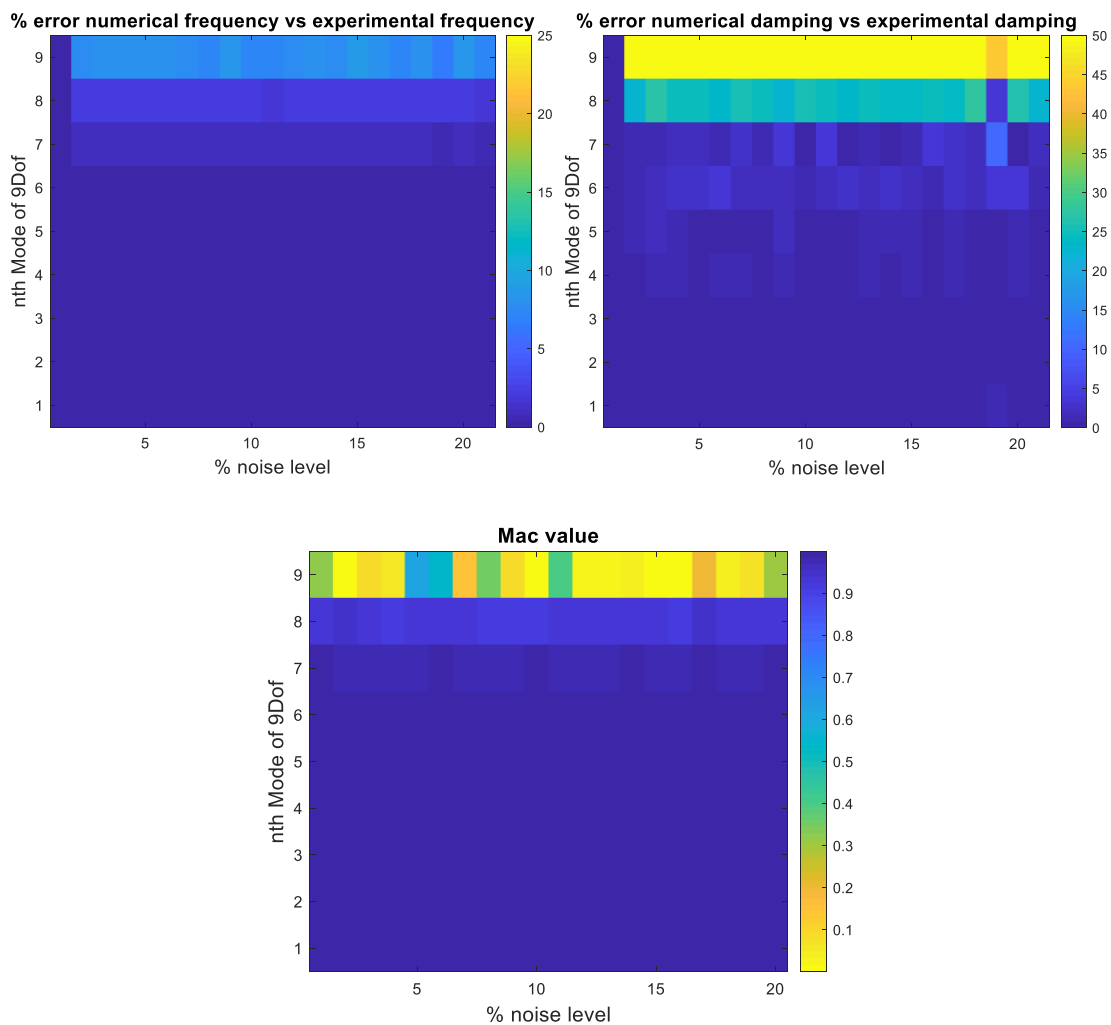


Figure 34. Noise in input signal. On the top: [%] error numerical vs VF frequency (on the left), [%] Error numerical vs VF damping (on the right); MAC value between numerical vs VF mode shape

In presence of disturbance on input signal (percentage of noise equal to 2%, 10%, until 20%), the identification process provides results by means that are better than the previous case. The error is low on the evolution of frequencies: it is approximately equal to 1-5%. The error on the damping, instead, increase but now, respect to before only for the 8<sup>th</sup> and 9<sup>th</sup> modes reaches the 40% error. As for MAC value is valid the same consideration of damping ratio. Only 9<sup>th</sup> mode is not correlation with the real one (Figure 34).

### 6.4.3 Noise in output signals

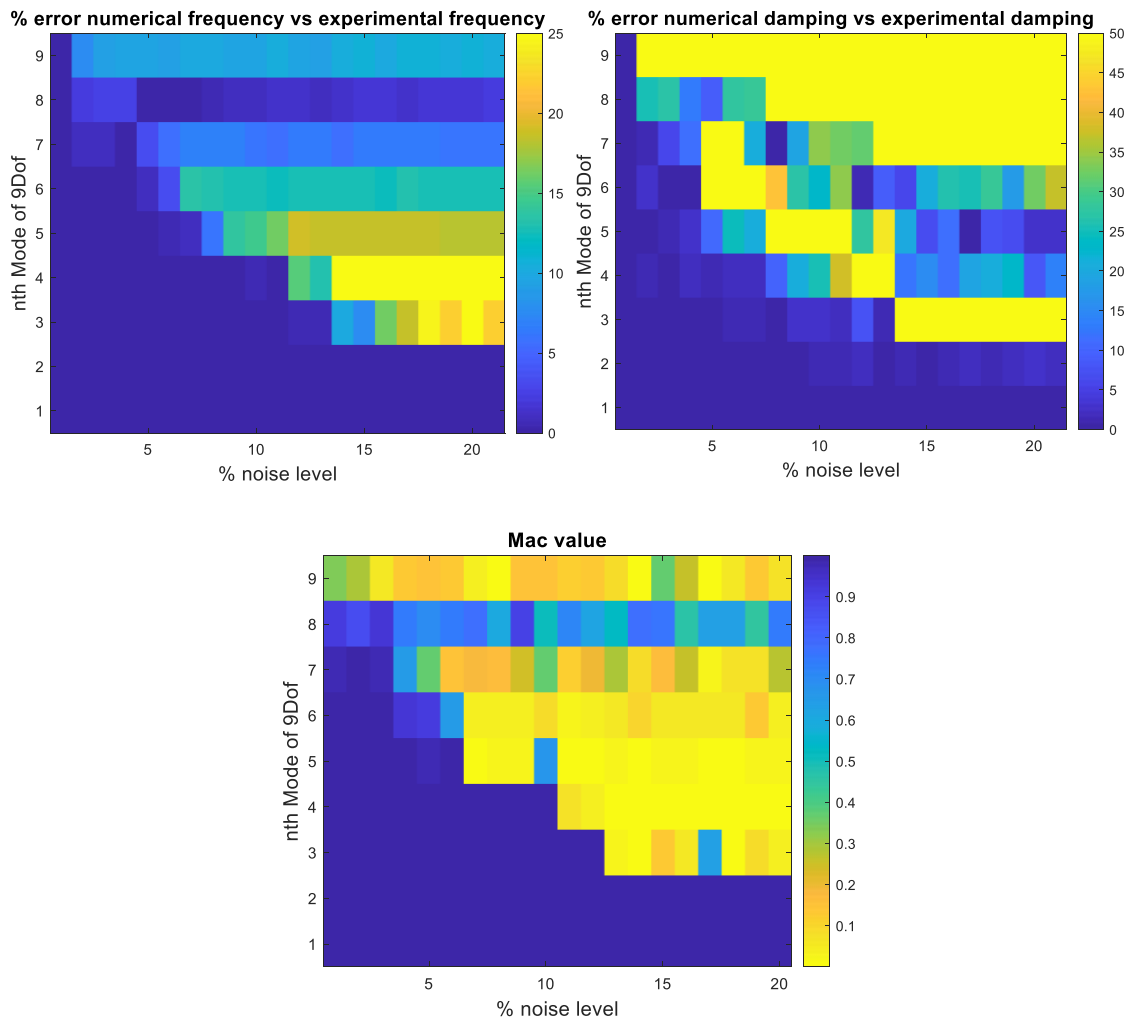


Figure 35. Noise in output signal. On the top: [%] error numerical vs VF frequency (on the left), [%] Error numerical vs VF damping (on the right); MAC value between numerical vs VF mode shape

In presence of disturbance only on the output signals (percentage of noise equal to 2%, 10% and 20%), the identification process provides results that are not distant from the exact solution. The errors are low on the evolution of frequencies: it is approximately equal to 1-5% for noise range of 1-10% and 20% for very high noise level. The error on the damping, instead, increases confirming the difficulty of estimating the structural history. The dispersion in the presence of noise equal to 20% of the signal can be very high and the coefficient of error is equal to 0.4 (40%). The MAC values of the first, second and third mode shapes are very close to one, giving an indication that the numerical and experimental mode shapes are highly correlated. For noise range from 10% of output signals, to catch exactly modes becomes difficult. In conclusion modal parameters of Vector Fitting method are more affected by noise presence in output signals than the input. This affirmation can be demonstrated with the trend of RMSE to the increase of the number of iterations and the noise level, as reported here below in Figure 36.

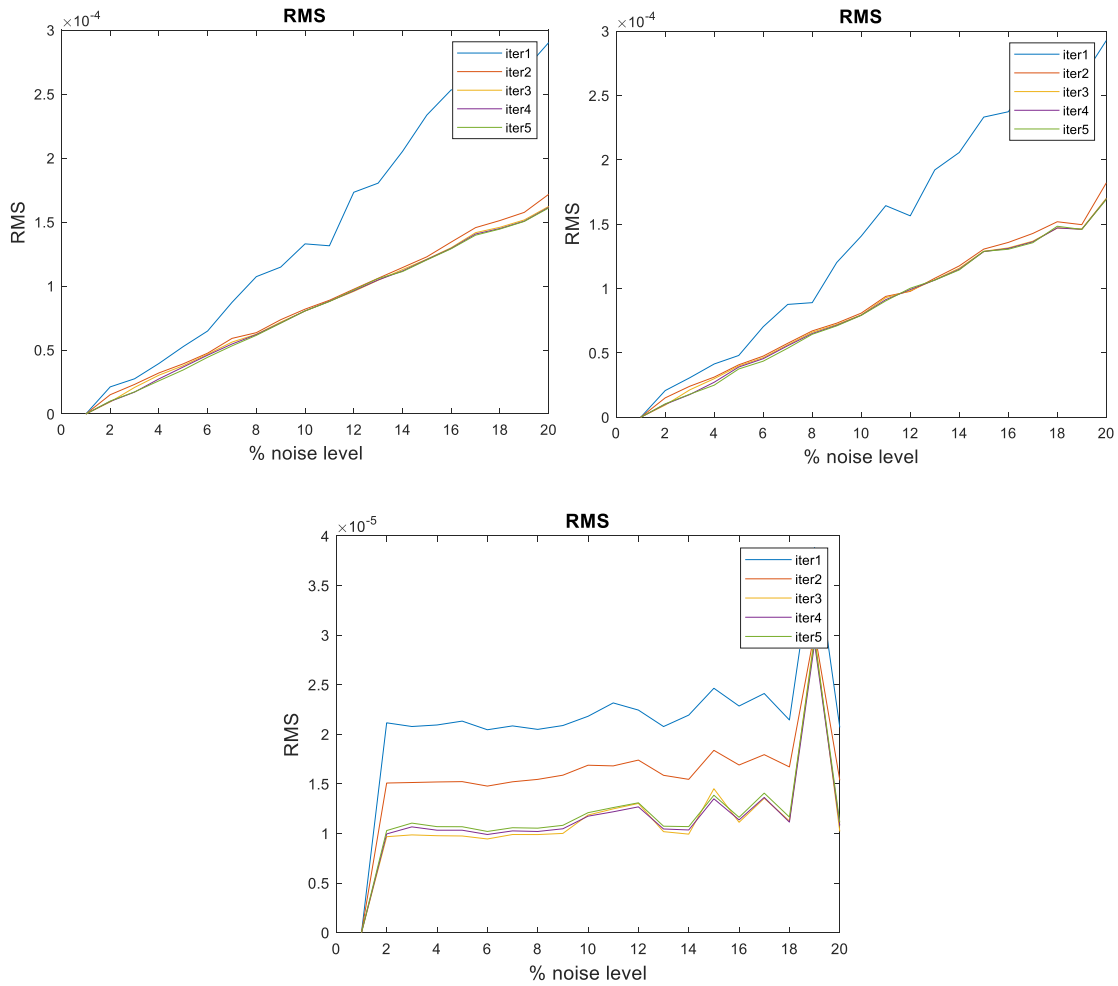


Figure 36. RMSE value to the increase of noise level and the number of iterations for each case studies: noise in output signals (on the top on the left), noise in input and output signals (on the top on the right), noise in input only (on the bottom)

Figure 36 shows the RMSE (Room Mean Square Error) for each of the 5 iterations utilised in the VF algorithm for increasing the noise level. The graphics are related to a range of noise percentage of 1-20%. The root-mean-square deviation (RMSD) or root-mean-square error (RMSE) is a frequently used measure of the differences between values predicted by a model or an estimator and the values observed. This value is higher when there is an important presence of perturbation. For a model that provides accurate predictions, the standardized mean error should be close to zero, and the root-mean-square error and average standard error should be as small as possible. It is interesting to note that, when the presence of noise is only in outputs signals or contemporary in input and output signals, the RMSE parameter grows linearly (Figure 36, on the top). Instead, when only input signal is affected by noise, RMSE trend is characterized by a plateau. For the first two cases the RMSE's values are about  $2E-4$ , while for the last analysis don't exceed the  $2E-5$  order. From these pictures it can also be inferred how rapidly the fitting of the proposed algorithm converge, as even in the worst case, convergence is achieved after 2-3 iterations

# 7 Experimental tests

This work summarizes the analysis of test data obtained from four different case studies in order to point out the strengths and limitations of Vector Fitting method.

Firstly, the dynamic identification of simpler experimental preliminary tests as a prototype airwing and a clamped box beam, both developed in the laboratory of Cranfield University, was estimated. For the first test, the curve fitting process was applied on the undamaged structure, in the second two u-shaped slots were made on the beam to simulate a damage state, assumed to be linear.

Subsequently, the chapter focuses on more complex structures. One of this is a three- storey frame developed in the Laboratory of Los Alamos, the other is based on a series of experimental campaigns performed on masonry arch bridge model in the laboratory of the Department of Structural, Geotechnical and Building Engineering of the Polytechnic of Turin. Different damage's types and levels have been applied in both tests in order to show the development of the modal parameters calculated with the Vector Fitting process. In addition, the influence of measurement noise was considered, especially in the masonry arch bridge test. In all tests the Fast Relaxed Vector Fitting version (vectfit3.m code) in used.

## 7.1 Preliminary tests

### 7.1.1 Prototype HAR Wing

The first experimental case study is the aluminum spar of a High Aspect Ratio (HAR) wing. The prototype airwing was modelled in the framework of the BEARD project at Cranfield University.

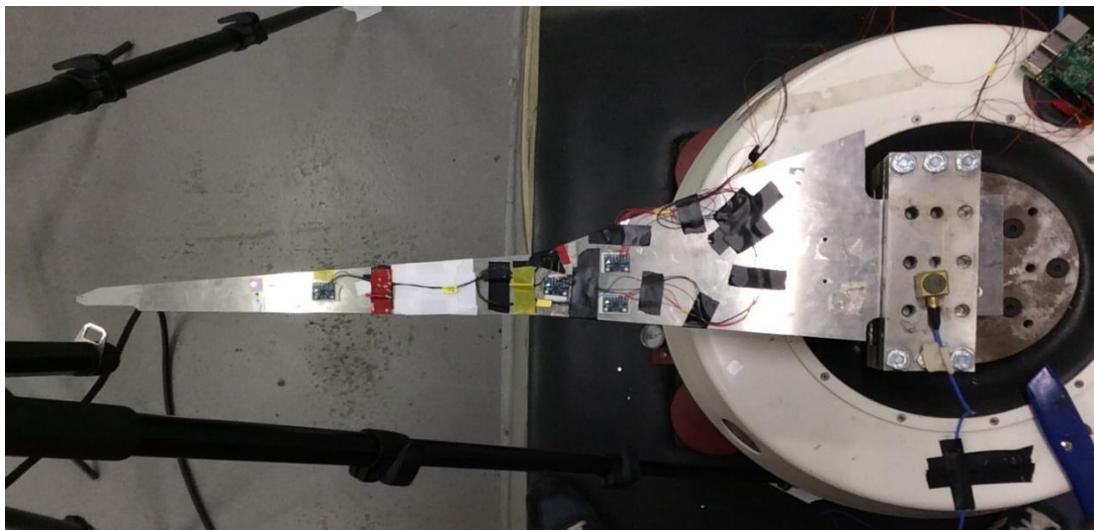


Figure 37. Test structure (Civera, Fragonara, & Surace, 2019)



Figure 38. Lateral view (Civera, Fragonara, & Surace, 2019)

The details of the airwing spar are shown in Table 4. The structural component of the beam is supposed to completely absorb the aerodynamic forces applied to the airwing, as its skin was realised to minimize the effects on its dynamical response.

<b>Density <math>\rho</math></b>	2850 kg/m <sup>3</sup>
<b>Young's Modulus <math>E</math></b>	$7.31 \cdot 10^{10}$ Pa
<b>Poisson Ratio <math>\nu</math></b>	0.33
<b>Free length (clamp to tip) <math>l_{tip}</math></b>	706.0 mm
<b>Thickness <math>t</math></b>	2.0 mm
<b>Max width at clamped section <math>b_{max}</math></b>	180.00 mm
<b>Mid-length width at the section of changing tapering (<math>l = 258</math> mm) <math>b_l</math></b>	56.10 mm
<b>Min width at tip section <math>b_{min}</math></b>	17.04 mm

Table 4. Geometrical and mechanical properties of the wing spar (Civera, Fragonara, & Surace, 2019)

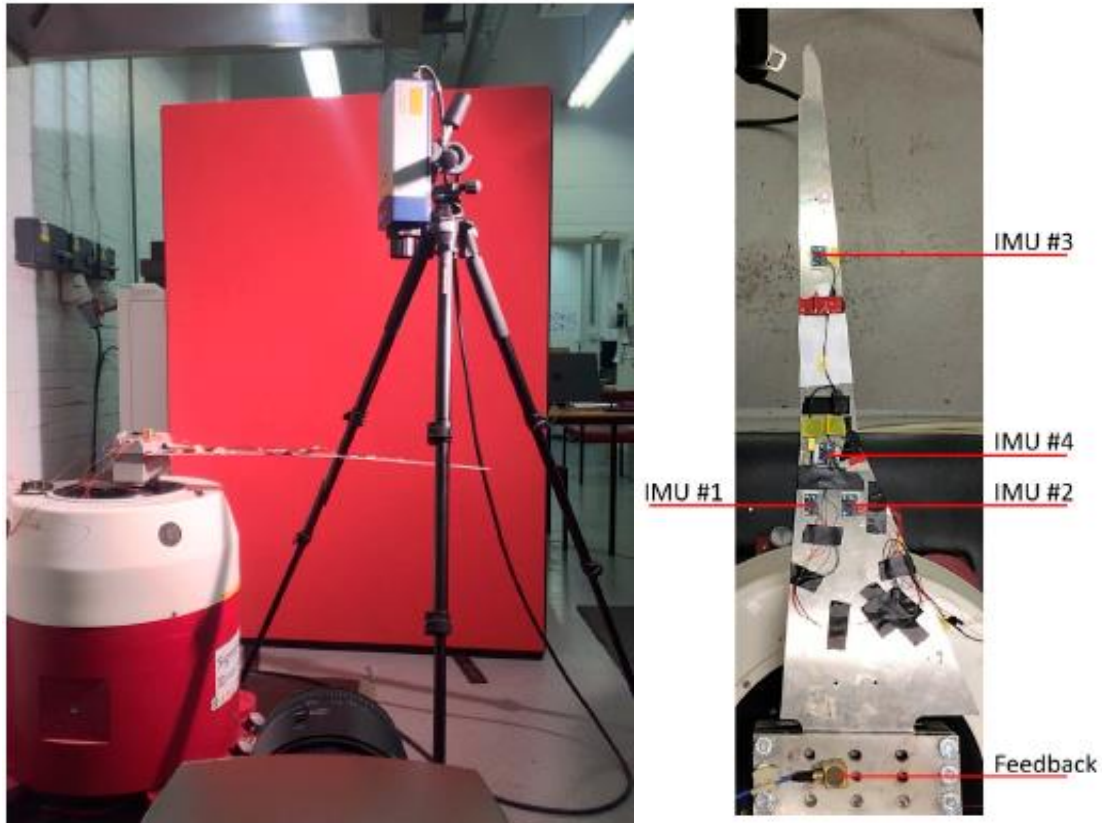


Figure 39. Experimental setup: Modal shaker, high-speed video camera and laser velocimeter (on the left) and IMU sensors' position along the wing (on the right) (Civera, Fragonara, & Surace, 2019)

The description of the experimental test is reported thanks to the paper intituled “*Using Video Processing for the Full-Field Identification of Backbone Curves in Case of Large Vibrations*” written by Cecilia Surace et al.: “Recordings were performed with an Olympus \*I-speed 3, high-speed camera, pointed to the spar trailing edge. Polytec \*OFV-505 single point LDV was used for calling the phase quadrature of the output signal. The input was applied as an external acceleration at the clamped end by means of a Data Physics\* Signal Force modal shaker and its DP760 close-loop control software. The software was set to increase the input frequency of 1 mHz at any step. The duration of the frequency steps was not constant; an automatic settling time option was used, considering 1% of tolerance between consecutive periods of the output. Laser velocimeter was used to check the frequency at a given point relatively close to the spar tip.” The experimental setup is shown in Figure 39.

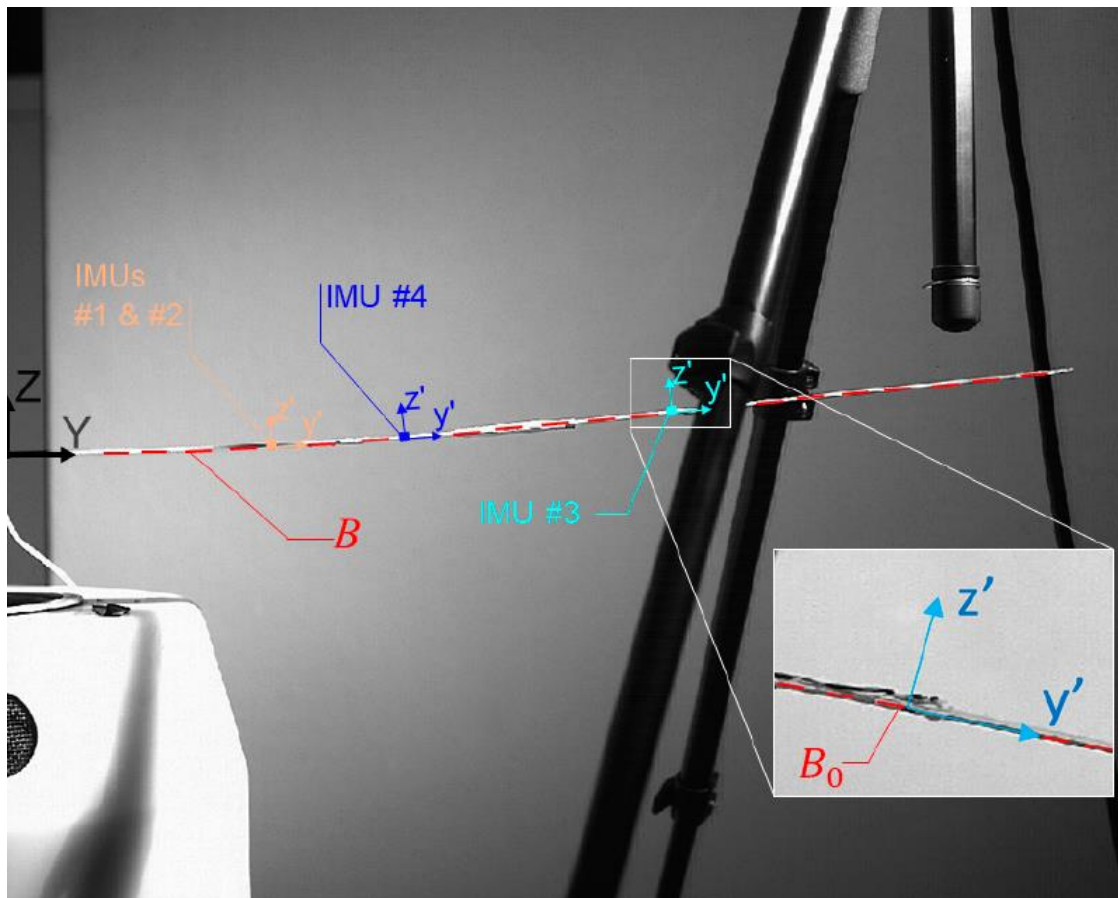


Figure 40. Global and local reference system (Civera, Fragonara, & Surace, 2019)

Four Raspberry PI® inertial measurement units (IMUs) were used for the analysis. The sensors were placed at  $Y = 200, 250$  and  $450$  mm from the clamped end and positioned as in Figure 40 and Figure 37. The acquisition setup consisted of the 4 IMUs, cables, tape to attach the cables to the structure and adhesive foils to attach sensors to the spar extrados, for a total weight of 11 grams. This has been proven here and in previous studies to not affect the quality of measured accelerations, while being minimally invasive.

A stepped sweep sine procedure was performed. A band-limited range of frequency of 5.33-5.50 Hz was used to excite the structure. The test was supported to isolate the first natural frequencies. The amplitude of the input is 0.035 g. The acceleration histories of the system are illustrated in the plot below:

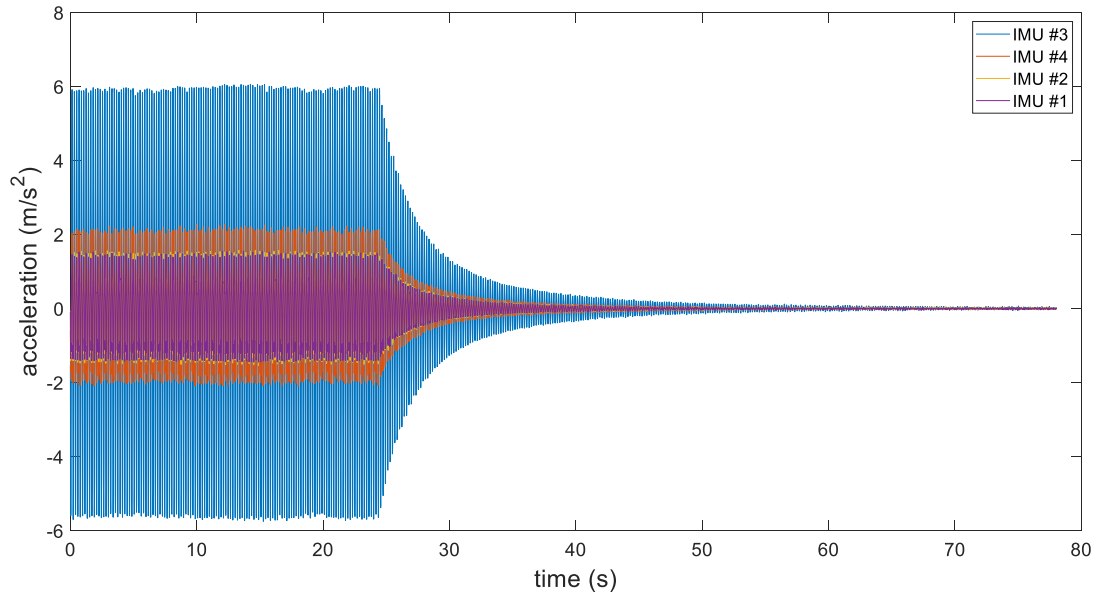


Figure 41. Acceleration histories for 4 IMUs (dwelling and free decay)

The sampling frequency is 2048 Hz. As for the numerical tests, the Frequency Response Function estimates is computed as the ratio of Fast Fourier Transforms of the output on the input force (Eq. 113):

$$H(f) = \text{OUTPUT}(f) / \text{INPUT}(f)$$

The free decay is neglected from the evaluation of the FRF and it is illustrated in Figure 42. It is clear the influence of noise in FRF estimate. In fact, the airwing's study is only a preliminary case in order to optimize the Vector Fitting ability in the next ones. A peak at 5 Hz is visible and represents the first mode of the airwing.

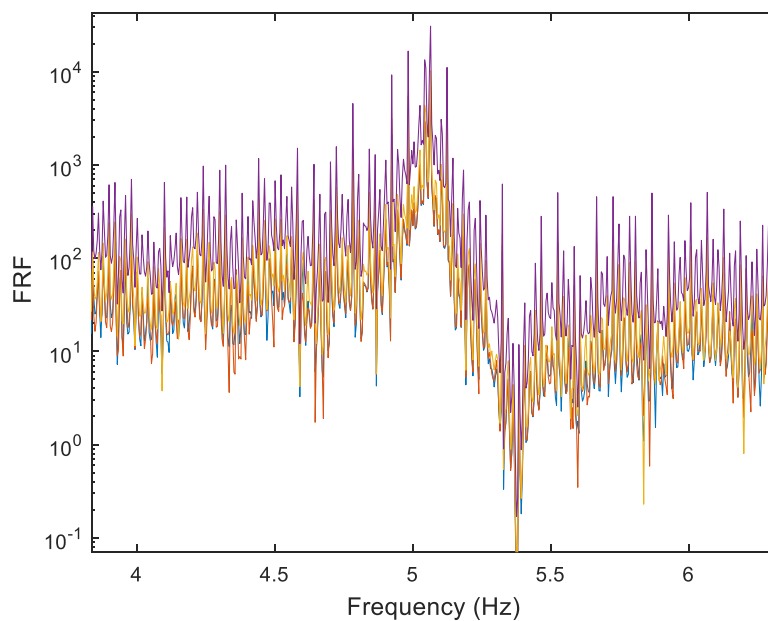


Figure 42. FRFs of Channels 1-4

The fitting was applied to  $H(f)$  using a model order  $N=10$ , with 5 iterations. Each element in  $H(s)$  was in the fitting process weighted with the inverse of its magnitude. The resulting approximation is shown in Figures 43-44. The magnitude and phase of Fast Relaxed Vector Fitting process are shown below for the range of frequency 4-6 Hz. Note how the curve fitting minimizes the measurement noise and it identifies the first natural frequency. Deviation has not been reported for better comprehensibility of the image.

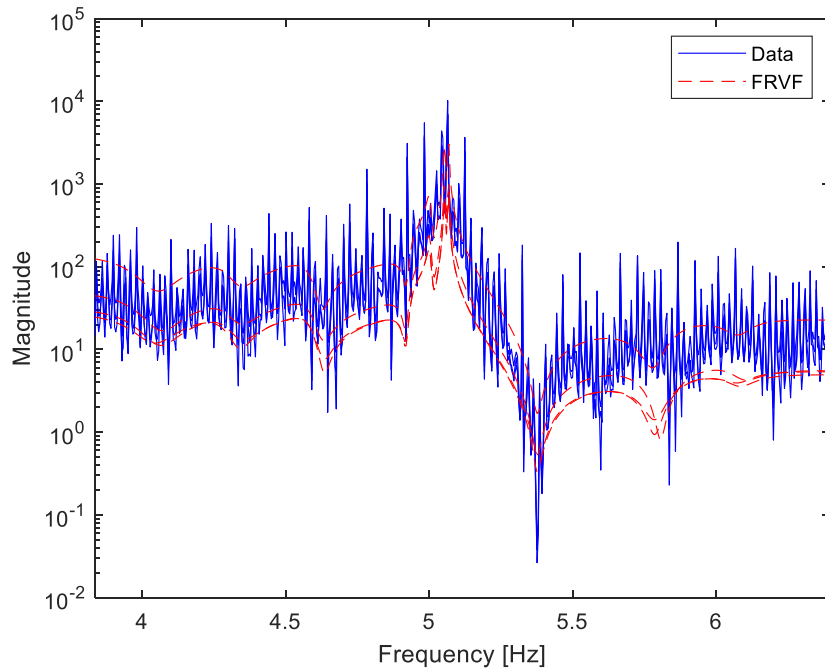


Figure 43. VF magnitude for the range 5.3-5.5 Hz (first mode)

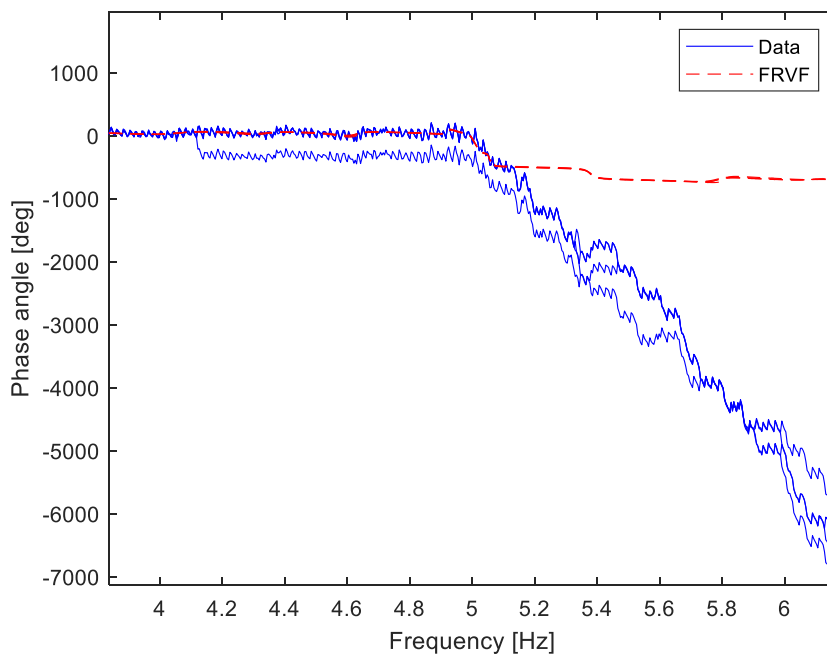


Figure 44. VF phase for the range 5.3-5.5 Hz (first mode)

The Vector Fitting fits the phase of the data until the frequency 5.2 Hz. It is supported by the fact that the system was excited to cover only the first mode.

In order to give a general view of the confidence of the results, we compared them with the finite elements model (FEM) of the prototype airwing designed with the software ANSYS. The modal parameters obtained with FEM analysis is reported in Figure 45. With the coordinates and displacements given by this analysis, it was possible to plot on Matlab a airwing's 3D model that give us a completely view (Figure 46).

FEM		VF	
Frequency (Hz)	5.4	Frequency (Hz)	5.1 (5%)
Damping (%)	0.3	Damping (%)	0.4
Mode shape	0.0890	Mode shape	0.2240
	0.0900		0.2242
	0.1376		0.3231
	1		1

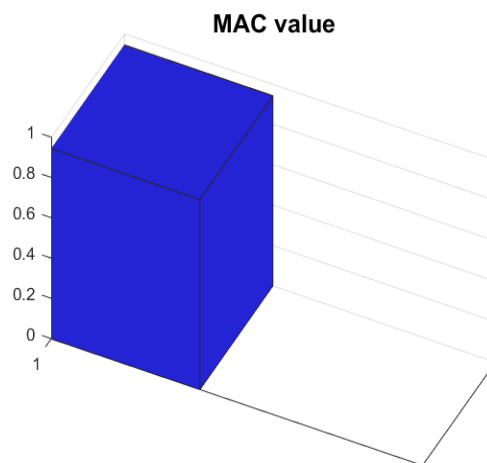


Figure 45. On the top: modal parameters calculated with VF process (on the right) and with FEM analysis (on the left). On the bottom: MAC value

The percentage of frequency error is 5%, probably due to the noise measurements. The mode shapes are normalized respect the maximum displacement, that for the first mode is represented by that of the last sensor (IMU #3). In chapter 6 we have introduced the modal criterion MAC (Modal Assurance Criterion) to evaluate the confidence of the curve-fitting process. In the experimental test it is fundamental parameter to estimate the robustness of the VF technique. MAC value is comprised between 0 and 1 and it is an indicator of the quality of the experimental

modal vector. A value close to 1 indicating close correlation. In this case the MAC value is 0.9433 (Figure 45)

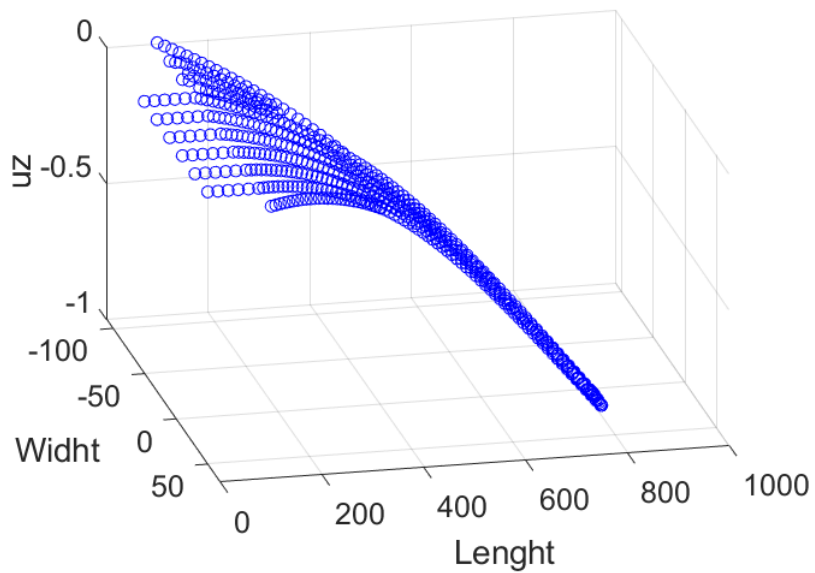
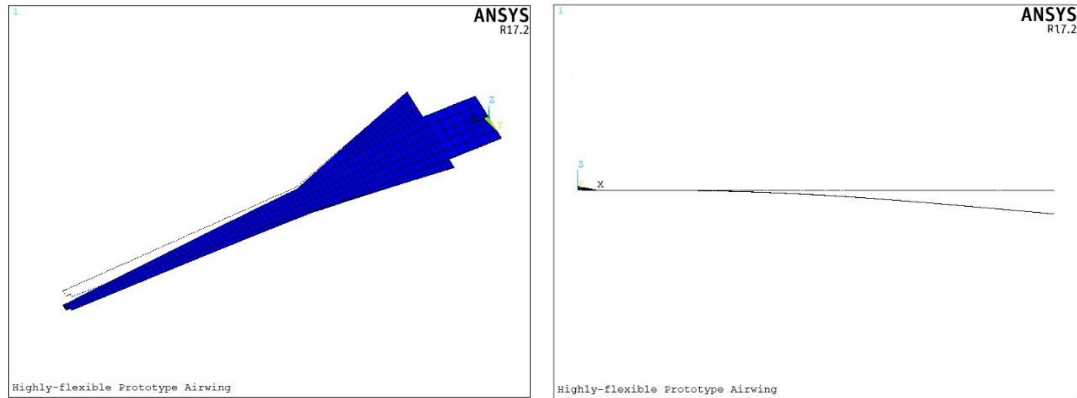


Figure 46. FEM airwing model (manual calibrate): representation of first mode

In the 3D plot (Figure 46), the length used is 806 mm because the framed part of 100 mm is considered. In this way the new positions of the channels are respectively 300, 300, 350, 550 mm.

The following Figure 47 shows the first mode shape of the prototype wing. The grey points represent the position of the IMUs along the wing from the clamped end (framed part is not given).

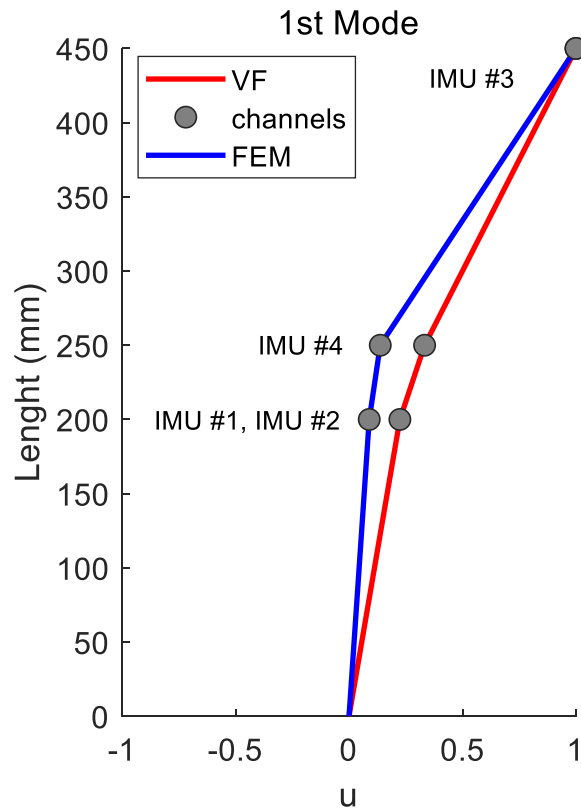


Figure 47. First mode shape of wing with Vector Fitting analysis

In Figure 47 we have imposed the same displacement for the sensor IMU #1 and IMU#2. In reality a small difference exists between the two displacements due to a small torsion. But as it is of the order of  $10E-5$ , it is possible to neglect it.

### 7.1.2 Cantilever box beam

The experimental case study consists in an aluminium cantilever box beam. The tests were performed at laboratory of Cranfield University with a Data Physics® Signal Force™ modal shaker, already mentioned in the previous section. Otherwise from the first experimental test, damage conditions are now applied on the beam, in order to simulate the changes in real-world structures caused by varying operational and environmental conditions.



*Figure 48. Experimental Setup*

In this test Data Physics® Signal Force™ modal shaker and DP760 close-loop control system were used to induce 10 triangular impulses at the clamped base of 11 milliseconds, with a peak value of 5g. As the previous airwing's test, the measurements were performed with an Olympus • I-speed 3 camera. The camera was mounted on the levelled tripod and it was assumed to be perfectly static. An-open face lighting fixture with a tungsten light source was use for the illumination.



Figure 49. Lateral view of the cantilever box beam

The elapsed time between two impulse is 2000 milliseconds. The sampling frequency is  $f_s=2048$  Hz. The Nyquist's limit of acquisitions is 1024 Hz. Many sample points per period are necessary for accurate time-frequency estimation. This is particularly important for impact tests, where instantaneous variations in frequency and amplitude in the free decay response are present and high temporal frequency resolution is needed. For this reason, only the frequencies from 0-300 Hz are inspected. In this way the study is limited on the development of the first and second frequencies, because the third mode is above 300 Hz.

<b>Density <math>\rho</math></b>	2170 kg/m <sup>3</sup>
<b>Young's Modulus E</b>	69 GPa
<b>Moment of Inertia I</b>	$1.63 \cdot 10^4$ mm <sup>4</sup>
<b>Free length l</b>	716.0 mm
<b>Thickness t</b>	2.0 mm
<b>Cross-section A</b>	184.0 mm <sup>2</sup>
<b>Side (H=W)</b>	25 mm

Table 5. Material and geometrical properties

The target damage has been simulated by means of two shaped- slots, regular and equal throughout the whole beam width, artificially inserted by sawing the box beam. The first notch was positioned at  $x_1 = 205$  mm from the cantilever beam. The second notch was introduced at  $x_2 = 319$  mm in the mid-span of the beam. The two notches distance about  $\Delta x = 114$  mm. These cracks were artificially made by sawing the beam (cut thickness 1 mm). The crack growth was simulated by further sawing the specimen. The second slot was cut with a 5:1 mm inclination ( $\beta = 90^\circ - 78.7^\circ = 11.3^\circ$ ) to investigate both effect growth in length and inclination of crack (slanted cuts). Damage steps are summarized in the Table 6:

Damage step	Damage depth	
	$d_1$ (mm)	$d_2$ (mm)
no damage	-	-
Step#1	1	no damage
Step#2	5	no damage
Step#3	10	no damage
Step#4	15	no damage
Step#5	15	5
Step#6	15	10
Step#7	15	15

Table 6. Damage levels ( $d_1$  and  $d_2$  are intended as vertical components of length:  $l_1 = d_1$  and  $l_2 = d_2 / \cos(\theta)$ )

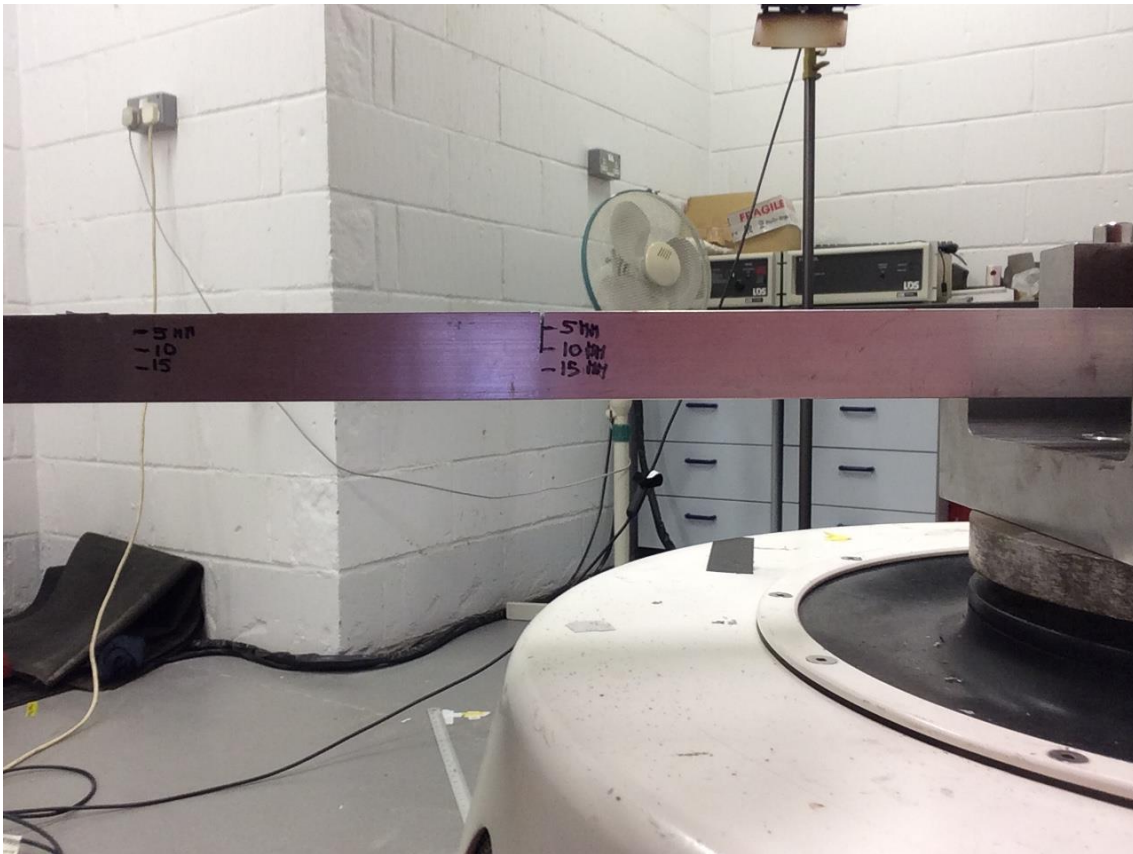


Figure 50. Box beam lateral view: in black different level of slots (5,10,15 mm)

Main assumptions made for these experiments is that hand-made slots are a good approximation of real damage. The presence of damage in the beam influence the modal parameters, such as the frequency. In fact, this is a simply case to analyse the trend of Vector Fitting method under damage conditions. Due to the unavailability of data, the work focuses on the four last steps (Step#4-Step#7). More damage steps' details are reported in the Table 7.

Damage step	State conditions	Description
Step#4	Damaged	straight cut level 15 mm in $x_1$ + no damage in $x_2$
Step#5	Damaged	straight cut level 15 mm in $x_1$ + angled cut level 5 mm in $x_2$
Step#6	Damaged	straight cut level 15 mm in $x_1$ + angled cut level 10 mm in $x_2$
Step#7	Damaged	straight cut level 15 mm in $x_1$ + angled cut level 15 mm in $x_2$

Table 7. Analysed damage steps' details

Due to the presence of only one sensor on the cantilever beam, the analysis of mode shapes isn't discussed in this section. One triangular impulse was isolated for the estimation of the transfer function. In the following Figure 51 the impulsive force and the response of the system in terms of acceleration of Step #4 are represented.

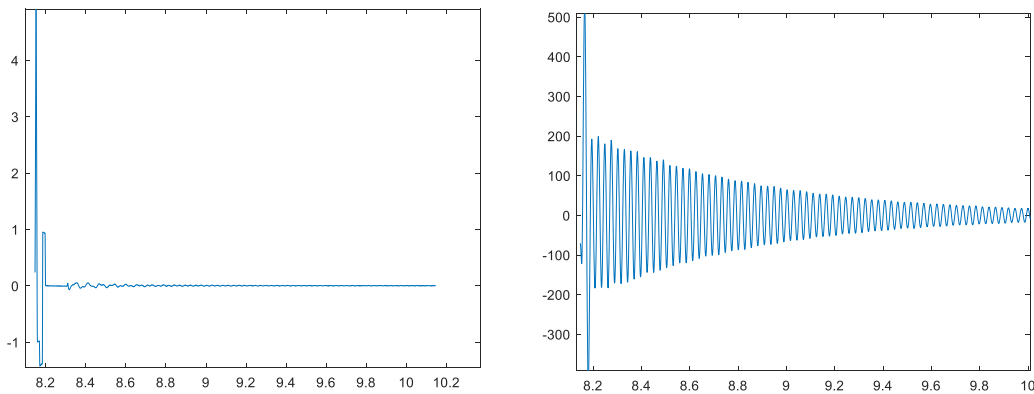


Figure 51. Force time history (on the left) and response time history (on the right)

The Frequency Response Function represents the transfer function  $H(f)$  calculated with the Eq. (113). Because of the presence of only one sensor, the FRF is composed by one complex function. Notice that the FRF is in semilogarithmic scale to compress the large signal amplitude and expand the small ones, allowing easier visualization of all frequencies in the signal (Figure 52).

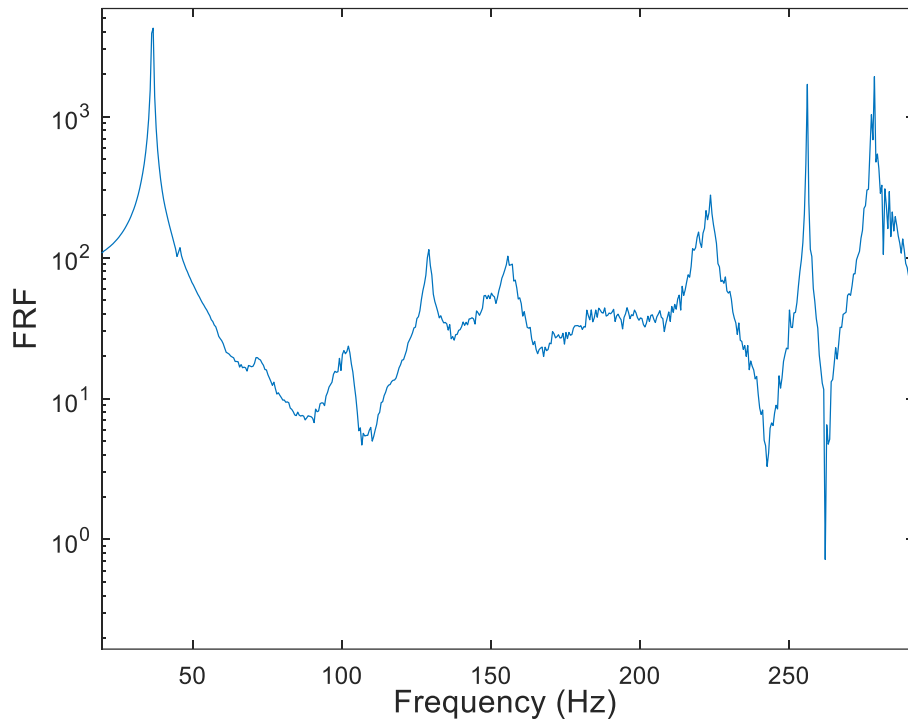


Figure 52. FRF  $H(f)$  of channel 1

All steps are processed with FRVF method. Different model orders  $N$  are selected so as to underline the fitting capacity even just for low order. Some examples of curve-fitting are illustrated in Figures 53-58 for Step #5.

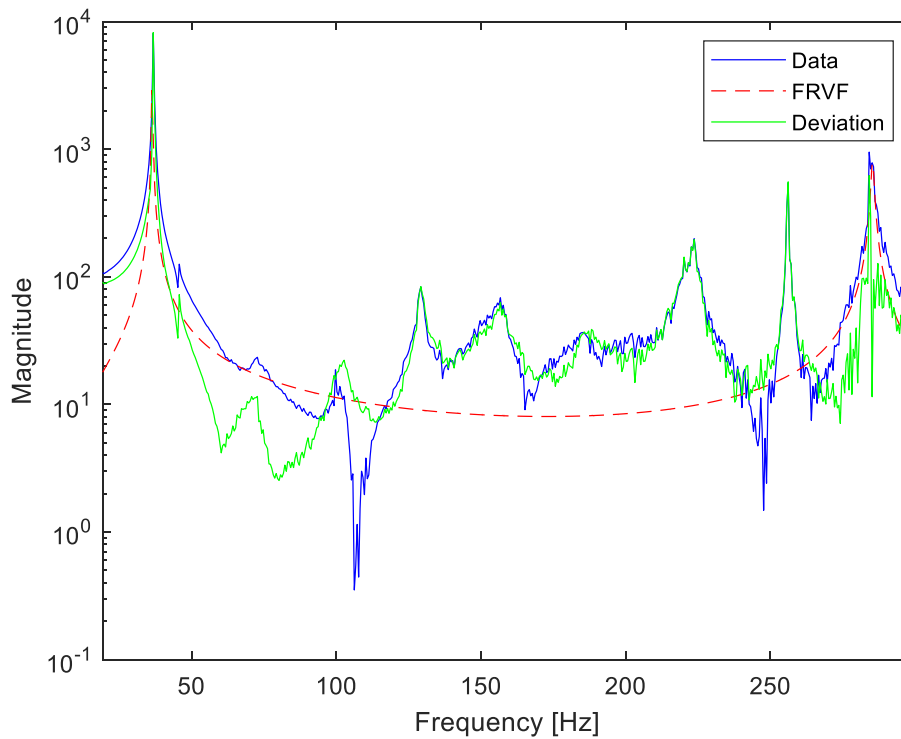


Figure 53. Magnitude of transfer function fitted by VF technique for Step #5 ( $N=2$ )

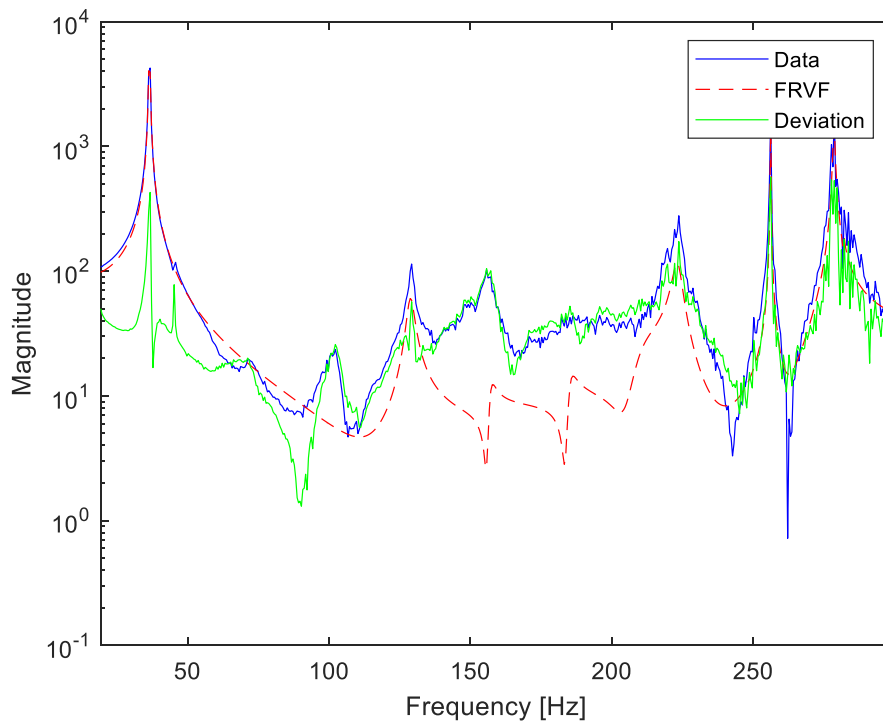


Figure 54. Magnitude of transfer function fitted by VF technique for Step #5 ( $N=10$ )

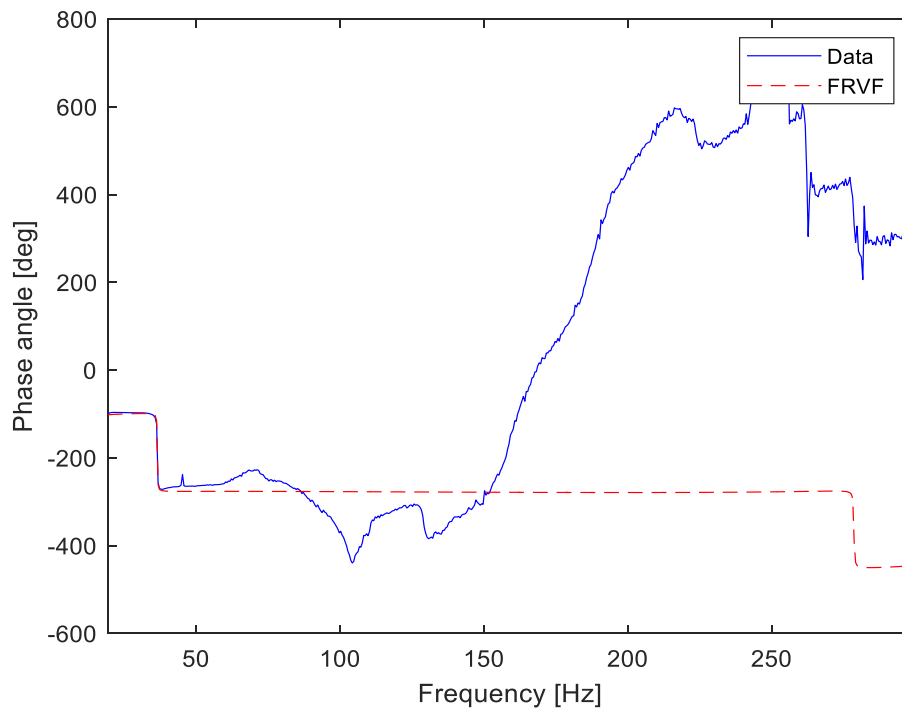


Figure 55. Phase of transfer function fitted by VF technique for Step #5 ( $N=2$ )

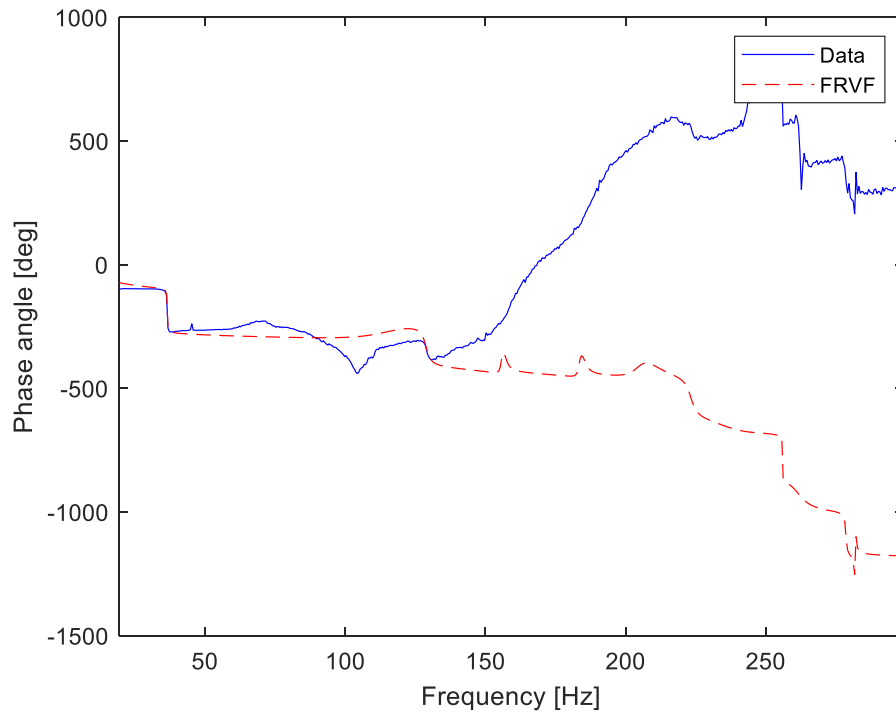


Figure 56. Phase of transfer function fitted by VF technique for Step #5 ( $N=2$ )

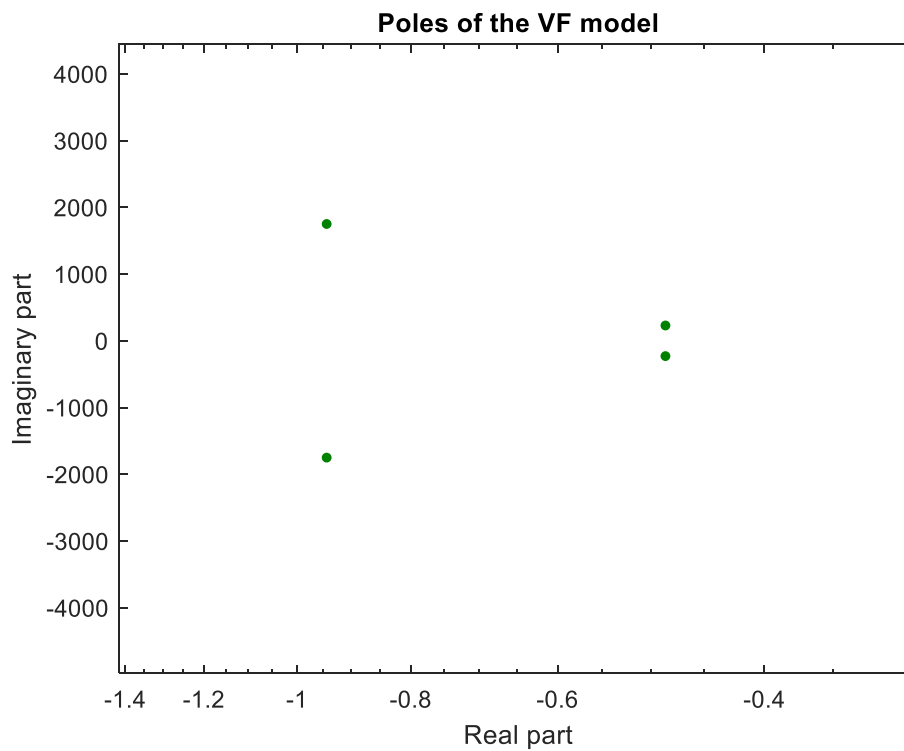


Figure 57. Poles of VF technique for Step #5 ( $N=2$ )

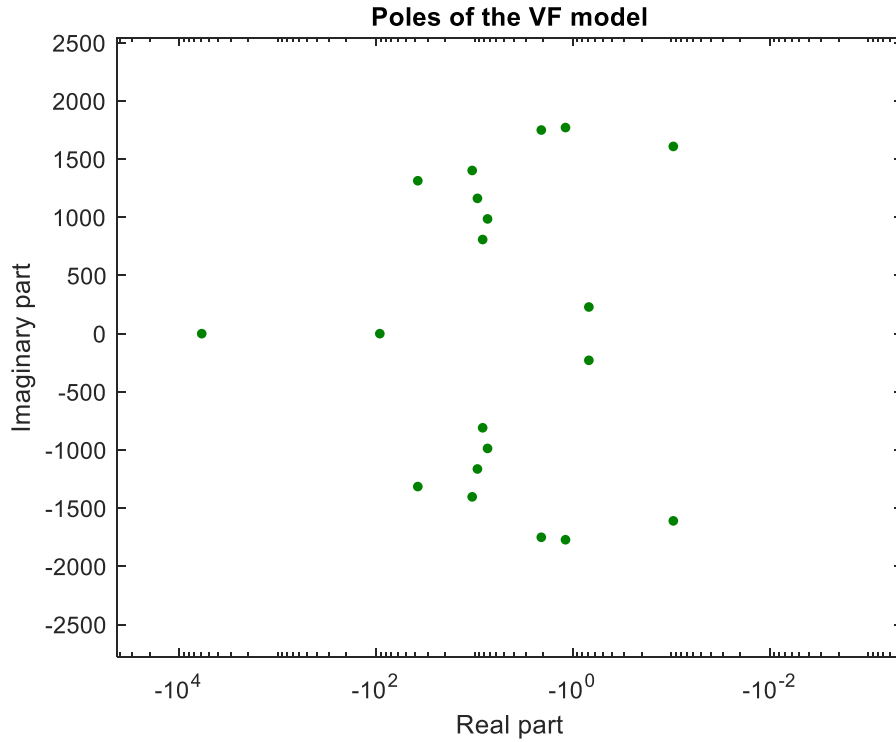


Figure 58. Poles of VF technique for Step #5 ( $N=10$ )

The plots 53-55 show the curve-fitting for  $N=2$  of the FRF. Despite the low model order, the FRVF capture the first and second natural frequencies. This is visible both in the magnitude and phase's plots. Increasing the model order ( $N=10$ ) the algorithm fits also peaks that are not real but due to the noise. In fact, one of the advantages of Vector Fitting method is its capacity to capture the real modes by using a low order. This process is evaluated for each state condition. Figure 59 shows the comparison between the FRFs obtained from all damage states. Note that the peaks related to first and second natural frequencies shift on the left increasing the damage state. In this way the frequency' values decrease (Table 8).

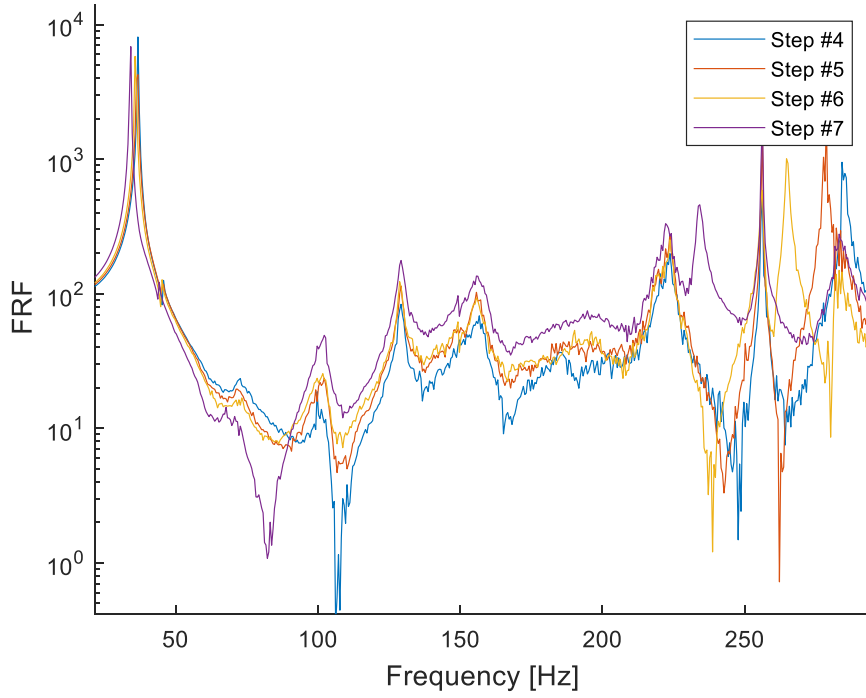


Figure 59. FRFs of the response at channel 1 for State #4, State #5, State #6 and Step #7

Damage step	Frequency	
	1° mode	2° mode
Step#4	36.38	285.33
Step#5	36.22	279.70
Step#6	35.76	269.03
Step#7	33.80	234.10

Table 8. First and second modes at increasing of damage

Once the modal parameters have been estimated for various orders ( $N_{\min}$  to  $N_{\max}$ ), one can produce a stabilisation diagram (Section 5.5) and cluster diagram (Section 5.6), using a segment of the correlation functions with a maximum length of  $L$  points, allowing to estimate a maximum system order ( $L$ . Zanotti Fragonara, Cranfield University). The stable poles from order  $N_{\min}$  to  $N_{\max}$  are determined on the basis of different stabilisation criterion, in terms of frequency, damping and MAC (Modal Assurance Criterion). In this set of test the following stabilisation criteria have been used:

$$\delta f \leq 0.5\%, \quad \delta \xi \leq 10\%, \quad (1 - MAC) \leq 10\% \quad (116)$$

Moreover, poles having unrealistic damping ratios (negative or larger than 10%) have been filtered out of the set of stable poles.

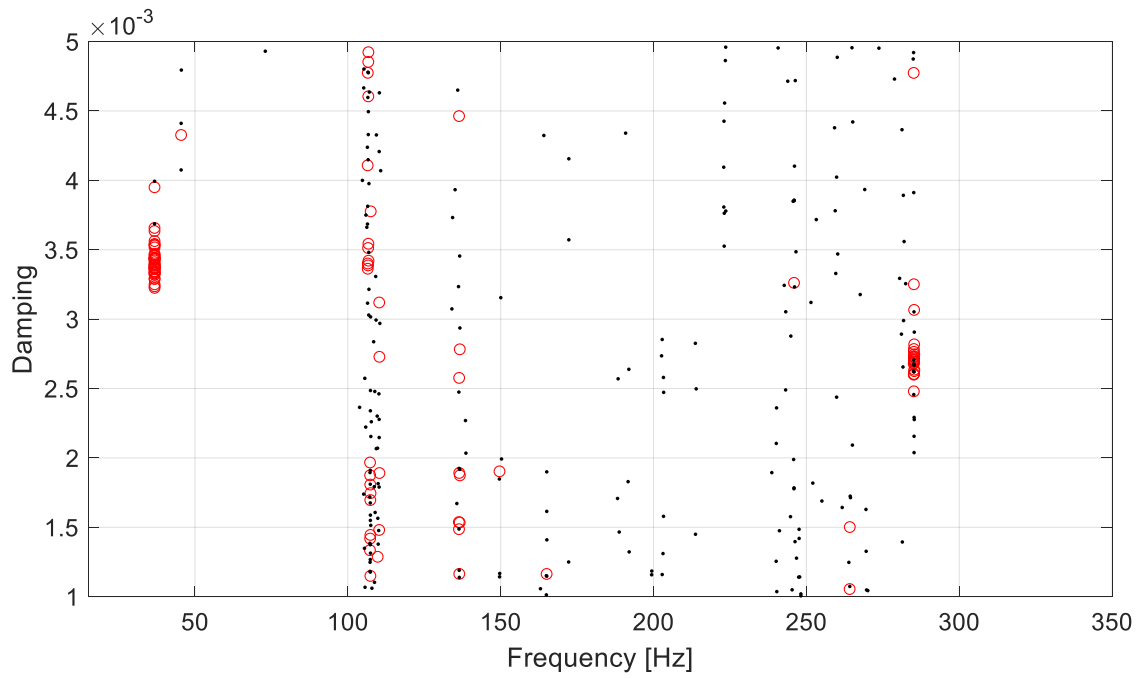


Figure 60. Clustering diagram for Step #4

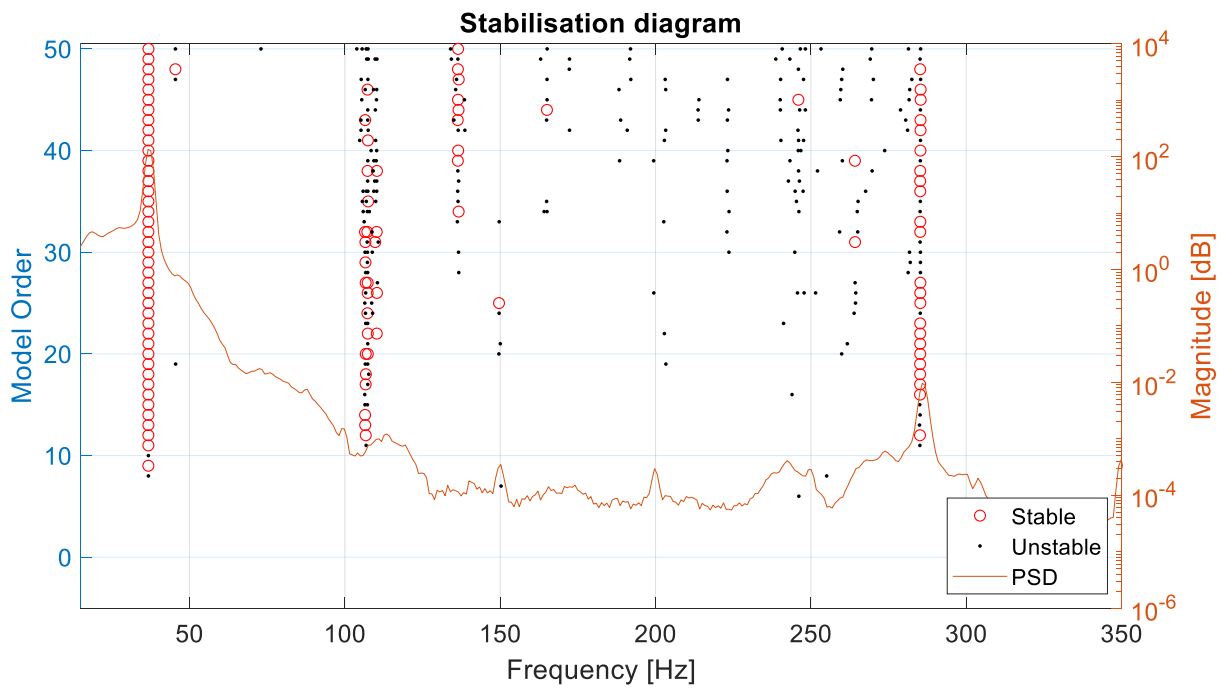


Figure 61. Stabilisation diagram for Step #4

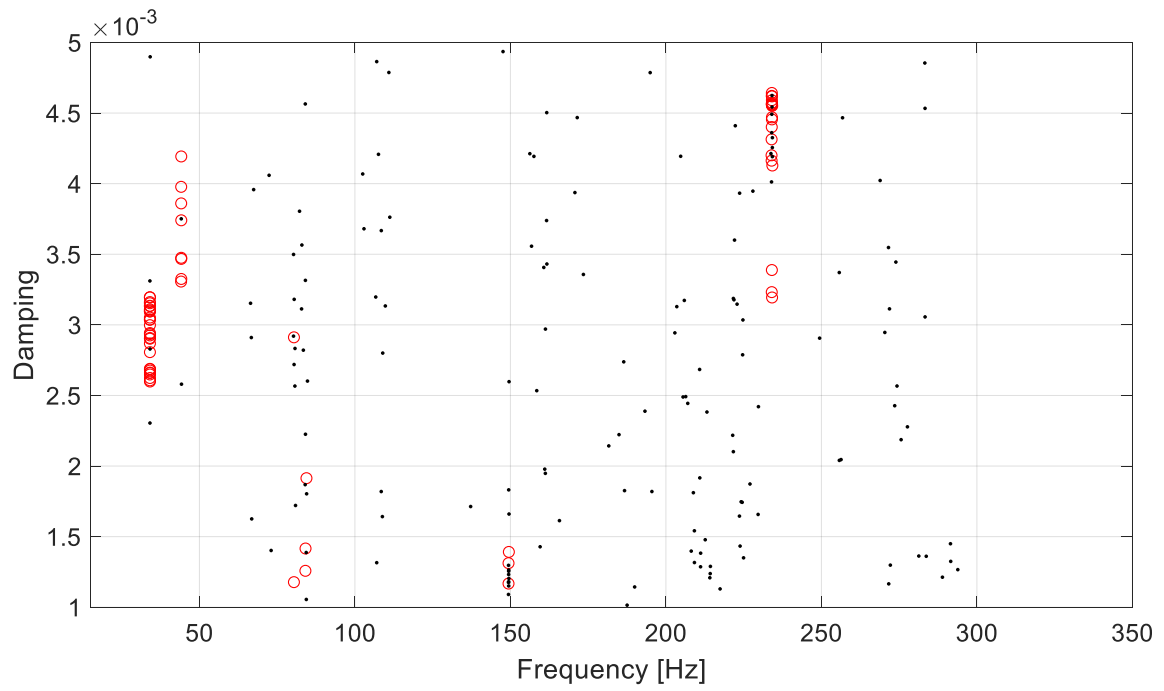


Figure 62. Clustering diagram for Step #7

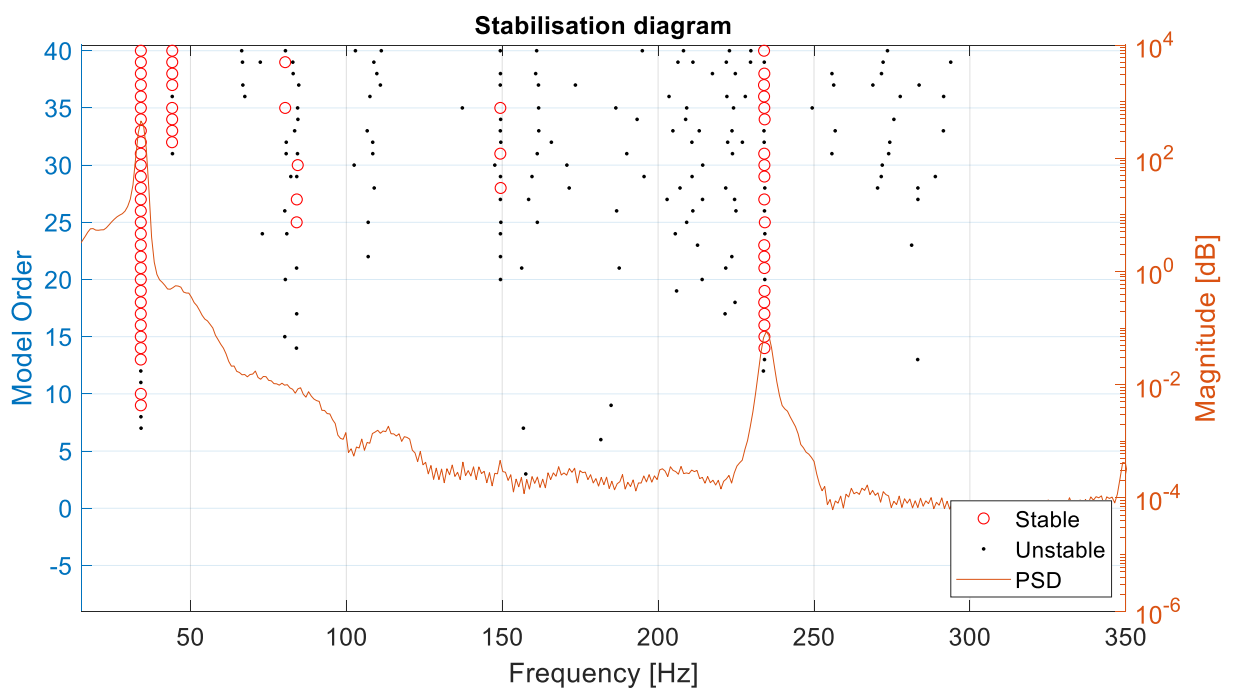


Figure 63. Stabilisation diagram for Step #7

Ultimately, to validate the performance of Vector Fitting the results of system identification is compared with the analytical frequencies of the undamaged beam and the experimental ones obtained from video during the tests. The first and second analytical frequencies of the undamaged beam are respectively 46.3 Hz and 287 Hz. The presence of damage leads at a gradual decrease and shift of the first frequency respect the undamaged condition.

<b>Damage step</b>	<b>Frequency Video [Hz]</b>	<b>Frequency shift [%]</b>	<b>Frequency VF [Hz]</b>	<b>Frequency shift [%]</b>
<b>Step#4</b>	34.80	-24.80	36.38	-21.42
<b>Step#5</b>	34.50	-25.50	36.22	-21.77
<b>Step#6</b>	33.81	-27.00	35.76	-22.76
<b>Step#7</b>	32.22	-30.50	33.80	-26.99

*Figure 64. Evolution of the first frequency obtained from VF process and from video and comparison with undamaged condition*

## 7.2 Three storey structure

The three-storey structure is used as a third validation test. This research has been developed in the Engineering Institute (EI) at Los Alamos National Laboratory (LANL), in collaboration with the Laboratory for Concrete Technology and Structural Behaviour (LABEST) of the Faculty of Engineering of the University of Porto (FEUP). The EI is a research institute in collaboration between the LANL and the University of California, San Diego (UCSD), Jacobs School of Engineering. (Figueiredo, Park, Figueiras, Farrar, & Worden, 2009).

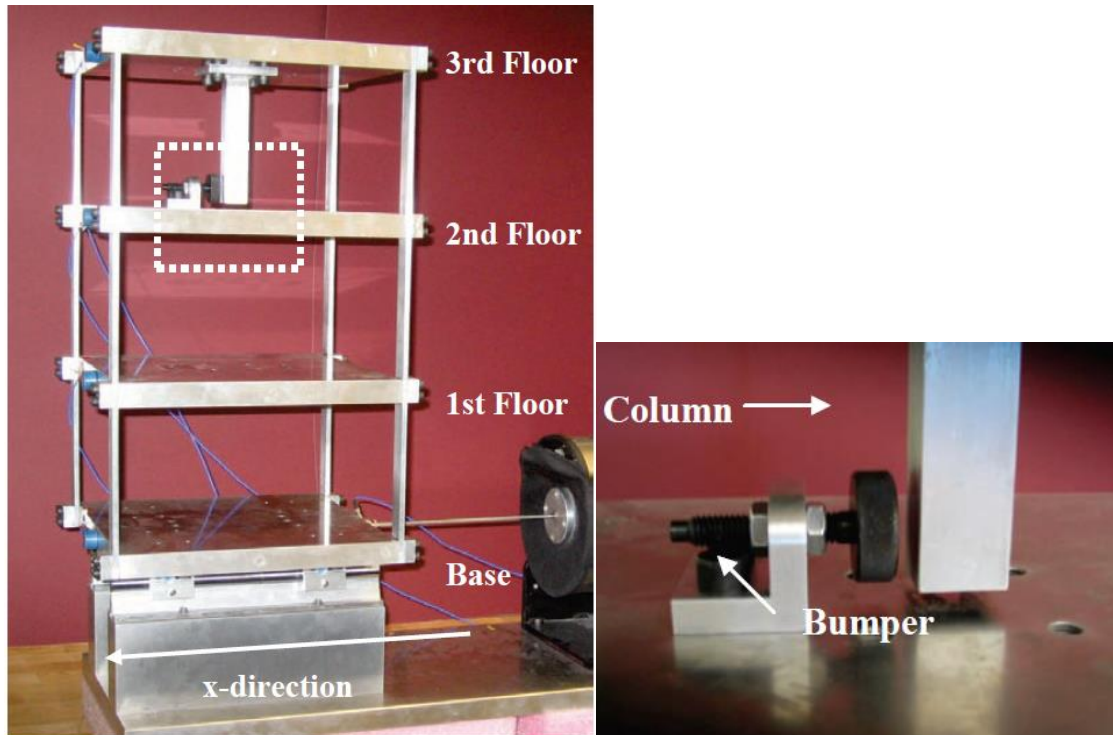


Figure 65. Test structure (Figueiredo, Park, Figueiras, Farrar, & Worden, 2009)

### 7.2.1 Structure description

The three-storey frame is characterized by an aluminium columns and plates assembled by using bolted joints, which slides on rails that permits movement in the x-direction only. At each floor, four aluminium columns (with dimensions of  $17.7 \times 2.5 \times 0.6$  cm) are connected to the bottom and top aluminium plates ( $30.5 \times 30.5 \times 2.5$  cm) forming a four DOF system. In addition, a column, with dimensions of  $15.0 \times 2.5 \times 2.5$  cm, in the centre of the structure is suspended from

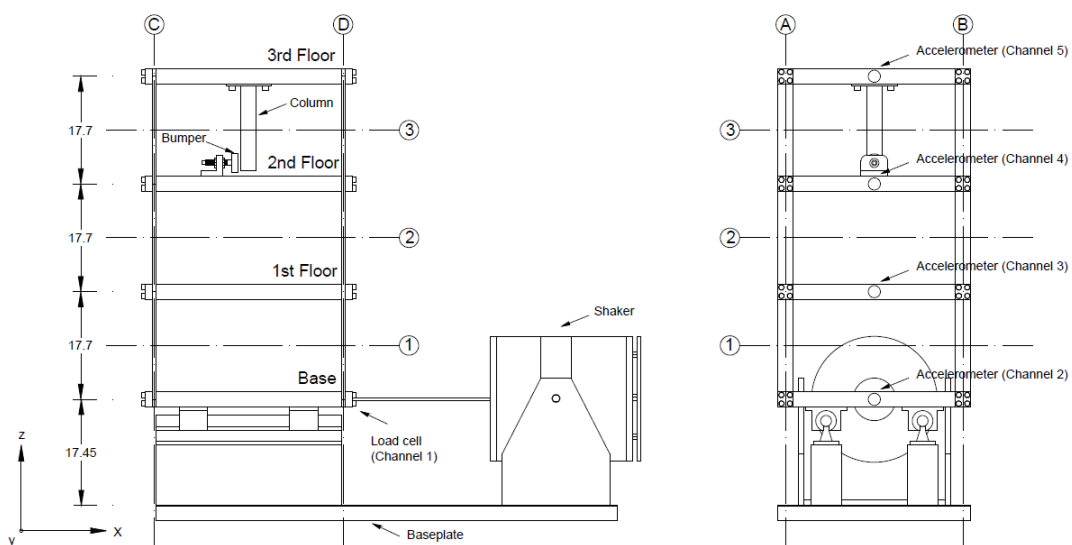
the top floor (Figure 66a). This column is used in order to simulate a source of damage that induces nonlinear behaviour when it touches a bumper mounted on the next floor. The position of the bumper can be modified to vary the extent of impacting that happens during a particular excitation level, as is shown in Figure 66b.



(a) Three-story building structure and shaker

(b) Bumper and suspended column

Figure 66. Details of test structure setup (Figueiredo, Park, Figueiras, Farrar, & Worden, 2009)



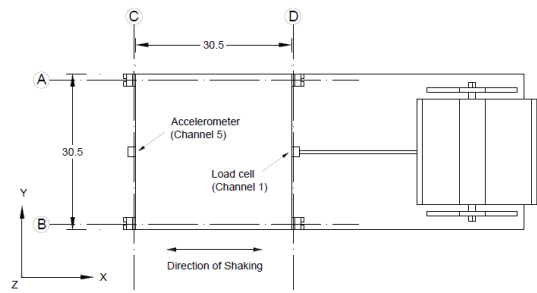


Figure 67. Dimensions of the three-story structure (dimensions are in cm) (Figueiredo, Park, Figueiras, Farrar, & Worden, 2009)

### 7.2.2 Data acquisition system

The data set consists in a collection of inputs, expressed in terms of time histories of applied forces, and of the respective output signals, in terms of recorded accelerations. That allows identifying the system in terms of its FRFs acceleration. The structure and shaker were built together on an aluminium baseplate (with dimensions of  $76.2 \times 30.5 \times 2.5$  cm), and the entire system remained on rigid foam. The foam is intended to minimize external sources of unmeasured excitation from being introduced through the base of the frame. A load cell with a sensitivity of 2.2 mV/N measures the input from the shaker to the structure. Four accelerometers were placed at the centre line of each floor to measure the system's response. The output channels, with nominal sensitivities of 1,000 mV/g, are connected to a Techron 5530 Power Supply Amplifier in order to provide the excitation signal to the shaker. The features of the five sensor channels (Channels 1–5) can be found in Table 9. A Dactron Spectrabook data acquisition system was used to process the data (Figueiredo, Park, Figueiras, Farrar, & Worden, 2009).

Channel Number	Transducer	Reference	Nominal Sensitivity
Channel 1	Load cell	PCB 208 C03 SN 22569	2.2 mV/N
Channel 2	Accelerometer	PCB 336C SN 10099	1000 mV/g
Channel 3	Accelerometer	PCB 336c SN 10120	1000 mV/g
Channel 4	Accelerometer	PCB 336c SN 9916	1000 mV/g
Channel 5	Accelerometer	PCB 336C SN 10100	1000 mV/g

Table 9. Characteristics of the sensors

The sensor signals were discretized with 8192 data points and are sampled at 320 Hz in 26.5 s in duration. For Nyquist criterion the maximum frequency is 160 Hz. The frequency resolution is 0.0391 Hz. A band-limited random excitation in the range of 20-150 Hz was used to excite the structure. This excitation signal was chosen in order to avoid the rigid body modes of the structure that are present below 20 Hz.

The analysis consists in 17 steps, in which all acceleration time histories of all floor (including the first floor) and the input force are measured.

Label	State Condition	Description
State #1	Undamaged	Baseline condition
State #2	Undamaged	Mass = 1.2 kg at the base
State #3	Undamaged	Mass = 1.2 kg on the 1 <sup>st</sup> floor
State #4	Undamaged	87.5% stiffness reduction in column 1BD
State #5	Undamaged	87.5% stiffness reduction in column 1AD and 1BD
State #6	Undamaged	87.5% stiffness reduction in column 2BD
State #7	Undamaged	87.5% stiffness reduction in column 2AD and 2BD
State #8	Undamaged	87.5% stiffness reduction in column 3BD
State #9	Undamaged	87.5% stiffness reduction in column 3AD and 3BD
State #10	Damaged	Gap = 0.20 mm
State #11	Damaged	Gap = 0.15 mm
State #12	Damaged	Gap = 0.13 mm
State #13	Damaged	Gap = 0.10 mm
State #14	Damaged	Gap = 0.05 mm
State #15	Damaged	Gap = 0.20 mm and mass = 1.2 kg at the base
State #16	Damaged	Gap = 0.20 mm and mass = 1.2 kg on the 1 <sup>st</sup> floor
State #17	Damaged	Gap = 0.10 mm and mass = 1.2 kg on the 1 <sup>st</sup> floor

Table 10. Data Labels of the Structural State Source

The steps can be defined in four groups. The first group is undamaged condition (State#1). This is the state with which we will then compare the others. The second includes the states when the mass and stiffness of the columns were varied, for example with a reduction of stiffness (State #3-#9) or with an addition of mass (State #2-#3). The mass,  $m$ , consisted of 1.2 kg (20% of the total mass of floor) being added to the base and to the first floor, as illustrated in Figure 68. The stiffness change was introduced by reducing one or more columns' stiffness by 87.5%. The third group consists on damaged state conditions through the introduction of nonlinearities into the structure by using a bumper and a suspended column, with different gaps between them. This is shown in Figure 68 (b). The gap between the bumper and the suspended column was progressively changed (0.20, 0.15, 0.13, 0.10, and 0.05 mm) in order to introduce different levels of non-linearity (States #10-#14) for a certain level of excitation. The last fourth group includes the state

conditions with damage in addition to mass changes typical of operational and environmental condition changes (States #15-#17) (Figueiredo, Park, Figueiras, Farrar, & Worden, 2009).

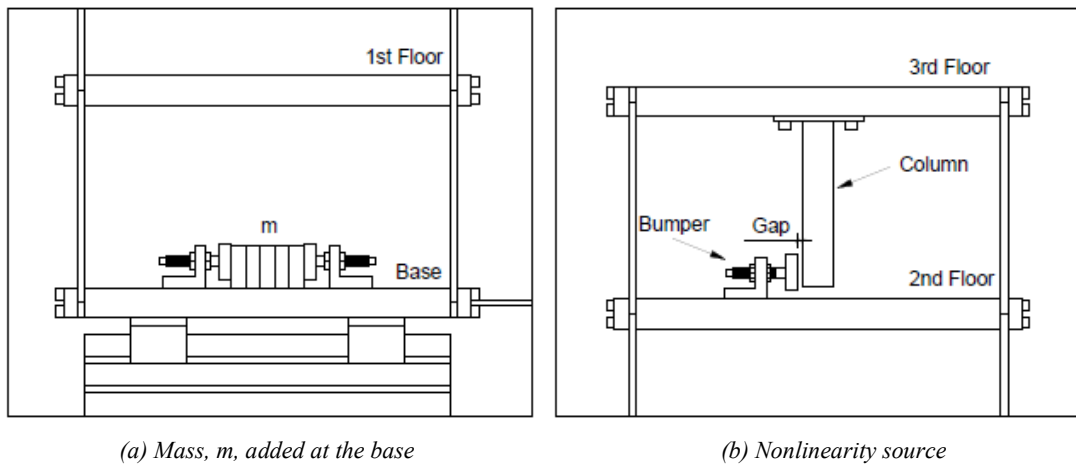


Figure 68. Structural details about the damage conditions (Figueiredo, Park, Figueiras, Farrar, & Worden, 2009)

### 7.2.3 Pre-processing phase

Vector Fitting’s implementation is applied to all the steps, in order to show the behaviour of the algorithm under linear and nonlinearity conditions. The data come from Literature as a well-known experiment performed at Los Alamos National Laboratory (LANL).

The level of nonlinearity depends on the amplitude of oscillation and the gap between the column and the bumper. As described above, this source of damage simulates the fatigue cracks that open and close upon dynamic loading.

For each state condition, 50 realizations were performed in order to take into account the variability in the data. Thus, for each of the five transducers, 50 time histories were measured in each structural state condition. In addition, the data acquisition system recorded the associated frequency response functions (FRFs) of the response at Channels 2–5 relative to the input measured with Channel 1. The FRFs are calculated as the ratio between of the Fast Fourier Transforms of the output of each Channel 2-5 and the input signal of Channel 1 (Eq. 113).

To illustrate the output results from the data-acquisition system for one test of State #1, Figure 69 and Figure 70 show the force-time history from Channel 1 and the acceleration-time histories from Channel 2-5, respectively. The FRFs relating the input excitation at Channel 1 and responses at Channel 2-5 for the State#1 are shown in Figure 71.

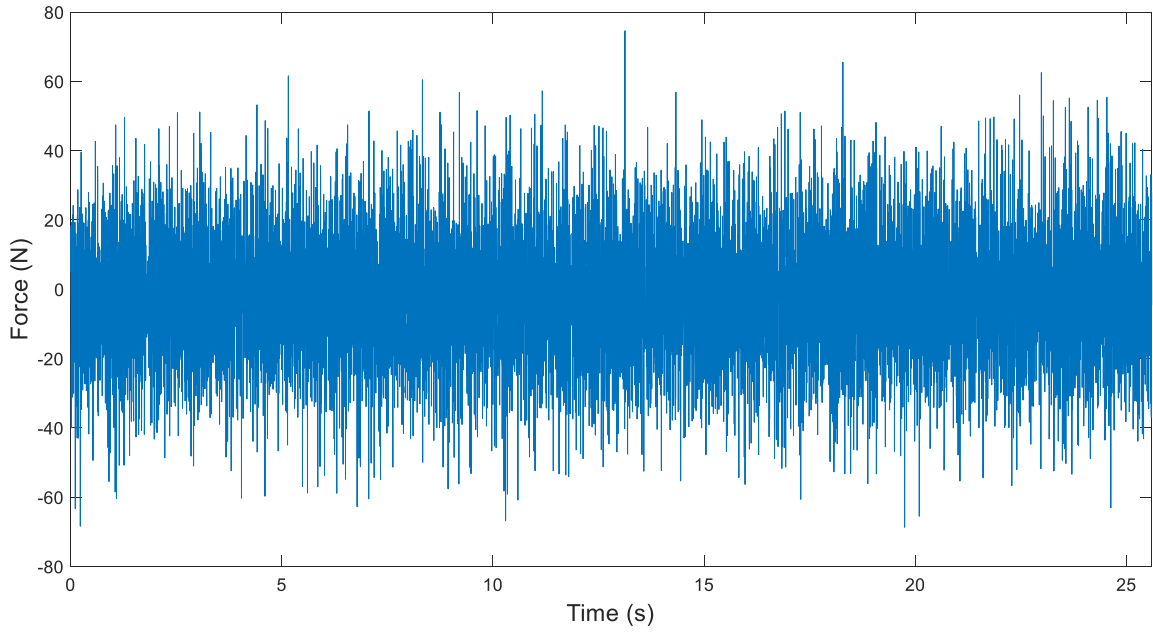


Figure 69. Force-time history from Channel 1 of State #1

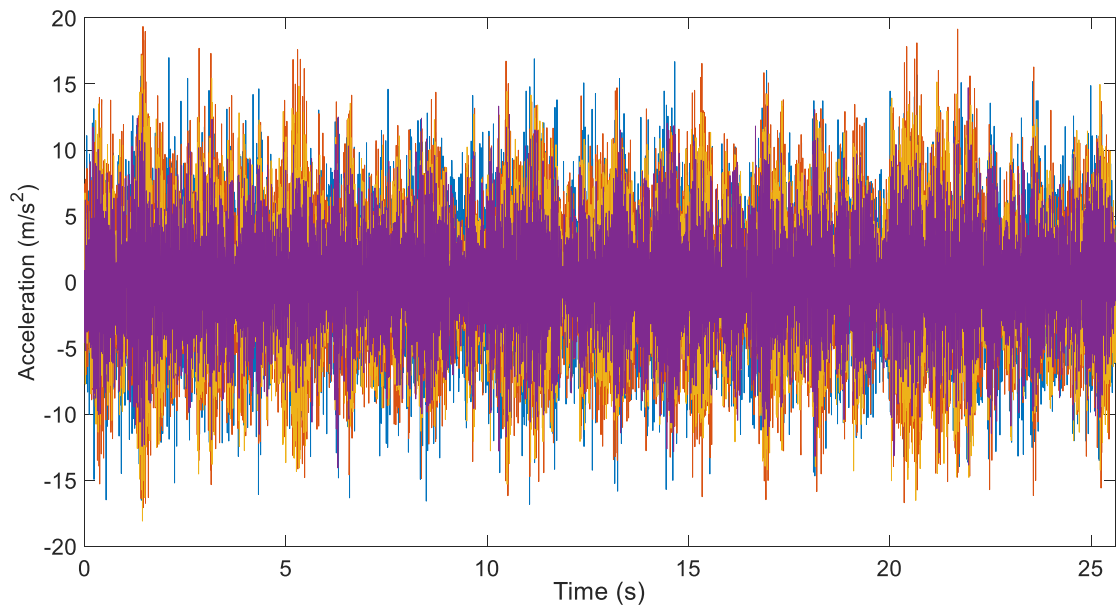


Figure 70. Acceleration-time history from Channels 2-5 of State #1

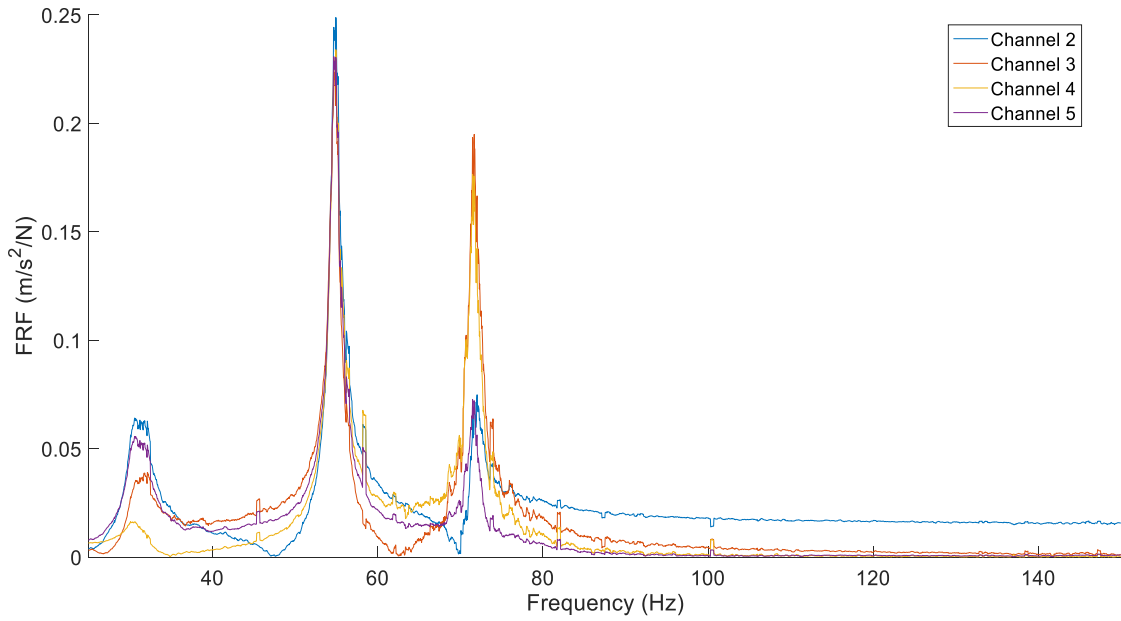


Figure 71. FRFs of Channels 2-5 of State #1

As stated above, in order to simulate the changes in real-world structures caused by changing operational and environmental conditions, several sources of variability were included in the test structure. This variability includes reducing the stiffness and adding mass at several different locations. Figure 72 shows the FRFs, of the response from Channel 5 and the excitation force at Channel 1, for the baseline condition state (State #1) and an undamaged state with operational changes corresponding to 87.5% stiffness reduction in column 3AD and 3BD (State #9). As expected, the case with the reduction of stiffness results in lowering the natural frequencies.

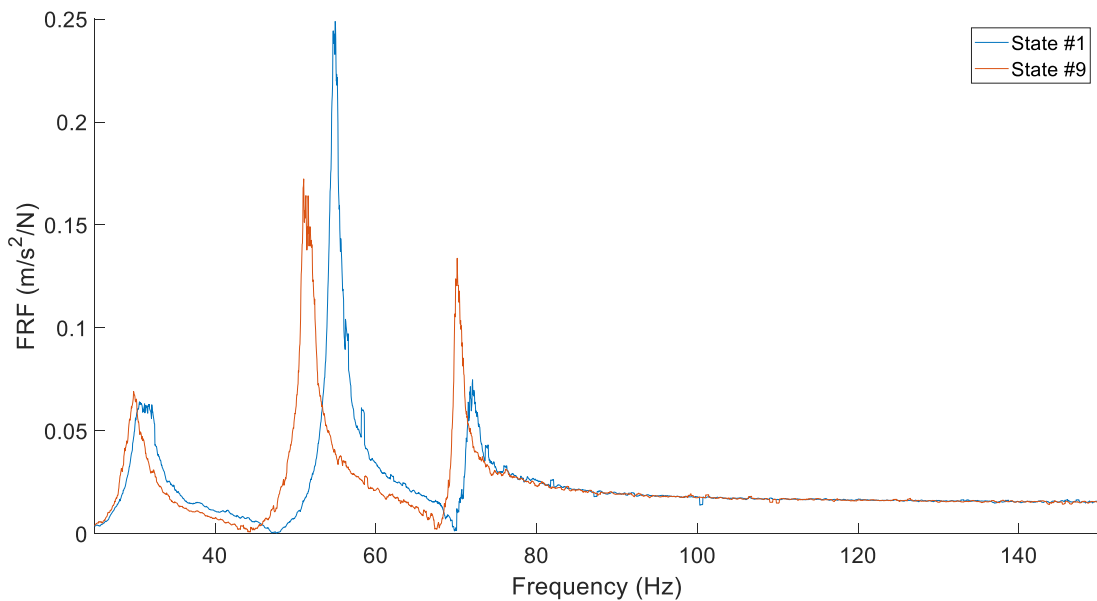


Figure 72. FRFs (based on ten averages) of the response at Channel 2 and the excitation force at Channel 1 for State #1 (baseline) and State #9 (87.5% stiffness reduction in column 3AD and 3BD).

The simulated damage was introduced through nonlinearities from impacts with bumper. When the structure is excited at the base, the suspended column touches the bumper. The level of nonlinearity depends on the gap between the column and the bumper and on the amplitude of oscillations (Figueiredo, Park, Figueiras, Farrar, & Worden, 2009). Figure 73 shows FRFs for the baseline condition state (State #1), the damaged state consisting of a gap of 0.05 mm (State #14), and for the damaged state consisting of a gap of 0.10 mm and 1.2 kg added on the first floor (State #17). Figure shows the shifts of the resonance frequencies and distortions of the FRF shape caused by the nonlinearities.

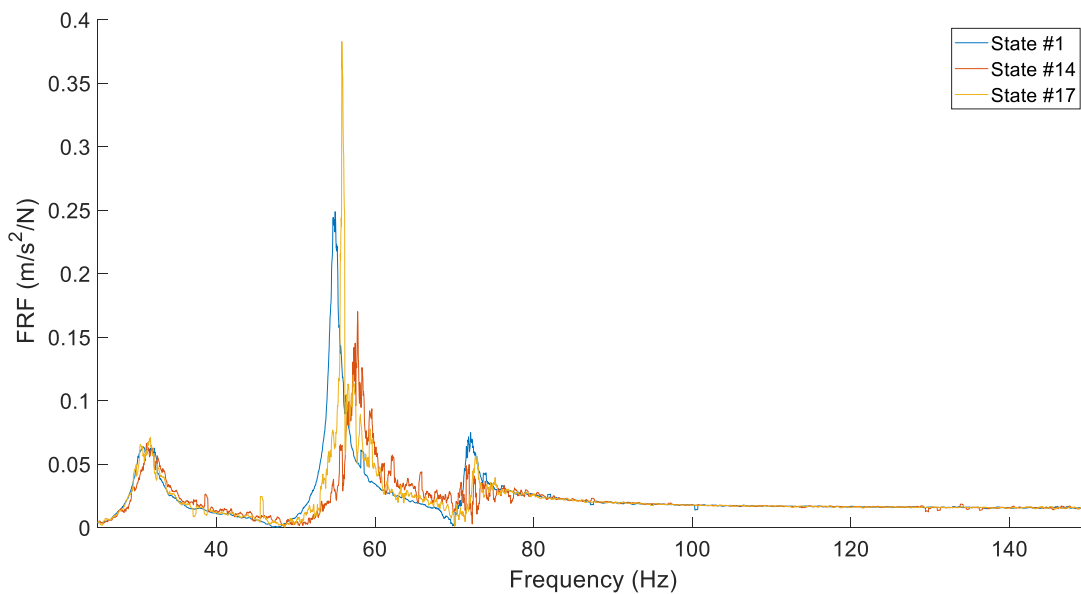


Figure 73. FRFs (based on ten averages) of the response at Channel 2 and the excitation force at Channel 1 for State #1 (baseline), State #14 (gap = 0.05 mm), and State #17 (gap= 0.10 mm and 1.2-kg added mass on the first floor).

Case #14 (gap= 0.05 mm) results in rising the natural frequencies. Due to the addition of a 1.2 kg mass, the resonant frequencies are in lowering again in the step #17 (gap= 0.10 mm and 1.2-kg added mass on the first floor), as shown in Figure 73.

#### 7.2.4 System identification

The experimental results are compared with numerical results presented in the paper "*Structural Health Monitoring Algorithm Comparisons Using Standard Data Sets*" of Charles Ferrar et al. (Los Alamos National Laboratory, 2009). The test structure is designed as four lumped masses at the floors, with the base that slides on rails, as shown in Figure 74.

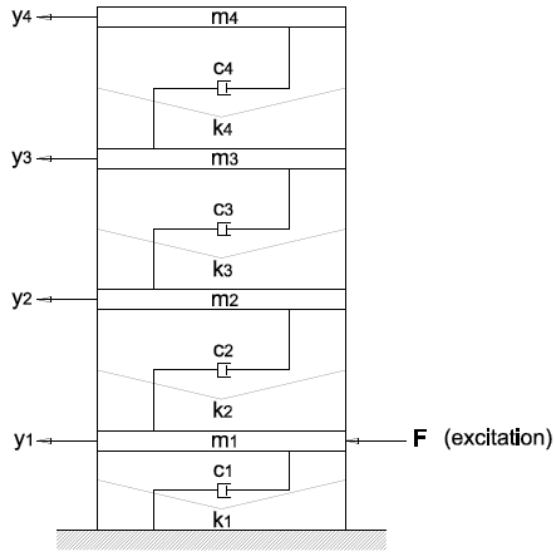


Figure 74. Building model of the test structure (Figueiredo, Park, Figueiras, Farrar, & Worden, 2009)

The stiffness  $k$  and damping  $c$  are intended to simulate the friction between the rails and the structure. From the equation of motion, knowing the stiffness, damping and mass matrices  $[K]$ ,  $[C]$  and  $[M]$ , can be evaluated the natural frequencies. In the paper previously mentioned, modal damping ratios are estimated from the measured experimental data by using the Rational-Fraction Polynomial (RFP) method. After the pre-processing phase, the system identification is estimated with Vector Fitting method by using the Matlab R2018b code *vectfit3.m*. The magnitude and phase' s plots for Step #1 (baseline step) are reports as follow:

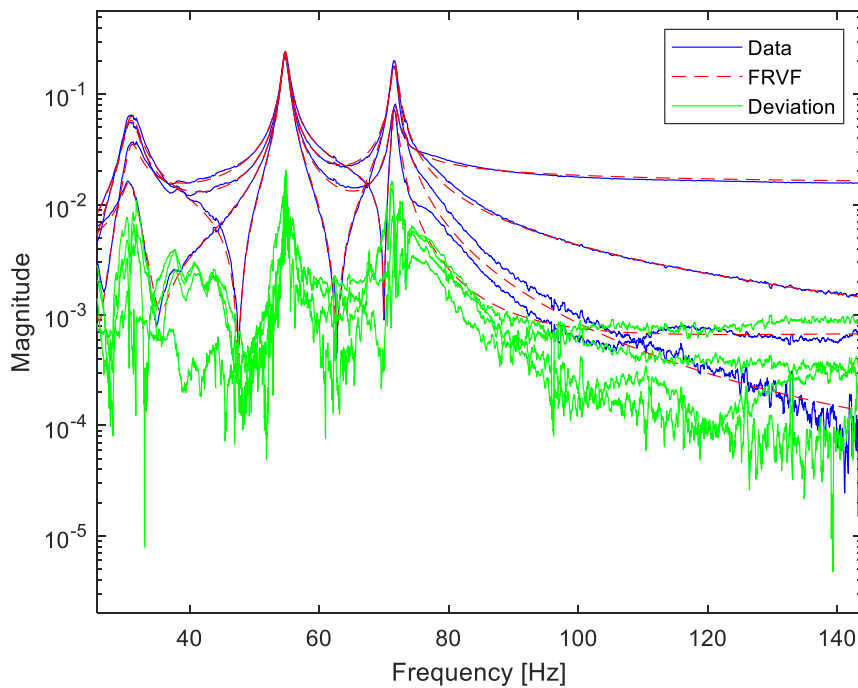


Figure 75. Magnitude of Vector Fitting curve for Step #1

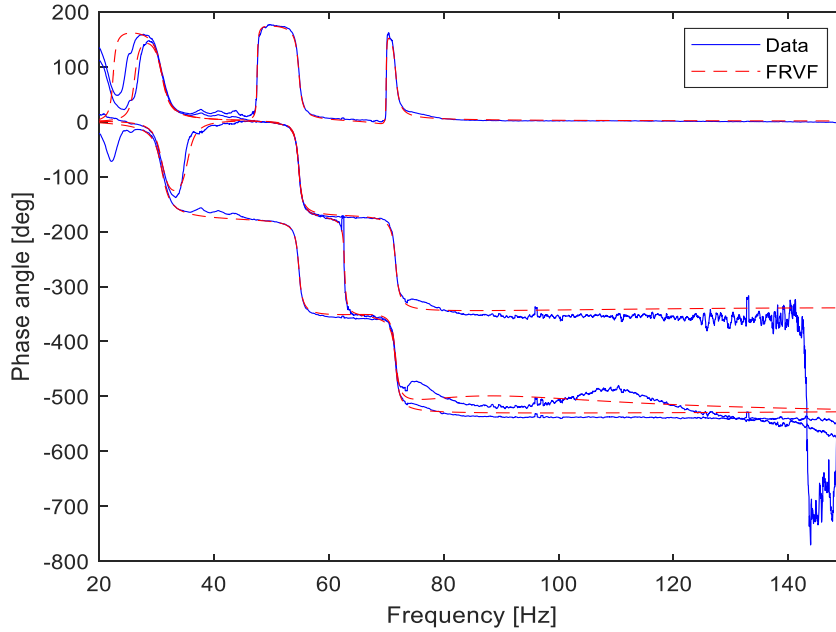


Figure 76. Phase of Vector Fitting curve for Step #1

Notice that the FRFs are in semilogarithmic scale to compress the large signal amplitude and expand the small ones, allowing easier visualization of all frequencies in the signal. The model order used in the previous plot is  $N=6$ .

The value of Root Mean Square Error (RMSE) is  $3E-3$  and it means that the deviation between the curve fitting and the data is low. The experimental natural frequencies and damping ratios for the baseline condition (State #1) obtained by using Vector Fitting method as well as the numerical natural frequencies are presented in Table 11.

Mode n°	Frequency [Hz]			Damping [%]		
	Experimental	Numerical	Error (%)	Experimental	Numerical	Error (%)
1	30.89	29.80	3.7	3.5	6.0	42
2	54.74	54.0	1.4	0.8	2.0	60
3	71.61	71.60	0.14	0.7	0.9	22

Table 11. Experimental and numerical natural frequencies and damping ratios for the baseline condition (State #1)

Once the modal parameters have been estimated for various orders, one can produce a stabilisation diagram (Section 5.5) and cluster diagram (Section 5.6). The stable poles from order  $N_{\min}$  to  $N_{\max}$  are determined on the basis of different stabilisation criterion, in terms of frequency, damping and MAC. In this set of test the following stabilisation criteria have been used (Eq. 116):

$$\delta f \leq 0.5\%, \quad \delta \xi \leq 10\%, \quad (1 - MAC) \leq 10\%$$

Moreover, poles having unrealistic damping ratios have been filtered out of the set of stable poles.

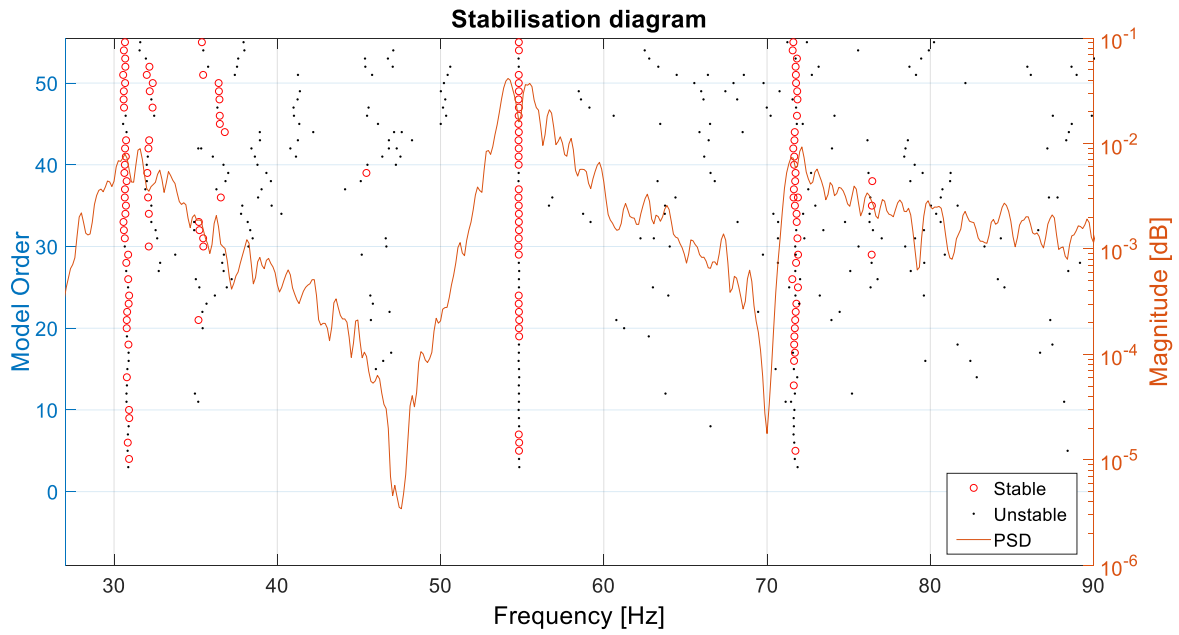


Figure 77. Stabilisation diagram over Vector Fitting identification for increasing model order and  $\delta f < 0.5\%$ ,  $\delta \zeta < 10\%$  and  $(1-MAC) < 10\%$

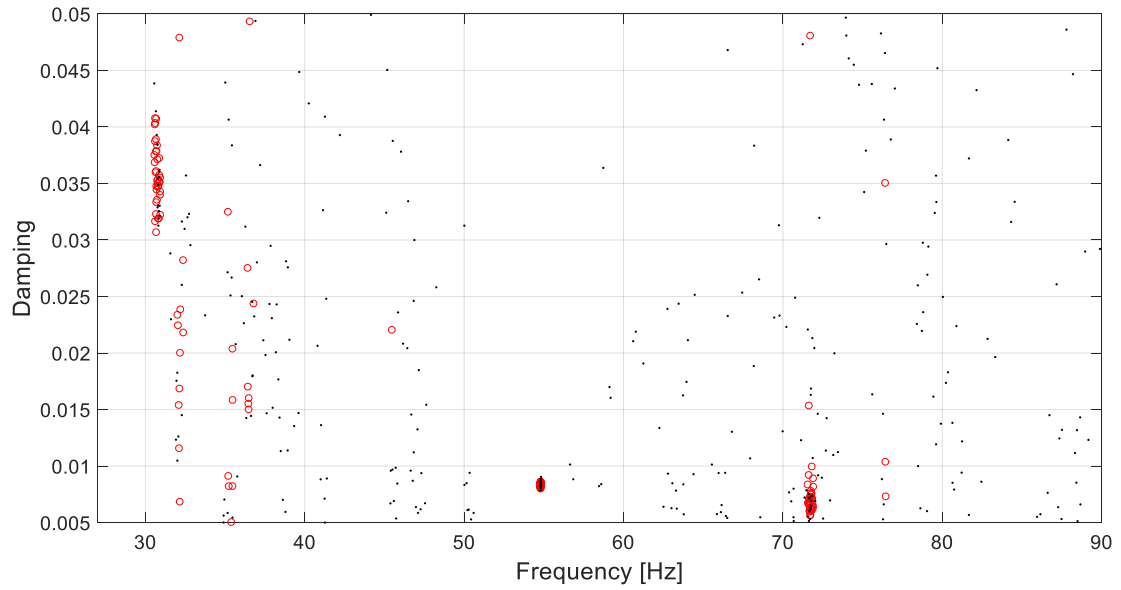


Figure 78. Cluster diagram

The comparing between the Vector Fitting and numerical mode shapes are reported in the graphs below.

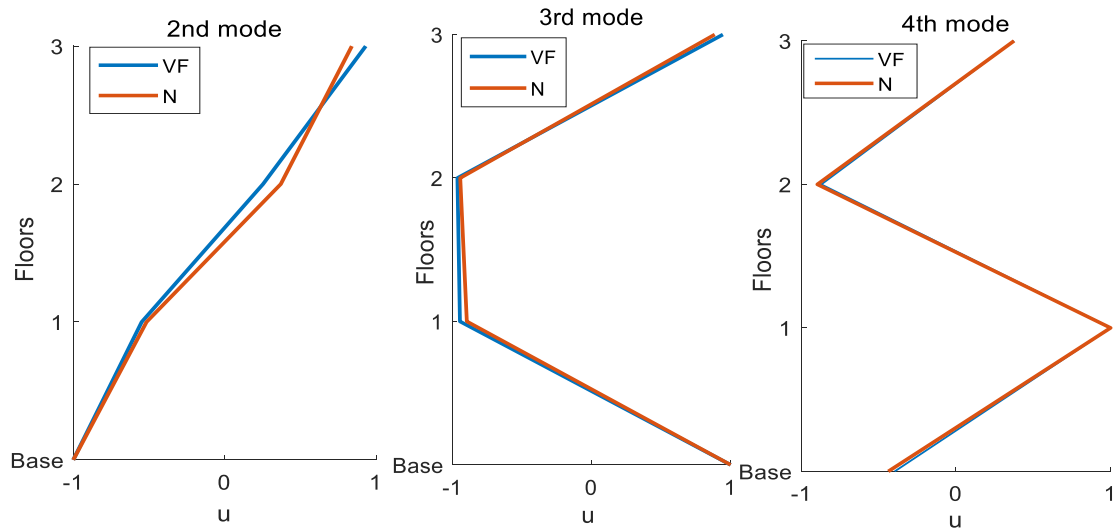


Figure 79. Vector Fitting and Numerical mode shapes of the State#1 (baseline condition).

As in shown in Figure 80, the MAC values obtained are respectively 0.991,0.999 and 0.999, giving an indication that the Vector Fitting mode shapes are well defined.

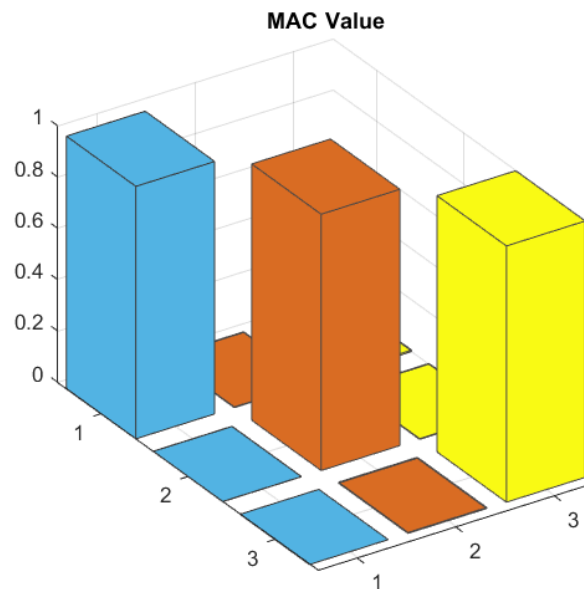


Figure 80. Correlation between Vector Fitting and Numerical mode shapes by MAC.

In order to determinate the effectiveness, we choose other system identification techniques to compare VF results. The first two of these are the Peak Picking and Rational Fraction Polynomial methods. The Peak Picking method is a simple frequency-domain algorithm that is used in this work to compare the mode shapes (Section 3.2). In such a way the natural frequencies are simply

determined from the observation of the peaks on the graphs of the averaged normalized power spectral densities and the vibration modes are calculated directly with the ratio of values of the peaks of FRFs. Because the raw data present 50 realizations for each step, it is possible to average off the FRFs in order to obtain a more accurate estimation.

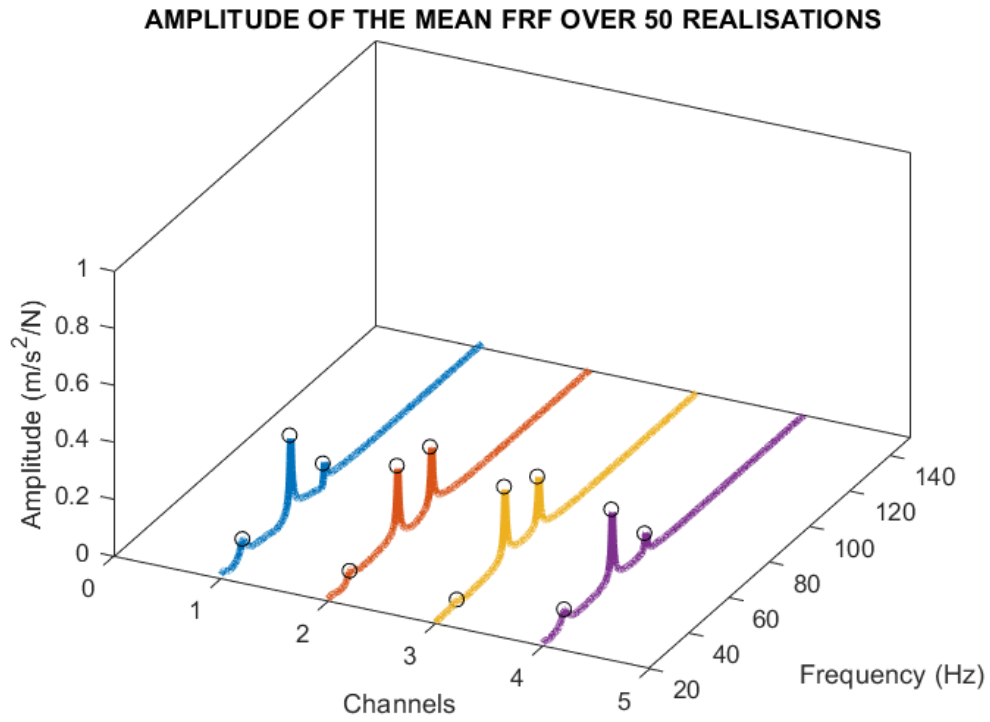


Figure 81. Amplitude of the mean of FRF over 50 realisations using Peak Picking method for Step #1

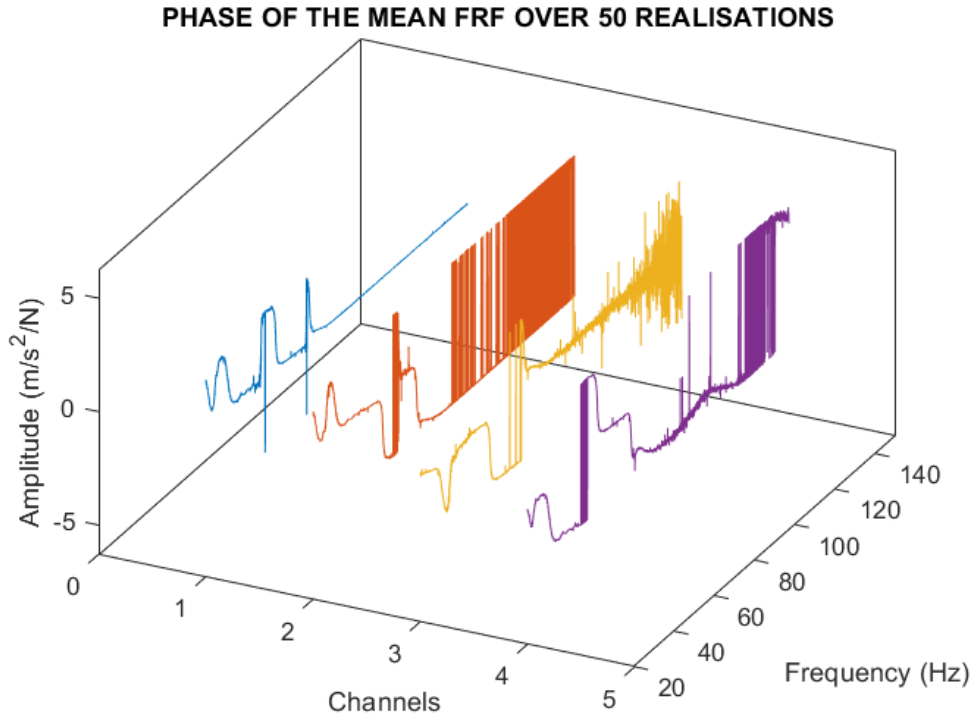


Figure 82. Phase of the mean of FRF over 50 realisations using Peak Picking method for Step #1

In Figure 83 are reported the comparing between the Vector Fitting and Pick Picking mode shapes. As also shown in Figure 84, the MAC values of the second, third, and fourth mode shapes are respectively 0.991, 0.998 and 0.999, giving an indication that the Vector Fitting and Peak Picking mode shapes are highly correlated.

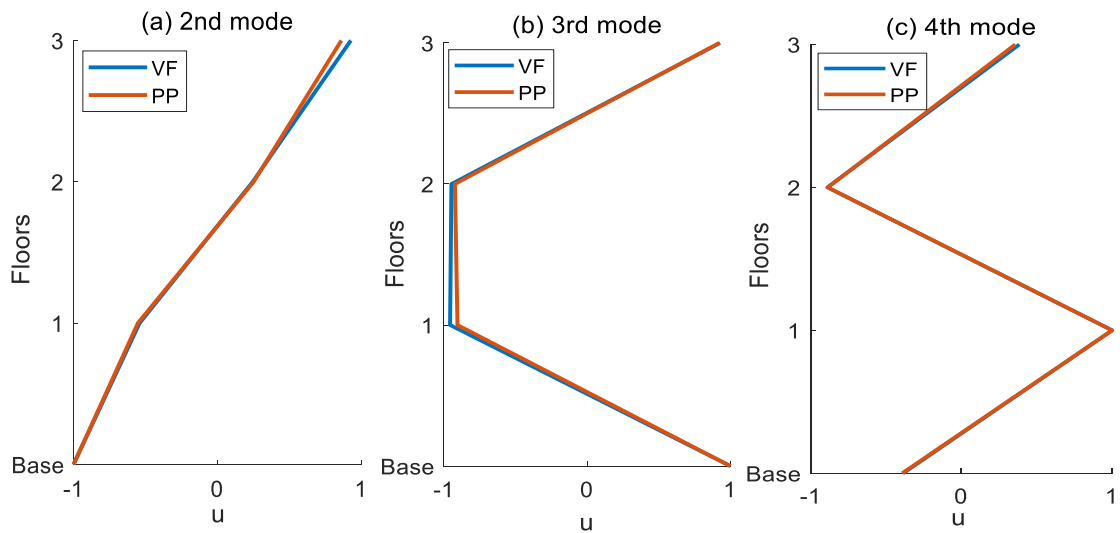


Figure 83. Vector Fitting and Peak Picking mode shapes of the State#1 (baseline condition).

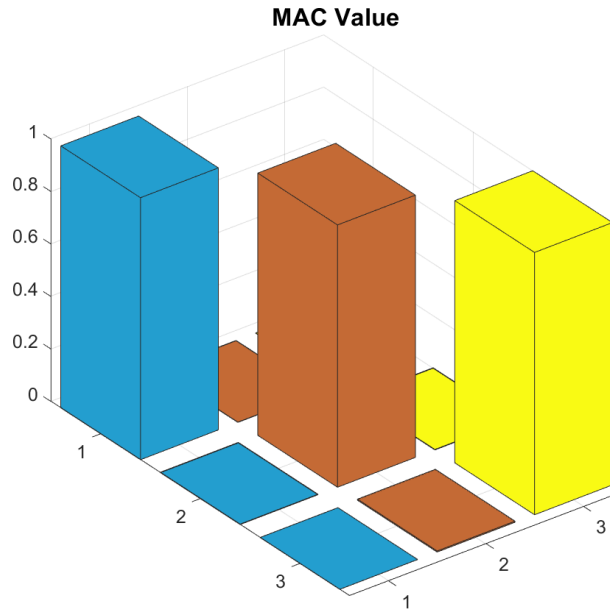


Figure 84. Correlation between Vector Fitting and Peak Picking mode shapes by MAC.

The Rational Fraction Polynomial is a frequency domain curve-fitting method that operates directly on the complex FRF as is explained in the Section 3.2. This comparison is interesting because the basis of this algorithm are closely related to the VF ones. We reported frequency and damping's values in the Table 12.

Mode n°	Frequency [Hz]		Damping [%]	
	Experimental VF	Experimental RFP	Experimental VF	Experimental RFP
1	30.89	30.70	3.5	6.0
2	54.74	54.2	0.8	2.0
3	71.61	70.7	0.7	0.9

Table 12. VF and RFP frequencies and damping ratios for the baseline condition (State #1)

Note that the damping ratio obtained from VF process is highly distant from RFP's one. It is caused by the difficulty of frequency-domain curve-fitting to calculate the damping which depends on the width of the FRF's peaks.

In the end, for complete the analysis we apply the data sets to a time-domain identification method. This is the N4SID method which is defined as a 'numerical algorithms for subspace state space system identification' from Van Overschee and De Moor in the paper "A Unifying Theorem for Three Subspace System Identification Algorithms" (1995). The convenience of using N4SID is the availability of a MATLAB function (i.e., n4sid) and its reliability. This is no more than the input-output version of stochastic system identification (SSI). In fact, SSI method ignores the

input system matrices  $B$  and  $D$  that represent the deterministic subsystem. Importantly, N4SID is widely considered as the default choice for mechanical systems. Yet, its use is hampered in other sectors, such as for the identification of electrical circuits, by the fact that it becomes computationally too expensive for a large number of input and output channels. Frequency and damping ratio were carried out. Observe that the damping ratios calculated from VF technique are closer to results with N4SID than RFP 's ones.

Mode n°	Frequency [Hz]		Damping [%]	
	Experimental VF	Experimental N4SID	Experimental VF	Experimental N4SID
1	30.89	30.89	3.5	4.8
2	54.74	54.81	0.8	0.75
3	71.61	71.81	0.7	0.76

Table 13. VF and N4SID frequencies and damping ratios for the baseline condition (State #1)

In the second part of this section, the Vector Fitting method is applied to the others steps in order to show the variability of the algorithm using modal parameters as damage-sensitive features. The following figures illustrate the fitting of magnitude and phase of data of Step #14. It is clear the influence of nonlinearity on the FRF curve-fitting process. Despite this, the value of RMS is  $4E-3$ .

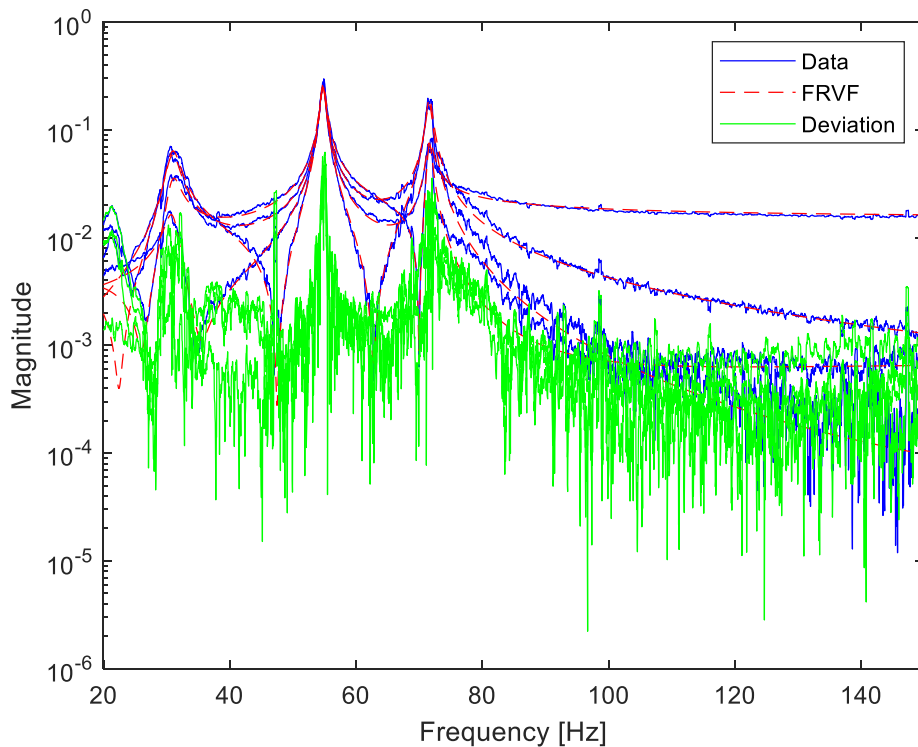


Figure 85. Magnitude of VF process of State #14

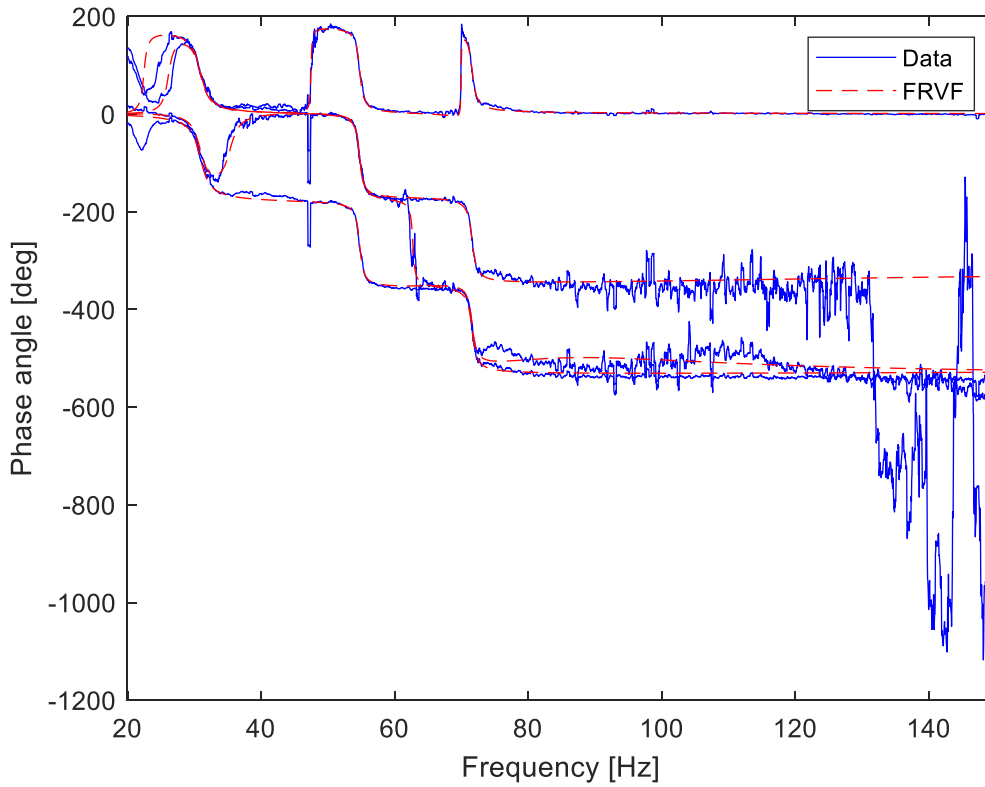


Figure 86. Phase of VF process of State #14

In order to highlight the differences from the baseline condition (State #1), in the tables below are reported the frequencies, damping ratios and mode shapes for all 17 steps. Precisely, the mean  $\mu$  and standard deviation  $\sigma$  for 50 realisations for each step are calculated. These statistical parameters measure the amount of variability, or dispersion, for a subject set of data values.

$$\mu = \frac{1}{N} \sum_{i=1}^n x_i \quad (117)$$

$$\sigma = \sqrt{\frac{\sum_{i=1}^N \frac{(x_i - \mu)^2}{N}}{N}} \quad (118)$$

A low standard deviation indicates that the data points tend to be close to the mean (also called the expected value) of the set, while a high standard deviation indicates that the data points are spread out over a wider range of values.

In fact, one of the major advantages of frequency-domain measurements is that it becomes very easy and inexpensive to measure not only the transfer function, but also the estimate of the corresponding variance (Schoukens, 2001). To this end, it is sufficient to repeat the measurements and calculate the sample variance.

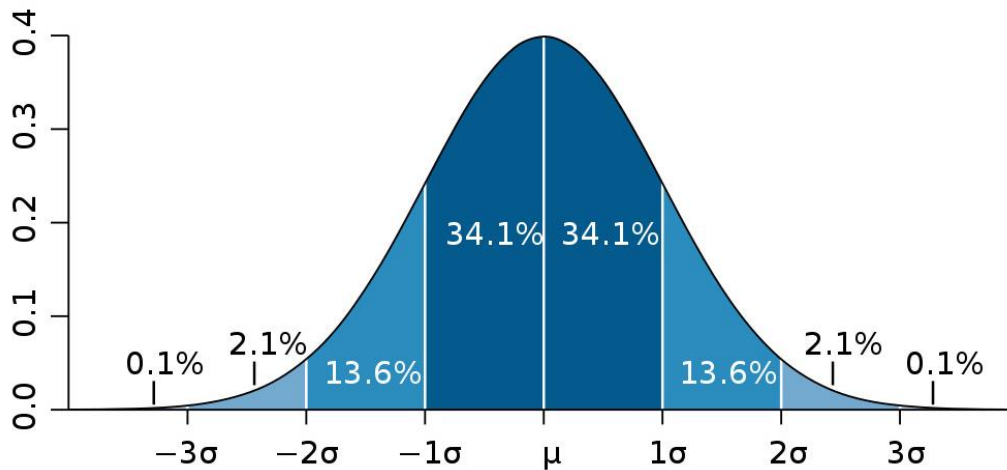


Figure 87. A plot of normal distribution (or bell-shaped curve) where each band has a width of 1 standard deviation (MIT, 2012)

	FREQUENCY					
	2° modo		3° modo		4° modo	
	$\mu$	$\sigma$	$\mu$	$\sigma$	$\mu$	$\sigma$
State #1	30.89	0.069	54.74	0.041	71.61	0.046
State #2	29.91	1.361	53.65	0.042	71.29	0.036
State #3	30.83	0.108	53.82	0.048	69.19	0.035
State #4	30.65	0.112	51.54	0.069	70.05	0.027
State #5	30.25	0.118	47.30	0.065	68.92	0.035
State #6	30.04	0.097	54.65	0.051	67.18	0.041
State #7	27.55	0.074	54.58	0.047	62.19	0.043
State #8	29.82	0.075	51.34	0.044	70.17	0.032
State #9	28.43	1.122	47.56	0.040	69.16	0.049
State #10	30.40	1.221	54.74	0.038	71.62	0.035
State #11	30.83	0.112	55.01	0.113	71.82	0.078
State #12	30.74	0.224	55.18	0.136	71.91	0.246
State #13	29.72	6.368	56.30	2.231	76.84	30.572
State #14	27.95	8.933	57.24	1.677	74.25	1.290
State #15	30.10	0.069	53.67	0.036	71.30	0.029
State #16	30.57	0.068	53.65	0.035	69.07	0.032
State #17	29.98	3.994	54.42	0.853	70.07	1.880

Table 14. Mean  $\mu$  and standard deviation  $\sigma$  of frequency for 50 realisations for 17 steps

One can observe that in general the differences decrease for the undamaged state conditions (States #2–#9) and increase for the damaged states with no mass or stiffness changes (States #10–#14). However, this trend is more visible for the third and fourth modes, because the first one is clearly more affected by perturbation. Note that the standard deviation of Step #14 and Step #13 is higher than the others. It is due to the nonlinearity of the damage state conditions. Instead, the reason for the standard deviation value close to 1 for the Step #2, Step #9 and Step #10 was caused by the presence of outliers. Outliers represent values that differs significantly from other

observation and may indicate experimental error due probably to the variability of the data. This concept can be displayed later with Boxplot diagram. For States #15, #16, and #17, it is clear that changes in frequencies associated with the damage are masked by the addition of mass and variation of stiffness.

	DAMPING					
	2° modo		3° modo		4° modo	
	$\mu$	$\sigma$	$\mu$	$\sigma$	$\mu$	$\sigma$
<b>State #1</b>	0.034	0.003	0.008	6.2E-04	0.007	3.5E-04
<b>State #2</b>	0.032	0.002	0.007	7.5E-04	0.006	4.2E-04
<b>State #3</b>	0.032	0.002	0.010	1.0E-03	0.006	3.7E-04
<b>State #4</b>	0.036	0.002	0.009	1.1E-03	0.004	3.6E-04
<b>State #5</b>	0.040	0.003	0.008	1.3E-03	0.003	2.3E-04
<b>State #6</b>	0.032	0.004	0.008	3.4E-04	0.009	4.8E-04
<b>State #7</b>	0.035	0.003	0.007	6.0E-04	0.011	8.0E-04
<b>State #8</b>	0.030	0.003	0.011	6.8E-04	0.005	3.7E-04
<b>State #9</b>	0.026	0.003	0.013	7.7E-04	0.004	5.1E-04
<b>State #10</b>	0.031	0.004	0.008	8.2E-04	0.007	9.2E-04
<b>State #11</b>	0.036	0.002	0.009	1.2E-03	0.008	9.1E-04
<b>State #12</b>	0.041	0.018	0.010	3.2E-03	0.008	2.4E-03
<b>State #13</b>	0.321	0.285	0.028	1.8E-02	0.034	1.4E-01
<b>State #14</b>	0.530	0.316	0.055	4.0E-02	0.030	1.3E-02
<b>State #15</b>	0.034	0.002	0.007	8.5E-04	0.006	4.4E-04
<b>State #16</b>	0.030	0.002	0.009	6.0E-04	0.006	4.0E-04
<b>State #17</b>	0.162	0.269	0.019	1.9E-02	0.015	1.0E-02

Table 15. Mean  $\mu$  and standard deviation  $\sigma$  of damping for 50 realisations for 17 steps

The damping ratios do not increase or decrease with the damaged state conditions. Theoretically, the impacts associated with damage should increase the energy dissipation, which should traduce itself in higher damping. However, the damping has greater sensitivity for characterizing damage than natural frequencies and mode shapes in various applications and its reliability is higher when the system is linear. It is justified by the fact that the damping ratio is calculated by linear fitting of a nonlinear system; the algorithm performs well the identification of the underlying linear system despite of the noise-like nonlinear distorsions in the FRFs. However, the standard deviation is close to 0. It means that there is no dispersion for damping ratio for data sets, except by Step #14 and Step #13. The peaks move on the frequency axis whit increasing of damage but the width remain the same.

	Mode shape (base displacement)					
	2° modo		3° modo		4° modo	
	$\mu$	$\sigma$	$\mu$	$\sigma$	$\mu$	$\sigma$
State #1	1	0	1	0	0.387	0.006
State #2	1	0	0.83	0.012	0.316	0.008
State #3	1	0	1.00	0	0.365	0.012
State #4	1	0	0.894	0.013	0.290	0.009
State #5	1	0	0.732	0.012	0.175	0.007
State #6	1	0.017	1	0	0.445	0.008
State #7	1	0	1	0.005	0.534	0.010
State #8	0.952	0.009	0.898	0.008	0.415	0.007
State #9	0.798	0.031	0.854	0.019	0.449	0.006
State #10	1	0.000	1	5.10E-04	0.383	0.011
State #11	1	0	1	0.005	0.400	0.020
State #12	1	0.009	0.995	0.011	0.399	0.031
State #13	0.989	0.026	0.925	0.091	0.410	0.065
State #14	0.984	0.068	0.808	0.126	0.347	0.096
State #15	1	0	0.826	0.011	0.317	0.009
State #16	1	0.006	1	0	0.360	0.014
State #17	0.976	0.038	0.983	0.059	0.386	0.073

Table 16. Mean  $\mu$  and standard deviation  $\sigma$  of base displacement for 50 realisations for 17 steps

	Mode shape (1° floor displacement)					
	2° modo		3° modo		4° modo	
	$\mu$	$\sigma$	$\mu$	$\sigma$	$\mu$	$\sigma$
State #1	0.540	0.006	-0.953	0.009	-1	0
State #2	0.491	0.008	-1	0	-1	0
State #3	0.556	0.008	-0.853	0.010	-0.867	0.013
State #4	0.475	0.014	-1	0	-0.925	0.016
State #5	0.370	0.012	-1	0	-0.747	0.017
State #6	0.632	0.009	-0.889	0.010	-1	0
State #7	0.723	0.009	-0.941	0.013	-1	0
State #8	0.552	0.009	-0.651	0.010	-1	0
State #9	0.543	0.015	-0.389	0.012	-1	0
State #10	0.519	0.049	-0.969	0.021	-1	0
State #11	0.522	0.013	-0.969	0.026	-1	0
State #12	0.507	0.026	-0.968	0.037	-1	0
State #13	0.487	0.196	-0.979	0.061	-0.974	0.075
State #14	0.412	0.404	-0.999	0.006	-0.86	0.266
State #15	0.490	0.006	-1	0	-1	0
State #16	0.542	0.009	-0.872	0.015	-0.867	0.014
State #17	0.467	0.206	-0.895	0.052	-0.822	0.205

Table 17. Mean  $\mu$  and standard deviation  $\sigma$  of 1<sup>st</sup> floor displacement for 50 realisations for 17 steps

	Mode shape (2° floor displacement)					
	1° modo		2° modo		3° modo	
	$\mu$	$\sigma$	$\mu$	$\sigma$	$\mu$	$\sigma$
State #1	-0.245	0.006	-0.946	0.008	0.883	0.009
State #2	-0.295	0.016	-0.858	0.008	0.918	0.012
State #3	-0.270	0.006	-0.724	0.006	1	0
State #4	-0.225	0.007	-0.672	0.006	1	0
State #5	-0.202	0.011	-0.441	0.005	1	0
State #6	-0.284	0.009	-0.939	0.008	0.836	0.015
State #7	-0.432	0.015	-0.976	0.019	0.784	0.018
State #8	-0.179	0.007	-1	0	0.710	0.006
State #9	-0.032	0.017	-1	0	0.595	0.006
State #10	-0.270	0.051	-0.944	0.016	0.885	0.019
State #11	-0.258	0.010	-0.925	0.016	0.880	0.022
State #12	-0.272	0.019	-0.894	0.032	0.871	0.046
State #13	-0.310	0.051	-0.775	0.092	0.897	0.076
State #14	-0.356	0.074	-0.613	0.106	0.932	0.283
State #15	-0.300	0.008	-0.856	0.010	0.909	0.021
State #16	-0.288	0.006	-0.723	0.010	1	0
State #17	-0.305	0.032	-0.643	0.042	0.960	0.283

Table 18. Mean  $\mu$  and standard deviation  $\sigma$  of 2<sup>nd</sup> floor displacement for 50 realisations for 17 steps

	Mode shape (3° floor displacement)					
	1° modo		2° modo		3° modo	
	$\mu$	$\sigma$	$\mu$	$\sigma$	$\mu$	$\sigma$
State #1	-0.926	0.009	0.927	0.009	-0.383	0.006
State #2	-0.955	0.027	0.903	0.012	-0.402	0.006
State #3	-0.994	0.007	0.776	0.008	-0.449	0.005
State #4	-0.835	0.024	0.807	0.007	-0.464	0.006
State #5	-0.689	0.006	0.735	0.010	-0.489	0.010
State #6	-0.886	0.021	0.919	0.009	-0.367	0.007
State #7	-0.859	0.011	0.991	0.015	-0.386	0.016
State #8	-1.000	0.000	0.821	0.006	-0.237	0.003
State #9	-0.998	0.015	0.645	0.007	-0.141	0.004
State #10	-0.933	0.019	0.938	0.015	-0.386	0.016
State #11	-0.923	0.011	0.923	0.018	-0.398	0.015
State #12	-0.931	0.028	0.915	0.025	-0.393	0.036
State #13	-0.860	0.233	0.852	0.250	-0.441	0.057
State #14	-0.710	0.336	0.841	0.066	-0.542	0.229
State #15	-0.957	0.008	0.900	0.011	-0.403	0.010
State #16	-0.996	0.005	0.789	0.011	-0.447	0.007
State #17	-0.935	0.183	0.770	0.044	-0.442	0.241

Table 19. Mean  $\mu$  and standard deviation  $\sigma$  of 3<sup>rd</sup> floor displacement for 50 realisations for 17 steps

Also, the mode shapes coordinates are least affected by variability on data set values. The standard deviation is close to zero. It means that the nonlinearity of the damage steps is not principally affecting the mode shapes, except of State #14 and #15.

The results reported in the previous tables are displayed with boxplot diagrams (Figure 88-89). Boxplot is a standardized way of illustrating the distribution of data based on a five numbers summary: “minimum”, first quartile (Q1), median, third quartile (Q3), and “maximum”. The spacings between the different parts of the box indicate the degree of dispersion (spread) and skewness in the data, and show outliers. In the x-axis there are the damage steps (#1-#17) while in the y-axis the frequency and damping’s values. The second, third and fourth modes are reported in the plots.

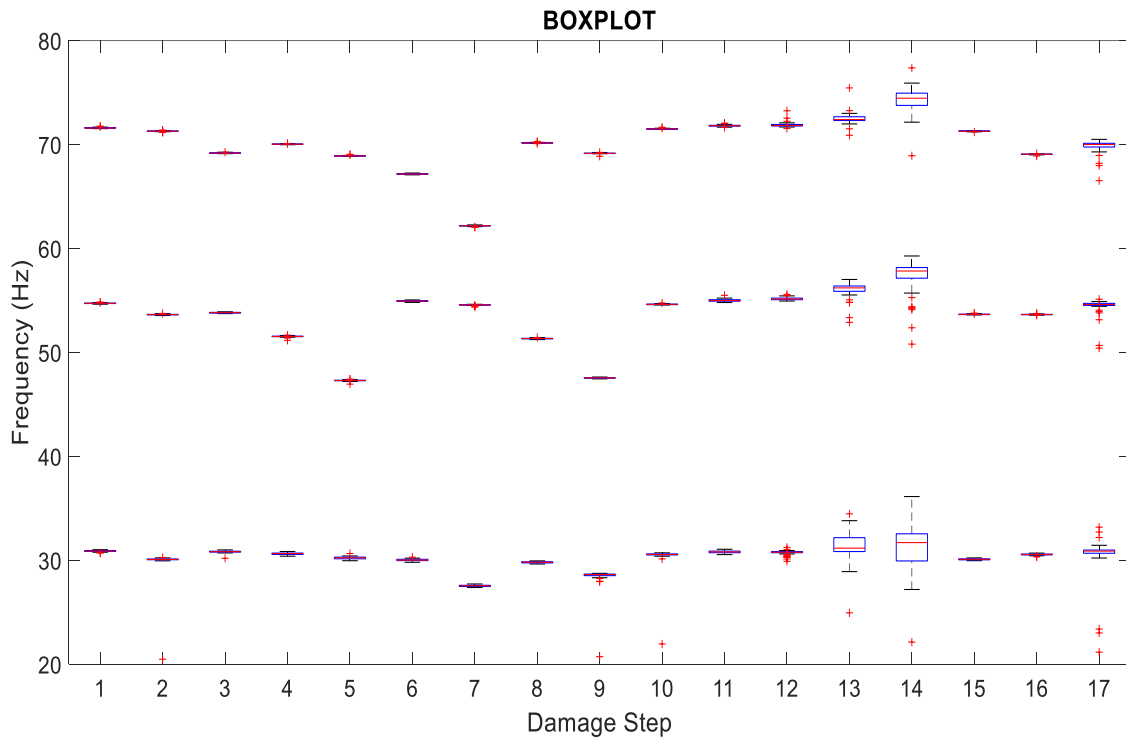


Figure 88. Box plot for frequency (second, third and fourth mode for 17 steps of damage)

It is very interesting to note that the trend of box plots reflects the one found in the previous tables. The growth and decrease of the frequency in the Step #1-#9 are due to the alternation of reduction of stiffness in one or more columns.

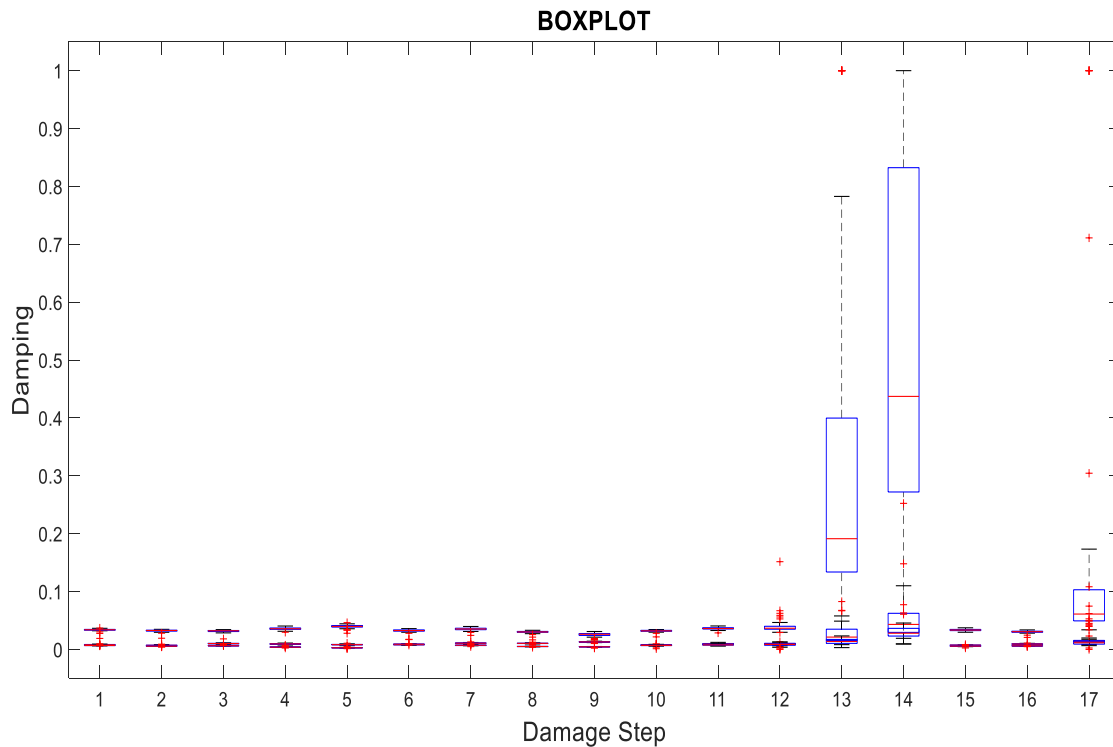


Figure 89. Box plot for damping (second, third and fourth mode for 17 steps of damage)

In these figures we note that the box plots effectively highlight the symmetry of the distribution for Step #14 and #13. High variability of the data sets also demonstrated by boxplot elongation. Because of the visibility of the outliers for the Step #2, Step #9, Step #10, it is possible to delete from the data set and recalculate the mean and standard deviation for the frequency values in order to carry out more realistic parameters (Table 20).

	FREQUENCY					
	2° modo		3° modo		4° modo	
	$\mu$	$\sigma$	$\mu$	$\sigma$	$\mu$	$\sigma$
State #1	30.89	0.069	54.74	0.041	71.61	0.046
State #2	30.13	0.1248	53.65	0.042	71.29	0.036
State #3	30.83	0.108	53.82	0.048	69.19	0.035
State #4	30.65	0.112	51.54	0.069	70.05	0.027
State #5	30.25	0.118	47.30	0.065	68.92	0.035
State #6	30.04	0.097	54.65	0.051	67.18	0.041
State #7	27.55	0.074	54.58	0.047	62.19	0.043
State #8	29.82	0.075	51.34	0.044	70.17	0.032
State #9	28.80	0.403	47.56	0.040	69.16	0.049
State #10	30.53	0.383	54.74	0.038	71.62	0.035
State #11	30.83	0.112	55.01	0.113	71.82	0.078
State #12	30.74	0.224	55.18	0.136	71.91	0.246
State #13	30.70	4.128	55.78	1.358	72.38	0.749
State #14	31.73	1.6621	56.98	1.800	73.71	1.651
State #15	30.10	0.069	53.67	0.036	71.30	0.029
State #16	30.57	0.068	53.65	0.035	69.07	0.032
State #17	29.98	3.994	54.42	0.853	70.07	1.880

Table 20. Mean  $\mu$  and standard deviation  $\sigma$  of frequency modified without outliers (50 realisations for 17 steps)

## 7.3 Masonry arch bridge

To analyse the effect of the noisy on Vector Fitting algorithm, a more complex case is analysed. This chapter focused on a masonry arch bridge that is a laboratory reconstruction of similar structures that are considered architectural heritage which needs to be preserved and valorised. Masonry arch bridges have an historical value as they are still present in many European countries. In this way it is important to study its behaviour in presence of vibrations and the damage evaluation during its life.

In 2006 a masonry arch bridge was built in the laboratory of the Department of Structural, Geotechnical and Building Engineering of the Polytechnic of Turin. The aim of this project is a local inspection on masonry structures in a destructive survey and a non-destructive evaluation in order to supply information about the mechanical characteristics of masonry as a composite material and of its components.

In this way, this section illustrates an application of Vector Fitting algorithm to a typical civil structure case. It is focused on the difficult of this category of algorithm to fitting transfer function with a high presence of noise and several compelling nonlinearities induced by the structural complexity and by the composite material (Portland mortar and bricks), with its internal texture and presence of local irregularities.

### 7.3.1 *Description of case study*

The bridge shows the typical characteristic of an Italian masonry arch bridge. The structure is a twin-arch bridge with a width of 1.60 m, a length of 5.90 m and a height of 1.75 m. The two arches have a radius of 2.00 m and an angular opening of  $30^\circ$ . The two span is 2.00 m long between the supports and the thickness of the arch is equal to 0.20 m. The model was created with clay bricks also scaled to  $130 \times 65 \times 30$  mm to respect the adopted modelling scale law. Low compressive strength elements were chosen and mortar with poor mechanical properties was used to bound them in order to ricreate the typical materials of historical buildings (G. Ruocci, A. Quattrone, L. Zanotti Fragonara, R. Ceravolo, A. De Stefano). The geometric is illustrated in Figure 90 and Figure 91.



Figure 90. View of masonry arch bridge in the laboratory of Politecnico di Torino

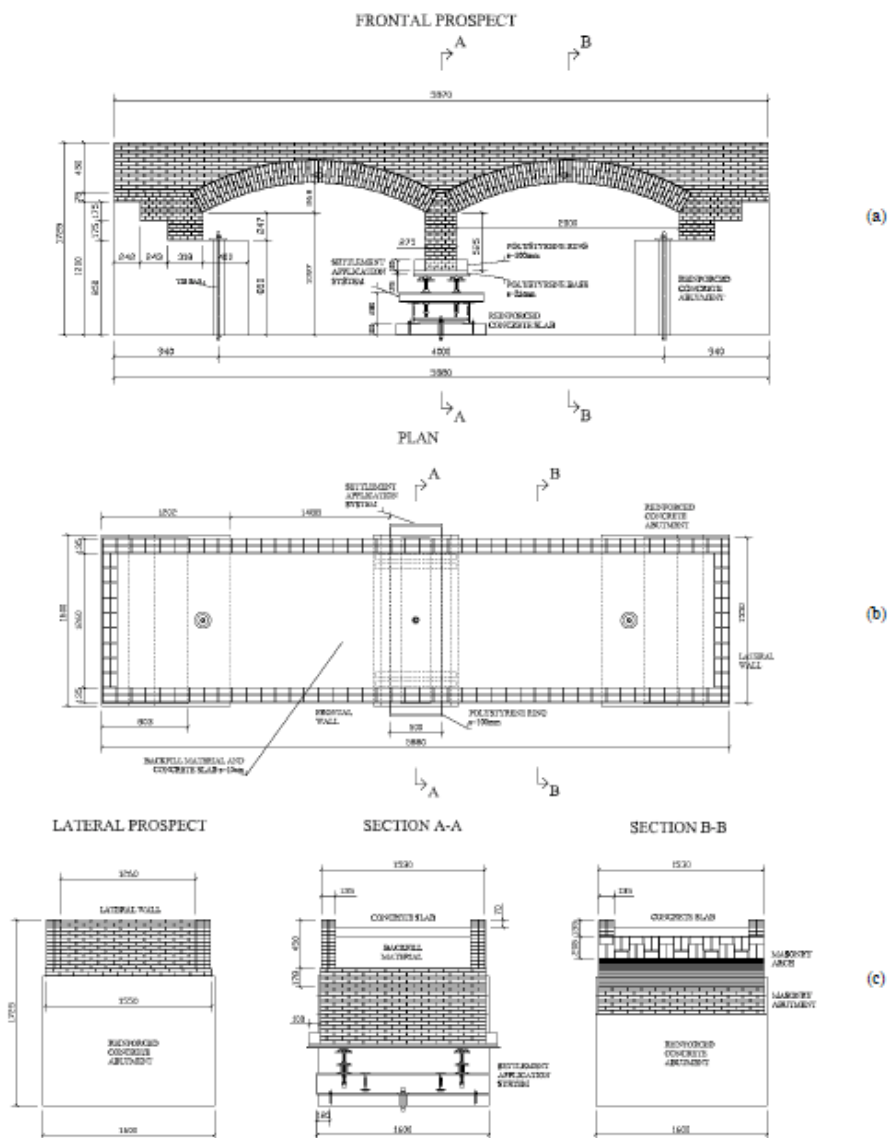


Figure 91. Geometric details of the masonry arch bridge model: front view(a), plan (b) and lateral sections (c) (Ruocci G., 2009)

The operations carried out for the bridge construction are furthermore elaborated in G. Ruocci's dissertation (*"Application of the SHM methodologies to the protection of masonry arch bridges from scour"*, Politecnico di Torino): *"First of all, the wooden formworks of the reinforced concrete abutments were placed in the area of the laboratory which was selected to host the bridge model. The steel reinforcing bars were positioned inside the formworks and the concrete was poured and vibrated. After a few days required for the curing and hardening of the concrete the blocks were freed from the formworks. The reinforced concrete blocks were fixed to the laboratory floor by means of steel tie bars. This solution was adopted to avoid the rocking of the abutment during the model construction and to reduce the uncertainty referred to the boundary conditions of the bridge model...[ ]"*. The two masonry abutments were assembled over the reinforced concrete blocks as illustrated in Figure 93.



Figure 92. The arch bridge model construction: reinforced concrete blocks formworks



Figure 93. The arch bridge model construction: reinforced concrete block and masonry abutment

*“The settlement application system was installed on the reinforced concrete slab previously created and fixed to the laboratory floor by means of a tie bar as for the lateral blocks. The system is composed by a set of steel beams yielded together in order to create a box structure able to bear the vertical components of the arches thrust and to provide the base for the mechanical device expressly designed to reproduce the scour effect. Indeed, the aim of the whole experimental test is to reproduce the effects of scour at the foundation of the central pier of the twin-arch bridge model. The mid-span masonry pier, which was cut at hypothetical middle-height section to allow the insertion of the settlement application system, is imagined to be placed inside the streambed and subjected to the scour of its foundation. Some hydraulic flume tests were carried out on a further scaled down model of the bridge pier in order to simulate the scour effects in the lab. The foundation settlements and rotations resulting from these investigations were then replicated on the bridge model by means of the four independent screws installed at the extremities of the settlement application system. The spherical plain bearings placed at the head of the screws allow the rotations of the plate which support the central pier about axes parallel to the longitudinal and transversal directions of the bridge. The lower section of the masonry pier lays on a polystyrene mould whose mechanical properties were designed to simulate the deformability and the restraint of the streambed material surrounding the foundation of the pier. A thin polystyrene layer divides the bottom of the pier from the upper face of the steel plate of the settlement application system. It simulates the sediments in the bed of the river. This polystyrene ring around the pier was progressively removed during the tests according to the results of some hydraulic flume tests. After the completion of both the arches the longitudinal and transversal spandrel walls were created to retain the backfill material which loads and stabilises the arch barrels. The*

*backfill is composed by sand, gravel and debris of different size. To create a regular plane a 10 cm thick layer concrete is placed over the backfill.”*



*Figure 94. Construction details*

### **7.3.2 Preliminary studies**

Experimental tests carried out on the masonry arch bridge model to investigate the characteristics of material behaviour. Masonry is non-linear and its mechanical properties are uncertain due to the presence of local irregularities and the internal texture. For the determination of the elastic properties that build up the structure, the Poisson coefficient, the elastic modulus and the density were measured in the laboratory, and both S and P wave velocities were obtained. Low-velocity values arise from the choice of low-compressive strength elements bound by a mortar with poor mechanical properties in order to reproduce the typical materials of historical constructions. (Serra, et al., 2016).

The characterization tests on the mortar samples were performed following the prescriptions proposed by the European standard code EN 998-2:2003 adapted to take into account the scaled measure of bricks. The collected samples belong to the M2.5 class of the European standard code EN 998-2:2003 which is one of the poorest in terms of mechanical properties. The characterization tests on the masonry samples were performed following the prescriptions proposed by the European standard code UNI EN 1052-1, EN 052-3:2002 and the American standard code ASTM E 518-02 (Ruocci, Fragonara, Quattrone, Stefano, & Ceravolo, 2013). Some of preliminary material tests are compression test and three-point bending test, used to classify the mortar for the bridge.

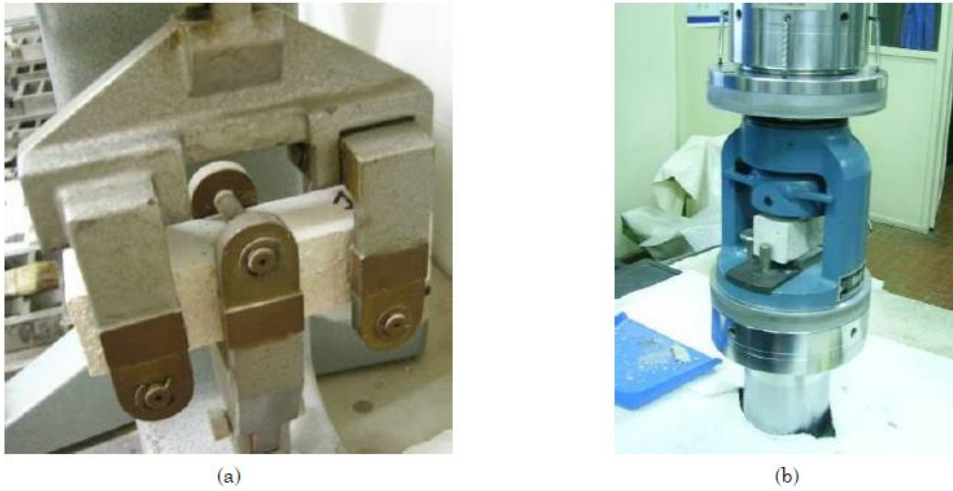


Figure 95. Details tests on mortar samples: three points bending test (a), compressive test (b) (Ruocci G. , 2009)

The others experimental material tests concern the masonry samples (Figures 96-98):

- Axial compression on cubic samples
- Diagonal compression on cubic samples
- Shear test on masonry triplets
- Four points bending test on a segment of the arch

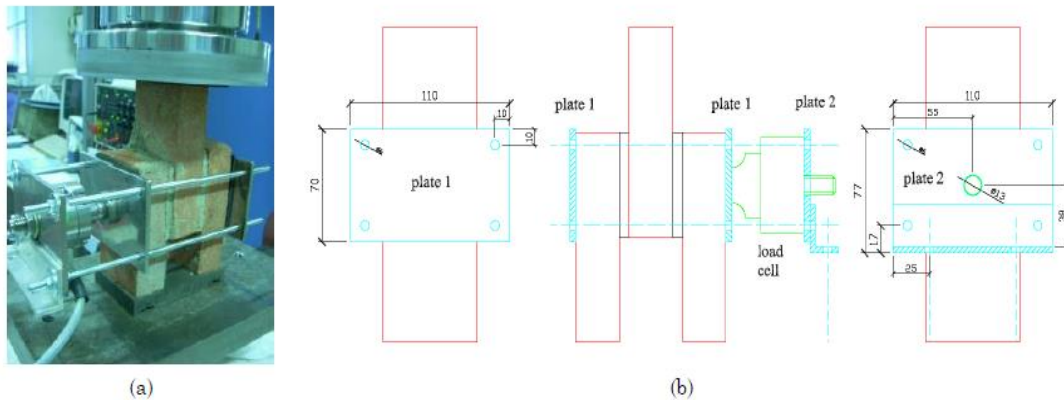


Figure 96. Shear test on masonry samples: experimental device (a), transducers deployment on the specimen (Ruocci G. , 2009)

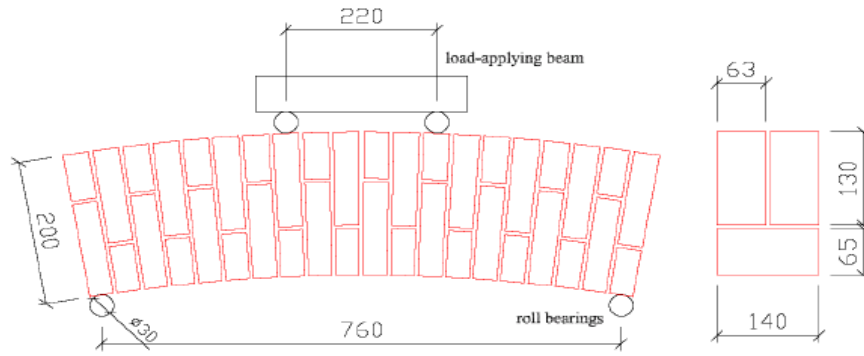


Figure 97. Four points bending test on the segments of the ridge arch: geometric details (Ruocci G. , 2009)

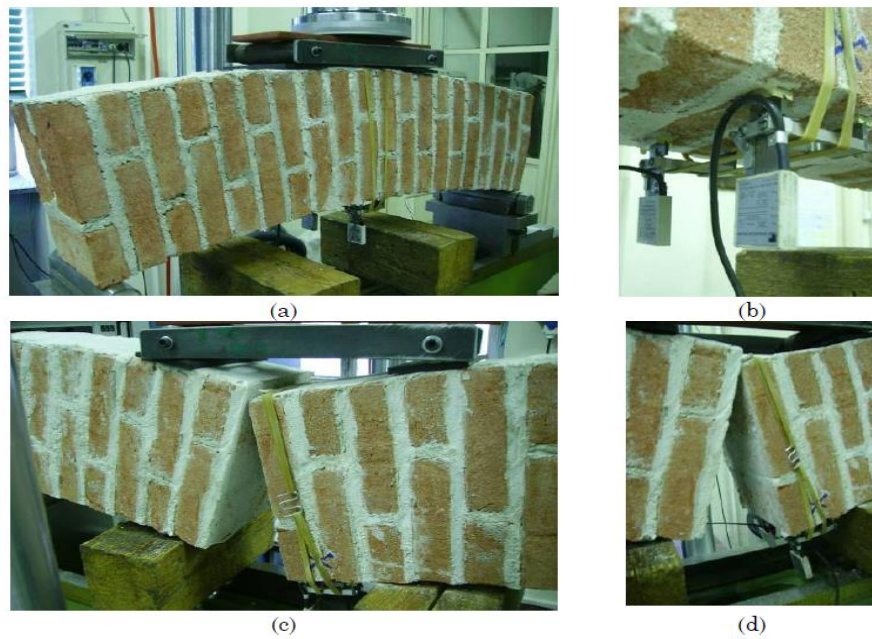


Figure 98. Four points bending test on the bridge: experimental device (a), transducers deployment on the specimen (b), specimen failure (c), failure particular (d)

Material	E (N/m <sup>2</sup> )	$\nu$	$\rho$ (kg/m <sup>3</sup> )	V <sub>p</sub> (m/s)	V <sub>s</sub> (m/s)
Reinforced concrete	3.0	0.15	2400	3633	2331
Masonry	1.5	0.20	1900	937	574
Backfill material	5.0	0.10	2000	160	107
Concrete	0.5	0.15	2200	1549	994

Table 21. Characteristics of materials

Test	$\mu$ (N/mm <sup>2</sup> )	$\sigma$ (N/mm <sup>2</sup> )
<b>Compressive tests: tensile strength</b>	4.278	0.352
<b>Compressive test: Young modulus E</b>	1451	472
<b>Diagonal tests: tensile strength</b>	0.304	0.088
<b>Diagonal tests: shear strength</b>	0.43	0.125
<b>Diagonal tests: shear Young modulus G</b>	940	436
<b>Shear tests (0.1 KN pre-compression): shear strength</b>	0.794	0.301
<b>Shear tests (051 KN pre-compression): shear strength</b>	1.013	0.188
<b>Four-point bending tests: R modulus of rupture</b>	0.22	//

*Table 22. Results of preliminary tests*

Furthermore, flume tests were carried out to study the erosion of the soil underneath the foundation and to scale the dimensions of the bridge.

### ***7.3.3 Experimental test***

Different damage steps have been applied to the structure accordingly with hydraulic flume tests. These campaigns are performed for a period of four years (2006-2010) in the Department of Structural, Geotechnical and Building Engineering of the Polytechnic of Turin. After 2010 the bridge has been destroyed. There are three main campaigns which differ for the period, state of the model, different excitation sources and damage steps. In the next two tables campaigns details are illustrated:

Experimental campaign	Damage steps	Settlement [mm]	Rotation [rad]	Polystyrene [%]
1 <sup>st</sup> campaign	HS (healthy state)	0	0	0
2 <sup>nd</sup> campaign	DS1	0	0	18 %
	DS2	0.25	0	25 %
	DS3	1	$4.21 \cdot 10^{-4}$	37.5 %
	DS4	2.25	$1.01 \cdot 10^{-3}$	47 %
3 <sup>rd</sup> campaign	DS5	2.25	$1.23 \cdot 10^{-3}$	56 %
	DS6	2.8	$1.23 \cdot 10^{-3}$	72 %
	DS7	3.6	$1.27 \cdot 10^{-3}$	81 %
	DS8	4.7	$1.30 \cdot 10^{-3}$	91 %
	DS9	7.6	$1.28 \cdot 10^{-3}$	100 %

Figure 99. Damage steps, middle settlement, pier rotation, polystyrene removed (Ruocci, Fragonara, Quattrone, Stefano, & Ceravolo, 2013)

The first campaign (October 2008 to March 2009) is characterized by the undamaged structure and the tests for understanding its “healthy” state (HS). Dynamic properties of the bridge demonstrated a decrease in the bridge stiffness through the several campaign. This may be due to the development of rheologic phenomena, as the concrete block creep or the mortar shrinkage. The second campaign (April 2009) started with the application of additional masses on the pier, in order to approximate the weight of the missing part of the pier (Ruocci, Fragonara, Quattrone, Stefano, & Ceravolo, 2013). In this campaign the first four settlement steps were imposed on the upstream side of the pier. In addition, parts of the polystyrene ring were removed in each step to simulate the erosion of the foundation according to the hydraulic flume tests (Ruocci, Fragonara, Quattrone, Stefano, & Ceravolo, 2013).

During the last campaign (September 2010 to October 2010) five settlement steps were applied. At the end of this campaign all polystyrene is removed. During the monitoring phases physical quantities are controlled under different excitations: acceleration measurements (ACC), temperature (T) and strain deformation (SG and OPT). Three different excitation sources are applied in the third campaigns: impact hammer (IH), shaker (S) and ambient vibration (AV) (Ruocci, Fragonara, Quattrone, Stefano, & Ceravolo, 2013).

	Time	Step	Excitation	Measurements
1 <sup>st</sup> campaign	Oct. 2008	HS	AV, IH	ACC, SG, T, OPT
	Nov. 2008	HS	AV, IH	ACC, SG, T, OPT
	Jan. 2009	HS	AV, IH	ACC, SG, T, OPT
	Feb. 2009	HS	AV, IH	ACC, SG, T, OPT
	Mar. 2009	HS	AV, IH	ACC, SG, T, OPT
2 <sup>nd</sup> campaign	Apr. 2009	HS	AV, IH	ACC, SG, T, OPT
		DS1	AV, IH, S	ACC, SG, T, OPT
		DS2	AV, IH, S	ACC, SG, T, OPT
		DS3	AV, IH, S	ACC, SG, T, OPT
		DS4	AV, IH, S	ACC, SG, T, OPT
3 <sup>rd</sup> campaign	Sep. 2010	DS5	AV, IH, S	ACC, SG, T, OPT
		DS6	AV, IH, S	ACC, SG, T, OPT
	Oct. 2010	DS7	AV, IH, S	ACC, SG, T, OPT
		DS8	AV, IH, S	ACC, SG, T, OPT
		DS9	AV, IH, S	ACC, SG, T, OPT

Figure 100. Experimental test timeline (Ruocci, Fragonara, Quattrone, Stefano, & Ceravolo, 2013)

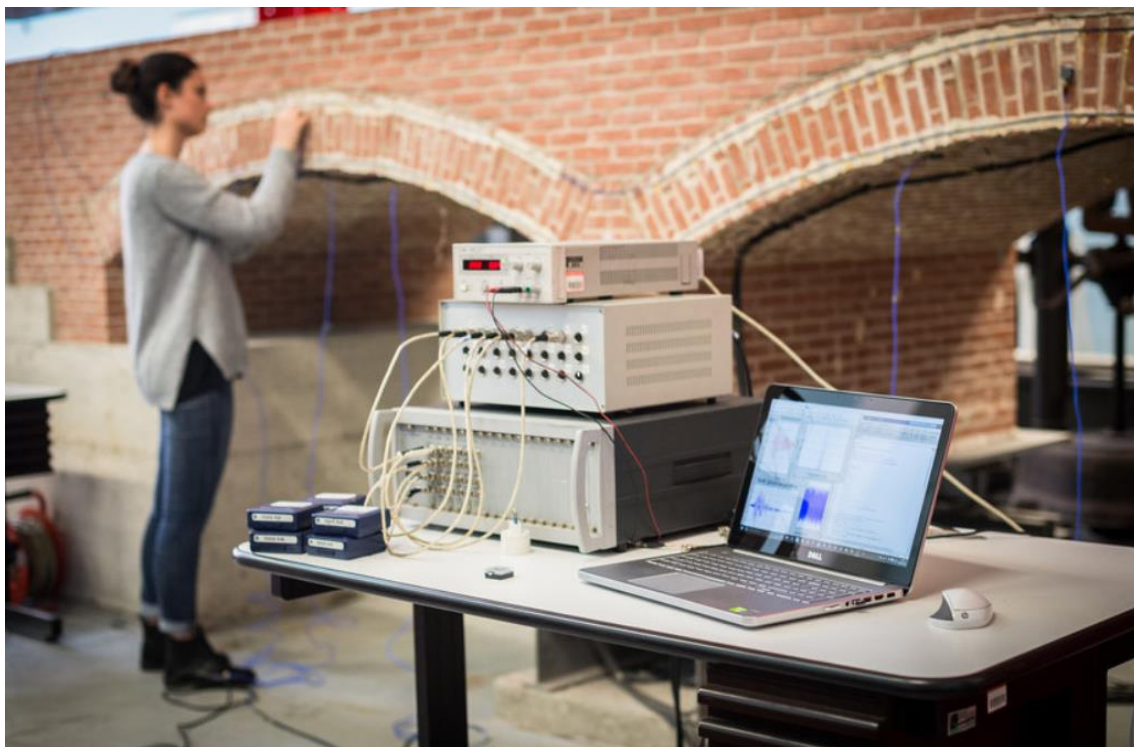


Figure 101. Test equipment

The selected sensors for the dynamic tests performed on the intact structure were capacitive accelerometers. The set of accelerometers lies of 18 monoaxial PCB Piezotronics accelerometers with a sensitivity of 1V/g, a resolution of  $30\mu\text{g}$  and a weight of 17.5g. In the November 2008

session was characterized by only 12 accelerometers were used. “The sensors are connected through coaxial cables to the LMS Difa- Scadas data acquisition system which supplied also the signals amplification. The acquired signals were recorded on the hard drive of a laptop computer interfaced with the data acquisition system and running a specific signal acquisition software”. (Ruocci, Fragonara, Quattrone, Stefano, & Ceravolo, 2013)

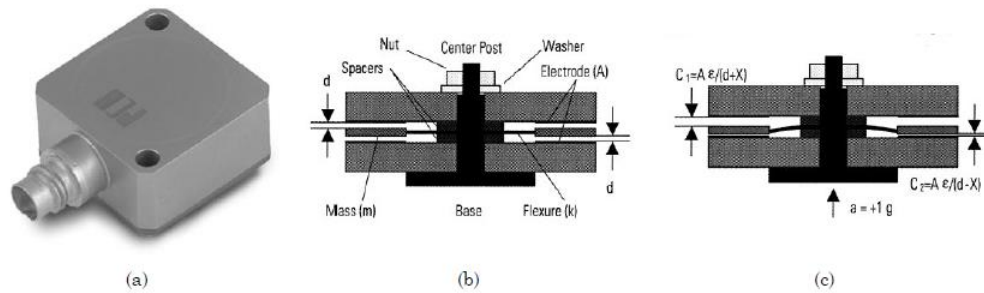


Figure 102. PCB capacitive accelerometer: model 3701G3FA3G (a), cross-section for the “0g” condition (b), cross-section for the “1g” condition (c) [www.pcb.com]

Due to better data quality, we apply the Vector Fitting algorithm to the third campaign data set (September-October 2010). After the second campaign in April 2009, other 5 damage steps were introduced in the experimental model, where the polystyrene ring around the pier was progressively removed in addition to the application of the controlled displacements. The first allowed to simulate the erosion of the foundation while the second reproduced the destructive effect. The polystyrene ring was removed cutting identical rectangular portions away. “The displacements were applied acting on the two screws of the upstream side of the settlement application system described before. Turning clockwise the screws were lowered and the plane spherical bearings allowed the settlement and tilt of the plate supporting the central pier. The applied settlements were rigorously controlled measuring the displacements of the 4 vertexes of the steel plate by means of the same resistive transducers LVDTs employed in the testing of the mechanical device”, as described by the author G. Ruocci in his paper. In Figure 103 the testing of the settlement application system is shown.



*Figure 103. The arch bridge model construction: testing of the settlement application system*

The effects of the prescribed displacement on the arch barrels were monitored by the same strain gages used to evaluate the consequences of the load placement. Three settlement steps were applied, leading to the following damage steps:

- Removal of the polystyrene ring and application of the 5th lowering step (STEP5)
- Removal of the polystyrene ring and application of the 6th lowering step (STEP6)
- Removal of the polystyrene ring and application of the 7th lowering step (STEP7)
- Removal of the polystyrene ring and application of the 8th lowering step (STEP8)
- Removal of the polystyrene ring and application of the 9th lowering step (STEP9)

	Period		Settlement (mm)
	14-sep	29-sep	
<b>P.R.</b>	14-sep	29-sep	-
<b>STEP#5</b>	30-sep	05-oct	2.25
<b>STEP#6</b>	05-oct	13-oct	2.8
<b>STEP#7</b>	14-oct	18-oct	3.6
<b>STEP#9</b>	22-oct	29-oct	7.6

Table 23. Settlement values

The first acquisition phase is aimed at the characterization of the reference configuration of the model after the relaxation phase followed by the last application of the failure created in April 2009. The phases of the load application are as follows:

- Removal of polystyrene ashlar
- Positioning of the LVDTs on the plate and on the references on the stack.
- Application of failure with simultaneous acquisition of accelerometers and strain gauges
- Execution of noise, hammer and shaker tests in position 6C, 9A and 15M.

The sensors are placed in two different setups for each vibration test in order to capture the larger number of modes of vibration (Figure 104). The sensors and the data acquisition system selected to perform the dynamic tests of the structure were the same employed in the tests carried out from others steps. The accelerometers have a sensitivity of 9.8 g/V.

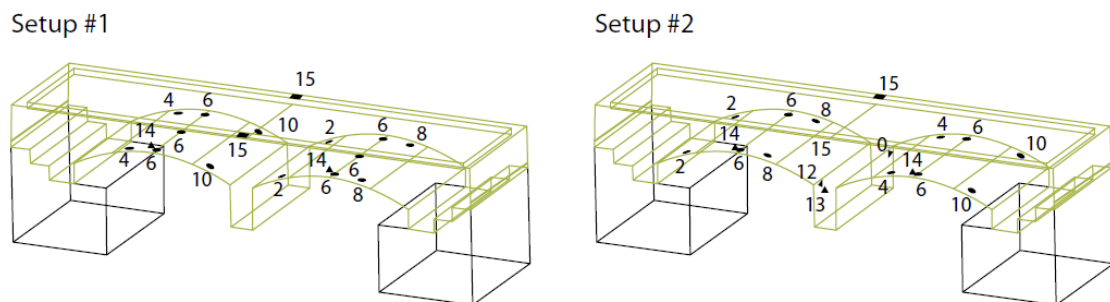


Figure 104. Description of Setup #1 and Setup #2

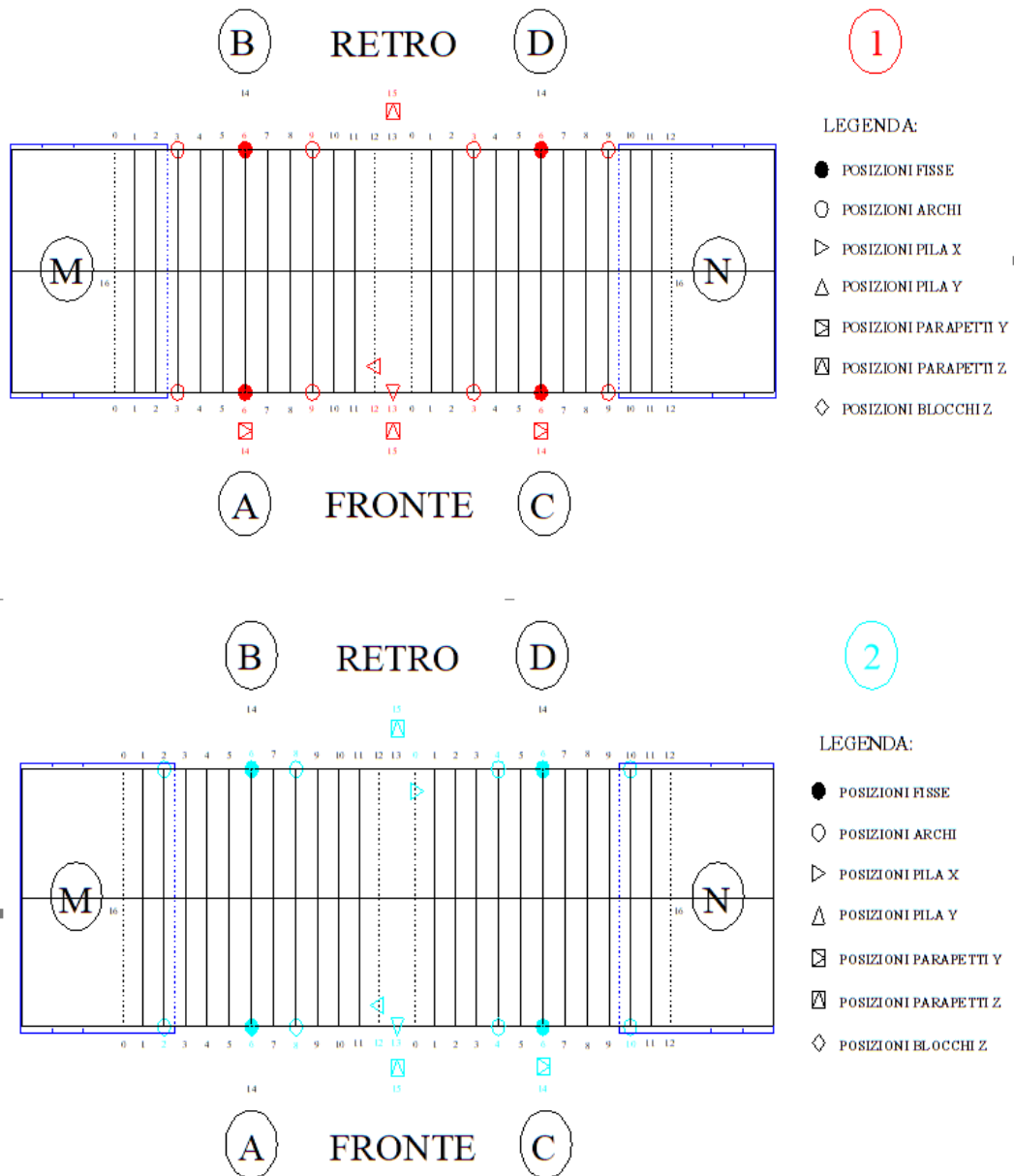


Figure 105. Scheme of accelerometers positioning: Setup#1 (1), Setup#2 (2)

The input excitation consists of an impulsive force of instrumental hammer. The instrumental hammer is a hammer with grey trip and nominal sensitivity of 0.228 mV/N. The sampling frequency is 400 Hz and a recording time of 45 seconds to acquire several impacts. Nyquist criterion the maximum frequency is 200 Hz. The frequency resolution is 0.017 Hz. Hammer impacts were made in 30 different points of the bridge with different directions in order to excite all modes. Table 24 shows hammer impacts details:

Hammer acquisition	Impact point	Direction	Hammer tip	Time (s)	Sampling Frequency (Hz)
1	M(abutment)	longitudinal	grey	60	400
2	N(abutment)	longitudinal	grey	60	400
3	15A	vertical	grey	60	400
4	15B	vertical	grey	60	400
5	15M	vertical	grey	60	400
6	13A	transversal	grey	60	400
7	14C	transversal	grey	60	400
8	14D	transversal	grey	60	400
9	14A	transversal	grey	60	400
10	13B	transversal	grey	60	400
11	12A	longitudinal	grey	60	400
12	12B	longitudinal	grey	60	400
13	0C	longitudinal	grey	60	400
14	0D	longitudinal	grey	60	400
15	12M	longitudinal	grey	60	400
16	0N	longitudinal	grey	60	400
17	9A	orthogonal to the arch	grey	60	400
18	9D	orthogonal to the arch	grey	60	400
19	9M	orthogonal to the arch	grey	60	400
20	9N	orthogonal to the arch	grey	60	400
21	6A	orthogonal to the arch	grey	60	400
22	6B	orthogonal to the arch	grey	60	400
23	6C	orthogonal to the arch	grey	60	400
24	6D	orthogonal to the arch	grey	60	400
25	6M	orthogonal to the arch	grey	60	400
26	6N	orthogonal to the arch	grey	60	400
27	3B	orthogonal to the arch	grey	60	400
28	3C	orthogonal to the arch	grey	60	400
29	3M	orthogonal to the arch	grey	60	400
30	3N	orthogonal to the arch	grey	60	400

Table 24. Hammer impact details for Step #5-#9

### 7.3.4 Pre-processing phase

In the phase of pre-processing the most significant acquisitions and impacts of hammer were selected. The acquisitions differ for the point and direction of hammer impact which consequently excite different modes. For example, the acquisitions orthogonal to the arch (17-30) excite better vertical or longitudinal modes, while the transversal at the pier ones (6-10) excite more the lateral modes. The acquisitions close to the abutments (1-2) are affected from a high level of noise and so weren't used for identification. In this work we show the most important steps and elements

that have been fundamental for the identification of the bridge's system. In the following figures the force-time history and the acceleration-time histories from channels 1-18 for the Acquisition 9 of Setup 1 of Step #7 are shown:

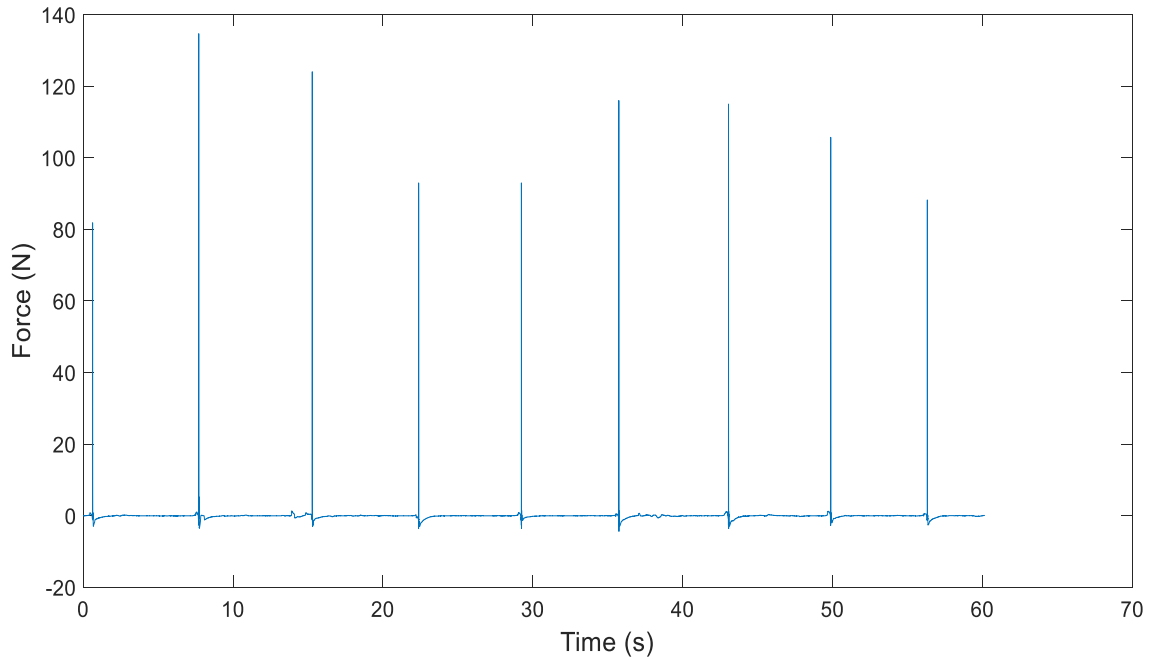


Figure 106. Hammer force-time history for Setup 1 (Step #7)

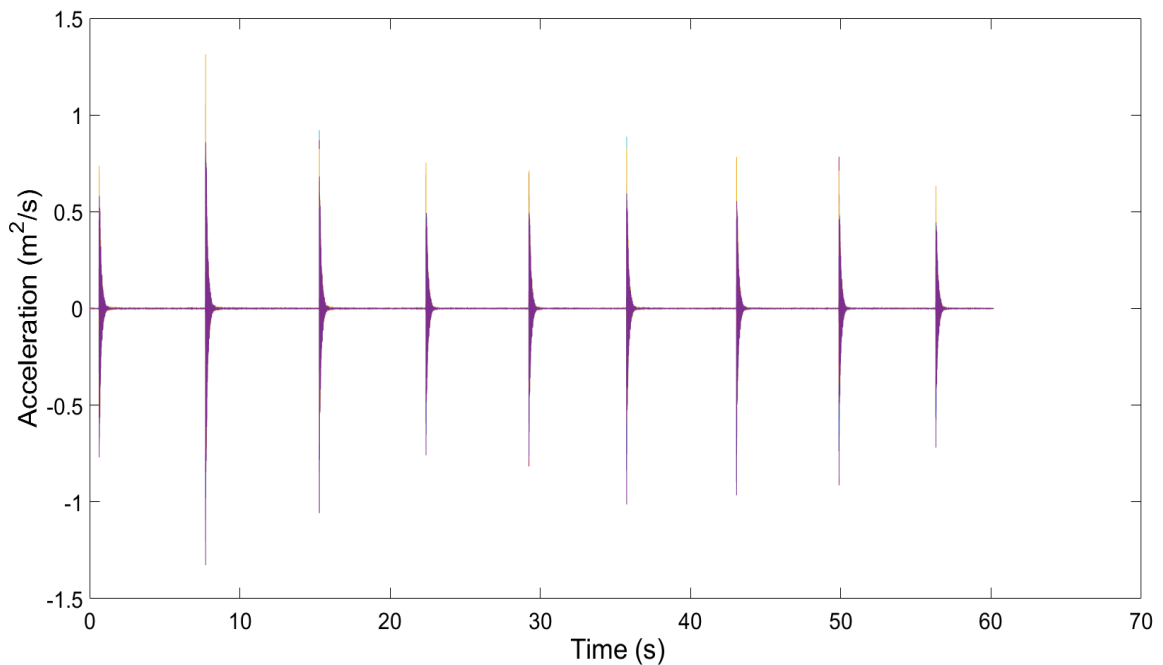


Figure 107. Acceleration-time histories from Channels 1-18 for Setup 1 (Step #7)

Note that there are 9 hammer impacts in all realisations. Between one hammer and the other about 7 seconds apart. Even if only one impact per acquisition was used in dynamic identification.

In this way the third hammer impact is selected to calculate the Frequency Response Function (FRF) for 18 channels. The selection of the impulse is made with an automated code using Matlab.

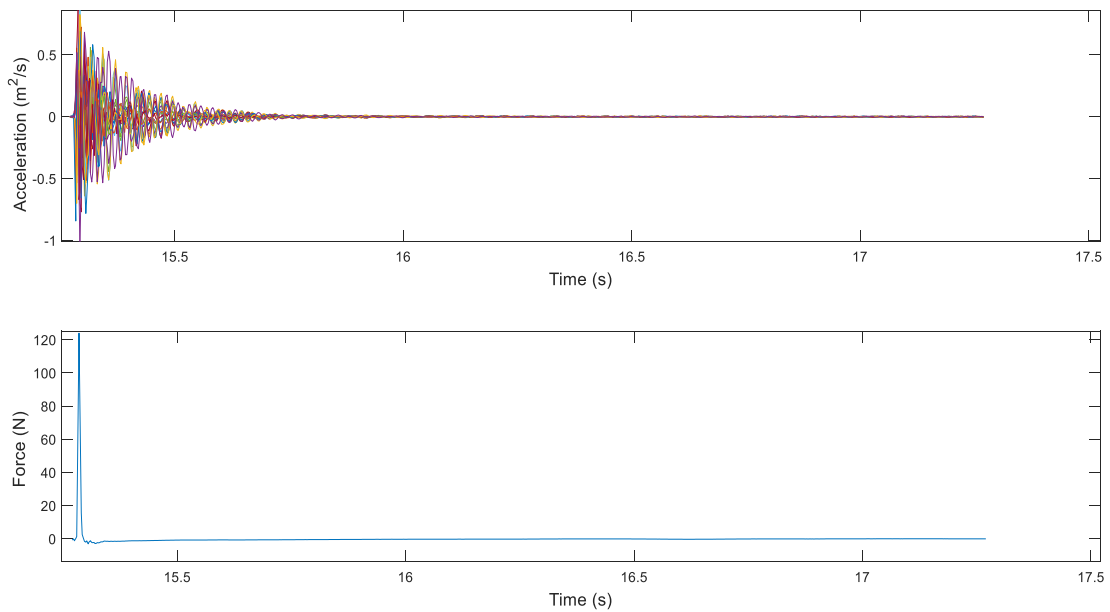


Figure 108. Acceleration-time histories selected of Channel 1-18 (on the top) and the corresponding time history of the third hammer impact (on the bottom)

As with the previous applications, the FRF is calculated as the ratio of the Fast Fourier Transform of the outputs of the system and the Fast Fourier Transform of input-force (Eq. (113)). In this way we obtained the FRF as an acceleration ( $m^2/s$ ) on force (N). As an example, we report the FRFs evaluated from data set of Setup 1 related to Step #7.

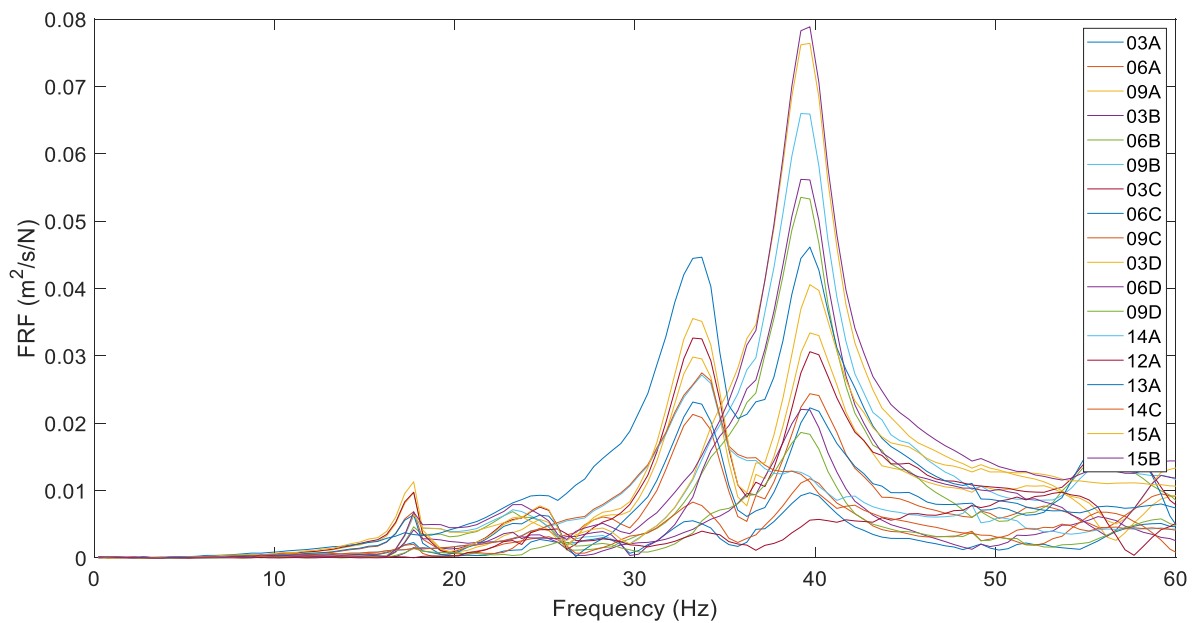
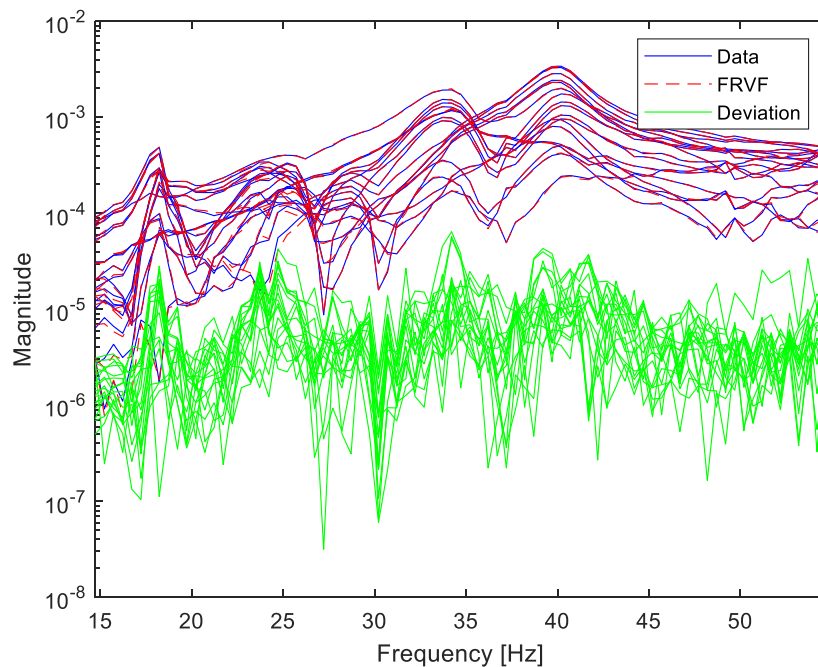


Figure 109. FRFs for Channels 1-18 for Setup 1 (Step#7)

### 7.3.5 System identification

A band-limited in the range of 15-60 Hz was used for system identification because from the previous analysis presented in the paper “*Experimental Testing of a Masonry Arch Bridge Model Subject to Increasing Level of Damage*” (Ruocci, Fragonara, Quattrone, Stefano, & Ceravolo, 2013) we know that the first mode of the bridge is around the value of 18 Hz. The work focuses on the identification of the first four modes (vertical, longitudinal, lateral and torsional), since they are considered the most relevant ones for the dynamic characterisation of the structure. The Vector Fitting algorithm is automatized to process the data set in faster way. The most important and significant plots are reported below in order to show the good quality of fitting process. In the figures the deviation between the data set and Vector Fitting curves are illustrated. The plots of magnitude and phase refer to the acquisition 9 of Step #7.



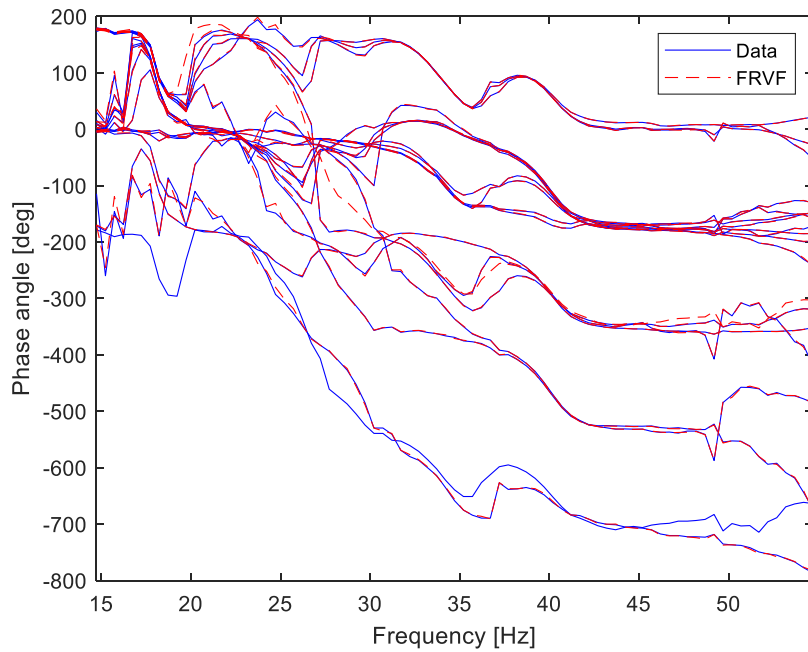


Figure 110. Curve fitting example for the FRFs from Channels 1–18 of State #7 (top side the magnitude and bottom side the phase)

With reference to the analysed acquisitions, it is possible to trace Power Spectrum Density (PSD) diagrams useful for detecting the presence of peaks at high energy content. In Figure 111 the PSDs related to 1-18 channels are shown. It is possible to observe a net peak at 36 Hz and 40 Hz, while less marked are ones at 18 Hz and 30 Hz.

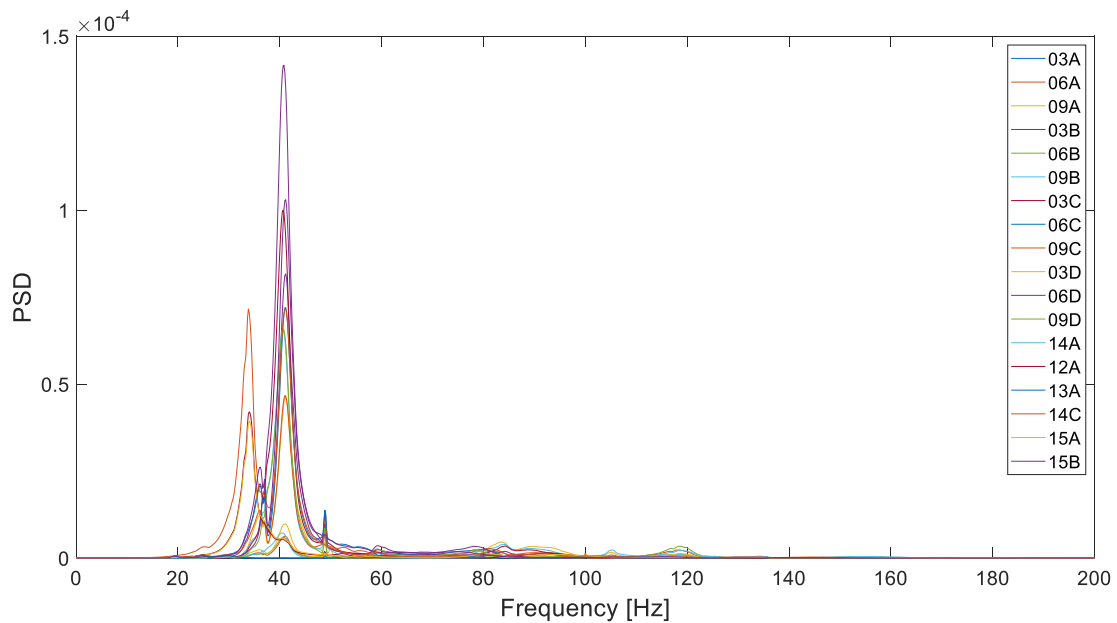


Figure 111. PSD of acquired signals for Setup1 (Step#7)

Once the modal parameters have been estimated for various orders, the stabilisation diagram (Section 5.5) and cluster diagram (Section 5.6) can be plotted. The stable poles from order  $N_{\min}$  to  $N_{\max}$  are determined on the basis of different stabilisation criterion, in terms of frequency, damping and MAC. In this set of test the following stabilisation criteria have been used:

$$\delta f \leq 0.5\%, \quad \delta \xi \leq 8\%, \quad (1 - MAC) \leq 10\%$$

For each setup, a PSD diagram and a stabilization diagram have been processed, in which the identifications show a certain stability with the changing order of the system. A cluster diagram is also reported for each setup, able to represent the system vibration modes in the form of cluster points on the frequency-damping plane. The modes identified in the cluster diagram correspond to the identifications extracted through the VF algorithm. It is assumed a linear dynamic analysis. It is useful to underline that the acquisitions made on both setups for identification have been exploited since the setups enhance the research of different modes. This allows to carry out a cross study of the recursivity of the different modes of vibration varying the acquisition setups, facilitating the separation between ‘real’ and ‘spurious’. It emphasizes the modal forms of the structure in order to characterize in the frequency range established previously. The Setup 1 is used for the most of steps because are less noisy and useful to identify the vertical and longitudinal modes. Indeed, the Setup 2 is used principally for Step #6 to reach the lateral mode.

In Figure 112 the stabilisation diagram for Setup 1 of Step #7 is reported. It is possible to observe stable modes at frequency 18.14 Hz and 40.10 Hz that correspond to clear identifications of the first and fourth to variation of model order. Also, a second and third stable frequencies are visible at 29.38 Hz and 34.26 Hz.

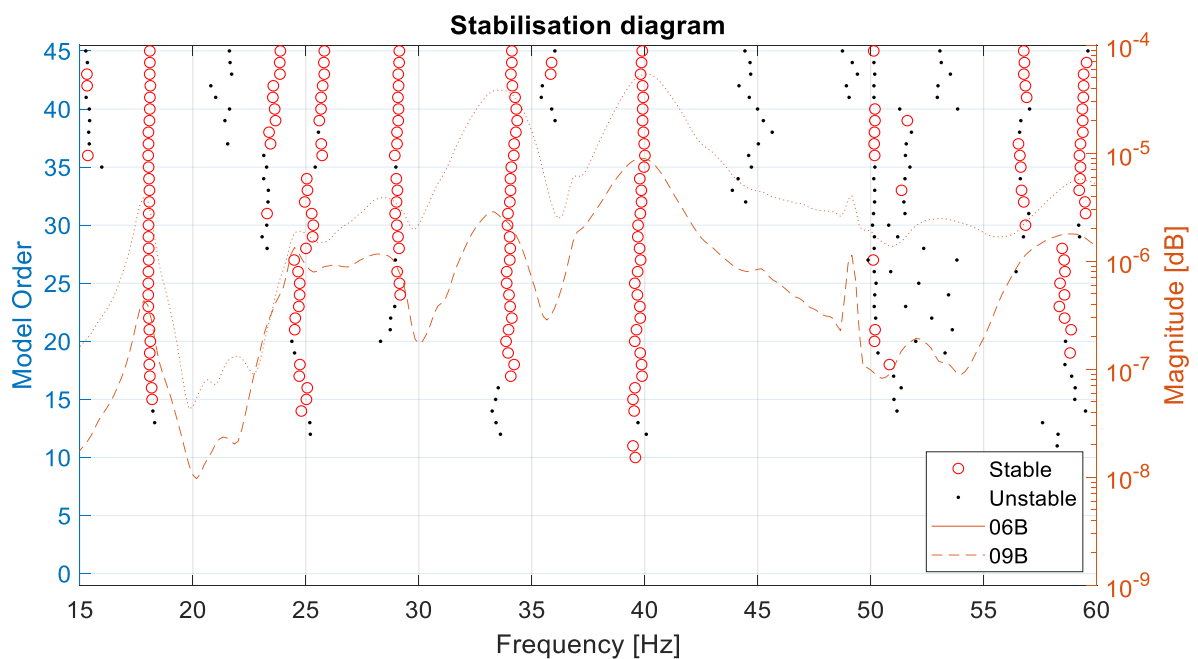


Figure 112. Stabilisation diagram for Setup 1 (Step #7)

The dynamic identification ends with the clustering diagram (Figure 113) which can evaluate the damping ratio associated with stable modes. It confirms the previous considerations.

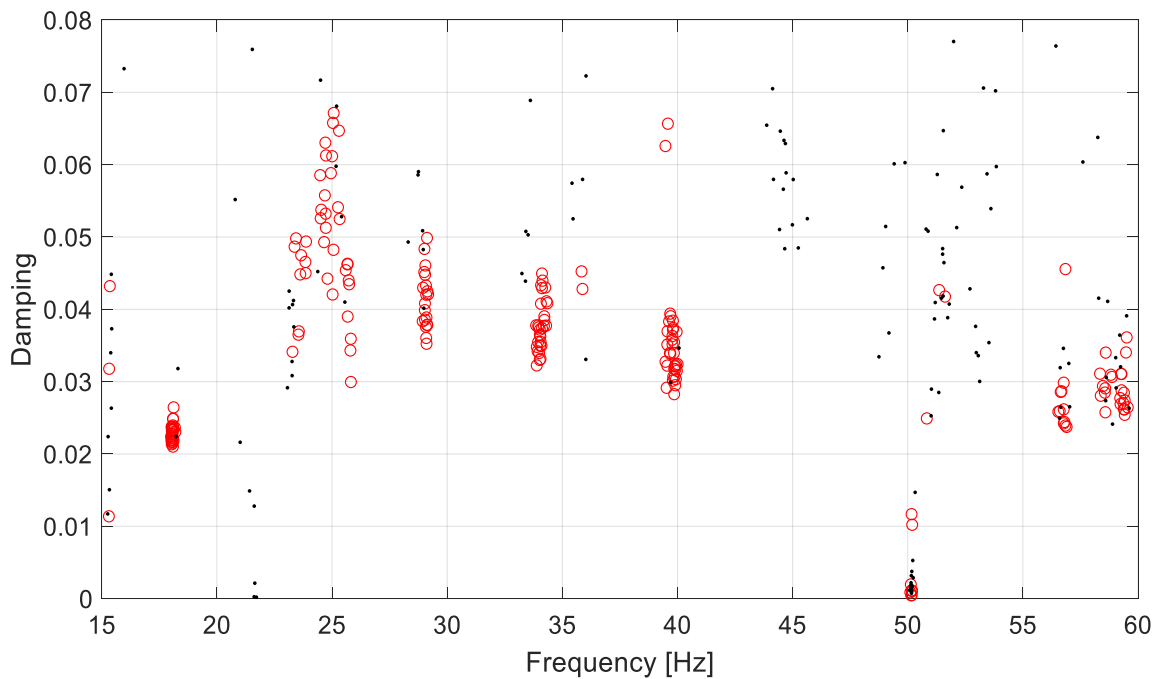


Figure 113. Clustering diagram for Setup 1 (Step #7)

The stabilization diagram is reported in Figure 112 to show the order of the system reached that it corresponds to  $N=45$  ( $N_{VF}=90$ ). Through the cluster diagram it is possible to discriminate the modes with close frequency and associate to the stable ones the corresponding damping value obtained as average of the values of various clusters. Vector Fitting turned out to be very fast algorithm. In fact, the time spent to give the stabilisation diagram for a range of order model from 0 to 45 is about 9 s.

To evaluate the mode shapes of the masonry bridge, the signals have been taken unfiltered because after a series of tests, we realized that filters can undermine the phase of the frequency response functions and consequently the displacements of bridge's modes during Vector Fitting curve-fitting process. After a careful analysis, dynamic identification of the bridge is carried out. Despite the changes introduced by damage states to the modal parameter, the knowledge acquired from the previous dynamic tests campaign allowed to limit the investigated configurations to those which provided the best modal identification results. The natural frequencies identified through the VF method were averaged among all the results obtained for each setup. A data cleansing process was further introduced in order to neglect those results which differed from the mean frequency more than the computed standard deviation. In this way, any possible outlier which would have affected the final result was disregarded. In the following tables, final modal parameters are reported for each test:

POST-RELAXATION							
1° Mode		2° Mode		3° Mode		4° Mode	
<b>Frequency</b>	19.84	<b>Frequency</b>	30.18	<b>Frequency</b>	36.92	<b>Frequency</b>	41.37
<b>Damping</b>	0.029	<b>Damping</b>	0.023255	<b>Damping</b>	0.020024	<b>Damping</b>	0.040221
<b>Mode shape</b>	0.298469	<b>Mode shape</b>	0.72433	<b>Mode shape</b>	0.198094	<b>Mode shape</b>	0.248716
	0.70471		1		0.697161		0.579711
	0.867518		0.404299		0.925126		0.661189
	0.13417		0.091603		-0.01691		-0.20125
	0.568746		0.32491		0.339874		-0.61182
	0.760432		0.048557		0.410187		-0.80873
	0.78299		-0.27258		0.885902		0.677785
	0.550786		-0.26222		0.696725		0.555846
	0.214142		-0.33921		0.257532		0.241066
	0.725679		-0.3734		0.459169		-0.98318
	0.457304		-0.48538		0.383365		-0.67475
	0.162134		-0.25382		0.136469		-0.25437
	-0.16392		0.065271		0.21489		-0.03416
	-0.18378		-0.79988		0.015546		-0.0039
	-0.26449		-0.15733		-0.27692		-0.54274
	-0.17197		0.05096		0.200138		-0.02711
	-1		-0.25896		-1		-0.8199
	-0.78369		0.228519		-0.42568		1
<b>MAC</b>	0.95	<b>MAC</b>	0.85	<b>MAC</b>	0.89	<b>MAC</b>	0.98

Table 25. Modal parameters and MAC value of post-relaxation

STEP 5 (DS5)							
1° Mode		2° Mode		3° Mode		4° Mode	
<b>Frequency</b>	18.19	<b>Frequency</b>	29.73	<b>Frequency</b>	36.58	<b>Frequency</b>	39.96
<b>Damping</b>	0.019173	<b>Damping</b>	0.022532	<b>Damping</b>	0.07982	<b>Damping</b>	0.019965
<b>Mode shape</b>	0.235918	<b>Mode shape</b>	0.589175	<b>Mode shape</b>	0.231601	<b>Mode shape</b>	0.133864
	0.723495		1		0.626299		0.357277
	0.94048		0.788746		0.818169		0.469251
	0.105395		0.355738		0.266693		-0.33341
	0.350767		0.308127		0.301446		-0.63042
	0.439061		-0.2424		0.311448		-0.68442
	0.824984		0.242293		0.914162		0.428824
	0.591693		-0.23856		0.728429		0.322565
	0.165476		-0.2344		0.245772		0.155153
	0.355912		-0.51585		0.39381		-1
	0.17969		-0.59374		0.15316		-0.57699
	0.074206		-0.49057		0.055712		-0.21308
	0.024474		0.091881		-0.09176		-0.06421
	-0.09894		-0.61778		0.048582		-0.02541
	-0.1249		-0.28965		-0.22589		-0.31068
	-0.03419		0.015343		-0.05615		-0.05492
	-1		-0.68167		-1		-0.54079
	-0.38051		0.460497		-0.34464		0.93829
<b>MAC</b>	0.92	<b>MAC</b>	0.7	<b>MAC</b>	0.85	<b>MAC</b>	0.94

Table 26. Modal parameters and MAC value of Step #5

STEP 6 (DS6)							
1° Mode		2° Mode		3° Mode		4° Mode	
<b>Frequency</b>	16.98	<b>Frequency</b>	28.09	<b>Frequency</b>	35.79	<b>Frequency</b>	42.53
<b>Damping</b>	0.01548	<b>Damping</b>	0.026445	<b>Damping</b>	0.012188	<b>Damping</b>	0.009159
<b>Mode shape</b>	0.169557	<b>Mode shape</b>	0.39084	<b>Mode shape</b>	0.251615	<b>Mode shape</b>	0.281348
	0.797415		1		0.742923		0.368429
	0.905232		0.915778		0.79986		0.308333
	0.083971		0.381077		0.112497		-0.08941
	0.360283		0.900473		0.134841		-0.72919
	0.451342		0.978301		0.061685		-0.90589
	0.752705		-0.67923		0.833271		0.338508
	0.507935		-0.75636		0.56558		0.335505
	0.034452		-0.31999		-0.03043		0.112127
	0.34119				-0.08813		0.197951
0.158217		-0.46933	0.159871	-0.56305			
0.017019		-0.40742	-0.17387	-0.20281			
0.086998		0.745401	0.173398	0.048849			
-0.10645		-0.69509	-0.15239	0.134287			
-0.13682		0.201069	-0.17166	-0.38679			
-0.03453		0.105671	0.110603	0.069689			
-1		-0.65348	-1	-0.31229			
-0.40321		-0.51722	-0.09235	1			
<b>MAC</b>	0.92	<b>MAC</b>	0.8	<b>MAC</b>	0.4	<b>MAC</b>	0.1

Table 27. Modal parameters and MAC value of Step #6

STEP 7 (DS7)							
1° Mode		2° Mode		3° Mode		4° Mode	
<b>Frequency</b>	18.14	<b>Frequency</b>	29.38	<b>Frequency</b>	34.26	<b>Frequency</b>	40.10
<b>Damping</b>	0.022692	<b>Damping</b>	0.04738	<b>Damping</b>	0.045652	<b>Damping</b>	0.033817
<b>Mode shape</b>	0.190227	<b>Mode shape</b>	0.684144	<b>Mode shape</b>	0.194417	<b>Mode shape</b>	0.105215
	0.577736		1		0.63997		0.2711
	0.84473		0.808176		0.863221		0.369381
	0.111236		0.308003		-0.03444		-0.30307
	0.38876		0.194002		0.076459		-0.69338
	0.554742		-0.45382		0.085946		-0.84791
	0.883982		0.460078		0.873276		0.32059
	0.586507		-0.19792		0.622764		0.243211
	0.177859		-0.26697		0.197943		0.140513
	0.56473				-0.6392		0.057947
0.38449		-0.76365	0.062424	-0.73053			
0.152142		-0.50707	0.057372	-0.25889			
-0.0091		0.137338	-0.496	-0.05186			
0.015663		-0.76597	0.058555	0.042034			
-0.10479		-0.37164	-0.87557	-0.46343			
-0.01552		0.138929	-0.51953	0.049622			
-1		-0.79493	-1	-0.44593			
-0.55767		0.581088	0.101407	1			
<b>MAC</b>	0.96	<b>MAC</b>	0.7	<b>MAC</b>	0.7	<b>MAC</b>	0.85

Table 28. Modal parameters and MAC value of Step #7

STEP 9 (DS9)							
1° Mode		2° Mode		3° Mode		4° Mode	
<b>Frequency</b>	18.43	<b>Frequency</b>	28.13	<b>Frequency</b>	31.87	<b>Frequency</b>	36.97
<b>Damping</b>	0.016176	<b>Damping</b>	0.046303	<b>Damping</b>	0.037123	<b>Damping</b>	0.064006
<b>Mode shape</b>	0.113659	<b>Mode shape</b>	0.306481	<b>Mode shape</b>	0.039749	<b>Mode shape</b>	0.176138
	0.558503		-0.21802		0.069337		0.444179
	0.862112		-0.42627		0.125554		0.531692
	-0.09059		0.070868		-0.016		-0.19807
	0.273664		-0.68672		-0.11192		-0.37456
	0.564193		-1		-0.10488		-0.52657
	0.956795		0.334762		0.169883		0.290485
	0.778778		0.225351		0.116873		0.204584
	0.351448		0.1394		0.052289		0.163464
	0.59963		-0.33699		-0.09834		-1
	0.476373		-0.24318		-0.04976		-0.8268
	0.225931		-0.19183		0.024917		-0.25108
	0.222316		-0.35455		-0.63359		0.111125
	0.22039		-0.15188		0.035862		-0.07284
	0.281204		-0.7458		-1		-0.21316
	0.254378		-0.46764		-0.66084		0.193847
	-1		0.367092		-0.19162		-0.51507
	-0.48124		0.637318		0.080886		0.83152
<b>MAC</b>	0.92	<b>MAC</b>	0.1	<b>MAC</b>	0.2	<b>MAC</b>	0.85

Table 29. Modal parameters and MAC value of Step #9

As in the previous tests of three-storey frame and box beam, also, in this case, the decrease of frequency is demonstrated. Figure 113 shows the trend of the first four natural frequencies of the third campaign and the interpretation of the curve is complex. In the post-relaxation phase, the first four frequencies increase (for example the first frequency rises to 19.84 Hz) and this meaning that relaxation raises the boundary condition stiffness. In fact, after the second campaign the pier was almost completely suspended. This phenomenon is mainly visible on the first and fourth modal shape, probably due to a more stable behaviour. Subsequently, the frequencies decrease linearly increasing the settlement of the pier. In Step #6 the fourth natural frequency is overestimated, probably due to presence of noise measurements.

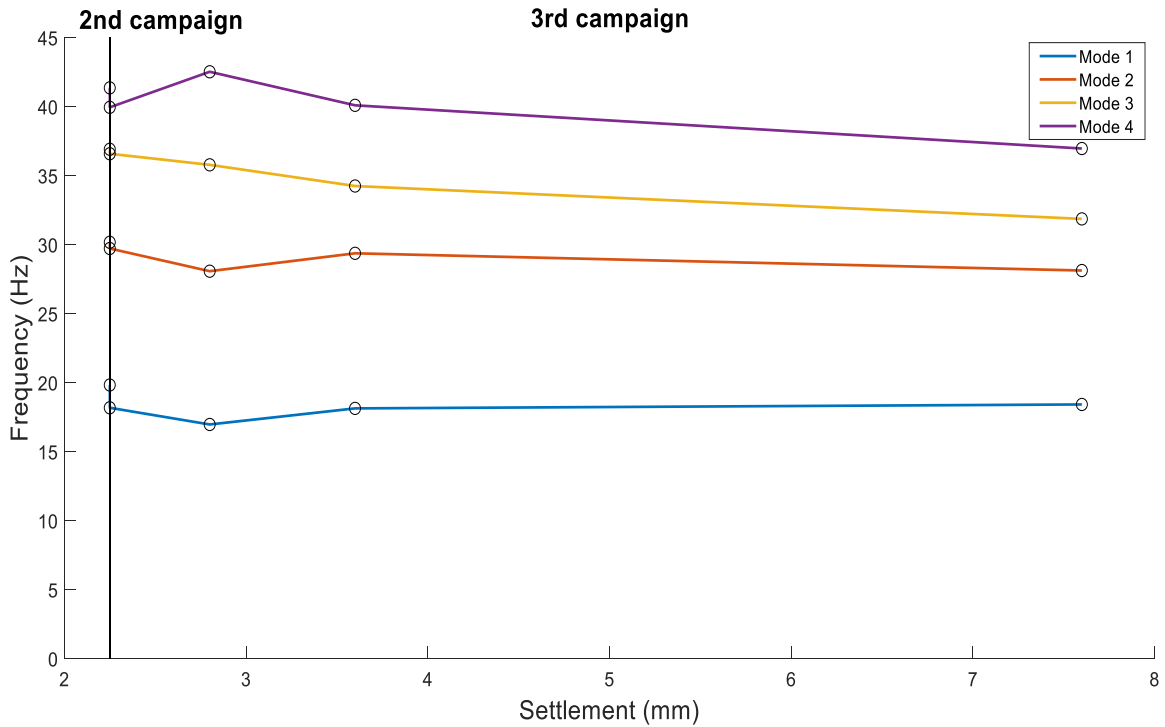
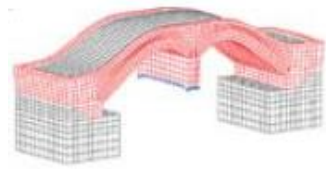
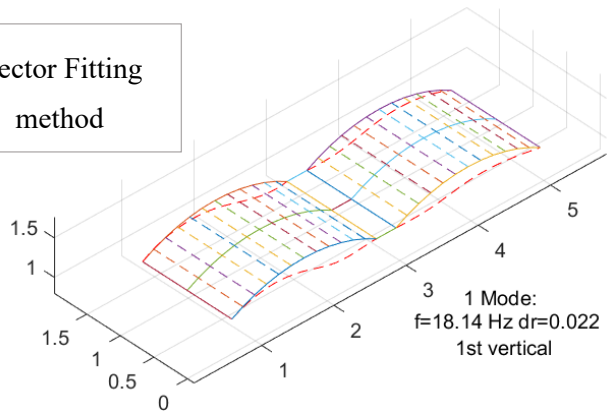


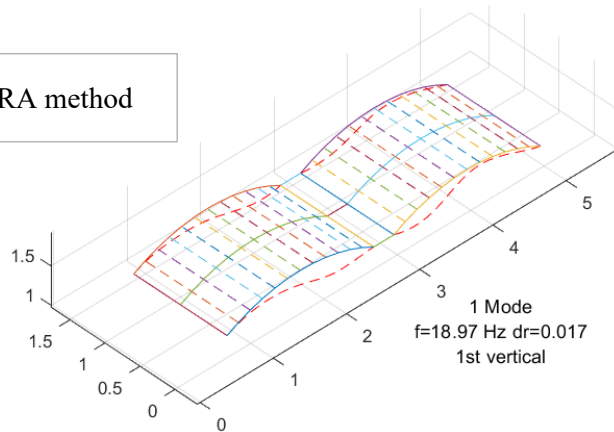
Figure 114. Natural frequencies of the first four modes through the various damage steps (left side: 2nd campaign, right side: 3rd campaign)

Differently from the natural frequencies and the damping ratios, the identified mode shapes were not significantly affected by the addition of the masses on the bridge deck. In order to clarify the significance of these results, a comparison is made with the identification obtained with Eigensystem Realization Algorithm (ERA) present in Ruocci, et al. (2013). The ERA method was used to analyse the free decay responses and it works in time-domain (Section 3.3). It should be underline that in this dissertation different comparison algorithms have been proposed in order to show a wider vision of the reliability of Vector Fitting method. In the following figures, the confrontation is reported in order to illustrate the possible difference between the two methos. The mode shapes are plotted by using a Matlab R2018b code developed by Ruocci, et al. (2013).

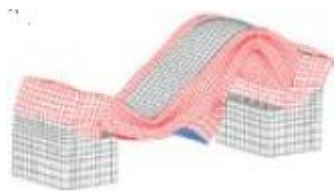
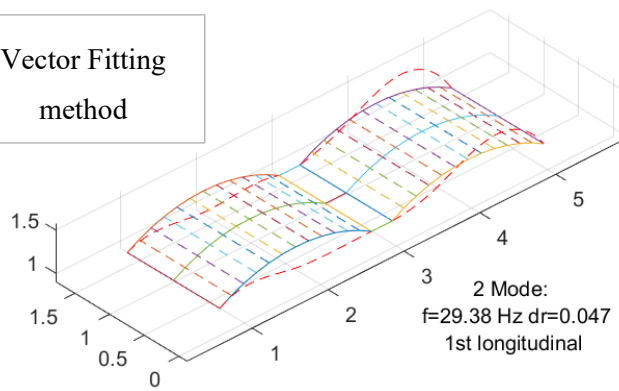
Vector Fitting  
method



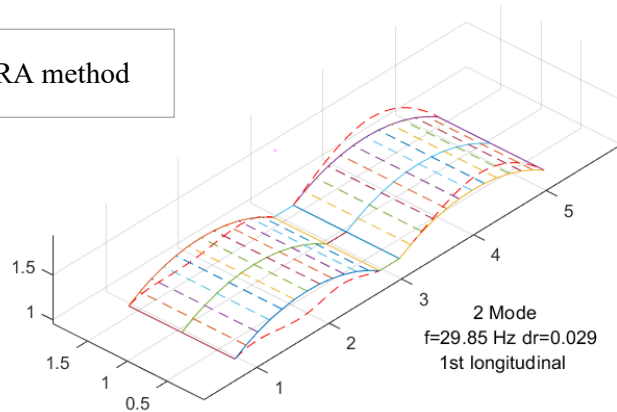
ERA method



Vector Fitting  
method



ERA method



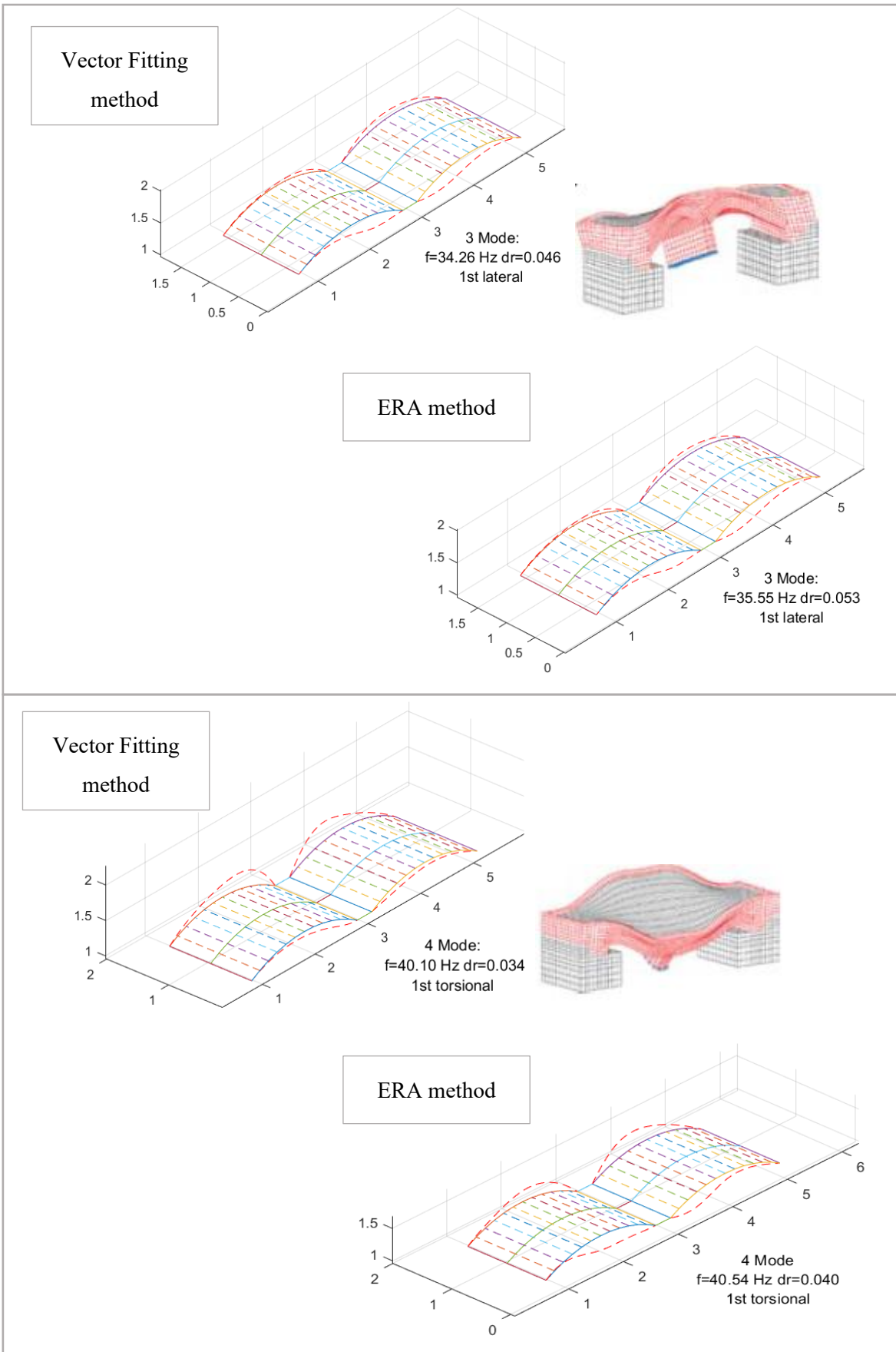


Figure 115. Experimental modal shapes (on the left obtained from VF; on the right obtained from ERA)

## 8 Conclusion

In this dissertation we have presented a new formulation of a parameter estimation technique called Vector Fitting that has been implemented for modal analysis of mechanical systems, such as civil systems. Vector Fitting is commonly used in electronic engineering, from high-voltage power systems to microwave systems and high-speed electronics. But being known the analogy between mechanical and electronic systems, the algorithm can be easily extended in mechanic and civil field. It works directly with Frequency Response Function (FRF) data in the frequency domain and the solved iteratively until convergence. We have used it on a wide variety of numerical measurements which contained various degrees of noise in order to validate the method. Subsequently, it was applied on several experimental test with undamaged and damage states. The first two cases are a prototype airwing and a cantilever box beam developed in the laboratory of Cranfield University. The beam is characterized by two u-shaped slots and it is interesting to show the change of the frequencies increasing the length of the notches. The damage conditions are linear. The second and also most important case consists in an aluminium three-storey frame that has been performed in the Engineering Institute (EI) at Los Alamos National Laboratory (LANL). In this case we analyse both linear (changing stiffness and mass) and non-linear (introducing a bumper and a suspended column) damage states. In this case Vector Fitting works as a linear fitting of a nonlinearity data sets. We have found this method to be comparable to the Rational Fraction Polynomials (RFP) method in terms of execution speed and accuracy and to the N4SID time-domain method.

The last experimental test is the masonry arch bridge placed in the laboratory of the Department of Structural, Geotechnical and Building Engineering of the Polytechnic of Turin. The high number of degrees of freedom, the non-linearity of material, the noise data will lead to a complex analysis. Despite this, the algorithm has shown its robustness and ability in the identification process. This is why, researchers often prefer frequency domain methods, which can improve, differently from the time domain techniques, the accuracy of the results considering the residual terms.

The confidence of the results has been estimated by using modal criteria, such as Modal Assurance Criterion (MAC), stabilisation and cluster diagrams and statistical relations. In summary, we can conclude that the salient features of the parameter estimation method presented in this work are sufficiently accurate and fast.

# Figure Index

Figure 1. A damped sinusoidal function and its spectrum (mirrored function at negative frequencies shown for completeness) .....	5
Figure 2. Receptance, mobility, inertance (Silva, 1978).....	9
Figure 3. On the left the real part of receptance and on the right the imaginary part (example with $m=1$ kg, $k=100$ N/m and $c=0.6$ Ns/m) ( (Maia & Silva, 1997).....	10
Figure 4. Nyquist plot of FRF (example with $m=1$ kg, $k=100$ N/m and $c=0.6$ Ns/m) (Maia & Silva, 1997).....	10
Figure 5. On the left the magnitude of receptance and on the right the phase (example with $m=1$ kg, $k=100$ N/m and $c=0.6$ Ns/m) ( (Maia & Silva, 1997) .....	11
Figure 6. Definition of Transfer Function.....	12
Figure 7. Schematic representation of the input-output and output-only identification methods ( (Ruocci G. , 2009).....	14
Figure 8. Nyquist plot of the receptance, showing the SDOF circle-fit approach (Maia & Silva, 1997) .....	15
Figure 9. Mechanical and electrical analogy.....	19
Figure 10. Mechanical system.....	20
Figure 11. Electrical system: mobility analogy.....	20
Figure 12. Electrical system: impedance analogy.....	21
Figure 13. Different definitions of Transfer Function.....	22
Figure 14. The pole-zero plot for a second-order system and its frequency response functions (MIT, 2004).....	27
Figure 15. S-plane nomenclature .....	28
Figure 16. Response of system under a damped excitation: demonstration of trend of pole (Marconi, 2010).....	30
Figure 17. The specification of the form of components of the homogeneous response from the system ( (MIT, 2004) .....	31
Figure 18. Weighting scheme (Gustavsen, 2008).....	34
Figure 19. Flow chart: experimental modal analysis (Giovanni Fabbrocino, 2007).....	39

Figure 20. Three masses frame scheme (on the left) and structure matrices (on the right) .....	44
Figure 21. Excitation force (on the top) and displacement response (on the bottom).....	45
Figure 22. FRFs of the response Channels 1-3 (plotted with reduced range of frequency 0-50Hz) .....	46
Figure 23. Vector Fitting process in the range of frequency 0-150 Hz (magnitude and phase)..	47
Figure 24. Vector Fitting process in the range of frequency 0-50 Hz (magnitude and phase)....	48
Figure 25. Trend of VF poles in comparison with demonstration is Section 4.4.3 .....	50
Figure 26. VF mode shapes of three storey frame test .....	51
Figure 27. Correlation between numerical and VF parameters: on the top the linear regression (left) and percentage of error (right) between numerical and VF frequencies, on the bottom correlation between numerical and VF mode shapes with MAC.....	52
Figure 28. FRFs of the response Channels 1-9 .....	54
Figure 29. Comparison between model response and the corresponding raw data and trend of poles. ....	56
Figure 30. Correlation between numerical and VF parameters: on the top the linear regression (left) and percentage of error (right) between numerical and VF frequencies, on the bottom correlation between numerical and VF mode shapes with MAC.....	57
Figure 31. Comparison between model response and the corresponding raw data for noise percentage 1-10% of signals: on the left the magnitude and on the right the phase .....	60
Figure 32. Evolution of the trend of poles of 9Dof (noise percentage 1-10%) .....	62
Figure 33. Noise in input and output signals. On the top: [%] error numerical vs VF frequency (on the left), [%] Error numerical vs VF damping (on the right); MAC value between numerical vs VF mode shape .....	63
Figure 34. Noise in input signal. On the top: [%] error numerical vs VF frequency (on the left), [%] Error numerical vs VF damping (on the right); MAC value between numerical vs VF mode shape.....	64
Figure 35. Noise in output signal. On the top: [%] error numerical vs VF frequency (on the left), [%] Error numerical vs VF damping (on the right); MAC value between numerical vs VF mode shape.....	65
Figure 36. RMSE value to the increase of noise level and the number of iterations for each case studies: noise in output signals (on the top on the left), noise in input and output signals (on the top on the right), noise in input only (on the bottom) .....	66

Figure 37. Test structure (Civera, Fragonara, & Surace, 2019) .....	67
Figure 38. Lateral view (Civera, Fragonara, & Surace, 2019) .....	68
Figure 39. Experimental setup: Modal shaker, high-speed video camera and laser velocimeter (on the left) and IMU sensors' position along the wing (on the right) (Civera, Fragonara, & Surace, 2019) .....	69
Figure 40. Global and local reference system (Civera, Fragonara, & Surace, 2019) .....	70
Figure 41. Acceleration histories for 4 IMUs (dwelling and free decay) .....	71
Figure 42. FRFs of Channels 1-4 .....	71
Figure 43. VF magnitude for the range 5.3-5.5 Hz (first mode) .....	72
Figure 44. VF phase for the range 5.3-5.5 Hz (first mode) .....	72
Figure 45. On the top: modal parameters calculated with VF process (on the right) and with FEM analysis (on the left). On the bottom: MAC value .....	73
Figure 46. FEM airwing model (manual calibrate): representation of first mode .....	74
Figure 47. First mode shape of wing with Vector Fitting analysis .....	75
Figure 48. Experimental Setup .....	76
Figure 49. Lateral view of the cantilever box beam .....	77
Figure 50. Box beam lateral view: in black different level of slots (5,10,15 mm) .....	78
Figure 51. Force time history (on the left) and response time history (on the right) .....	79
Figure 52. FRF $H(f)$ of channel 1 .....	80
Figure 53. Magnitude of transfer function fitted by VF technique for Step #5 (N=2) .....	80
Figure 54. Magnitude of transfer function fitted by VF technique for Step #5 (N=10) .....	81
Figure 55. Phase of transfer function fitted by VF technique for Step #5 (N=2) .....	81
Figure 56. Phase of transfer function fitted by VF technique for Step #5 (N=2) .....	82
Figure 57. Poles of VF technique for Step #5 (N=2) .....	82
Figure 58. Poles of VF technique for Step #5 (N=10) .....	83
Figure 59. FRFs of the response at channel 1 for State #4, State #5, State #6 and Step #7 .....	84
Figure 60. Clustering diagram for Step #4 .....	85
Figure 61. Stabilisation diagram for Step #4 .....	85

Figure 62. Clustering diagram for Step #7 .....	86
Figure 63. Stabilisation diagram for Step #7.....	86
Figure 64. Evolution of the first frequency obtained from VF process and from video and comparison with undamaged condition.....	87
Figure 65. Test structure (Figueiredo, Park, Figueiras, Farrar, & Worden, 2009).....	88
Figure 66. Details of test structure setup (Figueiredo, Park, Figueiras, Farrar, & Worden, 2009) .....	89
Figure 67. Dimensions of the three-story structure (dimensions are in cm) (Figueiredo, Park, Figueiras, Farrar, & Worden, 2009).....	90
Figure 68. Structural details about the damage conditions (Figueiredo, Park, Figueiras, Farrar, & Worden, 2009).....	92
Figure 69. Force-time history from Channel 1 of State #1 .....	93
Figure 70. Acceleration-time history from Channels 2-5 of State #1 .....	93
Figure 71. FRFs of Channels 2-5 of State #1 .....	94
Figure 72. FRFs (based on ten averages) of the response at Channel 2 and the excitation force at Channel 1 for State #1 (baseline) and State #9 (87.5% stiffness reduction in column 3AD and 3BD).....	94
Figure 73. FRFs (based on ten averages) of the response at Channel 2 and the excitation force at Channel 1 for State #1 (baseline), State #14 (gap = 0.05 mm), and State #17 (gap= 0.10 mm and 1.2-kg added mass on the first floor).....	95
Figure 74. Building model of the test structure (Figueiredo, Park, Figueiras, Farrar, & Worden, 2009) .....	96
Figure 75. Magnitude of Vector Fitting curve for Step #1.....	96
Figure 76. Phase of Vector Fitting curve for Step #1.....	97
Figure 77. Stabilisation diagram over Vector Fitting identification for increasing model order and $\delta f < 0.5\%$ , $\delta \xi < 10\%$ and $(1-MAC) < 10\%$ .....	98
Figure 78. Cluster diagram.....	98
Figure 79. Vector Fitting and Numerical mode shapes of the State#1 (baseline condition).....	99
Figure 80. Correlation between Vector Fitting and Numerical mode shapes by MAC. ....	99
Figure 81. Amplitude of the mean of FRF over 50 realisations using Peak Picking method for Step #1.....	100

Figure 82. Phase of the mean of FRF over 50 realisations using Peak Picking method for Step #1 .....	101
Figure 83. Vector Fitting and Peak Picking mode shapes of the State#1 (baseline condition). 101	
Figure 84. Correlation between Vector Fitting and Peak Picking mode shapes by MAC. ....	102
Figure 85. Magnitude of VF process of State #14 .....	103
Figure 86. Phase of VF process of State #14 .....	104
Figure 87. A plot of normal distribution (or bell-shaped curve) where each band has a width of 1 standard deviation (MIT, 2012) .....	105
Figure 88. Box plot for frequency (second, third and fourth mode for 17 steps of damage) ....	109
Figure 89. Box plot for damping (second, third and fourth mode for 17 steps of damage) .....	110
Figure 90. View of masonry arch bridge in the laboratory of Politecnico di Torino .....	112
Figure 91. Geometric details of the masonry arch bridge model: front view(a), plan (b) and lateral sections (c) (Ruocci G. , 2009).....	112
Figure 92. The arch bridge model construction: reinforced concrete blocks formworks.....	113
Figure 93. The arch bridge model construction: reinforced concrete block and masonry abutment .....	114
Figure 94. Construction details .....	115
Figure 95. Details tests on mortar samples: three points bending test (a), compressive test (b) (Ruocci G. , 2009).....	116
Figure 96. Shear test on masonry samples: experimental device (a), transducers deployment on the specimen (Ruocci G. , 2009).....	116
Figure 97. Four points bending test on the segments of the ridge arch: geometric details (Ruocci G. , 2009).....	117
Figure 98. Four points bending test on the bridge: experimental device (a), transducers deployment on the specimen (b), specimen failure (c), failure particular (d).....	117
Figure 99. Damage steps, middle settlement, pier rotation, polystyrene removed (Ruocci, Fragonara, Quattrone, Stefano, & Ceravolo, 2013) .....	119
Figure 100. Experimental test timeline (Ruocci, Fragonara, Quattrone, Stefano, & Ceravolo, 2013) .....	120
Figure 101. Test equipment.....	120

Figure 102. PCB capacitive accelerometer: model 3701G3FA3G (a), cross-section for the “0g” condition (b), cross-section for the “1g” condition (c) [www.pcb.com].....	121
Figure 103. The arch bridge model construction: testing of the settlement application system	122
Figure 104. Description of Setup #1 and Setup #2.....	123
Figure 105. Scheme of accelerometers positioning: Setup#1 (1), Setup#2 (2).....	124
Figure 106. Hammer force-time history for Setup 1 (Step #7) .....	126
Figure 107. Acceleration-time histories from Channels 1-18 for Setup 1 (Step #7).....	126
Figure 108. Acceleration-time histories selected of Channel 1-18 (on the top) and the corresponding time history of the third hammer impact (on the bottom) .....	127
Figure 109.FRFs for Channels 1-18 for Setup 1 (Step#7) .....	127
Figure 110. Curve fitting example for the FRFs from Channels 1–18 of State #7 (top side the magnitude and bottom side the phase) .....	129
Figure 111. PSD of acquired signals for Setup1 (Step#7) .....	129
Figure 112. Stabilisation diagram for Setup 1 (Step #7).....	130
Figure 113. Clustering diagram for Setup 1 (Step #7) .....	131
Figure 114. Natural frequencies of the first four modes through the various damage steps (left side: 2nd campaign, right side: 3rd campaign).....	135
Figure 115. Experimental modal shapes (on the left obtained from VF; on the right obtained from ERA) .....	137

# References

- A.Fiore, G. (2007). *Formulazione inversa per verifica strutturale mediante tecniche di acquisizione in campo dinamico*. Milano: Congresso nazionale AIPnD.
- Brüel, & Kjaer. (1988). *Structural Test Part 2- Modal Analysis and Simulation*.
- Bin Du, Yiheng Wei, Shu Liang, Yong Wang. "Rational approximation of fractional order systems by vector fitting method", *International Journal of Control, Automation and Systems*, 2016.
- Bonato, P., Ceravolo, R., De Stefano, A., Molinari, F., (2000) "*Cross-time frequency techniques for the identification of masonry buildings*". *Mechanical systems and signal processing*.
- Bjorn Gustavsen. "Comments on "a comparative study of vector fitting and orthonormal vector fitting techniques for EMC applications"", 2007 18th International Zurich Symposium on Electromagnetic Compatibility, 09/2007.
- Carlo Cappello, Daniele Zonta, Hassan Ait Laasri, Branko Glisic, Ming Wang. "Calibration of Elasto-Magnetic Sensors on In-Service Cable-Stayed Bridges for Stress Monitoring", *Sensors*, 2018
- Ceravolo, & Abbiati. (2013). *Time Domain Identification of Structures: Comparative Analysis of Output-Only Methods*.
- Civera, Fragonara, Z., & Surace. (2019). Using Video Processing for the Full-Field Identification of Backbone Curves in Case of Large Vibrations.
- Farrar, C. R., Worden, K. (2007); "An introduction to structural health monitoring".
- Farrar, "Case Studies", *Structural Health Monitoring A Machine Learning Perspective*, 2012.
- Ferranti F. et al, (2010). *Variance Weighted Vector Fitting for Noisy Frequency Responses*. *IEEE MICROWAVE AND WIRELESS COMPONENTS LETTERS*, 2010.
- Figueiredo, E., Park, G., Figueiras, J., Farrar, C., & Worden, K. (2009). *Structural Health Monitoring Algorithm Comparisons Using Standard Data Sets*.
- Formenti, M. H. (1982). *PARAMETER ESTIMATION FROM FREQUENCY RESPONSE MEASUREMENTS USING RATIONAL FRACTION POLYNOMIALS*.
- Giovanni Fabbrocino, C. R. (2007). *L'analisi dinamica sperimentale e il monitoraggio delle strutture esistenti*. Università degli Studi del Molise, Consorzio ReLUIS; Università degli Studi di Napoli, Consorzio ReLuis.
- Giua, A., & Seatzu, C. (2009). *Analisi dei sistemi dinamici*.

- Grivet-Talocia, S. (2006). *Improving the Convergence of Vector Fitting for Equivalent Circuit Extraction From Noisy Frequency Responses*.
- Gustavsen, B. (2006). Improving the Pole Relocating Properties of Vector Fitting. IEEE TRANSACTIONS ON POWER DELIVERY, VOL. 21, NO. 3, JULY 2006
- Gustavsen, B. (2008). USER'S GUIDE FOR VECTFIT3.m.
- Gustavsen, B., & Semlyen, A. (1999). RATIONAL APPROXIMATION OF FREQUENCY DOMAIN RESPONSES BY VECTOR FITTING. IEEE Transactions on Power Delivery, Vol. 14, NO. 3, July 1999.
- Hung, C.-F. "Identification of modal parameters from measured input and output data using a vector backward auto-regressive with exogeneous model", Journal of Sound and Vibration.
- Maia, N. M., & Silva, J. M. (1997). *Theoretical and Experimental Modal Analysis*.
- Marconi, P. L. (2010). *Trasformata di Laplace e Funzione di trasferimento*. Università di Bologna.
- MEKONNEN, Y. S. (2004). *IMPROVED HIGH-ORDER RATIONAL APPROXIMATION BY COMBINING*.
- MIT, M. I. (2004). *Understanding Poles and Zeros*.
- Mrozowski et al. (2008). *Macromodeling of Multiport Systems Using a Fast Implementation of the Vector Fitting Method*.
- Overschee, P. V., Moor, B. D., & Favoreel, W. (1997). *NUMERICAL ALGORITHMS FOR SUBSPACE STATE SPACE SYSTEM IDENTIFICATION (N4SID)*.
- R. Zanasi, R. M. (2006). *Controlli Automatici*.
- Richards, E. (2014). *Applications of Vector Fitting in the Solution of Electromagnetic Field Interactions*.
- Richardson, M., & Schwarz, B. (January 2003). Modal Parameter Estimation from Operating Data. *Sound and Vibration* .
- Ruocci, G. (2009). *Application of the SHM Methodologies to the Protection of Masonry Arch Bridges from Scour*. Torino.
- Ruocci, G., Fragonara, L. Z., Quattrone, A., Stefano, A. D., & Ceravolo, R. (2013). *Experimental Testing of a Masonry Arch Bridge Model Subject to Increasing Level of Damage*.
- Schoukens, R. P. (2001). *System identification: A Frequency Domain Approach*. New York.

- Serra, M., Festa, G., Ceravolo, R., Vassallo, M., Zollo, A., & Quattrone, A. (2016). *Damage detection in elastic properties of masonry bridges using coda wave interferometry*.
- Silva. (1978). *MEASUREMENTS AND APPLICATIONS OF STRUCTURAL MOBILITY DATA*. London.
- Systems, M. a. (2015). Musaf F.Badr.
- Wei-Xin Ren and Zhou-Hong Zong, *Output-only modal parameter identification of civil engineering structures*. China, 2004
- Worden, K., Manson, G., Fieller, N.R.J., (2000); "*Damage detection using outlier analysis*". Journal of Sound and Vibration.
- Yidnek S. Mekonnen, Jose E. Schutt-Aine. "Broadband macromodeling of sampled frequency data using z-domain vector-fitting method", 2007 IEEE Workshop on Signal Propagation on Interconnects, 2007
- Vincenzi L. (2007) *IDENTIFICAZIONE DINAMICA DELLE CARATTERISTICHE MODALI E DELLE PROPRIETÀ MECCANICHE DI STRUTTURE MEDIANTE ALGORITMI DI OTTIMIZZAZIONE*. Università di Bologna
- Zanotti L. F., & Pretrunin, I. (Cranfield University). *Experimental Modal Analysis*.



# Ringraziamenti

Al termine di questo percorso universitario ci terrei a ringraziare tutte le persone che mi sono state vicino e mi hanno permesso di raggiungere questo obiettivo.

Prima di tutto ci terrei a ringraziare il professore Rosario Ceravolo del Politecnico di Torino che mi ha dato l'opportunità di svolgere questo interessante tema di ricerca e di avere un'esperienza di ricerca e di crescita personale all'estero.

Ringrazio il professore Luca Zanotti Fragonara presso Cranfield University e il dottorando Marco Civera del Politecnico di Torino per avermi accompagnata in questo percorso di tesi all'estero e per i loro preziosi consigli.

Il ringraziamento più grande va ai miei genitori che mi hanno sempre sostenuta in questo percorso e ascoltata quando ne avevo più bisogno, senza di loro tutto questo non sarebbe stato possibile. Allo stesso modo vorrei ringraziare mia sorella Elisa che mi ha incoraggiata con la sua positività.

Un grazie di cuore va al mio gruppo di amici di Torino, in particolare a Debora, che si sono dimostrati grandi compagni di studio e con i quali ho passato le serate più belle e calorose. Allo stesso modo un pensiero va alle mie amiche di Firenze che mi hanno insegnato che la distanza non ha alcun valore se dietro c'è una grande amicizia. Un ringraziamento particolare va alla mia coinquilina Felicia dal carattere generoso e solare.

Infine ringrazio i miei nonni che con la loro infinita dolcezza mi sono stati vicini anche a distanza.